# Application of Hyperpolarised Helium-3 in Lung Functional Magnetic Resonance Imaging

by

Marius Ovidiu Mada, MSc

Thesis submitted to

The University of Nottingham

for the degree of Doctor of Philosophy

May 12, 2009

*... to my son*

# Acknowledgments

I want to first thank my son, Nicholas, for choosing to come into life in Nottingham, such a lovely place.

This research was funded through the EU Marie Curie Early Stage Training Program which provided me with a grant during these years. Also, The Welcome Trust funded the clinical study that was started during this research.

Over these years nothing was more important than having a wonderful supervisor, a true friend to trust. So, I thank John Owers-Bradley for being all of these and more. Thanks also to his wife, Lindsey, his great kids, Alasdair and Harriet and charming cat, Maximus. They all helped me learn to live and cherish life.

My thanks go to the only Taiwanese I know, Jau-Yi Wang, for helping me with physics problems, chocolate and delicious food.

Special thanks for my successor Iain Ball for great lectures on stars and supernovas, nice lattes and huge support. Also I would like to thank Ruslan Garipov for his great commitment and high expertise in Matlab and more. Thank you guys for a real good team.

I can not forget the team from Leicester: Professor Mike Silverman, Dr. Caroline Beardsmore, Manjith Narayanan for their great support and expertise. Also, thanks go to Sian Williams and Ketna Parmar for helping me with the kids.

Thanks have to go to Kuldeep Panesar, Ananth Venkatesan and Kunal Lulla for the great curry nights and also for the breathing exercises.

I won't forget Dave Holt and Chris Pallender for their high spirit and help.

I want to thank all volunteers and their family for their invaluable support for this research and future outcomes.

Family is always last, but not least. Again thank you to my lovely wife, Anya for pushing me forward to finish this job. Thank you to our gorgeous son, Nicholas for everything he is and does.

And, thank you, my dear reader for choosing to read this work.

# Abstract

Looking inside the lungs without the danger of ionizing radiation side effects became available with magnetic resonance imaging using hyperpolarised noble gases. This technique has the potential to become a real tool for assessing *in vivo* ventilation, perfusion and even lung microstructure.

The work covered in this research was aimed to improve the existing method for $^3$He polarisation and open the possibility to develop new modalities to probe the lung microstructure that could then be used in clinical trials. For this purpose, the polarisation facility was remodeled and new components were added. The rest of the work was focused on developing diffusion techniques that are more appropriate for the assessment of lung diseases.

The improvement of the $^3$He polarisation facility consisted in the optimization of the gas flow path, implementation of a new dispensing method and new controlling protocol. The capacity of the polarisation system was increased by using a more powerful laser. The outcome of this was an increase in polarisation rate and a significant reduction of the dispensing time. Altogether this allow for clinical studies to be performed without too much delay.

A clinical study aimed to distinguish differences between children born at term and premature was started on 70 volunteers. Three methods for measuring diffusion were used: spin echo diffusion weighted method, SPAMM tagging and MR diffusion spectroscopy. The first was previously used in the group and the last two were developed during this research. The results were correlated with basic pulmonary functional tests (spirometry and plethysmography) and also with the multiple breaths nitrogen wash-out results. No differences were found in the two groups. The results don't agree with the current theories on lung growth and suggest that alveolarisation occurs even after the age of 8, possibly up to adult age. This is very important to be investigated further due to its clinical importance.

# Publications

Mada M. O., Owers-Bradley J. R., Narayanan M., Silverman M., Wang J-Y. and Beardsmore C.S. Assessment of Peripheral Airways Development after Preterm Birth by Hyperpolarised $^{3}$He. *Proceedings of International Society for Magnetic Resonance in Medicine*, Toronto, 2008.

Narayanan M., Mada M.O., Owers-Bradley J.R., Beardsmore C.S., and Silverman M. Acinar Development after Preterm Birth. *Proceedings of American Thoracic Society International Conference*, Toronto, 2008.

# Contents

# List of Figures

# List of Tables

# Chapter 1

# Introduction

## 1.1 Preamble

Respiratory disorders are a major cause of death in Europe and world wide. In some countries, including UK, it is already the leading killer. Lung cancer, pneumonia and chronic obstructive pulmonary disease (COPD) are the main respiratory causes of death in Europe. The total financial burden of lung disease in Europe amounts to nearly 102 billion per year. COPD contributes almost one half of this figure, followed by asthma, pneumonia, lung cancer and tuberculosis. Despite this, methods to investigate and treat these patients remain relatively undeveloped.

Up to this moment we lack the techniques for probing the lung development and physiology. The existing modalities are not safe enough to be used on a large scale to monitor longitudinally the lung evolution. Also, they can not be used intensively in the early stage of development and can not provide an early diagnosis of diseases.

First attempts to measure lung function go back to 200 AD when Galen did do a volumetric experiment on human ventilation. He had a boy breath in and out of a bladder and found that the volume of the gas was, after a period, unchanged. The modern spirometry was brought by Hutchinson in the 19th century. Together with plethysmography, also developed in late 19th century, these are the most used methods for measuring flows and pulmonary volumes. These tests allow quantitative measurement of the function of an individual's lungs but can not provide direct measures of lung physiology and disorder.

The use of imaging technique like radionuclide imaging and X-ray Computed Tomography (CT) is prone to hazards due to the associated risk of exposure to ionizing radiation. The radionuclide imaging has very poor resolution and CT can not detect airways below the 10th generation, where gas exchange takes place.

Magnetic Resonance Imaging (MRI) offers the benefits of CT without the danger of ionizing radiation but it is not suitable for imaging the lungs due to the low fraction of polarised protons (5 in $10^6$ at 1.5 T). The density of protons in the lungs is very low and the differences in susceptibility between air and lung tissue generate magnetic field inhomogeneities which lead to signal loss and image distortion. These susceptibility effects increase with the field strength of the magnet. These limitations have restricted the resolution of MR images to around the 8th generation [1].

With hyperpolarised $^3$He MRI the polarisation is obtained using optical pumping. Good signal to noise ratios can be obtained even at low static magnetic field. A series of applications of hyperpolarised $^3$He MRI exists starting with static ventilation images that can identify regions with no ventilation in asthma patients. Dynamic imaging can provide information about the mobility of the aerosol [2], [3], [4], [5], [6], [7], [8], [9], [10]. Hyperpolarised $^3$He is very sensitive to the oxygen in the lungs. The paramagnetic nature of the latter will reduce the longitudinal relaxation time of $^3$He ($T_1$) in the lung [11], [12], [13], [14], [15]. This effect can be used to measure the partial pressure of oxygen within the lung and, consecutively, probe the lung perfusion. The size of lung microstructure can be assessed by measuring how fast $^3$He can diffuse within the lung. A single measurement can be made globally, for both lungs, or a diffusion map can be produced showing the differences in diffusion at different locations in the lung. Gas diffusion is restricted by the alveolar wall which translates in a smaller apparent diffusion coefficient in small peripheral airspaces and a larger apparent diffusion coefficient where the peripheral airspace size is enlarged due to poor lung development or lung damage.

This thesis focuses on probing the potential of $^3$He diffusion for lung functional MRI.

## 1.2 Overview of the Thesis

The thesis is divided into three parts. The first part, chapters 1, 2 and 3, give preliminary details about the field and the equipment used in this research. The second part, chapters 4 and 5, covers the experiments undertaken during this research. Finally the last part, chapter 6, draws conclusions from the research.

Chapter 1 gives an introduction to the field of the research.

Chapter 2 describes important aspects of the lung looking at anatomy, physiology and pathology. The second part of this chapter reviews the existing imaging techniques for lung investigation in order to prepare the terrain for the MRI with hyperpolarised $^3$He

Chapter 3 starts with an overview of the NMR and MRI principles. It then discusses the physics of metastable optical pumping of $^3$He and also includes a discussion on the diffusion effect in NMR.

Chapter 4 presents the work done on improving the $^3$He gas production and administration. Next, it details the results of the magnetic field orientation dependance experiment. Finally the specific constraints of using hyperpolarised gases are detailed and the available imaging techniques are described.

Chapter 5 starts with an introduction on the power of diffusion as a tool for lung description. The theory behind the diffusion and aspects of signal decay due to diffusion are presented next. A detailed description of the three methods for measuring diffusion used in this work is also presented in this chapter. Finally, a description of the study on child lung development and the results are given.

Chapter 6 summarises the research that has been presented in the thesis.

# Chapter 2

# The Lung: Anatomy, Physiopathology and Imaging

Before going any further with presenting insights of lung hi-tech imaging it is necessary to understand the architecture and functionality of the lung. We need to get the feeling of what challenges the lung is posing. Following I will highlight just the important information that we know about the lungs and the transition from the classic investigation methods to the modern approach.

The role of the lung is to perform gas exchange - the extraction of oxygen from the environment and elimination of carbon dioxide. In addition to its primary role in gas exchange, the lung serves a number of metabolic functions. These include production of surfactant and other compounds and metabolism of a variety of chemical mediators. Derangements in these functions can have a profound impact on the lung's ability to carry out gas exchange.

Lung diseases can affect the individual physiologic steps involved in gas exchange. For example, the obstructive airway diseases impede gas flow into and out of the alveoli, whereas the restrictive lung diseases disturb the relationship between ventilation and blood flow or create a barrier for diffusion of gas. The function of the lung is closely coupled to its structure; that is, form follows function.

## 2.1 Elements of Lung Anatomy

As with all other organs, lung anatomy varies from person to person and from healthy to unhealthy subjects. The anatomy changes with the respiratory cycle and, contrary to the automatic movement of the heart, the lungs have a mixed movement, automatic and voluntary, with an irregular frequency and amplitude. This causes the imaging to be more complicated and the results very variable.

### 2.1.1 Generalities

The lungs are encompassed by the chest wall on all sides and by the diaphragm inferiorly. The gas-exchanging function of the lungs is profoundly affected by the mechanical properties of the chest wall and diaphragm. Movement of the lungs within the thoracic cavity during respiration is facilitated by a space between the two structures - the *pleural space*- created by apposition of the inner lining surface of the chest wall, the *parietal pleura*, and the outer lining surface of the lung, the *visceral pleura*. The separation of the two linings is made by a thin film of pleural fluid which has also a lubricating role. Changes in pressure within the pleural space determines the inspiratory and expiratory airflow in healthy and diseased lungs.

The lungs are enclosed in a virtual space created by the pleurae extending medially. This compartment is called *mediastinum* and contains the major airways and great vessels.

### 2.1.2 Airway structure

The air arrives in the lungs through the trachea. The point of bifurcation into left and right main bronchi is at the level of *carina*. The airways may be viewed as a series of dichotomously branching tubes; each ”parent” airway gives rise to two ”daughter” branches (Fig. 2.1). On average, there are 23 generations of airways in the human lung. The first 16 are known as *conducting* airways because they provide a conduit for gas flow to and from the gas-exchanging regions of the lung. These include bronchi, bronchioles and terminal bronchioles. The last 7 generations include the respiratory bronchioles, alveolar ducts and alveolar sacs, all of which give rise to alveoli. The first-order respiratory bronchiole

(z=17 in Fig. 2.2 ) and all its distal gas-exchanging airways constitute a pulmonary *acinus* .

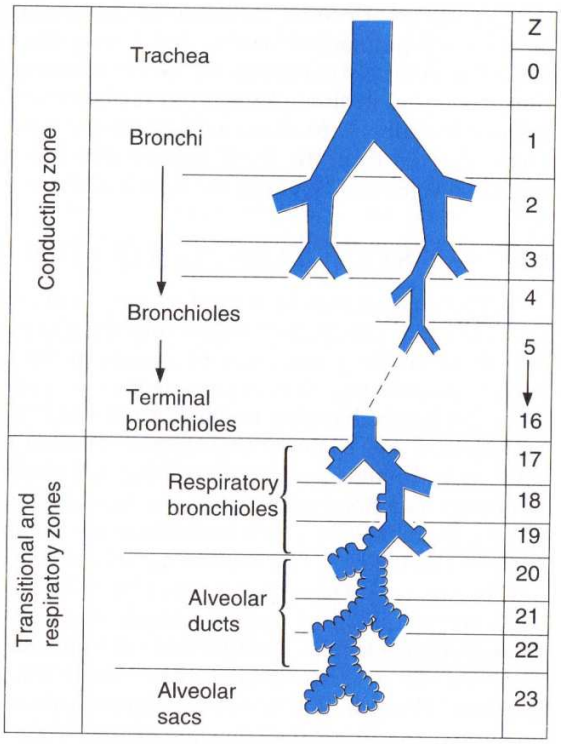


Figure 2.1: The tracheo-bronchial tree as a system of dichotomously branching tubes. The conducting zone, made up of the first 16 generations of airways to the level of the terminal bronchioles (z = 0-16), does not participate in the gas exchange. The transitional and respiratory zones, in which the gas exchange takes place, include the respiratory bronchioles, alveolar ducts, alveolar sacs, and alveoli (z = 17-23).(From Weibel ER. [16])

Although the diameter of each daughter branch is less than the diameter of the parent airway from which it is derived, the total cross-sectional area of each successive airway generation increases because of a marked increase in the number of airways (Fig. 2.3). The total exchange surface reaches 70 $m^2$ for 300 million alveoli [17]. Consecutive to this increase in surface area the gas flow rates decrease. Eventually, at the level of the respiratory bronchioles, gas movement occurs primarily by diffusion, rather than by "bulk flow". The alveoli can be modeled as spheres having diameters ranging from 75 $\mu m$ and 300 $\mu m$ [18]; in fact, they are polyhedrals [19] (Fig. 2.4).

Airway resistance is not distributed evenly throughout the respiratory system. Within

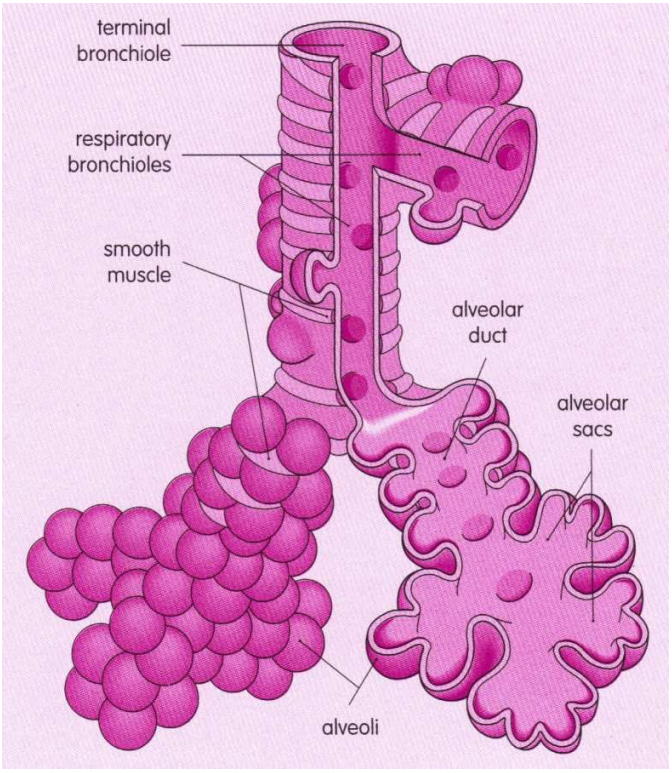


Figure 2.2: The acinus, or respiratory unit. This part of the airways is involved in gas exchange.

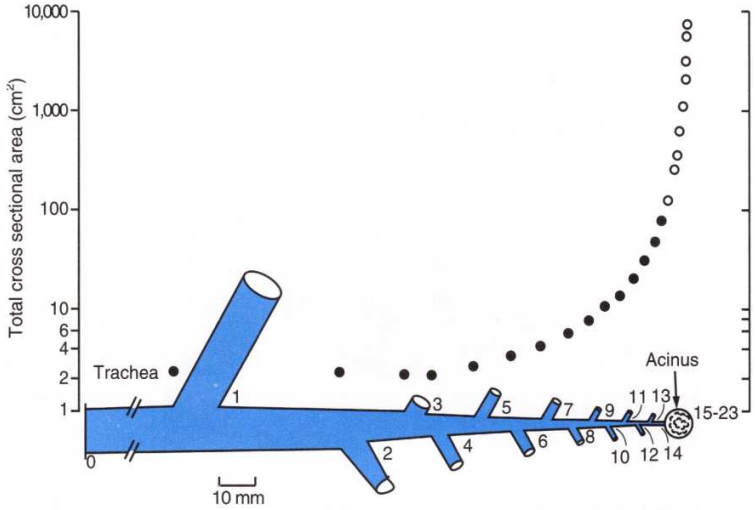


Figure 2.3: Total airway cross-sectional area in relation to airway generation. Although individual airway cross-sectional area decreases in succesive airway generations, total cross-sectional area increases markedly because of an increase in the number of airways. (From Weibel ER. [20])

the chest, the larger airways - trachea and lobar and segmental bronchi - provide 80% of the remaining airway resistance; small airways, less than 2 mm in diameter, contribute

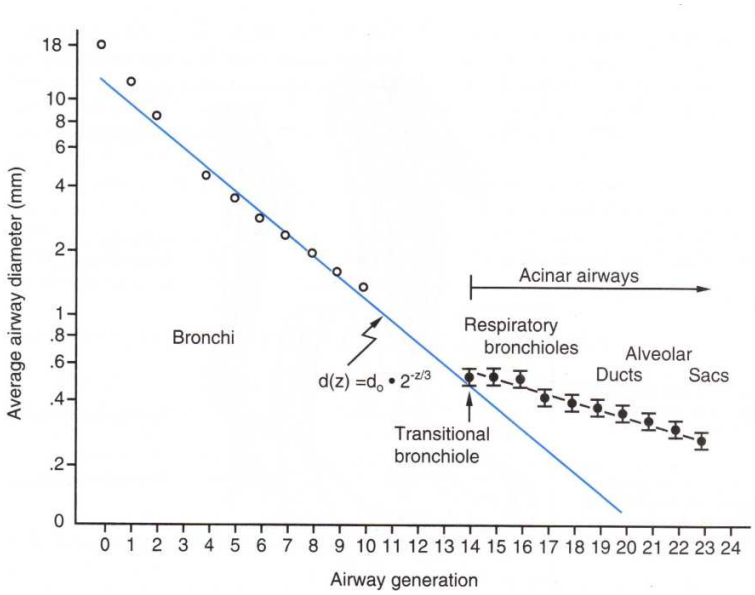


Figure 2.4: Average airway diameter as a function of airway generation. Individual airway diameter decreases in each successive generation of airways. For larger airways. to the level of the terminal bronchioles, airway diameter in a given generation (z) can be predicted if the diameter of the trachea ($d_0$) is known. (From Weibel ER. [21])

20%. The distribution of airway resistance is shown in Figure 2.5. Although the individual cross-sectional areas of the peripheral airways are small, their large number generates a large overall cross-sectional area and a lower resistance.

### 2.1.3 Vascularisation

The lung has a double arterial vascularisation: the pulmonary arteries bring blood with less oxygen, at low pressure and high debit; the bronchial artery delivers blood highly oxygenated, at high pressure and low debit, necessary for the perfusion of the conducting airways [22], [19].

## 2.2 Elements of Lung Physiology

The main function of the lung is the gas exchange between the air and the rest of the body, through the blood (oxygen intake and carbon dioxide outtake). This exchange, facilitated by the vast alveolar area, is realized between the air compartment (the tracheal bronchial

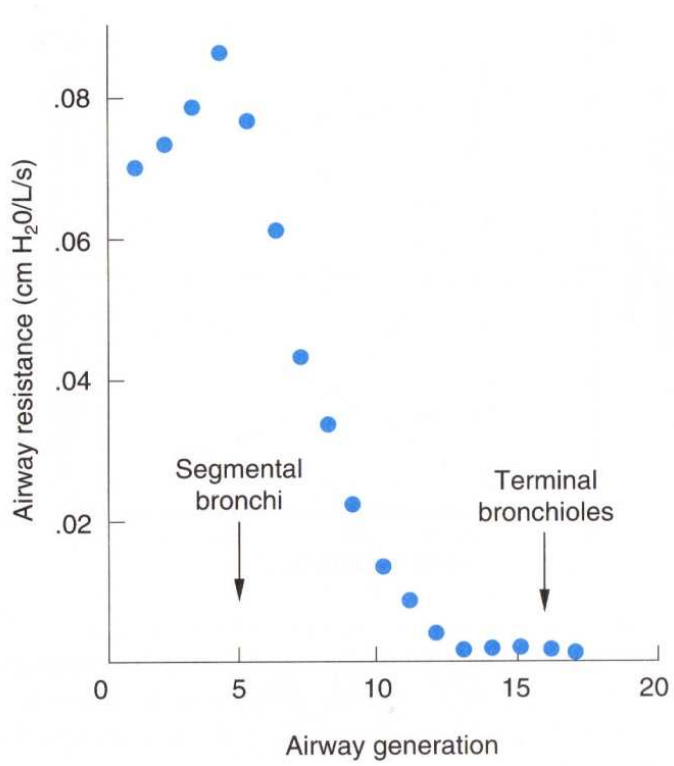


Figure 2.5: Variation of airway resistance with airway generation. Generation 0 is the trachea; higher generations of airways are denoted in moving from central to peripheral airways. (From Grippi M. [22])

tree) and the blood vessels.

Ventilation is the flow of air in and out of the respiratory system (breathing); it is defined physiologically as the amount of air breathed in and out in a given time. The function of ventilation is to maintain blood gases at their optimum level, by delivering air to the alveoli where gas exchange can take place. The movement of the air in and out of the lungs occurs due to pressure differences. The respiratory muscle brings about these pressure changes, but other factors are also involved, namely the physical properties of the lungs, including their elasticity and the resistance of the airways. Lung diseases that affect these physical properties therefore impair gas exchange by reducing the delivery of fresh gas to the lungs, ultimately leading to a mismatch in ventilation/perfusion ratio.

### 2.2.1 Anatomical dead space

Not all of the air entering the respiratory system actually reaches the alveoli and takes part in gas exchange. We need to introduce the concept of anatomical dead space, or those areas of the airway not involved in gaseous exchange. This space includes: nose and mouth, pharynx, larynx, trachea, bronchi and bronchioles, down to and including the terminal bronchioles.

The volume of the anatomical dead space ($V_D$) is usually about 150 ml (or 2 mL/Kg of bodyweight). Anatomical dead space varies with the size of the subject and also increases with increased inspiration because greater expansion of the lungs lengthens and widens the conducting airways. Anatomical dead space can be measured using Fowler's method, which is based on the single-breath nitrogen test (Fig. 2.6).

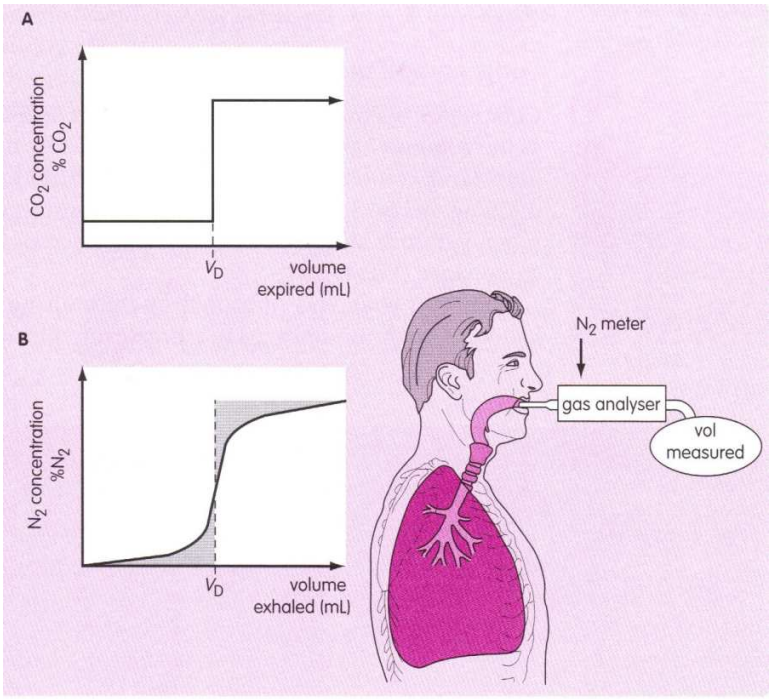


Figure 2.6: Measurement of the anatomical dead space. (A) using Fowler's method it would be expected that the gas expired from those areas not undergoing gaseous exchange (anatomical dead space) would contain no nitrogen and thus a stepwise change would occur to the nitrogen concentration of expired gas; the volume at which this occurs would be equal to the anatomical dead space volume. (B) In the real world, the dotted line shows the step change in nitrogen concentration and the solid line shows the actual change curve.

### 2.2.2 Physiological dead space

Even in the healthy lungs the anatomical dead space is not the only cause of ”wasted” ventilation. The total dead space is known as the physiological dead space and includes gas in the alveoli that does not participate in gas exchange.

*Physiological dead space* = *anatomical dead space* + *alveolar dead space*

Alveolar dead space comes about because gas exchange is less optimal in some parts of the lung. In a normal, healthy person, anatomical and physiological dead space are almost equal, alveolar dead space being very small ($<$ 5 mL). When lung disease alters ventilation/perfusion ratio, the volume of alveolar dead space increases.

Physiological dead space is calculated using the Bohr equation (2.1).

$$V_D/V_T = (P_ACO_2 - P_ECO_2)/P_ACO_2 \tag{2.1}$$

$V_D$ = Dead space volume, $V_T$ = Tidal volume, $P_A$C$O_2$ = Partial pressure of carbon dioxide in alveolar air, $P_E$C$O_2$ = Partial pressure of carbon dioxide in mixed expired air.

Normally, the partial pressures of carbon dioxide in alveolar gas and arterial blood are the same, hence:

$$V_D/V_T = (P_aCO_2 - P_ECO_2)/P_aCO_2 \tag{2.2}$$

### 2.2.3 Minute ventilation

Minute ventilation ($\dot{V}_E$) is the volume of gas moved in and out of the lungs in 1 minute and is normally 6-10 litres (Fig. 2.7).

The normal frequency of breathing varies between 12 and 20 breaths per minute. Normal tidal volume is approximately 500 mL in quiet breathing. Generally:

$$\dot{V}_E = V_T f \tag{2.3}$$

where $\dot{V}_E$ = minute ventilation, $V_T$ = tidal volume and $f$ = the respiratory rate (breaths/minute).

### 2.2.4 Alveolar ventilation

Since not all the air inspired reaches the alveoli, two values of minute ventilation need to be considered:

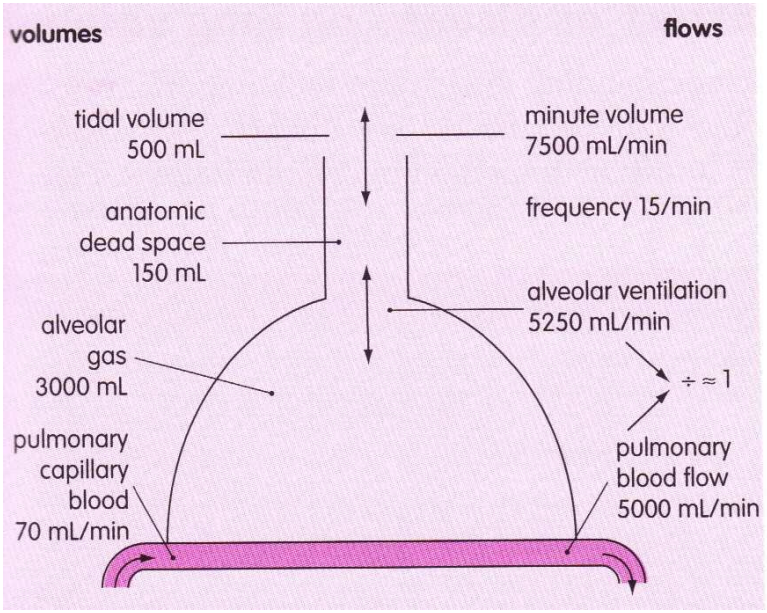


Figure 2.7: Ventilation in the simplified lung. (Criner & D'Alonzo 1999).

- Minute ventilation ($\dot{V}_E$), as described above;
- Minute alveolar ventilation ($\dot{V}_A$), which is the amount of air that reaches the alveoli in 1 minute.

For one breath:

$$V_A = V_T - V_D \tag{2.4}$$

where $V_A$ = the volume reaching the alveolus in one breath and $V_D$ = the volume of dead space. Hence, in 1 minute:

$$\dot{V}_A = (V_T - V_D)f \tag{2.5}$$

### 2.2.5 Distribution of ventilation within the lung

Pulmonary ventilation is the ratio of the debit of air arriving in the lung to the ventilated lung volume; therefore it is the inverse of the turnover; this parameter is hard to measure. Extending the definition, ventilation is used to express the ventilated pulmonary volume or the ventilation debit. The physiological pulmonary ventilation is:

$$V = f \times \frac{V_T - V_D}{FRC} = 15min^{-1} \times \frac{500ml - 150ml}{2500ml} = 2min^{-1} \tag{2.6}$$

The alveolar ventilation debit is:

$$\dot{V} = f \times V_T - V_D = 15min^{-1} \times 500ml - 150ml = 5250ml \cdot min^{-1} \tag{2.7}$$

comparable to the pulmonary blood debit.

At first glance, it might appear that the lung is functionally homogeneous, and that the portion of each breath reaching the gas-exchanging regions is uniformly distributed. The lung, however, is quite heterogeneous with regard to regional mechanical properties of the airways and parenchyma. This heterogeneity accounts for differences in the distribution of each breath.

In an upright subject, a pleural pressure gradient exists between the top and bottom of the lung. The pleural pressure is greatest at the top; it is least at the bottom. The gradient is about 0.25 cm $H_2O$ for each centimeter of vertical height. The larger apical transpulmonary pressure results in greater alveolar distention at the top of the lung (Fig. 2.8). This phenomenon is related to the subject's posture. In supine position, the posterior regions are the most ventilated.

This effect can be explained using the analogy with a spring: because of its own weight, a spring is more stretched at the top; when pulling it down, the lower coils will spread the most.

The larger transpulmonary pressure and alveolar size at the apex mean that this region functions along a different portion of the lung's pressure-volume curve than does the basilar area (Fig. 2.9).

Another key factor in ventilation distribution is the amplitude of the respiratory movement; a superficial respiration will ventilate the parahilar region whilst a deep respiration will ventilate also the base (Fig. 2.10) [23].

When tested with helium gas this distribution does not show very clear this pattern since the acquisition is too slow compared to the very fast diffusion of the gas so the distribution looks homogeneous in the whole lung (Fig. 2.11). Regarding the imaging side, the image obtained depends on how the contrast agent is administered (i.e. on bolus, along the whole respiration duration or using a closed circuit respiration), and also at what lung volume is delivered (e.g. FRC, RV) [24].

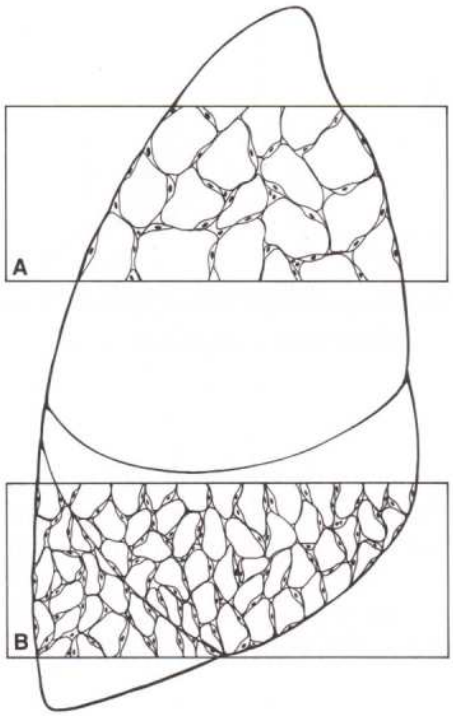


Figure 2.8: Schematic of apical and basal alveolar size. The lung is depicted at FRC. Apical alveoli (A) are larger than basilar (B).

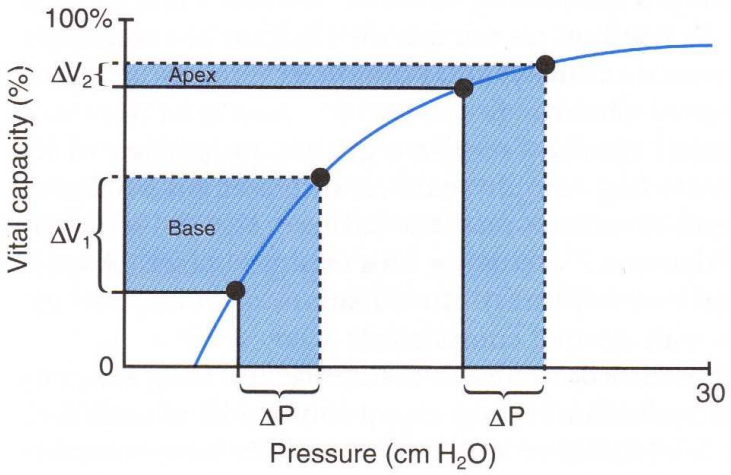


Figure 2.9: Pressure-volume plot of the lung. Changes in volume from two regions of the same lung are shown during application of inflation pressure, $\Delta P$. The change in lung volume at the base, $\Delta V_1$, is grater than the change at the apex, $\Delta V_2$.

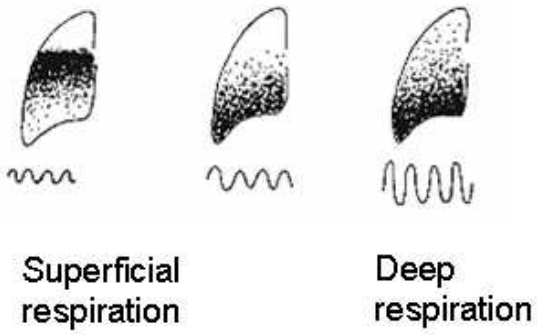


Figure 2.10: Ventilation distribution with respiration amplitude.

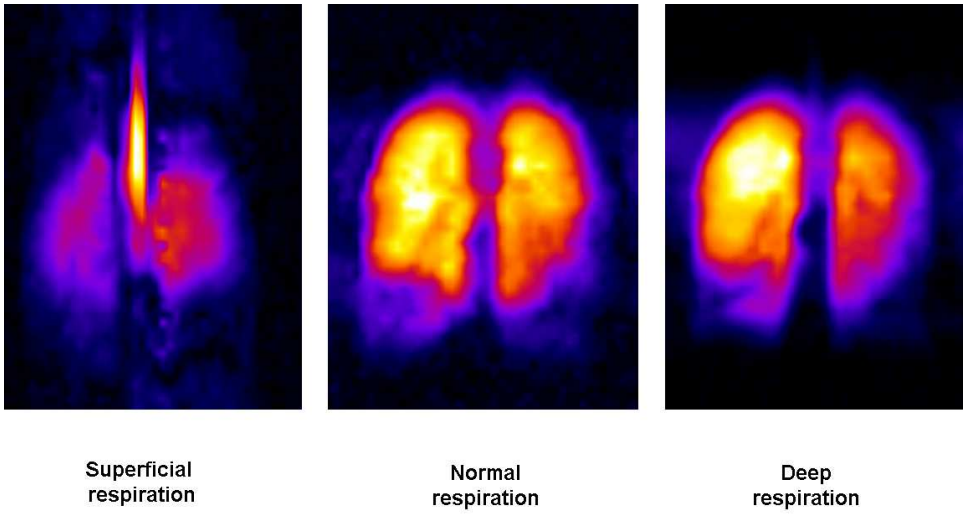


Figure 2.11: Ventilation distribution of $^{3}$He with respiration amplitude.

Despite the tremendously wide range of diseases that affect the lung by altering the distribution of ventilation, the underlying pathophysiologic mechanisms can be reduced to a basic few (Fig. 2.12).

### 2.2.6 Lung volumes

The gas held by the lungs can be thought of in terms of subdivisions, or specific lung volumes. Some of these volumes can be measured using spirometry. A detailed description

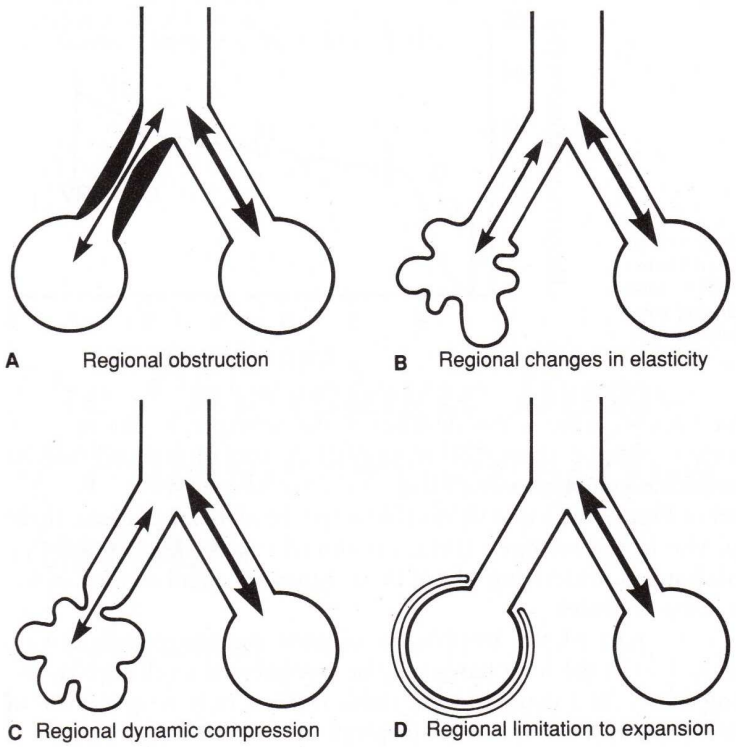


Figure 2.12: Models of non-uniform lung ventilation. (A) Partial obstruction of the airway to one lung unit. (B) Altered elasticity of one lung unit. (C) Localized dynamic compression of the airway to one lung unit. (D) Limited expansion of one lung unit during inflation.

of the lung volumes is given in Appendix A.

There are four main methods of measuring lung volumes:

- Spirometry
- Nitrogen washout
- Plethysmography
- Helium dilution

First three were employed in this work, in the Leicester laboratory. These techniques are considered in more detail in Appendix A.

### 2.2.7 Gaseous exchange in the lungs

#### Diffusion

Gas exchange between alveolar air and blood in the pulmonary capillaries takes place by diffusion. Diffusion in the lungs occurs across a membrane and is therefore governed by Fick's law (Fig. 2.13).

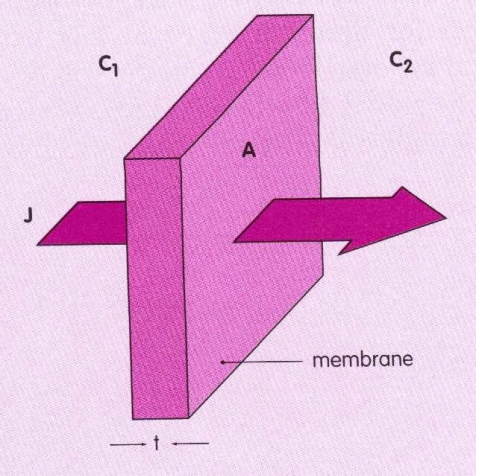


Figure 2.13: Diffusion - Fick's law. Fick stated that the rate of diffusion (J) of a gas through a membrane is: $J = K \times A \times \Delta C/t$; where: K is the diffusivity = S/MW, A = surface area, t = thickness of membrane, $\Delta C$ = concentration difference, S = solubility of substance in the membrane, MW = molecular weight.

It is clear that the blood-gas interface with its large surface area of 50-100 $m^2$ and average thickness of 0.4 um permits the high rate of diffusion required by the body. The rate of diffusion across the alveoli is also directly dependent upon the difference in partial pressure between gas in the alveoli ($P_A$) and in arterial blood ($P_a$).

#### Perfusion and diffusion limitation

At the gas-exchange surface, gas transfer occurs through a membrane into a flowing liquid. There are two processes (Fig. 2.14) occurring:

- Diffusion across the alveolar capillary membrane.
- Perfusion of blood trough pulmonary capillaries.

Uptake of a gas into the blood is dependent on its solubility and the chemical combination (e.g. with haemoglobin: Hb). If the chemical combination is strong, the gas is taken up by the blood with little rise in arterial partial pressure.

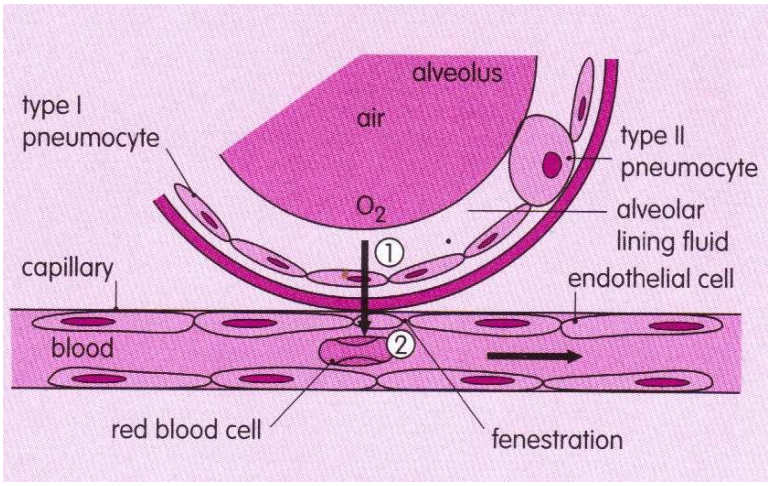


Figure 2.14: Gas transfer across alveolar capillary membrane. (1) Diffusion across membrane; (2) perfusion of blood through pulmonary capillaries.

### Oxygen uptake in the capillary network

The time taken for the partial pressure of oxygen to reach its plateau is approximately 0.25 seconds. The pulmonary capillary volume under resting conditions is about 75 mL, which is approximately the same size as the stroke volume of the right ventricle. Pulmonary capillary blood is therefore replaced with every heart beat, approximately every 0.75 seconds. This far exceeds the time for transfer of oxygen into the blood stream (Fig. 2.15).

### Carbon dioxide transfer

Graham's law states that gases with greater molecular weights diffuse more slowly than those that are lighter. Diffusion in liquids is directly dependent upon the solubility of the gas, but inversely proportional to the square root of its molecular weight. Carbon monoxide diffuses 20 times more rapidly than oxygen, but has a similar molecular weight.

Under normal conditions, the transfer of carbon dioxide is not diffusion limited.

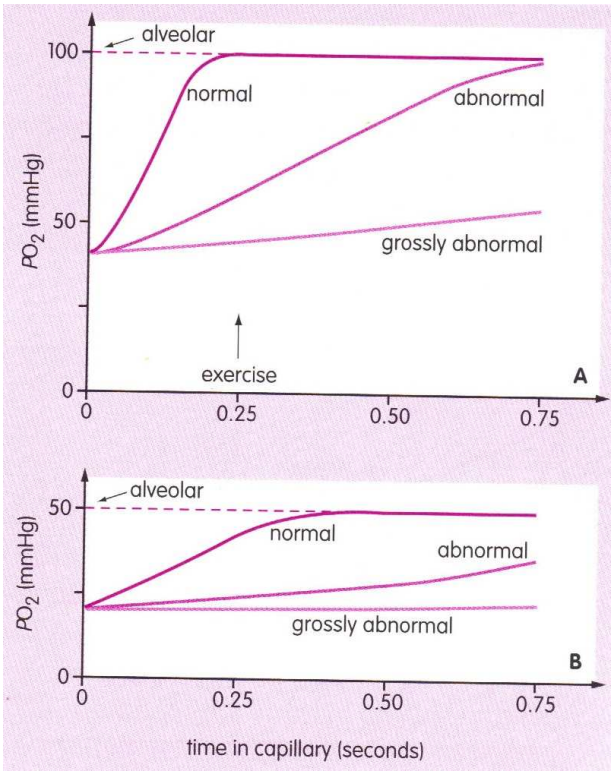


Figure 2.15: Pulmonary capillary pressure of oxygen vs. time in the pulmonary capillary network: (A) alveolar $PO_2$ normal; (B) low alveolar $PO_2$. Curves are for normal blood-gas interface and abnormal in diseased state. *Note that the difference between the normal and abnormal lungs increases at low alveolar* $PO_2$.(After West [25])

## 2.3 Elements of Lung Pathology

The following section gives an insight on the most frequent lung pathologies that could benefit from magnetic resonance imaging with hyperpolarised $^3$He.

### 2.3.1 Pulmonary embolism (PE)

An embolus is an abnormal mass of material that is transported in the bloodstream from one part of the circulation to another and which impacts finally in the lumen of a vessel that has a calibre to small to allow passage. The incidence of pulmonary emboli at autopsy has been reported to be 12%. There are no specific signs to indicate the PE so it is very hard to diagnose. Currently the methods used to diagnose PE are the radioisotope ventilation/perfusion scan and HRCT (**H**igh **R**esolution **C**omputed **T**omography) with

MRI in sight for the future [26], [27].

### 2.3.2 Disorders of the airways

#### Chronic obstructive pulmonary disease

COPD is an inflammatory lung disease characterized by infiltration of neutrophils and resulting in airway obstruction. The airway obstruction is unlike that seen in asthma , being progressive and only partially reversed by bronchodilators. Because of progressive decline in lung function, COPD is a significant cause of disability and death in smokers. It tends to be the third cause of death worldwide.

COPD is an umbrella term for different disease processes-the most important being chronic bronchitis and emphysema.

Smoking is the most important aetiology factor although only 15% of smokers will develop the disorder. Cigarette smoke generates inflammation by activating the inflammatory cells and by the effect of the oxidants (Fig. 2.16). These cause alveolar destruction (in emphysematous patient) and mucus hypersecretion (in bronchitic patient).

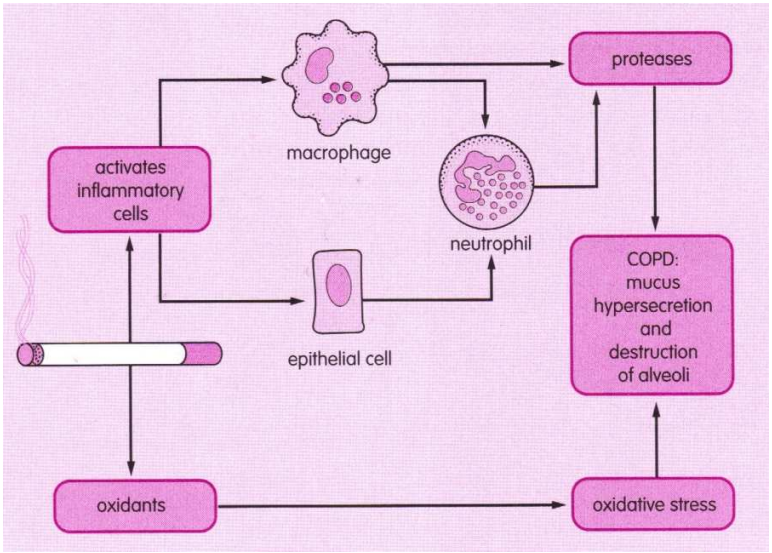


Figure 2.16: The overall pathogenesis of COPD. (After West [28]

Atmospheric pollution, occupational exposure and recurrent bronchial infections are also implicated. 2% of COPD patients have a genetic deficiency of a serum acute phase-

protein produced in the liver called $\alpha_1$-antitrypsin. This cause an early-onset emphysema (less than 40 years of age) and death.

**Emphysema** Emphysema is a permanent enlargement of the air spaces distal to the terminal bronchiole as a result of alveolar septal destruction (Fig. 2.17).

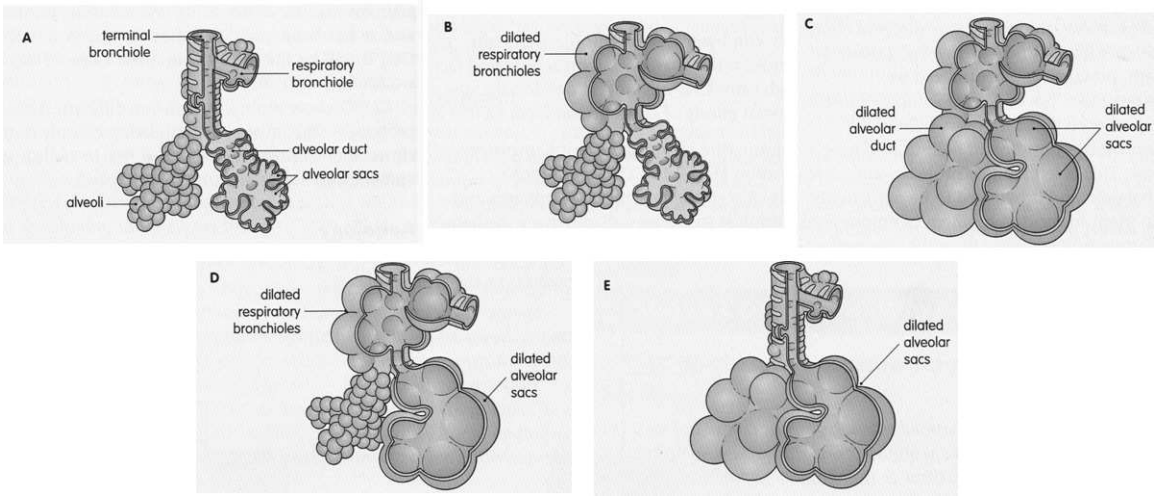


Figure 2.17: Main types of emphysema. (A) Normal distal lung acinus; (B) centriacinar emphysema; (C) panacinar emphysema; (D) irregular emphysema; (E) paraseptal emphysema.

**Chronic bronchitis** Chronic bronchitis is an airway disorder characterized by a persistent cough with sputum. The irritant effects of smoking cause the airway obstruction (Fig. 2.18).

### Asthma

Asthma is a chronic inflammatory disorder of the lung airways characterized by airflow obstruction, which is usually reversible, airway hyperresponsiveness and inflamed bronchi.

5% of the adult population in UK are receiving therapy for asthma while 20% of children have symptoms at some time in their childhood. Currently there are over 200 materials encountered at the workplace that are implicated in the occupational asthma.

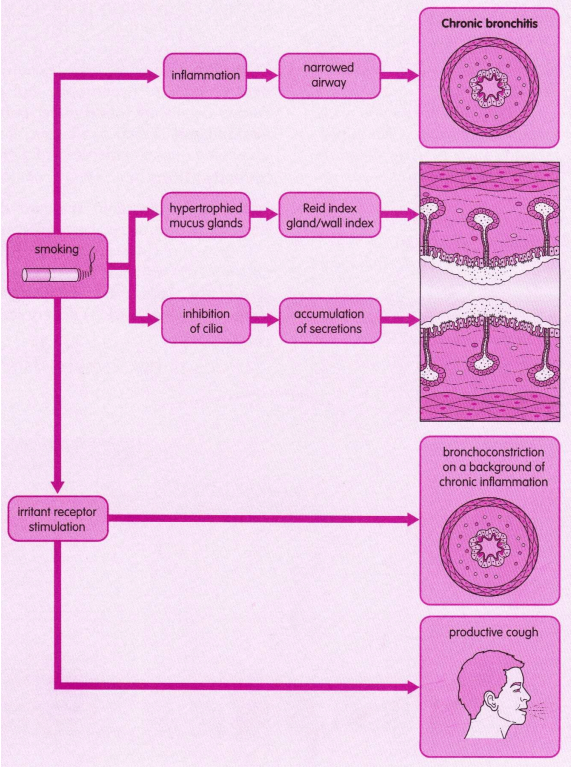


Figure 2.18: Pathogenesis of chronic bronchitis.

### Other airway disorders

**Bronchiectasis** Bronchiectasis is an abnormal and permanent dilatation of the bronchi and is associated with chronic infection. Most cases arise in childhood.

Infection leads to obstruction, dilatation of bronchi and often loss of cilia. The most common consequence is bronchial wall thickening. Usually the lower lobes are affected most commonly. High-resolution CT is the investigation of choice for detection of bronchial wall thickening.

**Cystic fibrosis** Cystic fibrosis is a genetic disease that affects the mucus-secreting glands. The thick secretion cause small airway obstruction, leading to recurrent infection and ultimately bronchiectasis.

## 2.4 Lung investigations and imaging techniques

There are a large number of investigations in respiratory medicine, ranging from basic bedside tests to more invasive procedures such as bronchoscopy. Some of the investigations described are performed only rarely in specialized pulmonary laboratories whilst others are performed by patients at home everyday.

This section will treat only the imaging methods. These techniques can be divided in two groups: anatomical imaging, which focuses on the structure and the functional imaging, which depicts the performance of the lung.

### 2.4.1 Anatomical imaging techniques

#### Plain radiography

Chest radiography is the most used medical imaging technique. It consists of obtaining a 2D image using a beam of X-rays (energy centered on 120 keV). The attenuation of the beam can be detected on a photographic film (conventional radiography) or on a semiconductor detector (digital radiography).

There are a number of standard radiographic examinations of the chest. One of the most used is the posteroanterior erect radiograph (PA chest) shown in Figure 2.19.

Apart from the lung parenchyma, the image shows the mediastinum, the heart shadow and the big vessels and the diaphragm. The lungs are extremely transparent to X-rays and they appear black on the image. The thorax and the heart are opaque.

This method can give a lot of information but it has the disadvantage of showing only a projection. Since the structures are superposed the diagnostic can be very difficult. To overcome this, it is a standard procedure to acquire a second, orthogonal image in a sagittal plane. The maximum spatial resolution is 200 $\mu m$.

The dose received for each image depends on the quality of the X-rays source and on the set-up (usually 50 $\mu Sv$) [29].

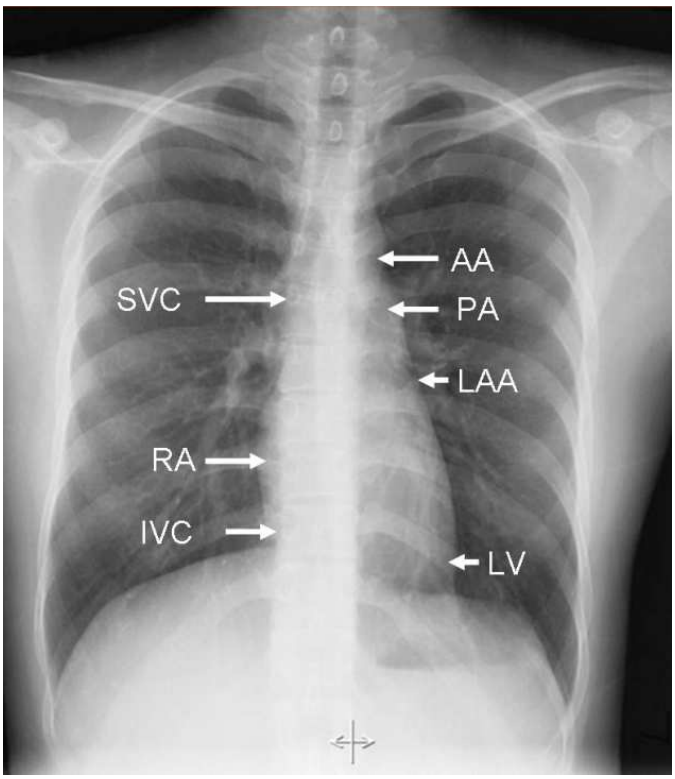


Figure 2.19: Normal posteroanterior chest radiograph. The lungs are equally transradiant, the pulmonary vascular pattern is symmetrical. AA = aortic arch; SVC = superior vena cava; PA = pulmonary artery; LAA = left atrial appendage; RA = right atrium; LV = left ventricle; IVC = inferior vena cava.

### Computed tomography

Before computed tomography, in conventional medical X-ray tomography, clinical staff made a sectional image through a body by moving an X-ray source and the film in opposite directions during the exposure. Consequently, structures in the focal plane appeared sharper, while structures in other planes appeared blurred. By modifying the direction and extent of the movement, operators can select different focal planes which contain the structures of interest. Before the advent of more modern computer-assisted techniques , this technique, imaginated in the 30's by the radiologist Alessandro Vallebona, proved useful in reducing the problem of superimposition of structures in projectional (shadow) radiography.

Computed tomography (CT) is a medical imaging method employing tomography de-

veloped by Sir Godfrey Hounsfield [30]. Digital geometry processing is used to generate a three-dimensional image of the inside of an object from a large series of two-dimensional X-ray images taken around a single axis of rotation.

CT produces a volume of data which can be manipulated, through a process known as windowing, in order to demonstrate various structures based on their ability to block the X-ray beam. Although historically the images generated were in the axial or transverse plane (orthogonal to the long axis of the body), modern scanners allow this volume of data to be reformatted in various planes or even as volumetric (3D) representations of structures.

Over the past 10 years CT improved by the use of helical CT; a gantry holding the source and detector array rotates as the patient is translated along the axis of rotation, multislice CT; similar in concept to the helical CT but there are more than one detector ring, dual-source CT; 256+ slice CT.

CT is excellent for detecting both acute and chronic changes in the lung parenchyma. For evaluation of chronic interstitial processes (emphysema, fibrosis, and so forth), thin sections with high spatial frequency reconstructions are used - often scans are performed both in inspiration and expiration. This special technique is called High resolution CT (HRCT). HRCT is normally done with thin section with skipped areas between them. Therefore it produces a sampling of the lung and not continuous images (Fig. 2.20).

Figure 2.20: CT of the chest, axial projection.

For detection of airspace disease (such as pneumonia) or cancer, relatively thick sections and general purpose image reconstruction techniques may be adequate. Intra venous contrast may also be used as it clarifies the anatomy and boundaries of the great vessels and improves assessment of the mediastinum and hilar regions for lymphadenopathy; this is particularly important for accurate assessment of cancer.

CT angiography of the chest is also becoming the primary method for detecting pulmonary embolism (PE) and aortic dissection, and requires accurately timed rapid injections of contrast (Bolus Tracking) and high-speed helical scanners. CT is the standard method of evaluating abnormalities seen on chest X-ray and of following findings of uncertain acute significance.

Xenon-enhanced CT scanning is a method of computed tomography (CT scanning) used for neuroimaging in which the subject inhales xenon gas while CT images are made. The method can be used to assess changes in cerebral blood flow in the period shortly after a traumatic brain injury. The diffusion of the gas into the tissues shows how much blood flow each area is getting.

A typical effective dose for a chest CT is 5-10 mSv.

### Bronchography

Bronchography is a radiographic examination of the bronchial tree by instillation of contrast medium directly into the trachea or bronchi. Until recently, bronchography was the method of choice in the evaluation of bronchiectasis. CT, and especially high resolution CT, has nearly completely surpassed the method, which at many centres is no longer performed. The most commonly used contrast medium for bronchography was an aqueous suspension of propyliodone (Dionosil). Several techniques existed for instillation of the contrast medium, including a cannula inserted over the extended tongue, a catheter introduced through the nostril or the mouth, and a direct needle puncture of the crico-thyroid membrane. Even coating of the bronchial mucosa was accomplished by injection of the contrast medium during inspiration (Fig. 2.21). Today, instillation of contrast medium via a fibreoptic bronchoscope would be preferred.


Figure 2.21: The bronchial tree of the right lung has been coated with contrast medium. 1: main bronchus, 2: upper lobe bronchus, 3: intermediate bronchus, 4: middle lobe bronchus, 5: lower lobe bronchus. (Courtesy of Dr. A.N. Kolbenstvedt, Rikshospitalet University Hospital, Oslo, Noway.)

### Pulmonary angiography

Pulmonary angiography is used for demonstration of the pulmonary arteries and veins. Using fluoroscopic guidance and ECG monitoring, a pulmonary catheter is passed into the trunk of the pulmonary artery over a guide wire. Generally, a femoral approach is used, but alternatively the internal jugular vein or the median cubital vein may be accessed. Imaging is done using digital subtraction angiography (DSA) (Fig. 2.22), however, conventional cut film series often show superior image quality.

### Chest ultrasonography

Ultrasound uses high-frequency sound waves to image internal structures. Chest ultrasonography is an examination mainly indicated in pleural diseases. It is usually performed

Figure 2.22: DSA showing normal right pulmonary artery. (Courtesy of Dr. K. Vatne, Rikshospitalet University Hospital, Oslo, Norway.)

with a 3.5 - 7.5 MHz linear or curvilinear probe placed in the line of the intercostal space (Fig. 2.23).

A variation of this technique, Doppler ultrasound, is a non-invasive method for detecting deep vein thrombosis. It is used in investigating patients with suspected pulmonary thromboembolism. Chest ultrasonography is frequently used to guide chest interventions such as thoracocentesis, biopsy or chest tube insertion.

### 2.4.2 Functional imaging techniques

The existing lung functional imaging can only show either the ventilation (air supply) or the perfusion (blood supply). There are no techniques that can be routinely used to provide information about the gas exchange in the lungs.

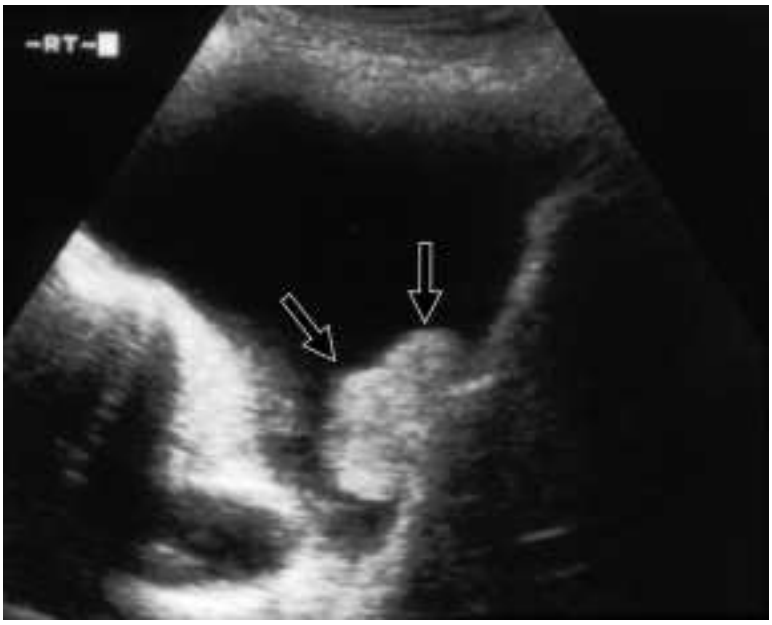


Figure 2.23: Chest Ultrasonography.

**Lung scintigraphy**

Ventilation-perfusion scintigraphy is a radionuclide imaging study of pulmonary circulation and ventilation. It is mainly used in:

- the detection of pulmonary embolism
- monitoring the natural history or treatment of thromboembolic disease
- quantitative evaluation of distribution of obstructive pulmonary disease
- preoperative evaluation of patients with emphysema, lung cancer and bronchiectasis.

Radionuclide lung imaging are methods by which one physiological aspect of lung function is evaluated. The most widely used techniques are: lung perfusion imaging using Tc-99m MAA (macroaggregates of albumin) labeled perfusion agents and lung ventilation imaging using either radioactive Xe or Tc-99m labeled aerosols . The clinical indications are mainly the diagnosis of pulmonary embolism and the semiquantitative assessment of the left-right distribution of pulmonary perfusion before performing ma-

jor lung surgery such as lung transplantation or pulmonary volume reduction surgery in emphysema patients.

Lung perfusion scanning is done by injecting 40 to 160 MBq (1-4 mCi) of Tc-99m-labelled MAAs (see aggregated albumin) in the supine patient to reduce orthostatic gradients, and during repeated deep inhalation. Both measures serve evenly to distribute the aggregates throughout the perfused lung areas. The aggregates are extracted during their first pass through the lung, thus imaging can begin immediately. Anterior, posterior, left and right lateral oblique and sometimes lateral projections are obtained (Fig. 2.24).

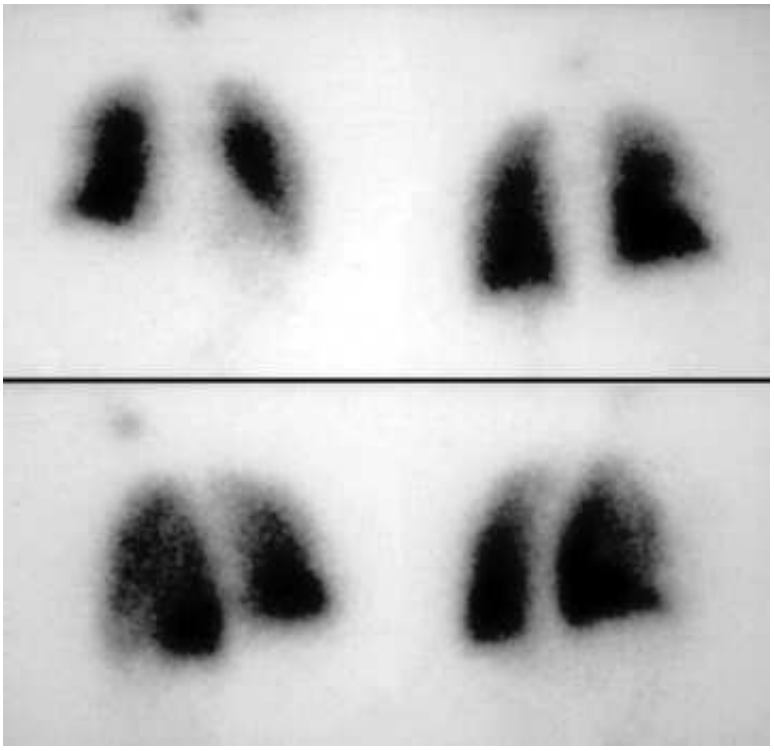

Figure 2.24: Normal perfusion scan in the four projections A-P (dorsal), P-A (ventral), LPO 45 and RPO 45.

Ventilation scanning is undertaken using radioactive Xe or Tc-99m labeled aerosols . The advantage of this technique is that the projection most clearly shows a perfusion defect can also be imaged during ventilation, but has the disadvantages of high cost and limited availability. The Rubidium-Krypton generator system is too expensive to be used in most clinical environments.

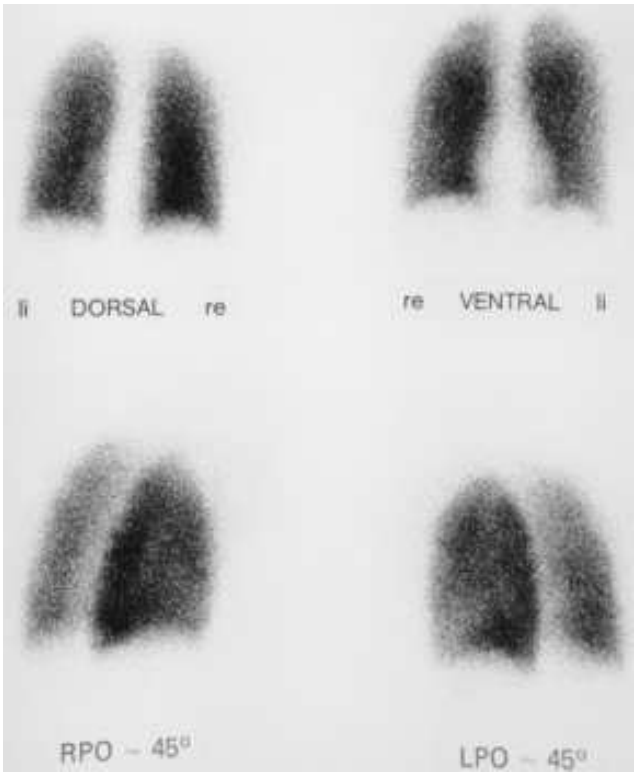


Figure 2.25: Normal ventilation scan with wash-in, equilibrium and wash-out phases.

## 2.5 Lung imaging by proton Magnetic Resonance

The physics of the Magnetic Resonance Imaging (MRI) is detailed in Chapter 3. This section gives an insight of the use of MRI in lung investigation.

### 2.5.1 Anatomical lung MRI

In the chest, MRI is mainly indicated for the evaluation of mediastinal or chest wall lesions. The most frequent indication is the characterization and preoperative assessment of a mediastinal mass. MRI is used to study the lungs too. The lung parenchyma is known to give a weak MR signal [31]. There are three explanation for this: first, the lung is mainly air so it has very little proton density [32]; second, the lung has a non-regular movement; and last, it consists of 70 $m^2$ air-tissue interface. This interface between structures with different magnetic susceptibility is the source of internal gradients which severely amplify the transverse relaxation. At 1.5 T, the transverse relaxation time measured by gradient echo sequence ($T_2^*$) is between 0.86 and 2 ms [33]; the transverse relaxation time

measured by spin echo ($T_2$) is 25 to 35 ms. The reversible part of $T_2^*$ measured by spin echo, ($T_2'$) is between 5 to 7 ms average; it is elevated at the bottom of the lung where the alveoli are less inflated. It also increases with certain diseases (35 ms in atelectasis and 140 ms in tumors) [32]. At 0.5 T, other authors reported a $T_2^*$ of 4 +/-1 ms [34].

This short relaxation time leads to a very weak signal [31] and implies very short echo times (TEs). With the latest development in gradients performance it is possible now to obtain TEs short enough to visualize the pulmonary parenchyma.

Mayo used a spin echo sequence at 1.5 T with TE=7 ms to obtain images of the lung tissue [35]; these images showed intrapulmonary structures (small vessels, septa) better than the sequences with TE of 20 ms.

Bergin used a projection-reconstruction (PR) sequence with 250 $\mu s$ TE that was able to correct the susceptibility artifacts [36].

Alsop used a gradient echo sequence with a very short TE (0.7 ms) at 1.5 T. To obtain this short times, the switching rate of the gradients was 150 $T.m^{-1}.s^{-1}$, a large bandwidth (62.5 kHz) and asymmetric echoes. The acquisition time was 16 s [33].

Heidemann described resolution enhancement in lung $^1$H imaging using half-Fourier acquisition single-shot turbo spin-echo (HASTE) sequences, with short echo time (TE) and short interecho spacing ($T_{inter}$) combined with partially parallel acquisition (PPA) strategy [37], [38].

### 2.5.2 Functional lung MRI

#### Oxygen contrast enhanced MRI

Oxygen is a paramagnetic agent which affects $T_1$. The idea of using the oxygen as a contrast agent was first tried to study the heart chambers by Young [39].

It was then applied to lungs by Edelman [40] who reported a variation of $T_1$ from 901 +/- 55 ms with ambient air ventilation to 826 +/- 62 ms with pure oxygen. The difference (75 ms) was enough to obtain ventilation images at 1.5 T using a IR-HASTE sequence: spin-echo single-shot half-Fourier with magnetization inversion (inversion time, TI = 720 ms) to cancel the signal of the lung ventilated with ambient air (128x256 matrix, inter-echo time 4.2 ms, effective TE 25 ms, RF sinc pulses, 1 ms duration, acquisition time 320

ms). An image of the variation of the signal reflected the ventilation (Fig. 2.26).

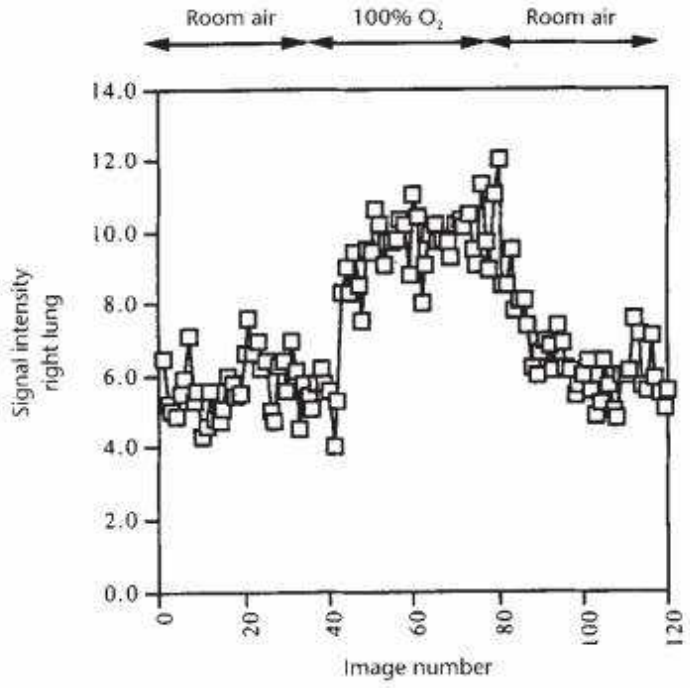


Figure 2.26: Dynamic lung imaging by MRI before and after administration of pure oxygen; the signal (arbitrary units) increases by the paramagnetic effect of the oxygen [40].

### Lung perfusion MRI

The term of lung perfusion imaging can be confusing: numerous authors consider that the perfusion imaging should be the vessel visualisation; stricto sensu, the perfusion is the process of delivery of arterial blood to a capillary bed in the biological tissue and the real perfusion imaging has to show/quantify the blood supply to the tissue.

The first application of MRI to the measurement of pulmonary perfusion was the phase contrast velocity measurement [41] of the pulmonary arteries. After, the use of contrast agents made possible the visualisation of the pulmonary arterial tree and pulmonary perfusion, first in animals [42], [43] and then in humans [44], [45] (Fig. 2.27). The main clinical application of this method was the diagnostic of the pulmonary embolism [46] first reported in 1997 by Amundsen [47].

More recently, the MRI angiography using the time of flight (TOF) was used. This sequence uses spin labelling without contrast agent to obtain images of the vascularisation

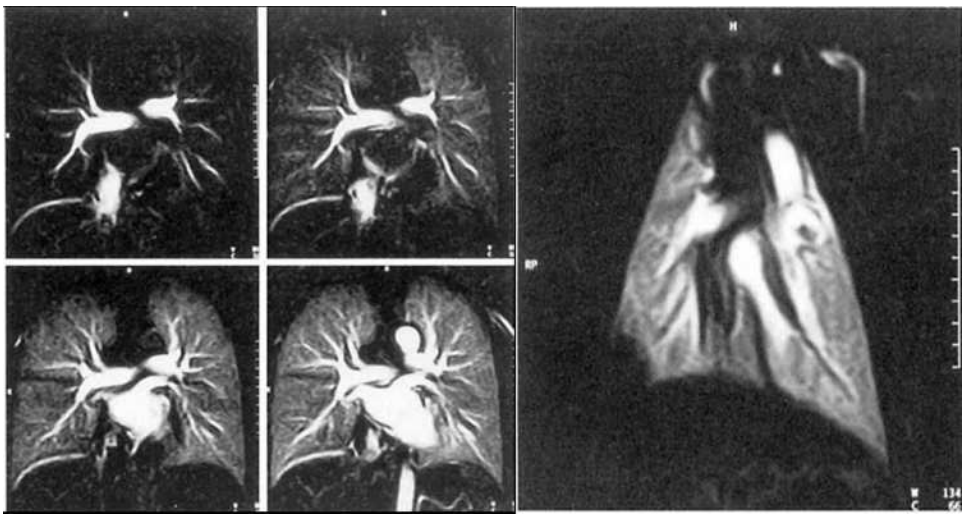

Figure 2.27: Pulmonary perfusion MRI with gadolinium contrast agent; acquisition obtained with a FLASH sequence; left image, healthy volunteer: clear view of the vascularization and pulmonary perfusion after substraction of an image acquired before the agent injection; right image, animal model of pulmonary embolism in pig [44]).

[48], [49], [50], [51], [52] (Fig. 2.28).

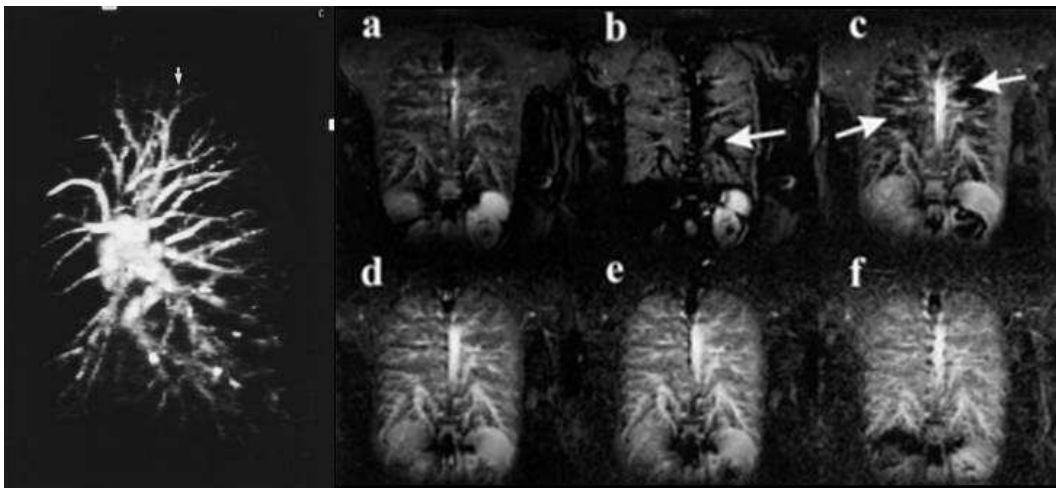


Figure 2.28: Images of pulmonary perfusion obtained without contrast agent from healthy volunteers, by spin labelling technique; left, visualisation of the pulmonary arterial tree up to the 7th generation ([49]); right, reference image (a), followed by functional images obtained with different inversion times, the short times (b: 500 ms & c: 700 ms) show the vessels and the long times (d: 1 s, e: 1.2 s and f: 1.4 s) show the pulmonary perfusion ([51]).

## 2.6 Conclusion

In multiple domains like neurology, oncology, cardiology, rheumatology, Magnetic Resonance Imaging has an important position among the medical imaging techniques, both anatomical and functional. By contrast, in pneumology, this method is hardly used: it is very difficult to visualise the parenchyma. Before the use of hyperpolarised gases MRI couldn't provide ventilation images with enough quality to be of potential use for clinical application.

On the other hand, the other available imaging techniques can not answer all the problems found in pneumology: in particular, the diagnosis of the air ways diseases like asthma and COPD is impossible in the early stages. These diseases need a technique that can provide more information on the ventilation than scintigraphy in order to be of clinical interest. The difficult diagnosis of pulmonary embolism could be facilitated by extra information from ventilation MRI.

Proton MRI of the lung is a method of low sensitivity in terms of the signal. With the other imaging techniques there is no real theoretical limit in signal augmentation: the electrical intensity in the X-ray tube can be increased in radiography and CT, the intensity of the ultrasound wave can be increased in ultrasonography, or the injected activity in scintigraphy. With MRI we are limited by the field strength and temperature, the available magnetization depends on the spin density of the region of interest. In order to overcome some of the limitations and get an advantage over the previous methods applied to lungs, it is necessary to think of using techniques of hyperpolarisation.

# Chapter 3

# Fundamentals of hyperpolarised $^3$He MRI

This chapter will review the physics of the Magnetic Resonance Imaging (MRI), focusing on aspects of hyperpolarised gas. The second part will present theoretical aspects of the hyperpolarised $^3$He.

## 3.1 Basics of Nuclear Magnetic Resonance

Nuclear magnetic resonance involves the natural resonance phenomena of transitions between specific energy states of nuclear orientation in a magnetic field . Magnetic resonance requires the existence of a magnetic moment and angular momentum. The usefulness of NMR is that it allows the study of specific spins in a magnetic material. Even in the presence of dominant magnetic material, spins that have a small contribution to the total magnetisation can be investigated with NMR. Due to the screening effect of the electrons in chemical compounds the resonance frequency of a free atom is different from that in bulk material. This effect is called *chemical shift*. Observing the chemical shift provides information about the chemical composition of the material. NMR also allows for non invasive studies of subjects and materials. These properties allow for the use of NMR in fields such as physics, chemistry, biology and medicine. This section introduces the basic principles of NMR in preparation for a discussion of magnetic resonance imag-

ing with polarized noble gases. Thorough discussions of NMR can be found in many texts [53], [54], [55], [56].

### 3.1.1 Magnetisation and Polarisation

Individual nucleons have a spin of $\frac{1}{2}$. The spins from individual nucleons couple together in a nucleus with orbital angular momentum to form the total angular momentum of $\hbar I$ where I is either integer or half integer. The magnetic moment related to a total angular momentum $\hbar I$ is:

$$\mu = \frac{ge\hbar I}{2m_p} \tag{3.1}$$

where g is the Landé factor, e is the charge of an electron, $\hbar$ is Planck's constant divided by $2\pi$, and $m_p$ is the mass of the proton. By defining the gyromagnetic ratio

$$\gamma = \frac{ge}{2m_p}$$

the magnetic moment is

$$\mu = \gamma\hbar I$$

In SI units, for protons (neutrons) $\gamma$ = 2.7522212 $\times$ $10^8$ rad $s^{-1}$ $T^{-1}$ ($\gamma$ = -1.83247188 $\times$ $10^8$ rad $s^{-1}$ $T^{-1}$) and for $^3$He $\gamma$ is $\gamma$ = -2.0378 $\times$ $10^8$ rad $s^{-1}$ $T^{-1}$. Any free system with a constant gyromagnetic ratio, such as a rigid system of charges, a nucleus, or an electron, when placed in an external magnetic field B (measured in teslas) that is not aligned with its magnetic moment, will precess at a frequency $f$ (measured in hertz), that is proportional to the external field:

$$f = \frac{\gamma}{2\pi}B$$

For this reason, values of $\gamma/(2\pi)$, in units of hertz per tesla (Hz/T), are often quoted instead of $\gamma$. For protons this value is 42.576 MHz/T and for $^3$He is -32.434 MHz/T.

If a magnetic moment is placed in a magnetic field the nucleus will be in an energy state of the Hamiltonian $\mathcal{H} = -\overrightarrow{\mu} \cdot B$. If the magnetic field is pointing in the z direction

$$\mathcal{H} = -\mu B_0 = -\gamma\hbar B_0 I_z.$$

The eigenvalues for this Hamiltonian are

$$E = -m\gamma\hbar B_0$$

where $m$ are sub states corresponding to different levels, $m = -I, ..., I-1, I$. The energy difference between two adjacent states is

$$\Delta E = \hbar\gamma B$$

and the energy absorbed is

$$\Delta E = \hbar\omega.$$

From these relations the transition between two adjacent states occurs when radiation of angular frequency $\omega$ ($= 2\pi\nu$) is applied

$$\omega = \gamma B.$$

When an isotropic non ferromagnetic sample is placed in a magnetic field, a magnetisation M is created

$$M = \frac{\chi}{1+\chi}\frac{B}{\mu_0}$$

where $\chi$ is the magnetic susceptibility and $\mu_0$ is the permeability of free space. For paramagnetic systems $\chi \ll 1$ so

$$M = \chi\frac{B}{\mu_0}. \tag{3.2}$$

For a collection of spin $\frac{1}{2}$ particles (eg. protons), each particle has two quantum substates, $m = \frac{1}{2}$ and $m = -\frac{1}{2}$. For thermal populations, statistical mechanics must be used to determine what fraction of the spins are aligned with the magnetic field and what fraction are pointing opposite to the field. Given that $\gamma$ is positive, in which case $\overrightarrow{\mu}$ is parallel to I. The fraction of the spins that are pointing parallel (antiparallel ) to the magnetic field direction is given by the Maxwell-Boltzmann distribution

$$N\uparrow\downarrow = \frac{e^{\frac{\pm\mu B}{kT}}}{e^{\frac{\mu B}{kT}} + e^{\frac{-\mu B}{kT}}}$$

where $\pm$ is used to represent a magnetic moment parallel(+) or antiparallel(-) to the applied field. $T$ is the temperature in Kelvin and $k$ is the Boltzmann constant. The net magnetisation is given by

$$M = N\mu\frac{N\uparrow - N\downarrow}{N\uparrow + N\downarrow} \tag{3.3}$$

$$= N\mu\frac{e^{\frac{\pm\mu B}{kT}}}{e^{\frac{\mu B}{kT}} + e^{\frac{-\mu B}{kT}}} \tag{3.4}$$

$$= N\mu\tanh\left(\frac{\mu B}{kT}\right) \tag{3.5}$$

$$= N\mu\tanh\left(\frac{\hbar\omega}{2kT}\right) \tag{3.6}$$

where $N = N\uparrow + N\downarrow$. The polarization of a sample is defined as

$$P = \frac{N\uparrow - N\downarrow}{N\uparrow + N\downarrow} \tag{3.7}$$

and the polarization due to a Boltzmann distribution of spins is given by

$$P_{thermal} = \tanh\left(\frac{\hbar\omega}{2kT}\right) \approx \frac{\hbar\omega}{2kT} \tag{3.8}$$

where the thermal subscript is given since the polarization is dependent upon temperature for a given field. Seen from equation 3.8, the polarization increases linearly with frequency and therefore with magnetic field strength. For protons in a 1.5 T (15,000 gauss) field at 300 K, the polarization is $5.1 \times 10^{-4}\%$.

This small value generates a small magnetisation; as an effect, the population in the parallel and antiparallel state are almost identical. This usually means a low sensitivity of the nuclear magnetic resonance (Fig. 3.2).

In order to increase the polarisation, according to 3.8, the only posibilities are to cool down the nuclear population (this is hard to do in biomedical applications) and increase the $\overrightarrow{B_0}$ field; nowadays, the most intense magnetic field achievable for human imaging is about 10 T which only provides a polarisation just above $10^{-5}$. The only solution

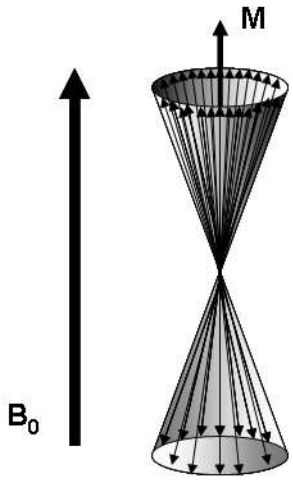


Figure 3.1: A net magnetisation due to individual magnetic moments precessing around a magnetic field. Note that the transverse magnetisation is averaged to zero.

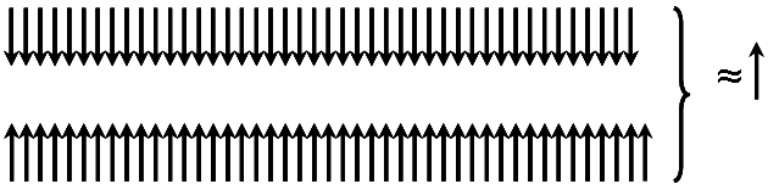


Figure 3.2: Small nuclear magnetisation as a result of similar population on the parallel and antiparallel levels.

to increase the NMR signal remains working in the non-equilibrium state: this is the principle of hyperpolarisation. In the hyperpolarised regime, the two populations are more different, the polarisation is therefore significantly increased and the magnetisation available is greater (Fig. 3.3). The ways of obtaining this hyperpolarised state will be presented in a later chapter.

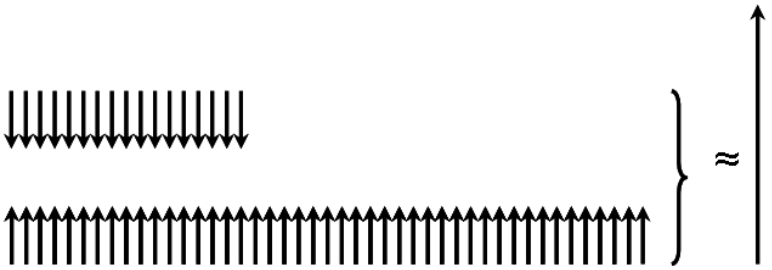

Figure 3.3: Principle of hyperpolarisation: the populations on the parallel and antiparallel levels are much more different from equilibrium; the polarisation is increased together with increase in magnetisation and NMR signal.

### 3.1.2 Magnetic Moment in a Magnetic Field

The motion of particles with spin I, in a constant magnetic field $B_0$ and a weak oscillating field $B_1$ perpendicular to $B_0$ can be calculated classically. Let J be the magnitude of the angular momentum **J**, classically given by $J = \hbar I$. An angle $\theta$ is defined as the angle between the z-axis and J (Fig. 3.4). The constant field $B_0$ defines the z-axis, and $B_1$ is oscillating in the x-y plane. The constant magnetic field produces a torque on the magnetic moment

$$\Gamma = \overrightarrow{\mu} \times B_0 = \gamma(J \times B_0).$$

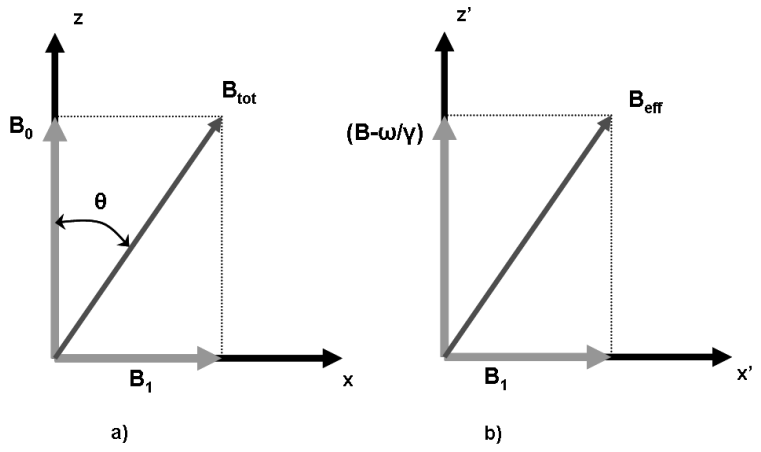


Figure 3.4: The magnetic fields in the a) lab and b) rotating frame.

The torque is equal to the time derivative of the angular momentum so

$$\frac{d\mathbf{J}}{dt} = \gamma(\mathbf{J} \times B_0) \tag{3.9}$$

To solve this equation it first must be shown that the magnitude of **J** is constant

$$\frac{dJ^2}{dt} = \frac{d(\mathbf{J} \cdot \mathbf{J})}{dt} = 2\mathbf{J} \cdot \frac{d\mathbf{J}}{dt} = 2\gamma\mathbf{J}(\mathbf{J} \times B_0),$$

where it is readily seen that the last expression is identically zero. Using the identities

$$\omega_0 = \frac{d\phi}{dt}$$

$$\frac{d\theta}{dt} = 0$$

and the individual components of equation 3.9

$$\frac{dJ_x}{dt} = \frac{d}{dt}(J\sin\theta\sin\phi) = \omega_0 J\sin\theta\cos\phi = \gamma J_y B_0$$

$$\frac{dJ_y}{dt} = \frac{d}{dt}(J\sin\theta\cos\phi) = -\omega_0 J\sin\theta\sin\phi = -\gamma J_x B_0$$

$$\frac{dJ_z}{dt} = \frac{d}{dt}(J\cos\theta) = 0$$

it is easily shown that

$$\omega = \gamma B_0$$

and

$$\overrightarrow{\omega_0} = -\frac{\left|\frac{d\mathbf{J}}{dt}\right|}{|\mathbf{J} \times \hat{\mathbf{z}}|}\hat{\mathbf{z}},$$

where $\hat{\mathbf{z}}$ is the unit vector in the z direction. From equation 3.9 the magnetic moment is seen to precess about $B_0$ with an angular frequency of $\omega_0$.

If a weak magnetic field $B_1(t)$ is rotating in the x-y plane about the z axis with angular frequency $\omega$ given by the expression

$$B_1 = B_1(\hat{x}\cos\omega t + \hat{y}\sin\omega t),$$

along with a static magnetic field $B_0 = B_0\hat{\mathbf{z}}$, the equation of motion for the spin is

$$\frac{d\mathbf{J}}{dt} = \gamma(\mathbf{J} \times \mathbf{B}) \tag{3.10}$$

where $\mathbf{B} = \mathbf{B}_0 + \mathbf{B}_1$ is the total magnetic field.

The time dependence in equation 3.10 can be eliminated by moving into the rotating frame of $B_1(t)$. In this new coordinate system, $B_1(t)$ and $B_0$ are static. In the lab frame the time derivative of the angular momentum vector is

$$\frac{d\mathbf{J}}{dt} = (\frac{\partial \mathbf{J}}{\partial t} + \overrightarrow{\omega} \times \mathbf{J}), \tag{3.11}$$

where $\frac{\partial \mathbf{J}}{\partial t}$ is the time derivative computed in the rotating frame. Substituting 3.11 into 3.10 the equation of motion in the rotating frame is

$$\frac{\partial \mathbf{J}}{\partial t} = \gamma \left[ \mathbf{J} \times (\mathbf{B}_0 + \mathbf{B}_1 + \frac{\overrightarrow{\omega}}{\gamma}) \right], \tag{3.12}$$

Rewriting equation 3.12 in the form

$$\frac{\partial \mathbf{J}}{\partial t} = \gamma \left[ \mathbf{J} \times (\mathbf{B}_0 - \frac{\omega}{\gamma})\hat{k}' + \mathbf{B}_1 \hat{x}' \right], \tag{3.13}$$

the spin vector is seen to precess about an effective magnetic field $\mathbf{B}_{eff} = (B_0 - \frac{\omega}{\gamma})\hat{\mathbf{k}}' + B_1\hat{\mathbf{x}}'$. At the resonant condition $\omega_0 = \gamma B_0$, the spin is precessing about the $\hat{\mathbf{x}}'$ axis with a frequency $\omega_1 = \gamma B_1$ (Fig. 3.5).

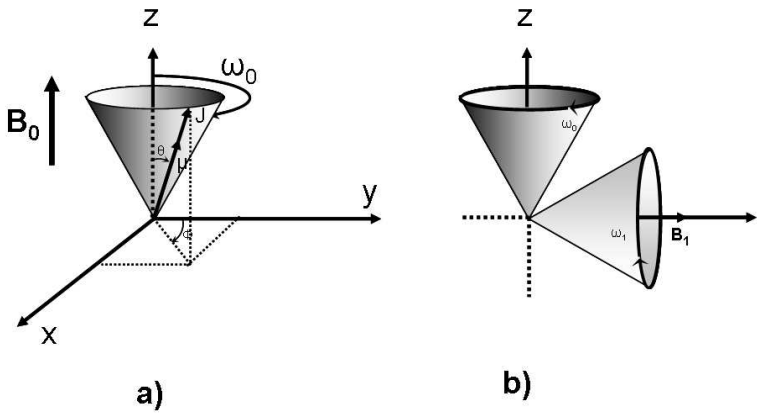


Figure 3.5: Precession of a spin **J** in a magnetic field $B_0$ at a frequency $\omega_0 = \gamma B_0$ a). Additionally, when a small rotating magnetic field $B_1$ is applied about the z direction, the spin will precesses about $B_1$ with a frequency $\omega_1 = \gamma B_1$ b).

There are two general types of methods in NMR, cw (continuous wave) and the pulsed methods. The cw method utilizes an RF field that is applied continuously. Resonance is typically achieved by varying the frequency through the resonant condition. The RF pulse method cycles on and off the RF utilizing various pulse sequences. If an RF pulse is turned on for a duration $\tau$, the magnetisation will rotate about $\mathbf{B}_1$ through an angle $\theta = \gamma B_1 \tau$. If $\tau$ is $90^\circ$ or $180^\circ$ the pulse is referred to as a $90^\circ$ or $180^\circ$ pulse (Fig. 3.6). Such pulses are commonly used in experimental pulsed NMR.

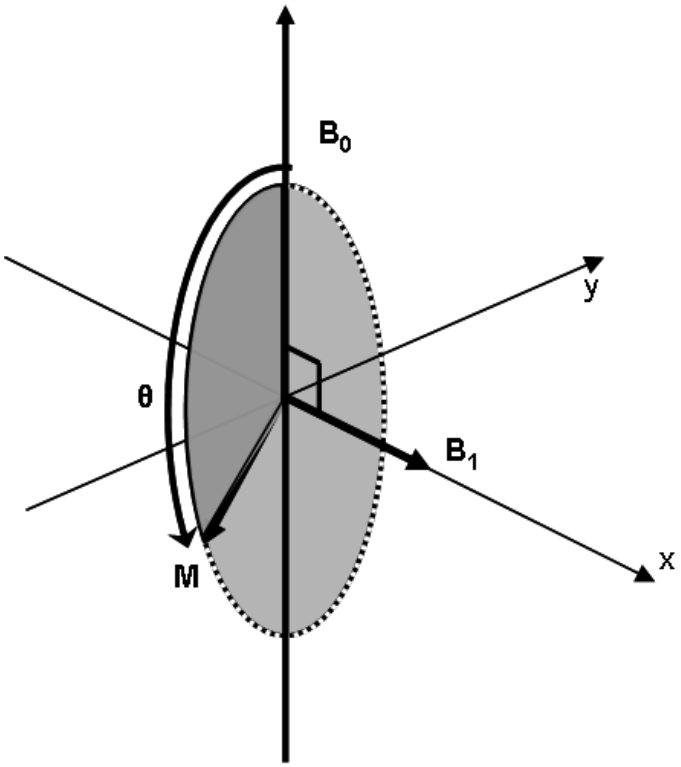


Figure 3.6: Diagram describing the nutation angle $\theta = \gamma\omega_1\tau$ which a magnetisation vector rotates through when a resonant RF pulse of duration $\tau$ is applied.

### 3.1.3 Spin Relaxation

The application of an RF excitation pulse applied to a system in thermal equilibrium will lift the system to the excited state. Once in the excited state, the system will return to thermal equilibrium with a time constant $T_1$. The energy that was absorbed to excite the nuclei is then transferred to its surroundings, the *lattice*. This process is referred to

as spin-lattice relaxation or longitudinal relaxation . In liquids and gases, the RF fields are moving magnetic nuclei that produce field fluctuations at the resonance condition $\omega_0 = \gamma B_0$. The rate at which nuclei relax is dependent on the motion of the molecule containing the nuclei. For instance, a proton in water may rotate faster than protons in tissue; This is because the protons in tissue may have a stronger rotational component at the resonant condition than do the protons in water. Therefore, the $T_1$ for protons in tissue would be shorter than those in water. One can easily see that the $T_1$ is dependent upon the magnetic field strength. Typically, the $T_1$ for protons in water is approximately 3 seconds, whereas protons in biological tissue is typically several hundred milliseconds at typical field strengths (1.5 T). By changing the magnetic field strength, the resonant condition may be closer to the motional frequency of protons in water, causing $T_1$ to shorten and increasing the $T_1$ in tissue. The change in the magnetisation along the direction of the magnetic field as it relaxes to thermal equilibrium is governed by the equation

$$\frac{dM_z}{dt} = \frac{-(M_z - M_0)}{T_1} \tag{3.14}$$

where $M_z$ is the longitudinal component of the magnetisation, and $M_0$ is the longitudinal component at thermal equilibrium. Since $T_1$ is the time constant describing the relaxation of the longitudinal component of magnetisation, it is referred to as the longitudinal relaxation time.

If a $90^\circ$ pulse has rotated the magnetisation into the x-y plane, the magnetisation will precess about $B_0$. As the magnetisation vector rotates about the z direction its magnitude decreases. This mode of relaxation is referred to as spin-spin, or transverse relaxation, and is given by the time constant $T_2$. Transverse relaxation is different from longitudinal relaxation in that it is not due to energy exchange to the lattice. Rather, unlike longitudinal relaxation, transverse relaxation is due to loss of phase coherence between spins. If the sample of interest were in a uniform field, all the spins would precess at the same frequency and in phase. However, magnetic field inhomogeneities and nuclear dipole fields within the bulk material will cause nuclei at different locations to precess at different frequencies. As the nuclei precess, their relative phases change, causing a loss in transverse magnetisation. Since transverse relaxation is affected by dephasing interactions $T_2 \leq T_1$.

$T_2$ is primarily due to local field imperfections and, thus, is less susceptible to magnetic field strengths than $T_1$. Since they produce larger static field components, slowly rotating molecules are causing more $T_2$ relaxation; this is readily observed in solids where $T_2$ is very short. The transverse magnetisation is governed by the equation

$$\frac{dM_{x,y}}{dt} = \frac{M_{x,y}}{T_2} \tag{3.15}$$

where $M_{x,y}$ is the component of the magnetisation in the x,y direction.

By combining equations 3.14, 3.15, 3.13 and the relationship $\mathbf{M} \propto \sum \mathbf{J}_i$ the well known Bloch equations [53] are reproduced in the rotating frame:

$$\frac{dM_x}{dt} = \gamma M_y(B_0 - \frac{\omega}{\gamma}) - \frac{M_x}{T_2} \tag{3.16}$$

$$\frac{dM_y}{dt} = \gamma M_z B_1 - \gamma M_x(B_0 - \frac{\omega}{\gamma}) - \frac{M_y}{T_2} \tag{3.17}$$

$$\frac{dM_z}{dt} = \gamma M_y B_1 - \frac{M_z - M_0}{T_1}. \tag{3.18}$$

Transverse spin relaxation due to magnetic field imperfections can be recovered using spin echoes. By applying a $90^\circ$ pulse, the longitudinal magnetization is rotated into the transverse plane where the spins precess. As time increases, spins in a larger field will precess faster than those in a smaller field causing them to dephase. In Figure 3.7 the faster spins are ahead of the slower spins. If a $180^\circ$ pulse is applied a time TE/2 after the $90^\circ$ pulse, the slower spins exchange place with the faster spins. After an additional time TE/2, the faster spins will catch up to the slower spins producing a spin echo. An example of a spin echo is shown in Figure 3.8.

The amplitude of the echo is smaller than that of the FID since the magnetization loss due to local dipolar fields is not recovered with a spin echo as in the case due to losses associated with magnetic field imperfections. When a refocusing $180^\circ$ pulse is given, both the spins and the dipolar fields are reversed. Thus the effect due to dipolar fields is unchanged using a spin echo. The use of a spin echo technique allows for the separation of dipolar and magnet inhomogeneity relaxation modes. Therefore, it is useful to define

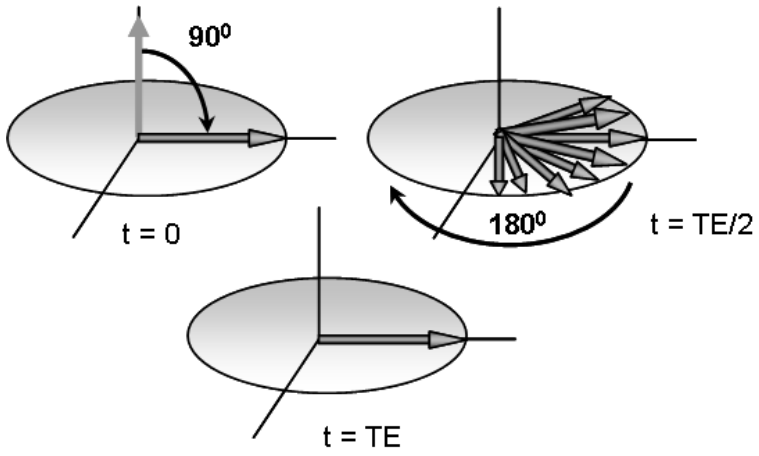


Figure 3.7: Formation of a spin echo. At time t=0 the net magnetization vector is in the x-y plane after having received a $90^\circ$ pulse. As time progresses, the spins begin to dephase due to magnetic field inhomogeneities. At time t=TE/2, a $180^\circ$ pulse is applied. At time t=TE the spins have rephased and an echo is observed.

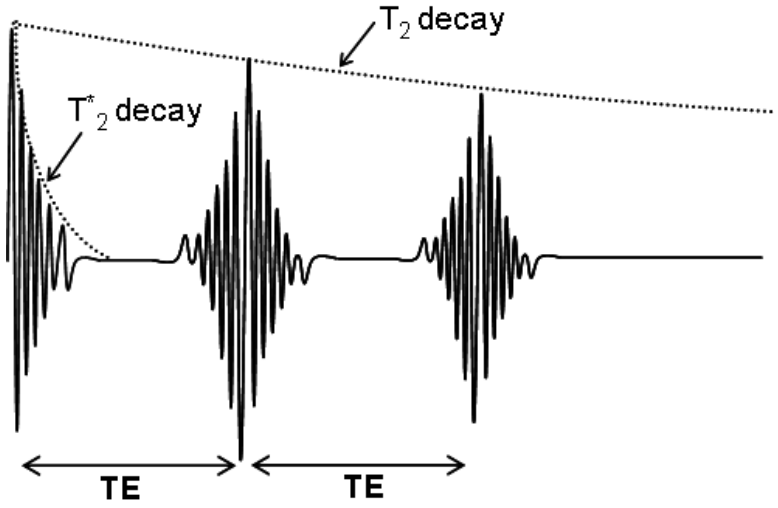


Figure 3.8: Signal observed during a spin echo. At t=0 a free induction decay is observed with a decay time constant of $T_2^*$. At time TE the center of the echo occurs. The echo amplitude decreases exponentially with a time constant $T_2$.

the transverse relaxation time constant due to non-reversible dephasing processes, such as dipolar fields, and diffusion as $T_2$ and the time constant related to the decay of the FID as $T_2^*$

$$\frac{1}{T_2^*} = \frac{1}{T_2} + \frac{1}{T_{2inh}} + \frac{1}{T_{2sus}} + \frac{1}{T_{2other}} \tag{3.19}$$

where $T_{2inh}$, $T_{2sus}$, and $T_{2other}$ are the transverse relaxation time constants due to inhomogeneities in the magnetic field, local differences in susceptibility and magnetisation, and other processes. Additional $180°$ pulses will produce similar echoes with decreasing amplitudes that fall off with the time constant $T_2$.

### 3.1.4 Acquisition Cycle in NMR

#### NMR at thermal polarisation

In the case of NMR at thermal polarisation, application of an RF pulse tips the magnetisation in the transverse plane; the signal is recorded during a time $T_2$. After waiting a time $t > 5 \times T_1$ to allow the magnetisation to recover fully, it is possible to send another RF pulse and get another signal and then repeat this for a any number of signals (Fig. 3.9).

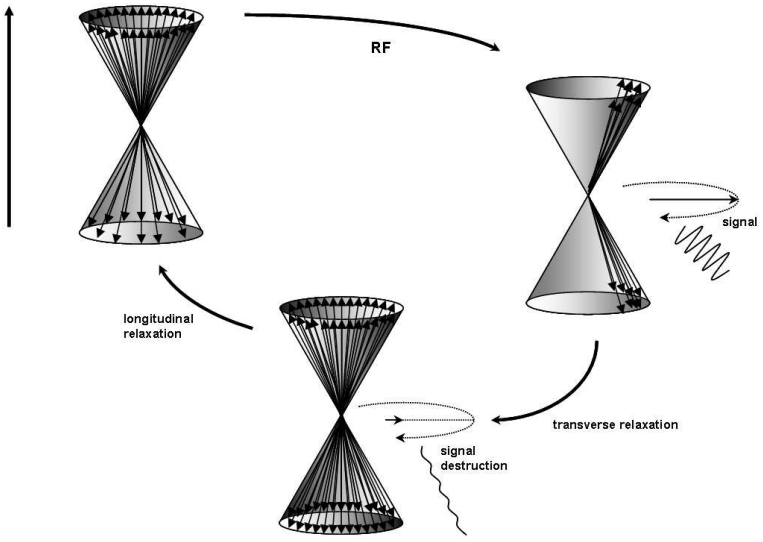


Figure 3.9: NMR at thermal polarisation: the microscopic magnetisations are represented by arrows: the effect of the RF pulse has a double effect: equalizes the parallel and antiparallel populations and puts in phase the magnetisations; starting from equilibrium, a $90°$ pulse tips the magnetisation in the transverse plane where it will generate a signal; after signal voidance (magnetisations dephasing), the longitudinal magnetisation is recovering and a new cycle can begin.

Usually, in NMR, the transverse relaxation ($T_2$) is considered a negative phenomenon since it destroys the signal. On the other hand, the longitudinal relaxation ($T_1$) is a positive one because it regenerates the signal reservoir; relaxing agents (contrast agents) are used to shorten $T_1$ and accelerate this regeneration.

**Single use magnetisation in the hyperpolarised regime**

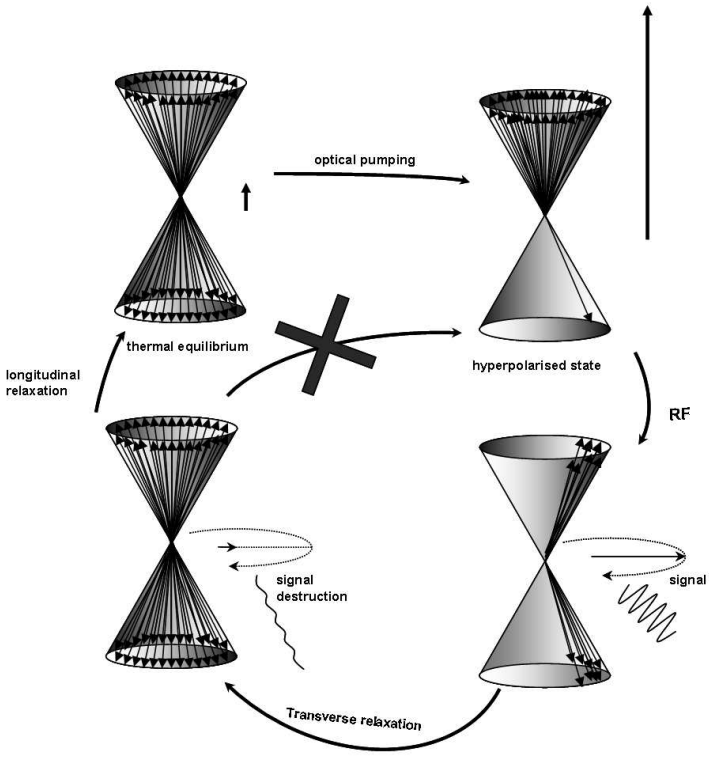


Figure 3.10: NMR in the hyperpolarised regime : starting with an equilibrium magnetisation, one can obtain a hyperpolarised state by optical pumping; an $90°$ RF pulse tips the magnetisation in the transverse plane where it generates a signal; after signal is destroyed because of the transverse relaxation, the longitudinal relaxation can not put the system back in the hyperpolarised state but in the equilibrium state meaning a state with very low magnetisation (virtually zero) compared to the magnetisation in the hyperpolarised state; since optical pumping is obtained only in very specific conditions (never in vivo), it is not possible to reproduce the cycle described in Figure 3.9.

In the hyperpolarised case, the longitudinal magnetisation is increased by optical pumping[1]; it is no more an equilibrium state. Applying an RF pulse tips the magneti-

[1] a description of optical pumping will be presented in a future section

sation in the transverse plane where it will generate a NMR signal. Immediately after the signal is destroyed, the longitudinal magnetisation generates the recovery of the magnetisation to the equilibrium state, which is not a hyperpolarised state anymore; it is a state with very low magnetisation compared to the hyperpolarised state. Since optical pumping need certain conditions that can not be obtained *in vivo*, this is a critical situation (Fig. 3.10). The hyperpolarised regime does not allow the cycling described in 3.1.4 .

The longitudinal relaxation, which is always recovering the system to its equilibrium, can be considered as a pejorative factor in the case of hyperpolarisation. It will transform a very high magnetisation level into a very low (almost zero) magnetisation. Therefore there are two aspects that are different from the classic NMR:

- once polarised, the gas has a life time dictated by $T_1$ during which it can be used for experiments. The goal is to maximise $T_1$, contrary to classic NMR where short $T_1$ is desired.

- cycling the magnetisation is impossible for medical applications since the optical pumping can not be done *in vivo*.

## 3.2 Magnetic Resonance Imaging

Nuclear magnetic resonance experiments were first reported independently in 1946 by Purcell et al. [57] at MIT, and by Bloch et al.[58] at Stanford. However, it was not until 1973 that the first two dimensional image of a live animal was reported by Lauterbur [59]. Mansfield and Grannell [60] demonstrated the relationship between the NMR signal and the spin density using Fourier techniques during the same year. In 1977 the first images were observed [61] using a whole body imager. Shortly afterwards, in the early 1980's, manufacturers obtained FDA approval for their magnetic resonance imaging systems. Today magnetic resonance imaging (MRI) is routinely used in experiments with resolutions of less than 0.1 mm for biological, mineral, and synthetic material research.

### Basic Principles of Spatial Localisation

Before obtaining an image, it is necessary to localise the magnetisation. The Larmor frequency - the frequency of the RF pulses that tip the magnetisation and also of the NMR signal - depends on the nucleus and the $\overrightarrow{B_0}$ magnetic field and it is in the order of tens of MHz. Since the frequency of precession for a moment is dependent upon the magnetic field strength, it is easy to impose a spatial dependence to the frequency by using a spatially varying magnetic field. Using linearly varying magnetic fields, the precession frequency will be a linear function of position. By defining the three dimensional gradient **G** as

$$\mathbf{G} = (G_x, G_y, G_z) - \left(\frac{\partial B_z}{\partial x}, \frac{\partial B_z}{\partial y}, \frac{\partial B_z}{\partial z}\right) \tag{3.20}$$

the magnetic field at position **r** can be written as

$$B(r) = B_0 + \mathbf{G} \cdot \vec{r} \tag{3.21}$$

where $B_0$ is the static magnetic field applied in the z direction. The position dependent angular frequency becomes

$$\omega(r) = \omega_0 + \gamma \mathbf{G} \cdot \vec{r} \tag{3.22}$$

**Localisation by slice selection** The first method of spatial localisation consists of applying a magnetic field gradient $G_z$ during the RF emission: only the spins situated in the region where the magnetic field corresponds to the frequency spectrum of the RF pulse will be tipped in the transverse plane. This selects a slice perpendicular to the z direction. The slice thickness is inverse proportional to the $G_z$ magnitude and proportional to the bandwidth of the RF pulse (Fig. 3.11).

**Localisation in frequency direction** When applying a gradient during signal recording this creates a linear frequency dependence of the signal on the position along the direction of the applied gradient (Fig. 3.12).

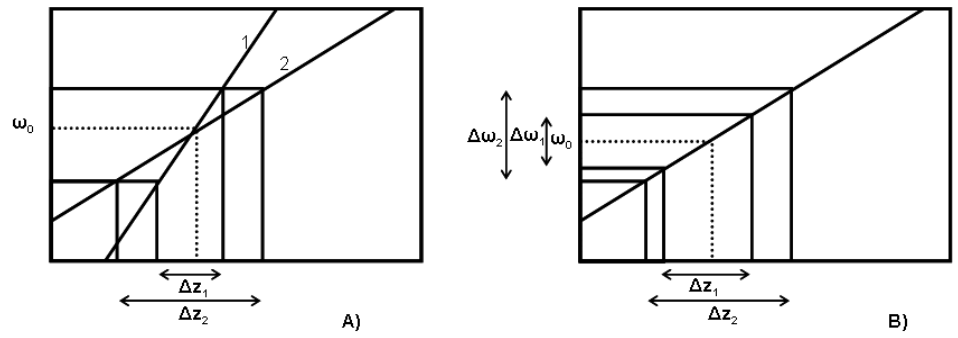


Figure 3.11: Figure A) shows how the slice thickness varies with different gradient strengths. Gradient 1 is greater than gradient 2 and the corresponding slice thickness $\Delta z_1$ is smaller than $\Delta z_2$. In figure B) the smaller bandwidth $\Delta\omega_1$ produces a thinner slice thickness $\Delta z_1$ than the larger bandwidth $\Delta\omega_2$ .

By identifying the frequencies and so the signal source, and by Fourier transformation, localisation becomes possible followed by the formation of a one-dimensional image.

The size of the pixel is small when the difference in frequencies between the two regions is large(the gradient is large) and the duration of signal observation is long.

Let's denote $T_{obs}$ the duration of signal observation, $t_{sample}$ the sampling period and $N_x$ the number of samples. The bandwidth of the signal is then $\Delta\nu = 1/t_{sample}$ and the frequency resolution: $\delta\nu = 1/T_{obs}$. If the field of view ($FOV_x$) consists of $N_x$ pixels of size $\delta x$, the following relationships are true:

$$FOV_x = \frac{2\pi\Delta\nu}{\gamma G_x} = \frac{2\pi}{\gamma G_x t_{sample}} \tag{3.23}$$

$$\delta_x = \frac{2\pi\delta\nu}{\gamma G_x} = \frac{2\pi}{\gamma G_x T_{obs}} \tag{3.24}$$

There is a symmetry between the image space and the signal space (Fig. 3.13): the size of one corresponds to the other's resolution (field of view $\Longleftrightarrow$ sampling time) and reciprocal (size of pixel $\Longleftrightarrow$ bandwidth).

Let's consider the transverse magnetisation in the rotating frame. In the absence of a gradient this magnetisation is fixed. By applying a gradient $\overrightarrow{G}$, the magnetisation located on an abscise *x* will rotate with an angular speed:

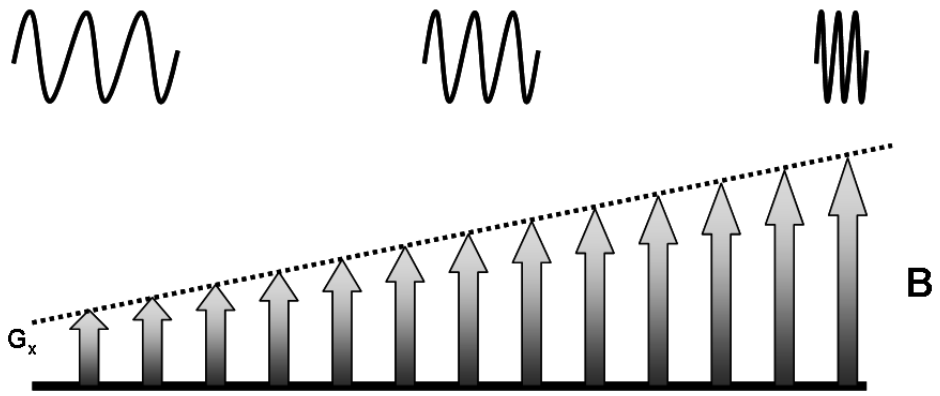


Figure 3.12: Applying a magnetic field gradient on x direction will determine a linear dependance of frequency and the position x.

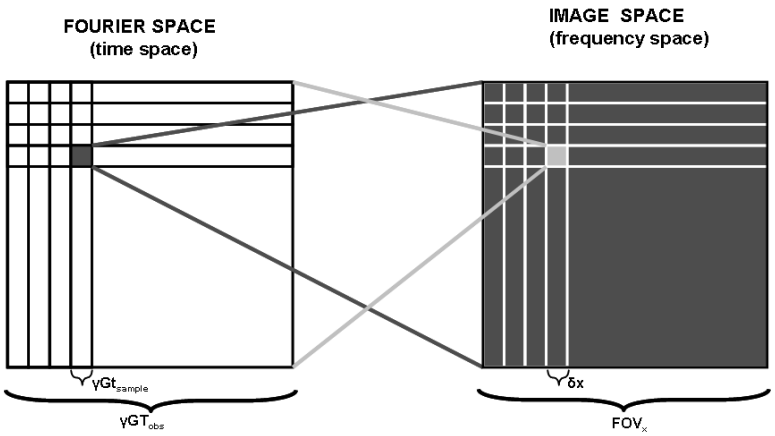


Figure 3.13: Illustration of the symmetry between the temporal signal space (called Fourier space) and the frequency image space: size of pixel is inverse proportional to the bandwidth; size of the field of view is also inverse proportional to the sampling time; each space can be obtained by Fourier transformation the other one.

$$\omega = \gamma G_x \cdot x \tag{3.25}$$

This will dephase and its evolution will be described by:

$$M(T) = M(0) \times \exp\left(i \cdot \int_0^T \gamma G_x(t) \cdot x dt\right) \tag{3.26}$$

the total signal being the sum of all the magnetisations.

**Localisation in phase direction** To get the second dimension of the image, the most popular method consists of repeating the signal acquisition in the presence of a gradient $G_y$ placed between the slice selection and signal reading (Fig. 3.15). By varying the gradient amplitude, the magnetisation is dephased and this dephasing depends on its position on the y axis. The equations 3.25 and 3.26 can be generalised:

$$\omega = \gamma \overrightarrow{G} \cdot r \tag{3.27}$$

$$M(T) = M(0) \times \exp\left(i \cdot \int_0^T \gamma \overrightarrow{G}(t) \cdot \overrightarrow{r} dt\right) \tag{3.28}$$

The dephasing between two consecutively sampled points (and dephased by $G_x$) and two successive lines (and dephased by $G_y$) is of the same nature and is given by Eq. 3.28 although there are two differences between the read and phase gradient:

- the read gradient is always applied during the signal acquisition
- two points sampled from the same line (discriminated by the read gradient) are obtained using the same RF pulse; two points from the same column are obtained by using different RF pulses

Image reconstruction is obtained by applying a second Fourier transform in the y-direction.

Hence, the acquisition consists of sampling the reciprocal image space, or Fourier-space (*k*-space) . The image is then obtained using a two-dimensional Fourier transform. The Fourier-space formalism, described in 1983 [62], [63], allows us to describe the image acquisition strategy in an easy way (Fig. 3.14 and Fig. 3.15). The hyperpolarised gas case is described later.

### Signal and noise

The hyperpolarisation technique is used to compensate for the lack of NMR signal from the gases. In addition, the polarisation at thermal equilibrium and hyperpolarisation are determined by different factors. Therefore it is useful to treat separately the signal to noise ratio for the two situations.

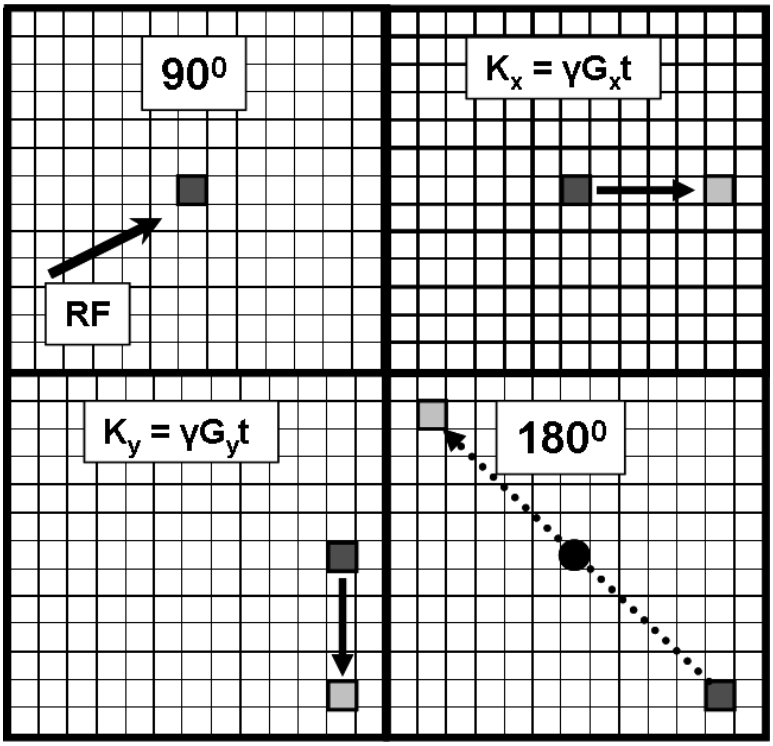


Figure 3.14: The rules of covering the *k*-space. First, the transverse magnetisation is at the center of the *k*-space; a gradient along the x-direction creates a horizontal displacement in the *k*-space; a gradient along the y-direction creates a vertical displacement in the *k*-space; a $180^\circ$ pulse creates a central symmetry in the *k*-space.

### Signal amplitude

**Signal in general** The NMR signal is an electromotive force $\xi$ induced in the coil by the precessing transverse magnetisation $\overrightarrow{M}$. This causes a magnetic flux variation:

$$\xi(t) = \iiint\limits_{\text{object}} -\frac{\partial}{\partial t}\left[\overrightarrow{b_1}(x,y,z)\cdot\overrightarrow{M}(x,y,z)\right]dxdydz \tag{3.29}$$

where $\overrightarrow{b_1} = \frac{d\overrightarrow{B_1}}{dI}$ is the magnetic field per unit of current created by the coil in transmission mode (the reciprocal theorem [64]).

Tipping the whole available magnetisation, $M_0 = ||\overrightarrow{M_x, y}||$; assuming $\overrightarrow{b_1}$ normal to $\overrightarrow{B_0}$ Eq. 3.29 is written as:

$$\xi(t) = b_1 \cdot M_0\omega_0\cos(\omega_0 t)\cdot V \tag{3.30}$$

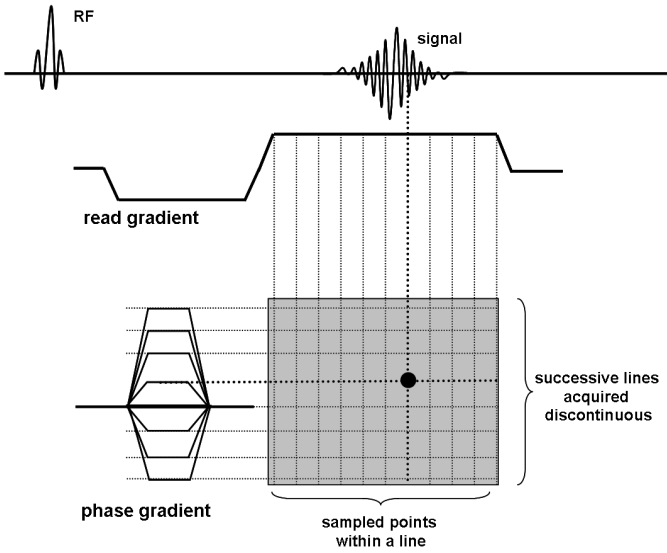


Figure 3.15: The *k*-space: after applying an RF pulse, we apply a gradient $G_y$ in the y direction and then a gradient $G_x$ during signal recording; each point stores the dephasing caused by the two gradients; repeating the acquisition while varying the amplitude of the encoding gradient allows for sampling of the temporal signal space called Fourier-space (*k*-space); the slice selection gradient is not represented on this plot.

V being the volume over which $\overrightarrow{b_1}$ is supposed to be uniform.

**Signal at thermal polarisation** At thermal equilibrium , the magnetisation is

$$M = n\frac{\gamma^2\hbar^2 B_0}{4kT_s},$$

where $T_s$ is the temperature of the sample. More general formulation is [65]:

$$M_0 = \frac{B_0 n\gamma^2\hbar^2 I(I+1)}{3kT_s} \tag{3.31}$$

For a number $N$ of spins $\frac{1}{2}$ the amplitude of the signal is:

$$\xi(t) = b_1 \cdot \frac{\gamma^3\hbar^2 B_0^2}{4kT_s} \times N \tag{3.32}$$

For MRI, considering the number of resonant atoms in the voxel $n \times \delta x \times \delta y \times \delta z$, the equation is:

$$\xi_{c-c}(t) = b_1 \cdot \frac{n\gamma^3\hbar^2 B_0^2}{4kT_s}\delta x \times \delta y \times \delta z \tag{3.33}$$

So, the signal is proportional to the sensitivity of the coil and the square of the main magnetic field.

**Signal in the hyperpolarised regime** In the hyperpolarised regime, the polarisation is not given by the Boltzman's statistics but it depends on the optical pumping. By replacing the value of magnetisation given by

$$M_z = n\frac{\gamma\hbar P}{2}$$

in 3.30, we get:

$$\xi = b_1 \cdot \frac{n\gamma^2\hbar B_0}{2}\delta x \times \delta y \times \delta z \times P \tag{3.34}$$

In the hyperpolarised case, the signal is linearly proportional to the main magnetic field and to the polarisation obtained by optical pumping.

**Sources of noise** The electronic noise comprises of two types: Johnson noise or thermal and Schottky noise or quantic noise (caused by the random motion of the electrons in a semiconductor). In real life, the quality of the components used in NMR allows us to neglect the Schottky noise.

The Johnson noise is the electronic noise generated by the thermal agitation of the charge carriers (usually the electrons) inside an electrical conductor at equilibrium, which happens regardless of any applied voltage. The value of the noise emitted by a resistor $R$ at temperature $T_R$ in a frequency range $\Delta\nu$ is:

$$\xi_N = 2\sqrt{kT_R R\Delta\nu} \tag{3.35}$$

A general method to reduce the thermal noise is the use of a narrow bandwidth; this is also limited by the signal life time.

There are multiple sources of thermal noise:

**Coil noise in general** Usually, the coils used in NMR experiments are resistive ones. At zero frequency, the resistance $R_c$ of a loop with resistivity $\rho_c$, of perimeter $2\pi a$ and section radius $r$ is:

$$R_C = \rho_c \frac{2a}{r^2} \tag{3.36}$$

At high frequency, the current only flows efficiently on the surface of the conductor down to a dept $\delta$ (the "skin" effect) :

$$\delta = \sqrt{\frac{2\rho_c}{\mu_0 \omega_0}} \tag{3.37}$$

where $\mu$ is the magnetic permeability. For copper, at 3 MHz $\delta$ is about 30 $\mu$m. Eq. 3.34 becomes:

$$R_c = \frac{a}{r}\sqrt{\frac{\mu_0 \rho_c \gamma B_0}{2}} \tag{3.38}$$

This is true for a right circular cylinder. In addition to this, for a real coil, there is a proximity factor $\zeta$ that reduces the conductivity of the coil at high frequencies. Current carrying wires influence other currents through the magnetic field that it produces. Hence:

$$R_c = \zeta \frac{a}{r}\sqrt{\frac{\mu_0 \rho_c \gamma B_0}{2}} \tag{3.39}$$

and the noise voltage:

$$\xi_c = \sqrt{\frac{a}{r} k T_c \zeta \Delta\nu}\sqrt[4]{8\mu_0 \rho_c \gamma B_0} \tag{3.40}$$

where $T_c$ is the coil temperature.

This type of noise can be reduced by changing $T_c$ or $\rho_c$ (superconductive coil )

**Coil noise at low magnetic field** Eq. 3.40 was calculated considering $\delta$ very small compared to the diameter of the wire. At low field $\delta$ may become similar to the wire radius; in this case, the "skin" effect does not occur and Eq. 3.38 is not true. From 3.37, the frequency corresponding to $\delta$ is:

$$\nu_0 = \frac{\rho_c}{\pi \mu_0 \delta^2} \tag{3.41}$$

Considering the conductivity of the copper to be $1.710^{-8}\Omega m$ [66], the frequency corresponding to a millimeter depth "skin" effect, is 4300 Hz. This gives a magnetic field of 100$\mu$T. The noise voltage is then:

$$\xi_B = \frac{2}{r}\sqrt{\frac{kT_R\rho_c p\Delta\nu}{\pi}} \tag{3.42}$$

independent of the field.

At low field there are other sources of noise like the Schottky noise or exterior magnetic fluctuations that can be dominant.

**Inductive coupling to object** The sample examined by NMR is inductively coupled to the coil; it is behaving like a noisy resistance. The resulting noise is inherent strictly because of the nature of the signal. Considering the case of a patient, there are models that can estimate the noise induce by his presence. Considering a model of a half-space plane conductor placed in contact with a loop of radius $a$. The resistance $R_S$ is then [67]:

$$R_S \simeq \frac{1}{3}\sigma_S\mu^2\omega_0^2 a^3 \tag{3.43}$$

where $\sigma_S$ is the conductivity of the object. Although this simple model does not correspond entirely to the real life, it gives an idea of the noise dependance. The noise voltage induced by the subject is:

$$\xi_S = 2\left(\sqrt{\frac{kT_S}{3}\sigma_S\Delta\nu}\right)\mu_0\gamma B_0 a^{3/2} \tag{3.44}$$

This type of noise is inevitable and can only be reduced by adapting the dimensions and the coil geometry to the field of view, in other words to avoid collecting noise from regions that don't provide signal.

**Capacitive coupling to object** The sample and the coil are two conductors placed face-to-face and so they behave like a capacitor. It is possible to minimise this coupling by distributing the tuning capacitance along the wire; this diminishes the electric field between the sample and the coil. In general this can be neglected if the coil is well designed. The resistance induced by dielectric losses $R_E$ can be written as [67]:

$$R_E = \tau\omega_0^3 L^2 C_d \tag{3.45}$$

where $\tau$ is a factor of dielectric losses, $L$ is the inductance of the coil, and $C_d$ is the distributed capacitance. The noise voltage is then:

$$\xi_B = 2\sqrt{kT_S\Delta\nu\tau C_d}L\gamma^{3/2}B_0^{3/2} \tag{3.46}$$

**Environment coupling** The coil is located in a complex environment surrounded by the magnet, gradient coils and transmit coils. All these metallic components can be coupled at frequency $\nu_0$. They can induce a resistance $R_B$. Generally, a screen prevents the coupling of the coil with the rest of the system at the frequency $\nu_0$.

**Review of different sources of noise** By neglecting the capacitive coupling, the total noise, as long as the magnetic field is not too low (less then 100 $\mu$T), can be written as:

$$\xi_B = \sqrt{k\Delta\nu}\left[\underbrace{\sqrt{\frac{a}{r}T_c\zeta}\sqrt[4]{8\mu_0\rho_c\gamma B_0}}_{coil} + \underbrace{2\sqrt{\frac{T_S}{3}\sigma_S}\mu_0\gamma B_0 a^{3/2}}_{sample} + \underbrace{2\sqrt{T_R R_B}}_{scanner}\right] \tag{3.47}$$

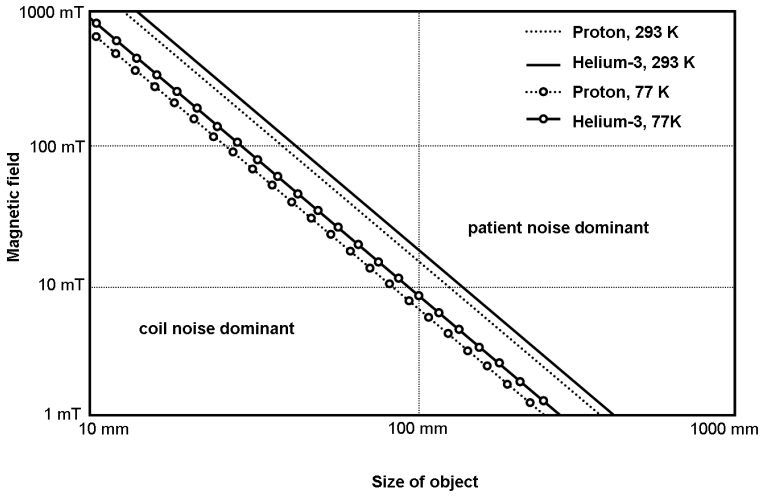


Figure 3.16: The conditions for patient noise dominance. (from [67]).

From Eq. 3.47, the condition of patient noise dominance over the coil noise is:

$$B_0 > \sqrt[3]{\frac{9}{2}\frac{\rho_c}{\sigma_S^2}}\left(\frac{a}{r}\zeta\right)^{2/3}\left(\frac{T_c}{T_S}\right)^{2/3}\frac{1}{\mu_0\gamma}a^{-2} \tag{3.48}$$

Considering a perfect coil with $\frac{a}{r}\zeta$ of 30 [67], the copper resistivity 1.7 $10^{-8}\Omega m$ [68], human tissue conductivity is 0.66 $Sm^{-1}$ [70], human temperature is 310 K, the resulting conditions are presented in Table 3.1 and Figure 3.16 [67].

For lung imaging with $^3$He (radius of order 200 mm), this figure indicates that the patient noise is dominant above 5 mT.

### Signal to noise ratio

**At thermal equilibrium** In the case of classic NMR at Boltzman's equilibrium, from Eq. 3.33, the signal to noise ratio is given by:

$$\begin{aligned} SNR &= \frac{\xi_{c-c}}{\xi} \\ &= \frac{K \cdot b_1 \cdot B_0^2 n \gamma^3 \hbar^2 (\delta x \delta y \delta z)}{4k^{3/2} T_S \sqrt{\Delta\nu} \left[ \sqrt{\frac{a}{r} T_c \zeta} \sqrt[4]{8\mu_0 \rho_c \gamma B_0} + 2\sqrt{\frac{T_S}{3}\sigma_S} \mu_0 \gamma B_0 a^{3/2} + 2\sqrt{T_R R_B} \right]} \end{aligned} \tag{3.49}$$

Table 3.1: The conditions of patient noise dominance (a is the coil radius or the size of the object)

| | proton | helium-3 |
|---|---|---|
| @ 293 K | $B_0 > 1.5510^{-4} T.m^2 \times a^{-2}$ | $B_0 > 2.0310^{-4} T.m^2 \times a^{-2}$ |
| @ 77 K | $B_0 > 6.3510^{-5} T.m^2 \times a^{-2}$ | $B_0 > 8.3410^{-5} T.m^2 \times a^{-2}$ |

In order to maximise the signal to noise ratio (SNR), we need to optimise the coil geometry ($b_1$), use a nucleus with high gyromagnetic ratio, limit the spatial resolution, reduce the bandwidth $\Delta\nu$, work at low temperature and at a high field.

**In the hyperpolarised regime**

$$\begin{aligned} SNR &= \frac{\xi_{signal}}{\xi_{noise}} \\ &= \frac{b_1 \cdot n \gamma^2 \hbar B_0 (\delta x \delta y \delta z) \times P}{2\sqrt{k\Delta\nu} \left[ \sqrt{\frac{a}{r} T_c \zeta} \sqrt[4]{8\mu_0 \rho_c \gamma B_0} + 2\sqrt{\frac{T_S}{3}\sigma_S} \mu_0 \gamma B_0 a^{3/2} + 2\sqrt{T_R R_B} \right]} \end{aligned} \tag{3.50}$$

The SNR is then proportional to the polarisation created by the optical pumping and is dominant over the SNR given by the $B_0$ strength.

## 3.3 Physics of the hyperpolarised $^3$He

The idea of increasing the NMR signal by moving away from thermal equilibrium is not new. To do NMR in the hyperpolarised regime there are two conditions that need to be fulfilled: the isotope needs to be nuclear magnetic resonance active (nuclear spin different from zero) and capable of being hyperpolarised. There are multiple methods that can be used; the first to have been used in NMR is the Overhauser effect [69]; however, this effect cannot be used *in vivo* in humans since it requires injection of free radicals and also the resonant frequency is in the microwave spectrum unless the magnetic field is very low (10 mT) [70]. The more recent use of hyperpolarised noble gases by optical pumping made possible the first images in this regime in humans.

There are two elements that are hyperpolarised by optical pumping: helium ($^3$He) and xenon ($^{129}$Xe) [71]; the latter has the advantage - or disadvantage depending on the application - of dissolving very quickly in the biological tissues and having a large chemical shift, which allows for using $^{129}$Xe in spectroscopy. However, only $^3$He will be treated in this section since is the only nucleus used in this work.

Following a brief description of some physical properties of helium there will be a discussion on the principle of nuclear hyperpolarisation followed by a more detailed description of two essential aspects of hyperpolarised gases NMR: signal gain by optical pumping and rapid diffusion.

### 3.3.1 Helium properties

Helium was discovered in 1868 by the French astronomer Pierre Janssen during a total solar eclipse. It is a colorless, odorless, tasteless, non-toxic, inert monatomic chemical element that heads the noble gas series in the periodic table and whose atomic number is 2. Helium is the second most abundant and second lightest element in the known universe. It's the element with the lowest boiling point (4 K) so is used as a cryogenic liquid.

Its dynamic viscosity $\eta$ (17 $\mu$ Pa.s for $^3$He and 20 $\mu$ Pa.s for $^4$He) is similar to air (18 $\mu$Pa.s) [68], [72]; the kinetic viscosity $\nu = \eta/\rho$ is 10 times higher than air. In similar condition, helium flow is less turbulent than air. Let's consider a flow $Q = 0.5L.s^{-1}$

through a pipe of diameter $d = 3mm$, a typical situation observed when inhaling the gas during the experiments reported in this work. The Reynold's number

$$Re = \frac{2Q\eta}{\pi d\rho} \tag{3.51}$$

is of order of 2000 for helium (indicating a laminar flow) and 16000 for air (indicating a turbulent flow).

Helium has two isotopes that are stable. The principal isotope ($^4_2He$) has the atomic mass equal to 4.0026 uma and a nuclear spin zero. The other isotope ($^3_2He$) has the atomic mass 3.016 uma; its nucleus consists of two protons and a neutron and has a spin $I = 1/2$, hence its NMR suitability.

The natural reserve of $^3$He is found in the atmosphere but the isotopic concentration is very low ($^3He/^4He \sim 1ppm$) and extraction is extremely expensive. The current production of $^3$He comes from military (side-product of $\beta^-$ disintegration of tritium). The cost per litre is approx. $£100$. $^3$He is very abundant in the universe; the lunar reserves are high and in higher isotopic concentration ($^3He/^4He \sim 400ppm$); there are plans to exploit these deposits to allow for the production of energy from nuclear fusion [73].

Having a zero valence, helium is chemically inert. It does not have chemical toxicity. Helium is used, mixed with oxygen, as a vector gas both in diving to avoid nitrogen narcosis and in medical emergency when there is an elevated bronchial resistance and helium prevents the turbulent flow due to its high kinetic viscosity and diffusivity [74], [75].

The speed of sound in helium is (at $0°C$) $965m.s^{-1}$ ($331m.s^{-1}$ in air); this will change the timbre of a person's voice when inhaled.

At $37°C$, helium is slightly soluble in blood and water compared to xenon which is almost 20 times more soluble.

### Production of nuclear orientation

The following section is a brief theory of the techniques used to create the nuclear orientation. There are multiple articles that describe in detail these methods. The first description of the hyperpolarisation by optical pumping was made in 1963 [76]. There is also a good

review of the technique of optical pumping by metastability exchange done by Brossel $et.al$ [77] and other articles on the LASER side and other aspects on optical pumping [78], [79], [80].

There are two categories of methods used to enhance the nuclear polarisation:

- obtaining a superior polarisation at equilibrium in different conditions (the "equilibrium" method or the "brute force")
- using the transitions between different states to obtain a greater polarisation ("non-equilibrium" method)

The first method consists of placing the $^3$He nuclei at high field and low temperature during a period a few times longer than the relaxation time in those conditions; the result is a state of higher polarisation than the initial state; by quickly heating the helium it is possible to use the sample at the room temperature assuming it is done in a shorter time than $T_1$ [81], [82].

The second method consists of polarising the nuclei directly in a non-equilibrium state.

**The principle of optical pumping** The nuclear hyperpolarisation can be achieved by a procedure called optical pumping which allows the transfer of angular momentum from polarised light to nucleus via electrons, thanks to the electronuclear coupling (hyperfine coupling) which exists at certain atomic levels.

The principle is to create a population difference between two magnetic sub-levels from a metastable state by absorbing and re-emitting polarised light. This is illustrated in Figure 3.17.

In our case, since $^3$He has two Zeeman states, the interaction is necessary with an external spin. There are two possible situations:

- the use of rubidium atom; hyperpolarisation is obtained by transferring the angular momentum through coupling of the electronic spin of Rb and the helium nucleus during collision [83], [84]

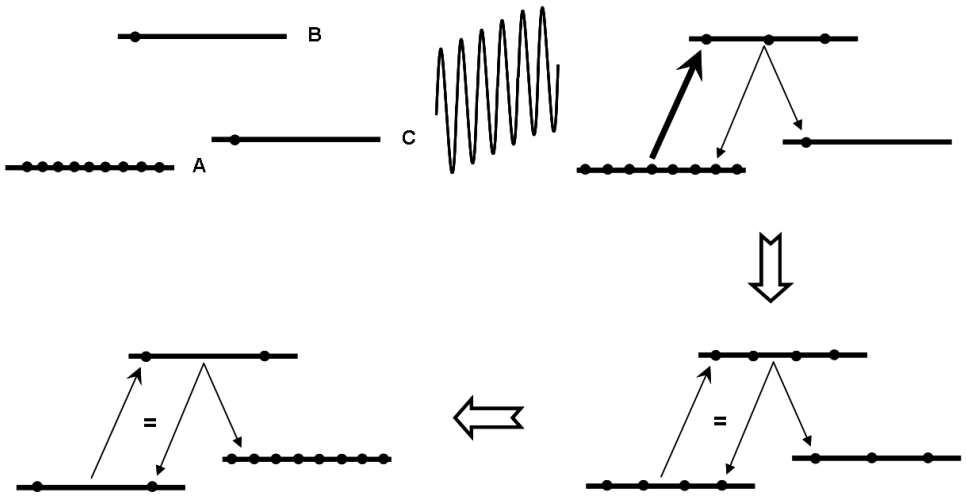


Figure 3.17: The principle of optical pumping in a system with three states: two magnetic sublevels (A and C) of a "fundamental state" (metastable state) and the excited state (B); A is irradiated by a photons beam corresponding to the transition ($A \leftrightarrows B$); state B will get populated, without exceeding population of A; however, since B can be de-excited to both A and C, state C will keep populating since it can not be de-excited by stimulated emission since the photons don't correspond to its transition; if C has a long radiative life-time(metastability), its population will increase at the expense of A via B: this is the optical pumping.

- the use of the electro-nuclear coupling (hyperfine) between helium atoms; this will be described in this section

**Optical pumping by exchange of metastability** The method was invented by Colegrove [76] and orients the helium atoms by optical pumping to a metastable state followed by transfer of the angular momentum to the atom in a stable state during collision (exchange of metastability).

**Obtaining the metastability** The metastable state is created by plasma (obtained by electric discharge in the gas). The result is a large variety of excited levels. Only rapid de-excitations (100 ns) populate the metastable level $2^3S$ (the radiative life-time is hours) (Fig. 3.18).

The $2^3S \rightarrow 1^1S$ transition is forbidden.

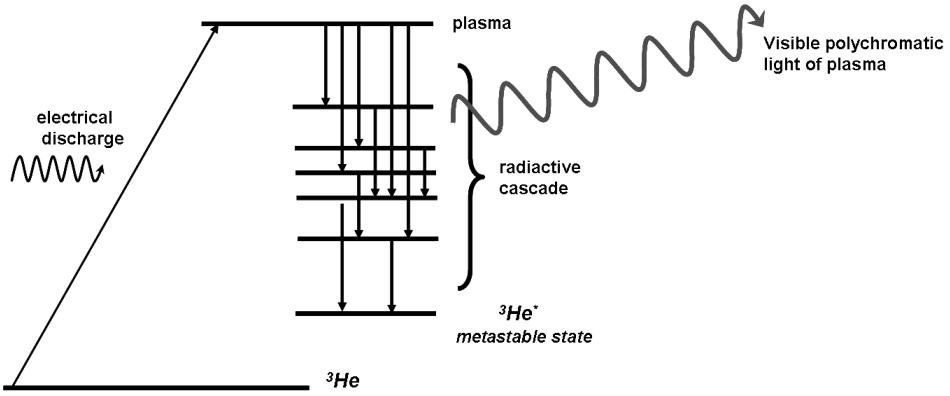


Figure 3.18: De-excitation in cascade inside the plasma will populate the metastable levels.

**Optical pumping of the metastable state** Optical pumping occurs between the metastable state 2S and the excited state P (Fig. 3.18). This transition (1.15 eV) corresponds to 1083 nm wavelength (near infra-red). The transition is obtained by using a narrow spectrum light (in this case a LASER).

There are 9 allowed transitions between the hyperfine sub-levels 2S and 2P: $C_1 - C_9$. By tuning the LASER it is possible to select any transition.

The goal of pumping is the transfer of angular momentum between two populations; it needs to select the transitions that involve angular momentum transfer ($\Delta m \neq 0$). For this, there are two possible approaches.

In the first method the transition selection is done by angular momentum transfer: for example a right circularly polarised light $\sigma^+$ will induce transitions with unity variation of the angular momentum projection ($\Delta m = +1$). Figure 3.19 shows the C9 transition between $2^3S_1, F = \frac{3}{2}, m_z = -\frac{3}{2}$ or $-\frac{1}{2}$ and $2^3P_0, F = \frac{1}{2}, m_z = -\frac{1}{2}$ or $+\frac{1}{2}$.

The excited state $2P$ will de-excite (the life-time of $2^3P$ is the order of 100 ns) in a radiative manner. The angular momentum of the emitted photons depend on the excited sub-levels and the transitions that can be observed are $\Delta m = +1, \Delta m = 0$ or $\Delta m = -1$ but the emitted light will not be polarised. The effect of the optical pumping followed by the de-excitation will be a positive transfer of the angular momentum to helium (Fig. 3.20).

This process is done at low pressure (the order of 10 mbar).

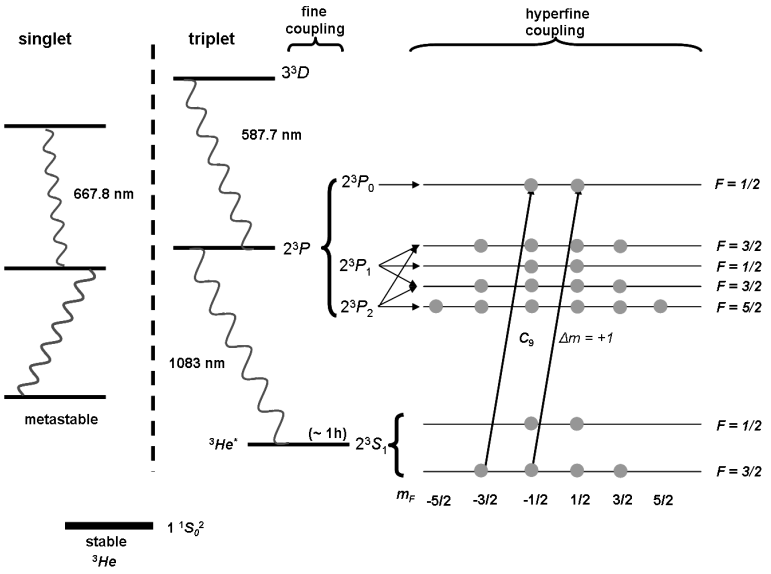


Figure 3.19: Energy levels of Helium-3 at low field; example of optical pumping of a metastable triplet on line C9 by light $\sigma^+$.

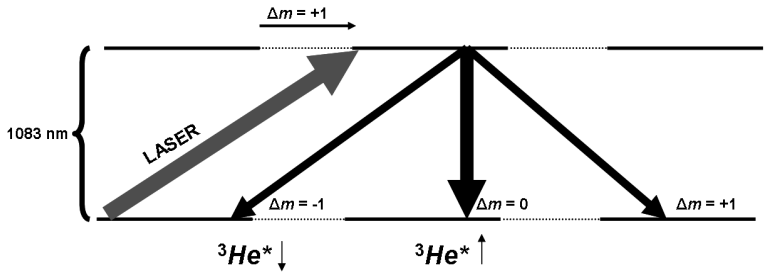


Figure 3.20: During the pumping by a polarised light $\sigma^+$, the angular momentum is incremented; at the time of de-excitation, the direction of the variation is isotrope and can only vary according to the sub-levels; however, the statistic effect is the rise of the angular momentum by pumping and de-excitation.

**Exchange of metastability** In experimental conditions, the proportion of metastable atoms is approximate $10^{-6}$ of the helium atoms. During the collision between the atoms in the fundamental state and the polarised metastable atoms, an exchange of metastability will occur: at the end of the collision, the nuclei could exchange electrons; the final state consists of a non-polarised metastable state (2S) and a stable state (1S) whose nucleus is polarised by electronuclear coupling (hyperfine) (Fig. 3.21). The angular momentum of the stable atom is carried by the nuclear spin since its electronic angular momentum

is zero. In the end this corresponds to a transition from parallel to anti-parallel state. In order for the nuclear polarisation to exist, it is necessary to run the optical pumping in the presence of a magnetic field. The field is not necessary to be high since a field too strong will accentuate the Zeeman effect and reduce the hyperfine interaction.

The effective cross-section of the metastability exchange is in the order of $\sigma \simeq 10^{-20}$ m$^2$. The interval between two collisions depends on pressure (is in the order of 0.2 $\mu s$ at 1 torr for the metastable atoms and 0.2 s for the stable atoms).

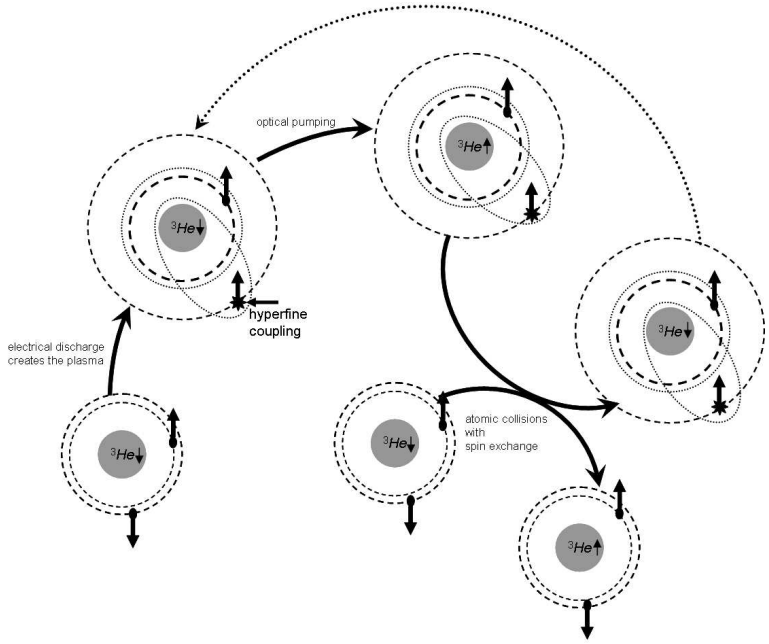


Figure 3.21: Optical pumping cycle: the electrical discharge creates a plasma, containing metastable atoms with electronuclear coupling; the optical pumping transfer angular momentum to these atoms. During collision, can transfer their angular momentum to the atoms in the fundamental state; they can then start a new pumping cycle.

The process of optical pumping is always competing against relaxation phenomena. In practice, the main source of relaxation of the metastable atoms is the collisions with the walls; the nuclear relaxation is due to plasma ($T_1$ is in the order of minutes). Using a more powerful LASER can increase polarisation, to some extent (the phenomena are not linear and saturation can occur). The collisions in a typical pumping cell, occur after diffusion over a distance the order of centimeters (diffusion coefficient is in the order of 0.1 m$^2$.$s^{-1}$).

To conclude, this method works at low pressure and high chemical purity. It needs an electric discharge to generate plasma, a monochromatic light source (LASER) at 1083 nm to select a $\Delta m = \pm 1$ transition and a weak magnetic field ($\ll 1T$). Recent work from Krakow group shows that MEOP can be achieved at magnetic field strength of 2 T and 64 mBar pressure ([85]). The present findings suggest that still higher polarizations can be achieved in higher magnetic fields, and motivate investigations at higher gas pressures. New ways of producing hyperpolarized $^3$He for magnetic resonance imaging and medical applications can be envisaged, as most clinical whole-body scanners operate at 1.5. This allows levels of nuclear polarisation superior to that of the equilibrium states to be generated.

### NMR signal gain in the hyperpolarised regime

We already know the size of polarisation at thermal equilibrium in normal conditions of field strength and temperature is $10^{-6}$. Even a modest hyperpolarisation state induces a considerable gain in signal. For a 10% polarisation the gain in signal is a factor of $10^5$.

**Comparison of the signal-to-noise ratio in proton NMR and hyperpolarised $^3$He** In the hyperpolarised regime, the polarisation is given by the optical pumping and does not depend on $B_0$ like at thermal equilibrium. In the MRI of the lung at 0.15 T, the dominant noise is the patient noise. The SNR for proton and helium are:

$$SNR_H = \frac{b_1 \cdot B_0 n_H \gamma_H^2 \hbar^2 (\delta x \delta y \delta z)}{4k^{3/2} T_S \sqrt{\Delta\nu} 2\sqrt{\frac{T_S}{3}\sigma_S \mu_0 a^{3/2}}} \tag{3.52}$$

$$SNR_{He} = \frac{b_1 \cdot n_{He} \gamma_{He} \hbar (\delta x \delta y \delta z) \times P}{4\sqrt{k\Delta\nu}\sqrt{\frac{T_S}{3}\sigma_S \mu_0 a^{3/2}}} \tag{3.53}$$

where $P$ is the value of the polarisation obtained by optical pumping.

Considering identical coils the SNR is then:

$$\frac{SNR_{He}}{SNR_H} = \frac{n_{He}}{n_H}\frac{\gamma_{He}}{\gamma_H}\frac{2kT_S}{B_0 \gamma_H \hbar} \times P \tag{3.54}$$

The nuclear density ratio of pure $^3$He and water at normal temperature and pressure

$$\frac{n_{He}}{n_H} = \frac{44.6 mol.m^{-3}}{111 \cdot 10^3 mol.m^{-3}} = 4.04 \cdot 10^{-4} \tag{3.55}$$

is compensated by a polarisation of 20% at 0.15 T:

$$\frac{SNR_{He}}{SNR_H} = 26 \tag{3.56}$$

**Dependence of signal-to-noise ratio on $B_0$ as a function of the dominant noise** According to 3.33 and 3.34, the signal depends quadratically upon field $B_0$ at thermal equilibrium and linearly in hyperpolarised regime.

If the dominant noise is the patient noise, the noise depends linearly on $B_0$ and quad root of $B_0$ if coil noise is dominant (after 3.47). At very low field (less than $100\mu T$), is negligible and the coil noise is independent of field $B_0$ (according to 3.42).

In practice, for magnetic fields less than 50 mT, the dominant noise is the patient noise, for objects bigger than 5 cm (Fig. 3.16). In these conditions, in hyperpolarised regime, the SNR is independent of $B_0$. At equilibrium, SNR is linearly dependent on $B_0$ (Table 3.2) ([86]. This relies on the assumptionwe can build equally sensitive coils that couple equally well to sample at any frequency.

The hyperpolarised regime gives an unusual situation in NMR: the independence of SNR to the main magnetic field. The low fields are easier to produce and less expensive.

Table 3.2: The dependence of SNR on $\overrightarrow{B_0}$.

| Signal regime | | patient noise dominant | coil noise dominant | coil noise dominant no "skin" effect |
|---|---|---|---|---|
| equivalent resistance | | $R_S \propto B_0^2$ | $R_C \propto B_0^{1/2}$ | independent $R_C$ |
| noise | | $B \propto B_0$ | $B \propto B_0^{1/4}$ | independent B |
| thermic | $Signal \propto B_0^2$ | $SNR \propto B_0$ | $SNR \propto B_0^{7/4}$ | $SNR \propto B_0^2$ |
| hyperpolarised | $Signal \propto B_0$ | no dependence | $SNR \propto B_0^{3/4}$ | $SNR \propto B_0$ |

## 3.4 Diffusion effect on NMR

Diffusion in gases is very fast. Diffusion in an inhomogeneous magnetic field causes the magnetisation carriers to lose coherence; this is the transverse relaxation mechanism. The effect of diffusion is used in proton MRI. In medicine it is used in brain imaging [87]. Diffusion in proton MRI is not a source of artefact apart from microscopy [88]. However, helium diffusion, being $10^4$ times more rapid than in water, will have a bigger impact.

This section will start with some theory on the free diffusion. The case of free diffusion in a uniform gradient will be treated for different types of gradients. Aspects of restricted diffusion will be detailed in a future chapter.

### 3.4.1 Free diffusion

The free diffusion occurs when there is no obstacle (apart from themselves) for the particles to move.

#### Theory of the free diffusion

The mean quadratic speed of a particle A (atom or molecule) can be written as:

$$\overline{\nu}_A = \sqrt{\frac{3kT}{m_A}} \tag{3.57}$$

$k$, being the Boltzman's constant, $T$ the gas temperature and $m_A$ the particle mass. For the helium atom at 37°C, m = 3.016 uma [68] and the mean quadratic speed can be found to be 1601 $m.s^{-1}$.

The mean free path $l$ is defined as the mean distance traveled during two consecutive collisions and the mean free time $\tau$ as the mean duration between these two collisions [89]. Hence:

$$l = \overline{\nu}_A \tau \tag{3.58}$$

Let's consider the diffusion of a particle A in an environment consisting of particles B. Denote $\sigma_{A-B}$ the effective cross-section of the collision between A and B . The relative mean quadratic speed between A and B can be written as:

$$\overline{V} = \sqrt{\overline{\nu}_A + \overline{\nu}_B} = \sqrt{\frac{3kT}{2}\left(\frac{1}{m_A} + \frac{1}{m_B}\right)} \tag{3.59}$$

The mean free time will be written as (Fig. 3.22 ) :

$$\tau = \frac{1}{n_B \sigma_{A-B} \overline{V}} \tag{3.60}$$

where $n_B$ is the volume density of the particles B.

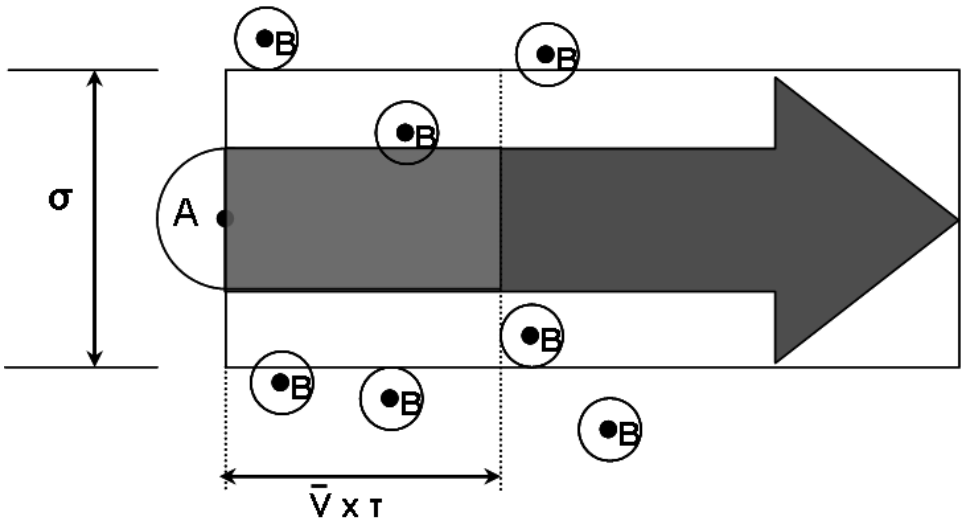


Figure 3.22: The mean free path: in a reference frame where the particle B is fixed, the mean speed of A is $V$; a collision will occur if B is inside a cylinder of diameter $\sigma$ and height $\overline{V} \times \tau$; the mean number of particles B in the cylinder ($n_B \sigma \overline{V} \tau$) must be equal to 1.

The mean free path is then:

$$l = \frac{\sqrt{2}}{n_B \sigma_{A-B} \sqrt{1 + \frac{m_A}{m_B}}} \tag{3.61}$$

Let's define the diffusion coefficient of A in B as:

$$D_{A-B} = \frac{1}{3} \overline{\nu}_A l \tag{3.62}$$

We show that:

$$D_{A-B} = \frac{(kT)^{3/2}}{\sqrt{3} P_B \sigma_{A-B}} \sqrt{\frac{1}{m_A} + \frac{1}{m_B}} \tag{3.63}$$

$P_B$ is the particle B pressure.

In the case of the auto-diffusion (B=A), Eq. 3.63 is simplified to:

$$D_{A-A} = \frac{(kT)^{3/2}}{\sqrt{6 m_A} P_A \sigma_{A-A}} \tag{3.64}$$

A simple way of calculating the effective cross-section of diffusion is to consider the atom has a apparent radius $r$. The effective cross-section is:

$$\sigma = 4\pi r^2 \tag{3.65}$$

for the auto-diffusion.

For particles of different nature (inter-diffusion), the effective cross-section is given by:

$$\sigma = \pi (r_1 + r_2) \tag{3.66}$$

$r_1$ and $r_2$ being the apparent radii of the particles. The effective cross-section depends on the atom radius and the energy of the particle. Correct determination of the diffusion coefficients should be done by direct measurement or calculated from potentials.

### Values of the diffusion coefficients for helium

Slaman [72] published the calculated values for the diffusion coefficients of helium at 1 atm (101300 Pa). These values agree with the measured values published by Liner [90] using chromatography.

The regression of $\log D$ as a function of $\log T$ shows an excellent correlation with the slope 1.7. The dependence of D on T is then:

$$D(T) = D(T_0) \times \left(\frac{T}{T_0}\right)^{1.7} \tag{3.67}$$

Using this formula and calculating D, the values are identical with those calculated by Slaman. After the results of the chromatography, Liner came with an empirical equation of D as a function of temperature:

$$D_{4He-3He} = 1.36 \cdot 10^{-5} \times T^{1.671}[m^2 s^{-1} K^{-1.671}] \tag{3.68}$$

The behaviour of the two helium isotopes should be the same since the effective cross-section is an atomic property. After 3.63, we get:

$$\frac{D_{3-3}}{D_{3-4}} = \sqrt{\frac{8}{7}} \tag{3.69}$$

$$\frac{D_{3-3}}{D_{4-4}} = \sqrt{\frac{4}{3}} \tag{3.70}$$

Liner also proposed empirical equations for the diffusion of $^4$He in nitrogen [90]:

$$D_{4He-N2} = 5.90 \cdot 10^{-9} \times T^{1.648}[m^2 s^{-1} K^{-1.648}] \tag{3.71}$$

Using Eq. 3.63, equation 3.71 becomes:

$$D_{3He-N2} = \sqrt{\frac{31}{24}} D_{4He-N2} \tag{3.72}$$

giving:

$$D_{3He-N2} = 6.71 \cdot 10^{-9} \times T^{1.648}[m^2 s^{-1} K^{-1.648}] \tag{3.73}$$

Table 3.3: Published values of helium diffusion coefficient at 101300 Pa. C = calculated values by Slaman - E = interpolation using the equation of Slaman - L = measured values by Liner

| Diffusion type | Temperature | Diffusion coefficient | Obs |
|---|---|---|---|
| self-diffusion $^3He$ | 293 K | $1.894 \cdot 10^{-4} m^2.s^{-1}$ | C |
| | | $1.892 \cdot 10^{-4} m^2.s^{-1}$ | E |
| | 303 K | $2.003 \cdot 10^{-4} m^2.s^{-1}$ | E |
| | 310 K | $2.082 \cdot 10^{-4} m^2.s^{-1}$ | E |
| | 313 K | $2.118 \cdot 10^{-4} m^2.s^{-1}$ | C |
| | | $2.117 \cdot 10^{-4} m^2.s^{-1}$ | E |
| inter-diffusion $^3He -^4 He$ | 293 K | $1.773 \cdot 10^{-4} m^2.s^{-1}$ | C |
| | | $1.771 \cdot 10^{-4} m^2.s^{-1}$ | E |
| | 303 K | $1.875 \cdot 10^{-4} m^2.s^{-1}$ | E |
| | | $1.88 \cdot 10^{-4} m^2.s^{-1}$ | L |
| | 310 K | $1.949 \cdot 10^{-4} m^2.s^{-1}$ | E |
| | 313 K | $1.983 \cdot 10^{-4} m^2.s^{-1}$ | C |
| | | $1.981 \cdot 10^{-4} m^2.s^{-1}$ | E |
| self-diffusion $^4He$ | 293 K | $1.642 \cdot 10^{-4} m^2.s^{-1}$ | C |
| | | $1.640 \cdot 10^{-4} m^2.s^{-1}$ | E |
| | 303 K | $1.737 \cdot 10^{-4} m^2.s^{-1}$ | E |
| | 310 K | $1.805 \cdot 10^{-4} m^2.s^{-1}$ | E |
| | 313 K | $1.837 \cdot 10^{-4} m^2.s^{-1}$ | C |
| | | $1.835 \cdot 10^{-4} m^2.s^{-1}$ | E |

Table 3.4 gives the values of helium diffusion coefficients in nitrogen at different temperatures.

In practice we used the diffusion coefficients from Table 3.5; the mean free path and mean free time were calculated using the following equations:

$$l = D\sqrt{\frac{3m}{kT}} \tag{3.74}$$

Table 3.4: Values of helium diffusion coefficient in nitrogen measured by Liner for helium-4 and adapted for helium-3, at different temperatures.

| Temperature | | Diffusion coefficient |
|---|---|---|
| inter-diffusion $^3He - N_2$ | 293 K | $7.80 \cdot 10^{-5} m^2.s^{-1}$ |
| | 303 K | $8.24 \cdot 10^{-5} m^2.s^{-1}$ |
| | 310 K | $8.55 \cdot 10^{-5} m^2.s^{-1}$ |
| | 324 K | $9.20 \cdot 10^{-5} m^2.s^{-1}$ |

$$\tau = \frac{Dm}{kT} \tag{3.75}$$

Table 3.5: Values of helium diffusion coefficient used in experiments; free displacement and the corresponding mean free time.

| | Vector gas | D | mean free path | mean free time |
|---|---|---|---|---|
| *in-vitro* 20° C | nitrogen | $7.80 \cdot 10^{-5} m^2.s^{-1}$ | 150 nm | 96 ps |
| | helium-4 | $1.78 \cdot 10^{-4} m^2.s^{-1}$ | 342 nm | 219 ps |
| *in-vivo* 37° C | nitrogen | $8.55 \cdot 10^{-5} m^2.s^{-1}$ | 160 nm | 100 ps |
| | helium-4 | $1.95 \cdot 10^{-4} m^2.s^{-1}$ | 364 nm | 227 ps |

$In - vivo$, gas composition is never the composition of the inspired gas due to the residual volume and the water vapour saturation; plus, the composition varies in time due to alveolar exchange.

### The Einstein's law

In open space, the distance traveled by a particle in a time t is given by the Einstein law (in 3D):

$$d = \sqrt{6Dt} \tag{3.76}$$

and in 1D:

$$d = \sqrt{2Dt} \tag{3.77}$$

For example, water diffusion coefficient at 37°C is $D_{H_2O} = 2.3 \cdot 10^{-9} m^2 s^{-1}$; in 1 ms the distance traveled is 4$\mu$m; in 1 s, 120 $\mu$m and in 1 hour, 7 mm (the convection is neglected).

This law is only applicable if the diffusion time is much longer than the mean free time. In the case of shorter times, the helium atom moves with a given speed and the traveled distance is simply proportional with the time it travelled: this is the Knudsen regime (Table 3.6).

Considering the long times, helium diffuses in the alveoli; the particles situated at the center of the alveoli will initially diffuse according to Einstein's law; the particles closer to the alveolar wall will collide with this and this will restrict the diffusion. It is than a transition from free diffusion to a restricted diffusion regime which will be presented in the next chapter. After even longer times, the helium atoms will travel longer distances through other neighbour and eventually the whole acinus .

Table 3.6 presents the temporal and spatial scale of the $^3$He diffusion at alveolar level. The calculation of these scales was done using Table 3.5 and the value of ADC $2 \cdot 10^{-4} m^2 s^{-1}$, taken as the average value published for the restricted diffusion inside the lung [91], [92], [93]. These limits are only for guidance. The transition between different regimes can not be clearly explained.

### 3.4.2 Free diffusion in the presence of a uniform magnetic field gradient

The source of longitudinal or transverse relaxation is the magnetic field variation "sensed" by the spins, this can be due to a variation of the magnetic field (temporal variation) or due to the spin motion in an inhomogeneous field (spatial variation). The longitudinal relaxation is created by an apparent variation of the transverse field $\overrightarrow{B_{x,y}}$ whereas the transverse relaxation is due to the apparent variation of the longitudinal field $\overrightarrow{B_z}$. The temporal variation can be produced in two ways: variation generated by the application of a RF and the RF noise.

Table 3.6: Temporal and spatial scale of helium-3 inside the lungs.

| inter-diffusion of $^3He$ in $^4He$ | | inter-diffusion of $^3He$ in $N_2$ | |
|---|---|---|---|
| time | space | time | space |
| Knudsen pre-diffusive regime: $\overline{\nu} = 1601ms^{-1}$ | | | |
| $\tau = 2.3 \cdot 10^{-10}s$ | $L = 0.37\mu m$ | $\tau = 9.1 \cdot 10^{-11}s$ | $L = 0.15\mu m$ |
| $D = 1.95 \cdot 10^{-4}m^2s^{-1}$ free diffusion $D = 8.55 \cdot 10^{-5}m^2s^{-1}$ | | | |
| $\tau_D = 0.45ms$ | $L = 300\mu m$ | $\tau_D = 1.5ms$ | $L = 300\mu m$ |
| diffusion restricted to the intra-alveolar scale ($ADC = 2 \cdot 10^{-5}m^2s^{-1}$) | | | |
| $\tau_D^{'} = 12.5ms$ | $L^{'} = 500\mu m$ | $\tau_D^{'} = 12.5ms$ | $L^{'} = 500\mu m$ |
| diffusion restricted to the supra-alveolar scale | | | |

In non viscous liquids, *a fortiori* in a gas, the correlation time $\tau_C$ is short compared with the Larmor period, and the transverse and longitudinal relaxation times, in an homogeneous field, are equal and independent on the magnetic field [94], the fast motion limit applies:

$$T_1 = T_2 = \left(\frac{2\gamma^4\hbar^2 I(I+1)}{r^6}\tau_C\right)^{-1} \tag{3.78}$$

**Bloch-Torrey equation in general**

When the particles carrying spins diffuse in a magnetic field gradient, the diffusion adds an extra term to the Bloch equation, and this transforms into Bloch-Torrey equation [95]:

$$\frac{d\overrightarrow{M}}{dt} = \gamma \cdot \overrightarrow{B} \wedge \overrightarrow{M} + \frac{1}{T_1}(\overrightarrow{M_{eq}} - \overrightarrow{M_z}) - \frac{1}{T_2}\overrightarrow{M_{x,y}} + D \cdot \overrightarrow{\bigtriangledown}^2\overrightarrow{M} \tag{3.79}$$

the term $D \cdot \overrightarrow{\bigtriangledown}^2\overrightarrow{M}$ corresponding to the effect of diffusion.

We can show that the attenuation due to free diffusion of the spins in the presence of an uniform gradient $G(\tau)$ is:

$$e^{-\gamma^2 D \cdot I} \tag{3.80}$$

where D is the diffusion coefficient and I is the following integral [95], [96]:

$$I = \int_0^T (\int_0^t G(\tau)d\tau)^2 dt \tag{3.81}$$

**Effect of a spin echo on the dephasing due to diffusion**

A $180°$ pulse will change the sign of the phase of the magnetisation. Changing the sign of a gradient will change the sign of the phase evolution. When considering only the amplitude of the signal, it is possible when calculating diffusion, to consider an $180°$ pulse as changing the sign of the gradients (Fig. 3.23) [97].

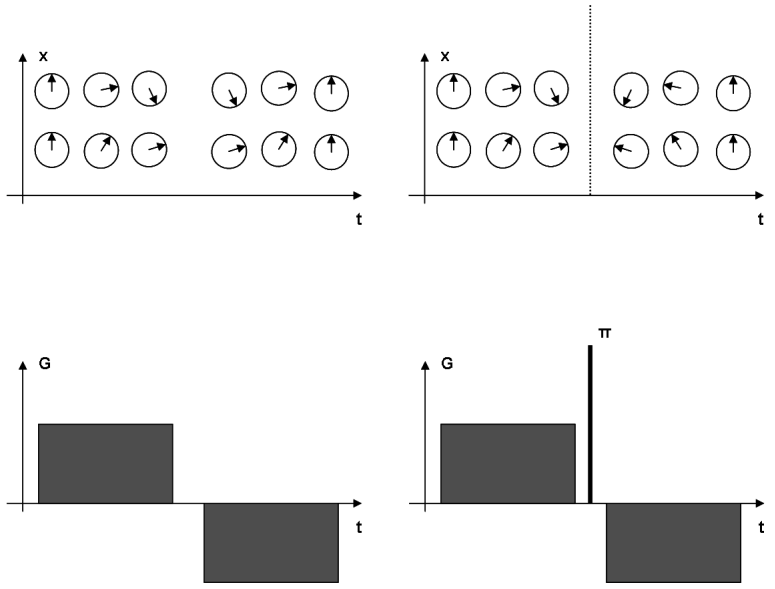


Figure 3.23: Changing the gradients sign (supposed uniform) change the sign of the phase variation; an $180°$ pulse change the sign of the phase (mirror); when only considering the amplitude of the signal, it is possible to replace the $180°$ pulse by a pair of gradients of opposite polarity.

This effect is only valid in the case of uniform gradients.

**Equation in the case of symmetric gradients**

In practice, the NMR sequences are created such as the signal is acquired at the time of a gradient echo. The gradients used are usually symmetric, generating an echo at time T, but the symmetry is not necessary to obtain a gradient echo:

$$\forall t \in [0, T], G(T - t) = -G(t) \tag{3.82}$$

Hence, the integral given by 3.81 is simplified to:

$$I = 2\int_0^{T/2}(\int_0^t G(\tau)d\tau)^2 dt \tag{3.83}$$

**Signal attenuation due to free diffusion in the presence of an uniform gradient for different gradient echoes sequences**

The calculated attenuation for different gradient shapes is given in Table 3.7. Equation 3.87 for a continuous gradient is given by Abragam [60]. Equation 3.88 for a double pulse gradient of fixed duration is the classical Stejskal-Tanner formula [98]. Equation 3.92, 3.93 are detailed in Annex A. 3.91 is obtained from 3.93 by considering $\delta = 0$ and 3.89 with m = 0. In the same manner 3.90 is obtained from 3.92 and 3.88.

In a NMR experiment in the presence of gradients, the diffusion introduces an extra signal attenuation that can be expressed as a reduction of the apparent transverse relaxation time:

$$T_{2,apparent} = \left(\frac{1}{T_2} + \frac{1}{T_2^\dagger}\right)^{-1} \tag{3.84}$$

where:

$$T_2^\dagger = \frac{T_{CP}}{D\gamma^2 I} \tag{3.85}$$

$T_{CP}$ being the interval between two consecutive signal acquisitions.

For a continuous gradient, 3.85 becomes:

$$T_2^\dagger = \frac{12}{D\gamma^2 G^2 T_{CP}^2} \tag{3.86}$$

The signal attenuation will increase as the gradient gets stronger, the diffusion is faster and the refocusing gradients are less frequent. $T_2^\dagger$ depends on $T_{CP}$; this means the $n^{th}$ echo acquired is not identical with the echo acquired at time $n \cdot T_{CP}$ [60].

Thus, applying multiple refocusing pulses will limit the coherence loss.

The signal attenuation between two consecutive echoes can be also expressed as a function of the characteristics lengths $l_D$ and $l_G$ (5.11, 5.12):

Table 3.7: Various diffusion gradients shapes and their integral I value.

| | gradient form | equation |
|---|---|---|
| continuous | 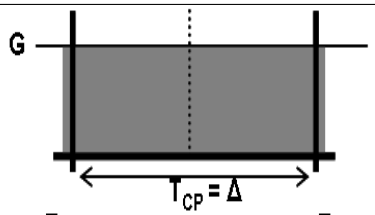 | $I = \frac{G^2 T_{CP}^3}{12} = \frac{G^2 \Delta^3}{12}$ (3.87) |
| rectangle | 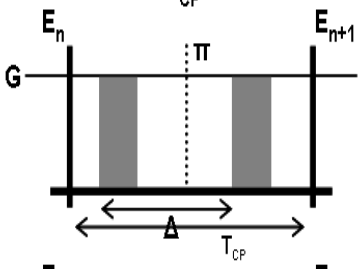 | $I = G^2 \delta^2 \left( \Delta - \frac{\delta}{3} \right)$ (3.88) |
| half-rectangle | 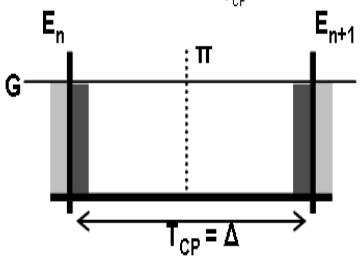 | $I = \frac{G^2 T_{CP}^3}{12} = \frac{G^2 \Delta^3}{12}$ (3.89) |
| triangle | 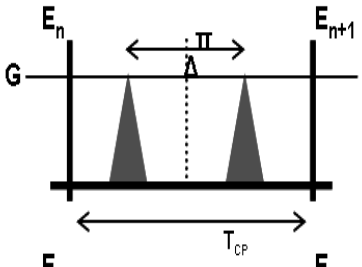 | $I = \frac{G^2 \delta^2}{12}(3\Delta - 2\delta)$ (3.90) |
| half-triangle | | $I = G^2 m^2 \left( \Delta - \frac{7}{15} m \right)$ (3.91) |
| trapezoid | 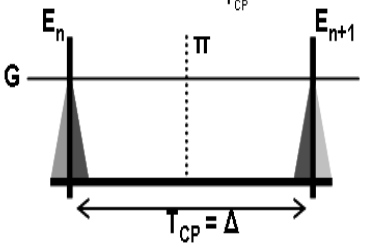 | $I = G^2 \delta^2 \Delta \left[ 1 - \frac{1}{3} \frac{\delta}{\Delta} \right] + x \left( 2 - \frac{\delta}{\Delta} \right) + x^2 \left( 1 - \frac{7}{6} \frac{\delta}{\Delta} \right) - \frac{7}{15} x^3 \frac{\delta}{\Delta}$ (3.92) where $x = \frac{m}{\delta}$ |
| half-trapezoid | 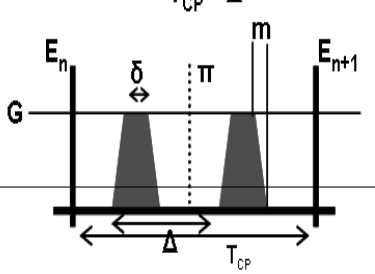 | $I = \frac{G^2 \delta^2 \Delta}{12} \left[ 1 - 2 \frac{\delta}{\Delta} \right] + 6x \left( 1 - \frac{\delta}{\Delta} \right) + 3x^2 \left( 1 - \frac{7}{3} \frac{\delta}{\Delta} \right) - \frac{14}{15} x^3 \frac{\delta}{\Delta}$ (3.93) where $x = \frac{m}{\delta}$ |
| | 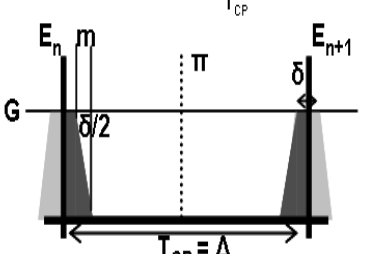 | |

$$\frac{S(T_{CP})}{S(0)} = \exp\left[-\left(\frac{l_D}{l_G}\right)^6\right] \tag{3.94}$$

Note that the formulas presented are valid for uniform gradients. The signal decay after a train of spin echoes is strictly monoexponential. The restricted diffusion in the alveoli and the internal non-uniform gradients make the problem more complicated.

# Chapter 4

# Practical Considerations on Hyperpolarised $^3$He MR

This work was accomplished on a 0.15 T permanent magnet(IMIG IGR). The $^3$He was polarised using an in-house polarisation system via the metastability exchange optical pumping technique described in Chapter 3. Chronologically, the experimental work started with measurements of the field orientation dependance of the $T_1$ relaxation time in different glass cells. The second group of experiments involved measuring $^3$He diffusion with different methods *in vivo*. For clarity purposes the diffusion measurements will be presented separately in the fifth chapter.

This chapter starts with a description of the specific hyperpolarised $^3$He constraints in MRI. The second part describes the progress made on the hyperpolarised $^3$He production facility and the results of the field orientation dependance experiment. Last part analyses the use of single shot (RARE) and multi-shot (FLASH) pulse sequences at low field (0.15 T) for hyperpolarised $^3$He MRI.

## 4.1 Specific Constraints in Hyperpolarised $^3$He MRI

Hyperpolarised gas NMR has two types of constraints: those linked to the rapid diffusion of the gas and those related to the absence of longitudinal magnetisation recovery in the hyperpolarised regime, considered as a signal reserve.

Because of its specificity and source of contrast, the helium diffusion will be described in detail in Chapter 5; some consequences of diffusion will be presented in this section together with some particular aspects of the consequences of longitudinal relaxation.

### 4.1.1 Hyperpolarised $^3$He Longitudinal Relaxation

In contrast to the case of thermal equilibrium, hyperpolarised $^3$He longitudinal relaxation does not cause the recovery of magnetisation but its virtual destruction to the thermal value. This section will present a review of the sources of longitudinal relaxation, some *in vivo* experiments to measure these effects and the consequences of the longitudinal relaxation.

#### Sources of longitudinal relaxation

#### The parietal relaxation

***In vitro* parietal relaxation** The walls of the gas container may have a relaxing effect due to the interaction of molecules with the surface. This is the main source of *in vitro* relaxation. A Pyrex® glass cell has a $T_1$ in the order of 1 hour. In order to reduce relaxation the glass has to be free of paramagnetic ions ($Fe^{3+}$ in particular) or it can be coated with metals (caesium, bismuth) [81]. $T_1$ can be increased to tens of hours [99].

**Parietal relaxation inside the lungs** Due to oxygen's necessary presence in the lungs, it is impossible to estimate the wall relaxation but it is generally accepted that this is dominated by the molecular interaction of oxygen and helium. Experiments were done *ex vivo* in pigs after the animal was sacrificed and the lungs were rinsed for 15 minutes with nitrogen. The parietal relaxation indicated a $T_1$ longer than 260 s [100]. In rats there were similar results ($T_1$ 270 s) [81]. Considering the surface to volume ratio, the alveolar wall is a good enclosure for the hyperpolarised gas.

These results are debatable since the experiments are not done in physiological conditions; the alveolar surface will change 15 minutes after death. In practice, nevertheless we can suppose the wall relaxation is not dominant.

**Dipole-dipole interaction between helium atoms** In practice this phenomenon is small; it depends on the species concentration [101]:

$$T_{1,dipole} = \frac{744\text{h.amg}^{-1}}{[^3He]} \tag{4.1}$$

This expression is valid at 23°C, the time being inversely proportional to the square root of the temperature, fixed species concentration, and in a broad spectrum of temperatures: 0.1 to 550 K [1]

From 3.1:

$$T_1 = 46.9\text{h.atm.K}^{-1/2}\frac{\sqrt{T}}{P} \tag{4.2}$$

$T_1$ is 803 h at 20°C and 1 atm. The gas internal relaxation is hence proportional to pressure but in practice it is negligible compared to wall relaxation, even at atmospheric pressure.

**Diffusion in the presence of the magnetic field gradients** This effect is more evident at low pressure due to diffusion being more rapid.

It depends on the radial field distribution (perpendicular to the main magnetic field)[99]:

$$\frac{1}{T_{1,gradient}} = \alpha \times \frac{1}{PB^2}\left(\frac{\partial B_r}{\partial r}\right)^2 \tag{4.3}$$

with $\alpha$ = 0.18 $\text{h}^{-1}\cdot$ bar $\cdot$ $\text{m}^2$ for a spherical cell with diameter 5 cm. Basically, the longitudinal relaxation being caused by a RF field, will depend on the variation of the $B_x$ and $B_y$ components of the relative magnetic field experienced by the helium nuclei ($B_z$ being the main component). When the helium atom diffuses, the spatial variation of the radial component of $\overrightarrow{B}$ will be important.

**The paramagnetic effect of oxygen** The effect of oxygen on the $^3$He relaxation is due to the binary collisions that have the same effect both on the longitudinal and transverse

[1] An amagat is a practical unit of number density. Although it can be applied to any substance at any conditions, it is defined as the number of ideal gas molecules per unit volume at 1 atm (= 101325 Pa) and 0°C (=273.15 K)

relaxation, and is proportional to oxygen concentration. This effect was measured by Saam et al. [15]:

$$T_1 = T_2 = 0.204\text{s} \cdot \text{amg}^{-1} \cdot K^{-0.42} \frac{T^{0.42}}{[O_2]} \tag{4.4}$$

or

$$T_1 = T_2 = 7.48 \cdot 10^{-4}\text{s} \cdot \text{atm}^{-1} \cdot K^{-1.42} \frac{T^{1.42}}{P} \tag{4.5}$$

for a large temperature range (200 K - 400 K). This measurement was done at 1.4 T but it should be field independent if the duration of a collision is dominated by the precessing time:

$$\omega\tau_C \ll 1 \tag{4.6}$$

At atmospheric pressure and $37°C$, for an oxygen fraction $f_{O_2}$, the relaxation times are:

$$T_1 = T_2 = \frac{2.58s}{f_{O_2}} \tag{4.7}$$

In the optical pumping cell, this relaxation is negligible because of the great efforts to keep the oxygen out of the environment. *In vivo* though, this effect is inevitable and dominant.

**Summary** *In vivo*, the diffusion effect is dominated by the paramagnetic effect of oxygen. *In vitro*, the dominant effect depends on pressure. At low pressure ($\sim$ 1 mbar), the effect of diffusion in a heterogeneous field may be important; in a homogeneous field, the dominant effect is the wall relaxation. At high pressure ($\sim$ 1 bar), the dominant effect is the wall relaxation. In practice the internal dipolar relaxation of helium is always small compared with the other sources of relaxation.

#### Experimental measurement of the longitudinal relaxation *in vivo*

In NMR, the classical method for measuring the longitudinal relaxation is the inversion recovery technique [102]. This method can not be used with hyperpolarised gases since

it's impossible to repeat the experiment with a second inversion; after the first run, the gas has returned irreversibly to thermal equilibrium and if inhaling a second batch there are always reproducibility issues (polarisation, gas volume, $T_1$).

The method used with hyperpolarised gases consists of applying multiple small tipping angles that allow to see the evolution of the longitudinal magnetisation after compensating for the loss of magnetisation due to the RF.

**Results** Figure 4.1 shows the signal evolution in a typical $T_1$ measuring experiment.

The apparent relaxation time has to be corrected for the effect of the RF using the following formula for $T_1$ determination:

$$\frac{1}{T_1^{app}} = \frac{1}{T_1} - \frac{ln(\cos\alpha)}{TR} \tag{4.8}$$

### The effects of longitudinal relaxation

**Constraints imposed by the longitudinal relaxation** At thermal equilibrium, the longitudinal relaxation has a positive effect since it recovers the available magnetisation. In the hyperpolarised regime, it is necessary to run the experiment in a short period compared to $T_1$.

*In vitro*, the longitudinal relaxation is mainly due to wall relaxation and is generally few hours. This long life-time allows for hyperpolarised gas production, storage and even long route transport before the actual use.

*In vivo*, the main destruction source is oxygen. The life-time is much shorter (tens of seconds) and hence it is needed to use rapid acquisition sequences.

**Potential applications** By measuring $T_1$ it is possible to get indirect information about the intrapulmonary oxygen concentration [11]. It is also possible to follow the oxygen as it travels through the alveoli [11] and calculate partial pressure of oxygen.

The measurement of the local oxygen concentration gives information about the ventilation/perfussion ratio; basically, regions that are well ventilated and bad perfused will have a high oxygen concentration, while well perfused and poorly ventilated ones have

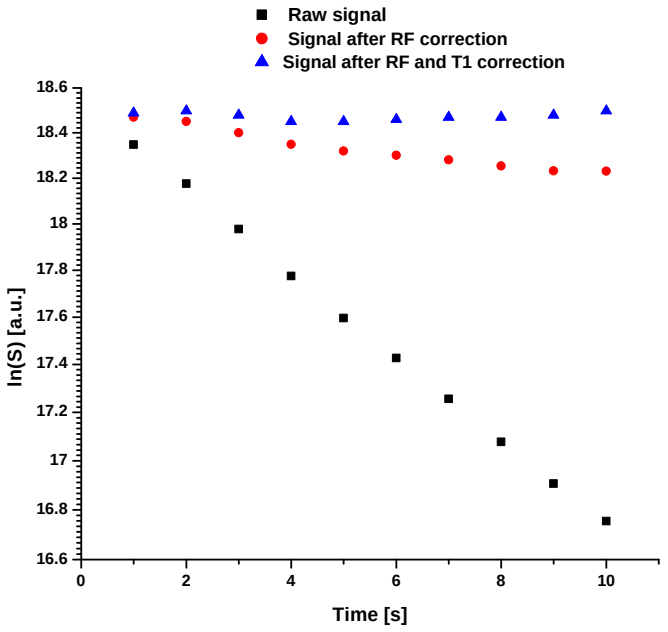


(a)

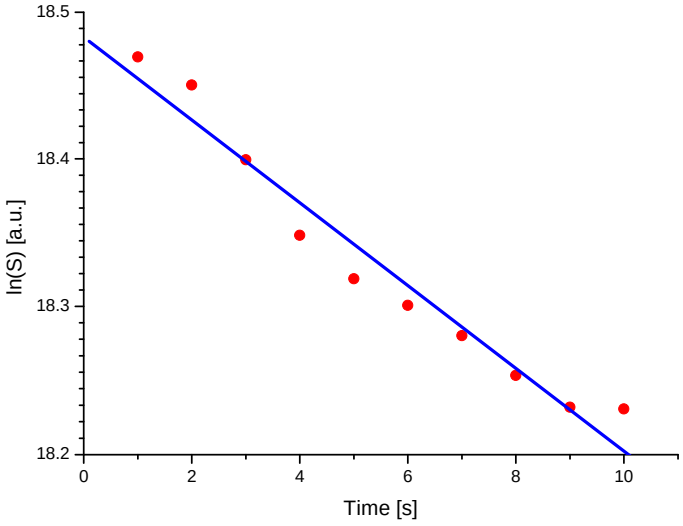


(b)

Figure 4.1: Signal evolution in a $T_1$ measuring experiment; (a) squares represent the raw signal, circles represent the signal after RF correction and up triangles represent the signal after RF and $T_1$ correction. (b) $T_1$ is calculated from the exponential decay of the signal after RF correction.

low oxygen concentration. The V/P ratio is very important in pathology since its heterogeneity can explain many respiratory diseases.

By tracking the oxygen travelling the alveolar-capillary barrier allows for the investigation of the basic function of the lungs: oxygen transport; in the absence of a severe fibrosis (that obstructs the oxygen passage), this parameter gives an indirect information about the pulmonary perfusion. In order to measure over 25 s the variation of a relaxation parameter, a high signal-to-noise ratio is needed. Plus, during this time, the gas can travel about 7 cm if considering a diffusion coefficient of 0.2 $cm^2.s^{-1}$; it is then difficult to get oxygen passage maps with high spatial resolution.

### 4.1.2 Tipping angle calibration

The lack of longitudinal magnetisation regeneration makes the tipping angle calibration a real challenge. In general, in the MRI experiments, sequences are preceded by a calibration sequence meant to determine the resonant frequency and to calibrate the tipping angle. When working with hyperpolarised gases, due to the limited quantity of gas, the lack of longitudinal magnetisation regeneration and short duration of apnea, make this calibration sequence very difficult to implement and is often abandoned. At high field it is possible to calibrate the angle by using a $^3$He phantom at high pressure (several bars), thermally polarised. At 0.15 T, the signal would be to small using this approach.

There is a variation of the tipping pulse given by numerous phenomena in different experimental conditions. After briefly enumerating them, there will be a description of the sequences used for calibration and how they are adapted to helium.

#### Inherent difficulties when calibrating the RF

**Off resonance pulses** The resonant frequency may often vary between experiments due to the susceptibility effect or due to the main magnetic field shifting (*a fortiori* in a permanent magnet). On resonance, the tipping angle is proportional to the duration and amplitude of the RF pulse; off resonance, the dependence is more complex.

In practice, this effect is a non-linearity source and can impede delivery of a 180° pulse.

**Short and long range instability** For a given setting, the amplifier response may not be constant with time, essentially due to thermal variations. On a short range, this happens when using repeated long pulses, a short interval apart; on a long range, there are temperature variations of the whole system or differences in the system settings.

**Correction by coil loading** When the coil is loaded with different samples, the equivalent impedance induced by the sample is also changing. The response to RF field will also change. The calibration of the angle using a phantom is not valid unless it's done on the subject.

### Sequences for angle calibration

Since the sequences that are normally used for angle calibration on protons don't work in the absence of the longitudinal magnetisation recovery, different types of sequences had to be used.

**Angle calibration at thermal polarisation** Consider a series of unknown RF pulses $\alpha_i$, repeated with a period TR starting from an initial magnetisation $M_0$ (at thermal equilibrium). The residual longitudinal magnetisation after *i* RF pulses will be:

$$M_i = M_0 - [M_0 - M_{i-1}(cos\alpha_i)]e^{-\frac{TR}{T_1}} \tag{4.9}$$

The signal will be:

$$S_i = M_{i-1} \sin \alpha_i \tag{4.10}$$

At thermal polarisation, the classical method implies using a *TR* bigger than $T_1$. The result is:

$$M_i = M_{i-1} = M_0 \tag{4.11}$$

and thus:

$$S_i = M_0 \sin \alpha_i \tag{4.12}$$

In order to get the $\pi/2$ angle it is enough to maximize signal and find the first minimum for $\pi$.

As mentioned before, this method fails with hyperpolarised $^3$He at 0.15 T.

**Angle calibration in the hyperpolarised regime: from the loss of longitudinal magnetisation** In the hyperpolarised regime, the transverse relaxation destroys magnetisation. If the experiment is done in a sufficient small time compared to $T_1$, TR can be neglected. If not, like it's generally the case *in vivo*, it is possible to compensate the longitudinal magnetisation if $T_1$ is known:

$$M_i = M_{i-1}(\cos\alpha_i)e^{-\frac{TR}{T_1}} \tag{4.13}$$

However, due to the long duration of the calibration process and need of reproducibility *in vivo*, the calibration is, in general, done *in vitro*. Equation 4.12 allows to calculate the signal variation for consecutive pulses:

$$S_i = S_{i-1} \times \frac{\sin\alpha_i}{\sin\alpha_{i-1}}(\cos\alpha_i) \tag{4.14}$$

$$\frac{S_i}{S_{i-1}} = \frac{\sin\alpha_i}{\tan\alpha_{i-1}} \tag{4.15}$$

From 4.15 it is possible to determine the angle if $\alpha_{i-1}$ and $\alpha_i$ are identical:

$$\alpha_i = \alpha_{i-1} = \arccos\frac{S_i}{S_{i-1}} \tag{4.16}$$

**Angle calibration in the hyperpolarised regime: the rapid method** In order to accelerate the calibration process, it is possible to use in the same sequence both big and small angles; if $\alpha_0$ and $\alpha_1$ are identical, then:

$$\alpha_1 = \alpha_0 = \arccos\frac{S_1}{S_0} \tag{4.17}$$

$\alpha_1$ being determined, $\alpha_2$ is calculated from:

$$S_2 = S_1 \times \frac{\sin\alpha_2}{\tan\alpha_1} \tag{4.18}$$

$$\alpha_2 = \arcsin\left(\frac{S_2}{S_1}\tan\alpha_1\right) \tag{4.19}$$

The measuring principle is as follows: repeat many times an angle big enough to precisely measure the cosine, once calculated, its value is used to determine the available longitudinal magnetisation and calibrate the signal given by the tipping field.

### 4.1.3 Acquisition strategies for hyperpolarised gases

Because of the limitations specific to hyperpolarised gases it is not possible to use all sequences for imaging. A brief review of the available sequences for imaging at 0.15 T is presented.

The large variety of MRI sequences can be divided in: "single-shot" sequences - when the magnetisation remains in the transverse plane during the acquisition and "multi-shot" sequences - when each line of the Fourier plane is acquired by tipping small amounts of the magnetisation. There are also hybrid sequences that allow one acquire multiple lines with every magnetisation tipping.

#### Single-shot sequences

**Relaxation limitations** The use of a single-shot sequence with hyperpolarised gases seems logical because of the non renewable magnetisation. In order to acquire the whole *k*-space the duration of the transverse magnetisation has to be long. $T_2$ apparent ($T_2^{app}$) has to be less than the acquisition time $T_{ACQ}$. If we consider an observation time for each line $T_{obs}$ and a matrix with $NY$ lines, we get an acquisition time:

$$T_{ACQ} = NY \times T_{obs} \tag{4.20}$$

**Types of sequences** Once the magnetisation is tipped in the transverse plane, the read out of the *k*-space can be done:

- using a unique gradient echo: either an echo planar imaging sequence (EPI) , developed by Mansfield in 1977 [103] or a spiral sequence [63]. These sequences are very rapid but generate lot of artefacts [34].

- using spin echoes ; this technique, RARE (Rapid Acquisition with Relaxation Enhancement) published by Henning in 1986 [104], is a bit longer but more robust with regards to artefacts.
- using an intermediate sequence that combines EPI and RARE: GRASE (GRAdient and Spin Echo) that acquires multiple lines per gradient echo before a refocusing 180° pulse.
- finally the acquisition can be done by using stimulated echoes (BURST)

### Multi-shot sequences

**Tipping angle choice** Since the longitudinal relaxation is a source of signal destruction, a multi-shot sequence has to use small tipping pulses to preserve the longitudinal reserve of signal. However, this angle has to be big enough to provide enough signal for each line.

There were certain authors [81],[8] that used multi-shot sequences with 90° pulses for animal imaging; since after each line the signal is destroyed, it is necessary to provide fresh helium for every line. In order to have reproducible conditions to acquire each line, it is necessary to use an artificial ventilator and sedate the animal. This is not possible with humans.

**The use of a fixed angle** The classical approach is to use a constant angle $\alpha$. The available signal for line n is:

$$S(n) = M_0(\cos\alpha)^{n-1}\sin\alpha \tag{4.21}$$

and the ratio of the first and last line signal is:

$$\frac{S(NY)}{S(1)} = (\cos\alpha)^{NY-1} \tag{4.22}$$

In Figure 4.2 there is an example of three angles. An angle too big will destroy the signal very quickly and an angle to small will generate too small signal.

Note that the effect of TR is similar to the effect of $T_2$ in the single-shot sequence:

$$T_2 = \frac{TR}{\ln(\cos\alpha)} \tag{4.23}$$

Contrary to the decay due to diffusion, this effect can be controlled by reducing the tipping angle, but losing SNR.

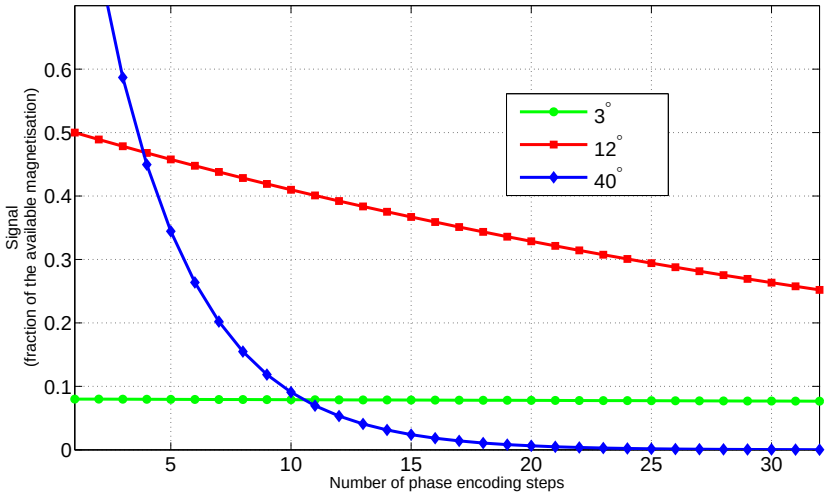


Figure 4.2: Theoretical curves illustrating the effect of three different flip angles on the signal for NY=20 lines.

No matter if using a single-shot or multi-shot sequence, there is always a filtering phenomenon in the phase encoding direction that has to be minimized. Considering Eq. 4.23, $\alpha$ can be written as:

$$\alpha = \arccos\left(e^{-\frac{1}{NY-1}}\right) \tag{4.24}$$

The signal attenuation between the first and last line is then $1/e$ and the equivalent $T_2$ is $(NY-1)\cdot TR$.

Other possibility is to maximize the signal from the last line and hence choosing an angle:

$$\alpha = \arctan\sqrt{\frac{1}{NY-1}} \tag{4.25}$$

The optimal angle as a function of the number of phase encoding steps is given in Figure 4.3.

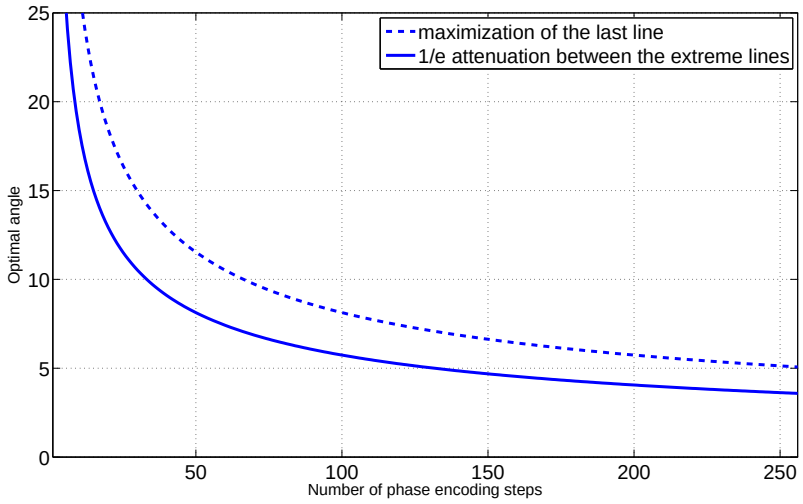


Figure 4.3: Optimal tipping angle as a function of phase encoding steps, according to the two options (maximization of the last line and $1/e$ attenuation between the extreme lines).

**The use of a variable angle** Using a variable angle [105] leads to equal available signal for all lines:

$$\sin \alpha_{n-1} = \cos \alpha_{n-1} \times \sin \alpha_n \tag{4.26}$$

$$\alpha_{n-1} = \arctan(\sin \alpha_n) \tag{4.27}$$

and to maximize it, it is necessary to use all remaining signal for the last line, thus:

$$\alpha_{NY} = 90^\circ \tag{4.28}$$

These two conditions lead to [131]:

$$\alpha_n = \arctan \frac{1}{\sqrt{NY - n}} \tag{4.29}$$

This technique allows one to use all signal and avoid the *k*-space filtering in the phase encoding direction. The method is not always achievable because not all systems allow RF pulse tabulation.

Figure 4.4 shows an example of how the angle is changing when reading the Fourier space while Figure 4.5 shows the longitudinal and transverse magnetisation evolution in

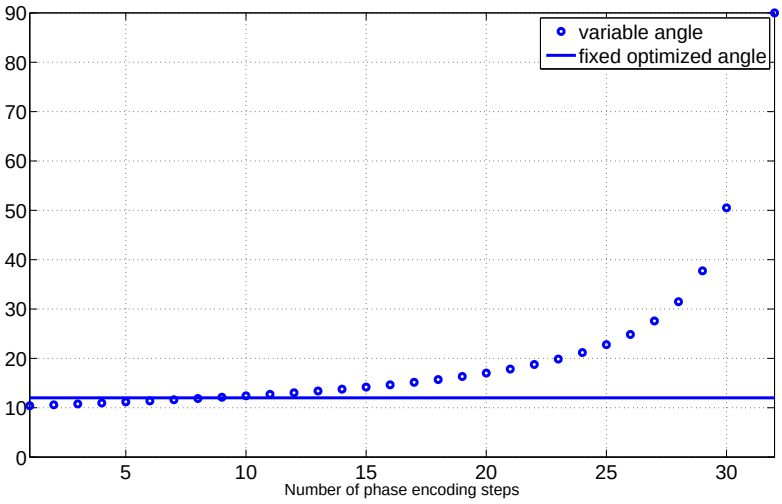


Figure 4.4: Theoretical value of the tipping pulse as a function of the phase encoding step for a 32 lines matrix: comparison between a fix and variable angle [8].

the two cases (fixed and variable angle). It is clear that using a fixed angle gives a better signal for the first lines.

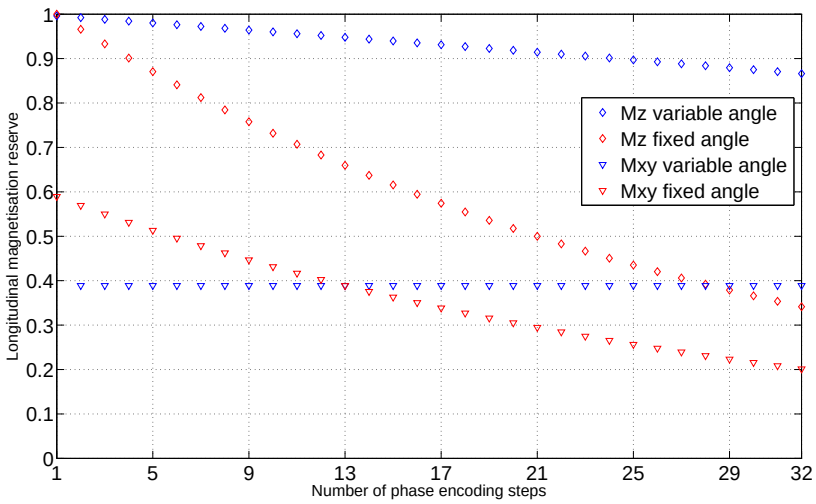


Figure 4.5: Theoretical evolution of longitudinal and transverse magnetisation during the acquisition: comparison between a fix and variable angle [8].

### Types of sequences

The *k*-space read out can be done:

- in Cartesian manner, line by line, using a classic gradient echo sequence with small tipping angles called FLASH (Fast Low Angle SHot).

- in a polar manner, radius by radius, using a projection-reconstruction sequence (PR); this has the advantage of an extremely short echo time but the image reconstruction it's not easy [81].

## 4.2 Aspects of Gas Production and Administration

During the experiments presented in this work, the system for producing the hyperpolarised helium underwent multiple transformations (Fig. 4.6) The initial production facility was developed during the work of Fichele and a complete description can be found in his thesis [106]. The system was improved during the work of Waters [107] by adding a semiautomated gas handling system computer controlled using LabView.


Figure 4.6: A photograph of the final polarisation system indicating the newly added components. **a** - the cylinder pump used for dispensing the $^3$He **b** - the peristaltic pump with 4 rollers; **c1** and **c2** - the new storage cells, **c2** is placed next to the optical pumping cell **d** to allow recording the NMR spectra of both **c2** and **d**; **e** - one of the new valves used to control the gas flow; **f** - the new 20 W Ytterbium fibre laser used to polarise the $^3$He.

Producing hyperpolarised gas is subject to a lot of constraints (magnetic environment,

chemical purity necessary for pumping[2], vacuum system, medical use) thus, necessitates a complex system with carefully designed components (a great know-how).

The optical pumping needs a narrow spectrum light. In the very early attempts, $^4$He lamps were used [76] but to obtain higher power, the LASER was introduced. The use of fiber LASER [108] allows for high power and practicability.

### 4.2.1 General Principle of the Polarisation System

The optical pumping was done in a clean and vacuumed Pyrex glass cell. In order to obtain this it is necessary to have a system capable of delivering a high vacuum. The cell was filled with $^3$He at low pressure (1 to 10 mbar). This cell was connected through a pipe network to the $^3$He and $^4$He sources, the vacuum pump and pressure gauges.

The cell was fitted with two circular electrodes connected to a high frequency (the order of 1.2 MHz) voltage source (the order of 1 kV). The voltage was amplitude modulated in order to modulate the proportion of metastable atoms (see Fig. 4.7).

A 1083 nm LASER was used for the optical pumping. The beam travels through a polarising cube and then a $\lambda/4$ plate which creates the circularly polarisation $\sigma^+$[3]; the beam then traverse the cell parallel with the $\overrightarrow{B_0}$ magnetic field (Fig. 4.7). The LASER was tuned to the $C_8$ or $C_9$ transitions. The necessary duration to fully polarise the gas depends on the gas pressure and LASER power (few seconds to few minutes for the experiments described in this work).

Since optical pumping needs to be done at a lower pressure than the atmospheric pressure, in order to use the gas for medical applications, it is necessary to compress the gas to higher pressures.

[2] a high chemical purity of the cell is necessary in order to avoid contamination with atoms that can destroy the metastable population or accelerate the relaxation

[3] this $\lambda/4$ plate is necessary at low field because it allows the selection of a transition $\delta m = \pm 1$; it is also useful at high field since it allows for all the energy of the beam to contribute to pumping

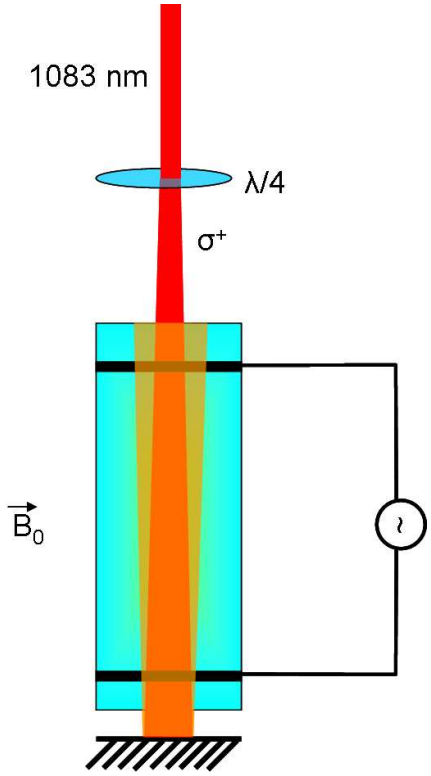


Figure 4.7: Diagram of the polarisation system: LASER light is $\sigma^+$ polarised in a magnetic field $\overrightarrow{B_0}$ and shines through the pumping cell where the plasma is maintained by electrical discharge; the unabsorbed light is reflected back into the cell using a mirror at the bottom of the cell (the piping network is not shown on this diagram).

### 4.2.2 Polarisation System

The polarisation system underwent many changes during my work. There were many set ups tried but only three configurations will be described.

The polarisation system is divided into two sections. The section outside the $B_0$ field, contains the vacuum pumps and the $^3$He and $^4$He supply. The section inside the $B_0$ field, contains the optical pumping cell (OPC), peristaltic pump and the storage cells (STGC) and is in contact with the polarised $^3$He. Figure 4.8 shows the circuit diagram of the system.

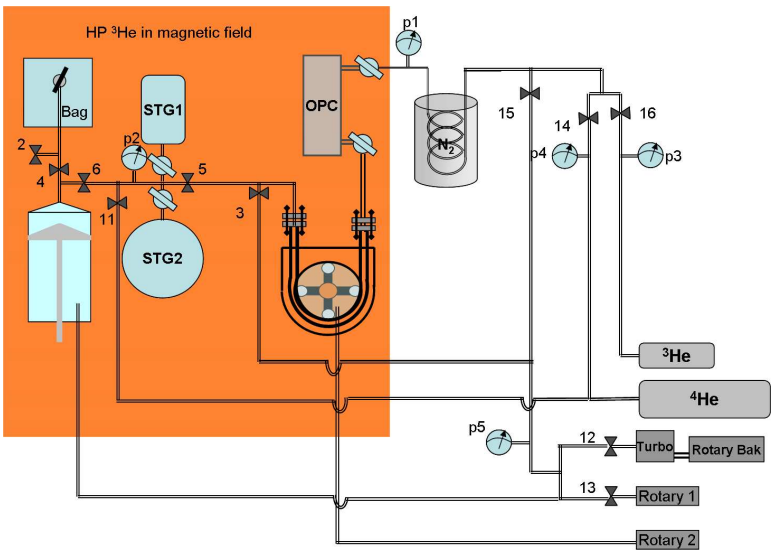


Figure 4.8: Schematic of the polarisation system.

### Vacuum system

The polarisation system is kept under high vacuum ($10^{-3}$ mbar) to ensure that the system is clean and the $^3$He gas is not contaminated by impurities that would destroy the polarisation. The high vacuum is obtained using two pumps. The first is a Leybold rotary vacuum pump which can pump the system down from atmospheric pressure to around $1.5 \cdot 10^{-2}$ mbar. This pump also acts as the backing pump for a turbomolecular vacuum pump (Leybold Model D50), which can achieve pressures as low as ($9 \cdot 10^{-7}$ mbar). An Edwards Speedivac ES50 rotary pump (Edwards High Vacuum) is used to evacuate the peristaltic pump manifold. There are three vacuum lines in the gas system - a low vacuum line and a high vacuum line connected to the unpolarised section of the system and a low vacuum line connected directly to the peristaltic pump manifold. A low vacuum line, from the unpolarised section of the system, was also connected to the back of the cylinder pump (See section 4.2.2)

### Gas flow path

The pipework in the section outside the magnetic field (see Figure 4.8) consists of a mixture of 1/4" stainless steel pipes and 6 mm copper pipe. The flow of $^3$He and $^4$He gas from the pressurized gas cylinders is controlled by manually operated low and high flow

trickle valves. The two gas lines from the pressurized gas cylinders pass through getter filters to absorb impurities in the gas. Gas delivery to the section within the magnetic field is controlled with a series of solenoid valves (14, 15, 16). Copper piping, 6 mm diameter, is used for supplying the vacuum. The liquid nitrogen trap causes any oxygen gas contaminating the supply gases to condense in the trap from where it can be later pumped out by the vacuum system. A thin brass capillary prevents the polarised gas from diffusing into the section outside the magnetic field where unwanted local magnetic fields could depolarise the gas. The section within the magnetic field contains the optical pumping cell, the compression system and the two storage cells. Here the pipework is a mixture of 6 mm PFA and copper tubing. Capillaries before and after the optical pumping cell isolate the polarised gas from the rest of the circuit. The flow of the helium can be controlled by opening or closing glass stopcocks on either side of the optical pumping cell. The gas then passes through a series of non-magnetic air actuated valves (Swagelok®) to the peristaltic pump. Within the peristaltic pump the helium passes through Masterflex® Tygon® peristaltic tubing. On the far side of the peristaltic pump the gas passes into the two storage cells which can be manually isolated from the system. The storage vessels are also connected to a second pump, a cylinder compressor, which is used to transfer the gas into the bag. This will be described in Section 4.2.2

This section of the polarisation system was the most challenging one since there were many configurations employed to date. With increasing the complexity of the flow path, the rigid copper tubing was no longer practical since we were adding more gas lines in an already tight space. At present we have replaced most of the copper tubing and fittings with PFA hard plastic.

### Optical pumping

Low pressure ($p < 10$ mbar) $^3$He is polarised using metastable optical pumping. The metastable state is obtained by applying a high voltage oscillating RF field to the gas in the optical pumping cell. A sinusoidal voltage from a signal generator (1.18 MHz, 0.1 V) passes through an RF amplifier which amplifies the signal to 10 V (2 W). Finally, a step up transformer with 100 turns on the secondary and only 2 turns on the primary increases

the voltage of the signal to 500 V (50 times step up) which is applied to two single turn coils wrapped around the optical pumping cell. The metastable $^3$He is polarised by applying circularly polarised light from a 1083 nm, continuous wave, Ytterbium fibre laser (Keopsys®). The beam is then expanded up to 3 cm diameter using a lens system. Expanding the laser beam illuminates the polarisation cell more fully and greatly reduces the hazard posed by the laser beam. A door interlock switches the laser off if anyone enters the room and protective glasses are worn while the laser is being used. A mirror below the optical pumping cell fully reflects the beam and increases optical absorbtion. The optical pumping cell provides a clean environment in which the $^3$He can be illuminated with the laser beam and polarised. It sits in a homogeneous magnetic field generated by DC current flowing through 7 large coils which surround the polarisation rig. The strength of this field is 2.4 mT corresponding to Larmor frequency of 66.5 kHz. Two orthogonal pairs of Helmholtz coils are positioned round the optical pumping cell. These allow the polarised $^3$He to be excited using an RF pulse and the free induction decay to be recorded.

### Gas compression

This part of the polarisation system is very important because the polarised gas must be pressurized to provide enough signal for imaging. There are mainly three types of pumps that can be used to pressurise the HP $^3$He: diaphragm, peristaltic or cylinder. No matter what pump is employed it must be free of any depolarising materials.

**Initial compressor** In our case the compression is made by a peristaltic pump built by Fichele and described in his thesis [106]. The diagram of this compressor is shown in Figure 4.9. The initial compressor had only two rollers as described in [106]. This is to prevent the tubing from being pulled away from the inlet or the pump-head to be jammed. This eventually reduces the efficiency of the pump since the compression ratio is smaller with two rollers compared with four.

Since the goal was to optimize the amount of gas and polarisation available it was not long before the initial configuration limited it. The signal amplitude in the storage cell drops above a certain pressure as shown in Figure 4.10.

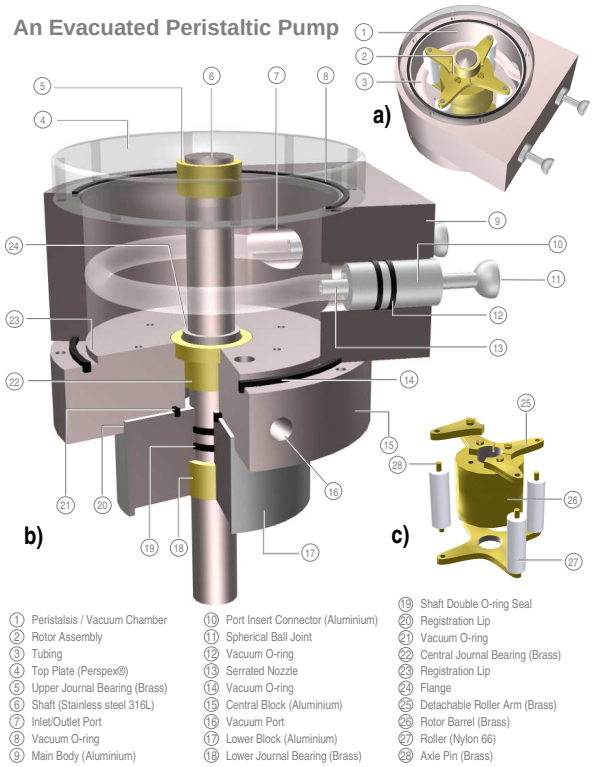


Figure 4.9: Peristaltic pump diagram. Reproduced from thesis of S. Fichele, Univ. of Nottingham 2002

**4-Rollers compressor** Although there is a slight improvement compared to the 2-rollers compressor this updated compressor is still not satisfying our requirements. In Figure 4.10 it is depicted a diagram of the signal evolution with the growing pressure in the storage cell before and after adding two more rollers as tested in this work.

These attempts to obtain higher amounts of hyperpolarised $^3$He suggest that there are some limitations due to the relaxation time and pressure in the storage cell. The building pressure increases the signal in the first stage up to 40 mBar and then there is the relaxation time that destroys the signal.

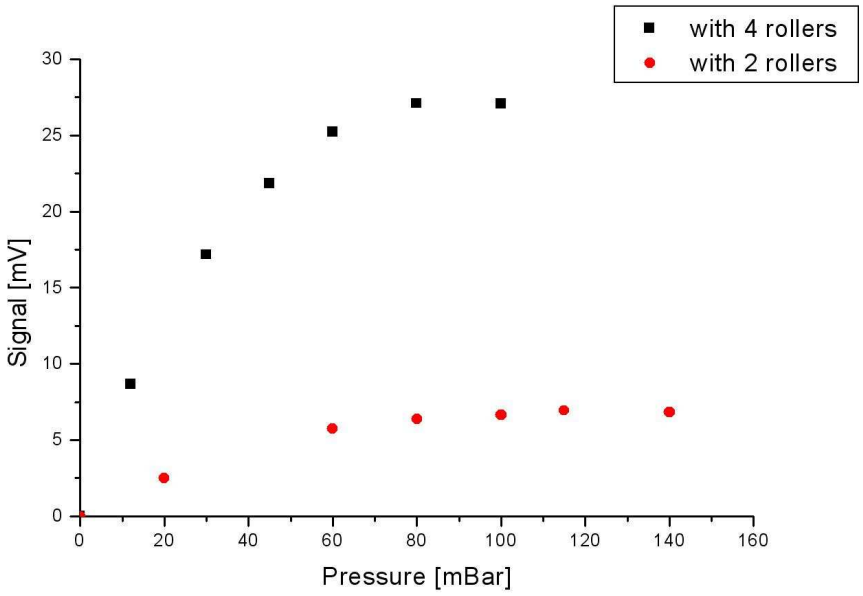


Figure 4.10: Signal amplitude vs. Pressure in the storage cell. Dots represent the signal evolution when compressing with 2 rollers and squares represent the signal evolution when compressing with 4 rollers.

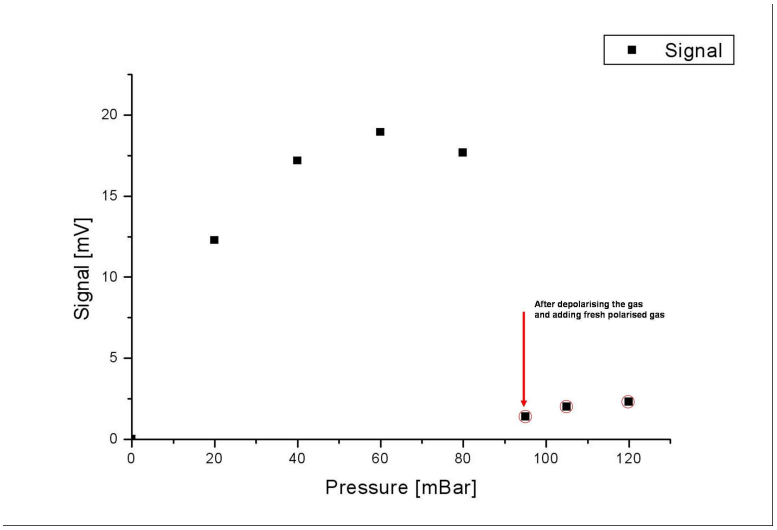


Figure 4.11: Signal amplitude vs. Pressure in the storage cell after destroying the polarisation and adding fresh polarised gas.

Figure 4.11 presents a situation where the gas was collected up to a pressure that is no longer growing the signal, the gas was depolarised with successive RF pulses and then

fresh polarised gas was added. It is obvious from this figure that higher compression rates and/or longer relaxation time cells are needed in order to store the hyperpolarised gas for lung imaging.

One way to increase the compression rate of the pump was to increase the volume of the inside tubing. A larger tubing (10 mm NORPRENE® tube) was used but due to some mechanical constraints the pump did not work and the idea was abandoned.

**The cylinder compressor** First, the idea was to create a two-stage compression system using the peristaltic pump as the first stage compressor and a cylinder pump as the second stage compressor. This was a solution employed by some groups (NIST [109] and Mainz [110]) and it was thought to be achievable at a smaller scale in this work.

**First attempt: the syringe** First attempt was to use a 60 ml plastic syringe (BD Plastipak®) as a compressor and an air-driven piston (SMC® ) to drive the cylinder.

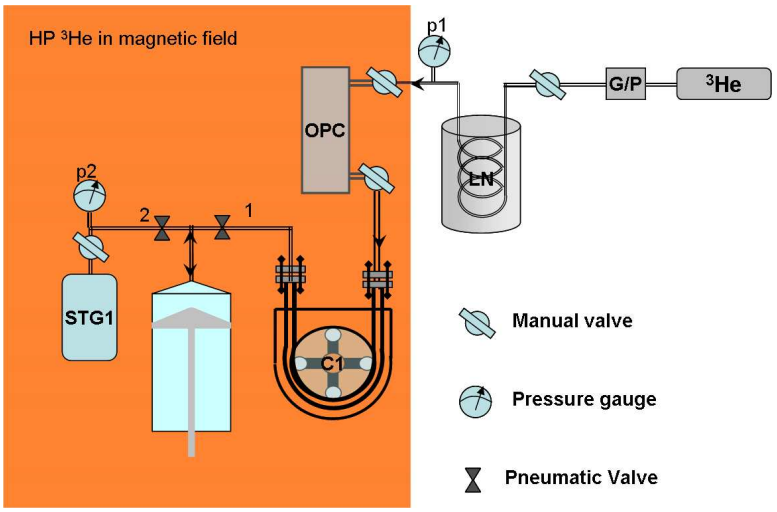


Figure 4.12: Diagram of the syringe compressor system. Arrows indicate the $^3$He flow while compression is in progress. The labeled system components are storage cell (STG), peristaltic compressor (C1), syringe compressor (C2), pneumatic valves (1,2), getter/purifier (G/P), liquid nitrogen trap (LN).

The syringe and the piston were connected together, aligned and fixed onto a rail. The outlet of the syringe cylinder is connected through a T, which was glued with black epoxy, to the pneumatic valves 1 and 2 (Swagelok®) that control the compression. When the gas

is ready to be collected the automated system for compression is started. The automated system for gas compression uses the control unit built by the electronics workshop and a virtual instrument design in LabView 7 by Martin Bellwood with my new sequences. The control unit provides 16 switching channels to control the pneumatic valves, the peristaltic pump and the piston that drives the syringe cylinder. The virtual instrument is used to set up the sequences that are used to operate the valves and to transmit, via a RS232, the command to the control unit. The sequence to control the compression consists of 5 steps. In step 1 both pneumatic valves 1 and 2 are open and the cylinder is in its top position. This step is just before starting the collection. Collection starts in step 2 when the piston moves to the bottom position, both valves close for 2 s. In step 3, pneumatic valve 2 remains closed, piston moves to top position, valve 1 opens and hyperpolarised $^3$He passes from the OPC to the syringe cylinder with the C1 (See Figure 4.12). This accumulation stage lasts 8 s. Then, in step 4 the valve 1 closes, piston moves down and valve 2 remains closed for 2 s. In the final step valve 2 is open to the STG for 4 s. The whole sequence is repeated until the storage cell has reached its set pressure. To prevent the fast relaxation rates in the last phase of the compression, where there is a large surface to volume ratio, the piston moves very fast [110].

The first tests with this system have showed a short relaxation time in the storage cell compared with a single stage compression. This indicates a source of depolarization inside the second stage compression.

Measuring $T_1$ relaxation time in the syringe cylinder was difficult to perform because there was no NMR coil available. The measurements were made on an identical syringe filled with hyperpolarised $^3$He and placed near the NMR coils around the OPC. The value obtained vas 31 minutes in uncompressed state. Considering this value is a lot greater than the time that gas stays inside the syringe one can conclude this is not the loss source.

Another step was to test the pneumatic valves for leaks. All valves were found to be leak tight.

Replacing the black epoxy with a white one we found that this was improving the $T_1$ relaxation time. Although, when the piston was moving, the $T_1$ was still short.

The pressure inside the vacuum system was fluctuating when the piston was moving.

The moving piston was allowing air to enter inside the syringe cylinder and thus, to depolarize the $^3$He. One quick solution was to add oil on the back of the rubber piston to have a seal. The seal works well for piston moving up but fails when moving down because the oil moves slower than the rubber piston and it remains attached to the cylinder wall braking the seal. The oil eventually passed inside the gas chamber and the syringe had to be abandoned.

Summarizing, the perfect cylinder pump will have vacuum on the back of the piston. Also, there is the need to have a buffer cell between the peristaltic and the cylinder pumps so the pressure inside the OPC remains low and does not affect the polarisation process.

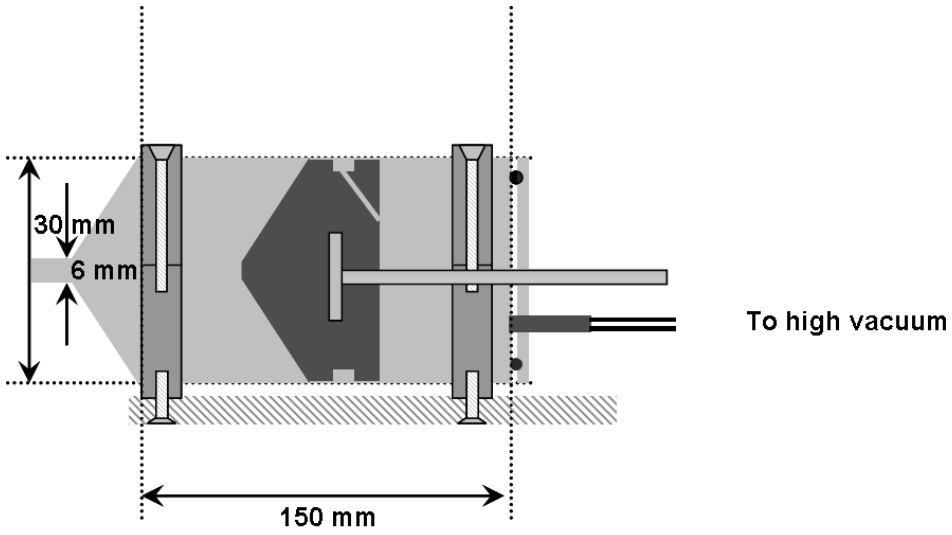


Figure 4.13: Diagram of the piston.

**The cylinder compressor: prototype** A new cylinder pump was designed and built having the same dimensions as the syringe and with a vacuum line on back of the piston. The cylinder is made of plastic and has a rubber piston from a syringe on an aluminium threaded rod. Because the piston has an H profile, there was some air trapped inside so a thin copper pipe had to be added to expose this space to the back vacuum (See Fig. 4.13). The cylinder's inside wall needed to be lubricated with a hydrogen-free PTFE grease to prevent the system from locking.

The compression ratio, which is the ratio of the total compressor volume to the dead volume $K_{C2} = V_{C2}/DV$, was determined by measuring the pressure changes in the con-

necting tubing with the piston in the top and bottom positions [111]. These measurements yielded $K_{C2} = 11$. This ratio multiplied by the peristaltic pump ratio ($K_{C1} = 10$) gives a total gain of 110. The new configuration is shown in Figure 4.14.

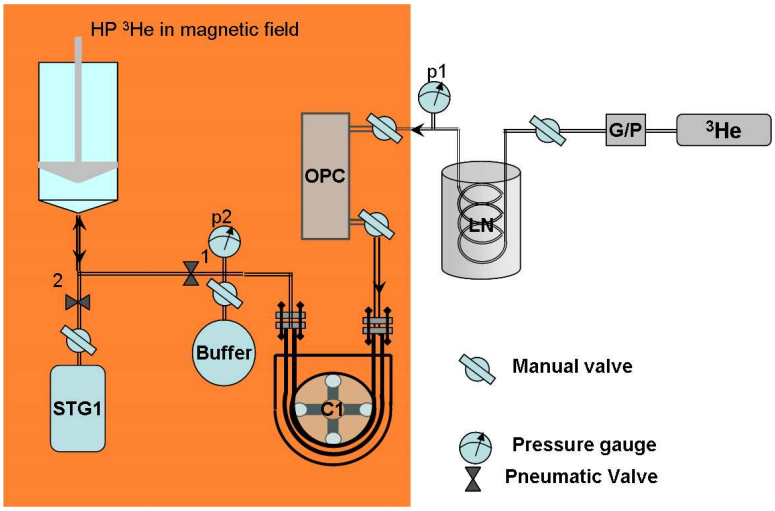


Figure 4.14: Diagram of the cylinder compressor system.Arrows indicate the $^3$He flow while compression is in progress. The labeled system components are storage cell (STG), buffer cell (BUFF), peristaltic compressor (C1), cylinder compressor (C2), pneumatic valves (1,2), getter/purifier (G/P), liquid nitrogen trap (LN).

The valve control sequence had to be changed. First the hyperpolarised $^3$He is collected with the peristaltic in the buffer cell up to 10 mBar, with valves 1 and 2 closed and piston in the top position, when the pressure reaches 10 mBar the automated compression sequence is started. The sequence is as follows: step 1 - valve 1 is open to the buffer cell for 7 s allowing gas to enter the cylinder; step 2 - valve 1 closes; step 3 - piston moves to bottom position for 3 s; step 4 - valve 2 opens for 2 s to allow the compressed gas to pass in the storage cell; step 5 - valve 2 closes; step 6 - piston moves to top position.

There is the possibility of using either cell as buffer cell or storage cell. The results were promising but there were still some issues regarding the compression ratio. The dead volume is contained mostly in the pneumatic valves so increasing the ratio implied increasing the compression volume i.e a larger cylinder and reducing the length of the pipes (See Appendix A for detailed description of the pneumatic valves).

**The cylinder compressor: final version** A larger cylinder was designed and built using the prototype and scaling up the diameter. The driving piston had to be replaced with a bigger one. A diagram of the cylinder pump is given in Figure 4.15.

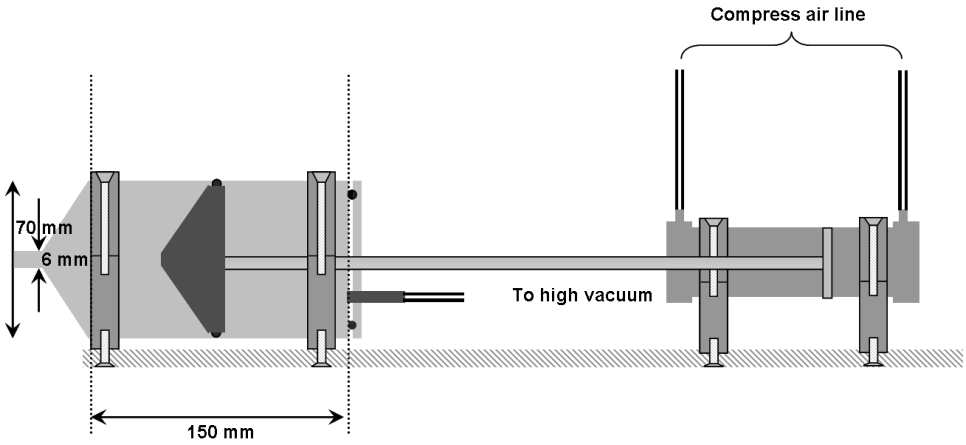


Figure 4.15: Diagram of the final cylinder pump.

**$^3$He storage** There were two types of glass cells used for storage: 1720 Corning and 180 GE in this work. Initially only the Corning cell was used because it was placed inside a NMR coil ensemble and the signal from the hyperpolarised $^3$He could be recorded using the NMR spectrometer. The Corning was replaced eventually with GE 180 since the relaxation time was longer in the latter. A detailed description of the storage cells and experiments carried on them are described in section 4.3.

### Changes to polariser

**Upgraded gas manifold** The previous version of gas manifold was very long and contained many plastic-copper interfaces that were sensible to leaks. There was the need to rearrange the components and shorten the gas manifold in order to prevent future leaks. It was also important to place all depolarisation sensitive components near the center of the Helmholtz coils ensemble, where the magnetic field is more homogeneous.

- The NMR coils used for probing the storage cell were removed. A new GE 180 storage cell was placed near the NMR coils for the optical pumping cell. This

allows to pick up signal from both cells at the same time. There are two distinctive peaks for the two cells (Figure 4.16), as they experience slightly different $B$ fields

- The stand for bag filling was replaced with a new one, placed near the storage cell
- The length of the tubing is minimal hence the compression of the cylinder pump is improved

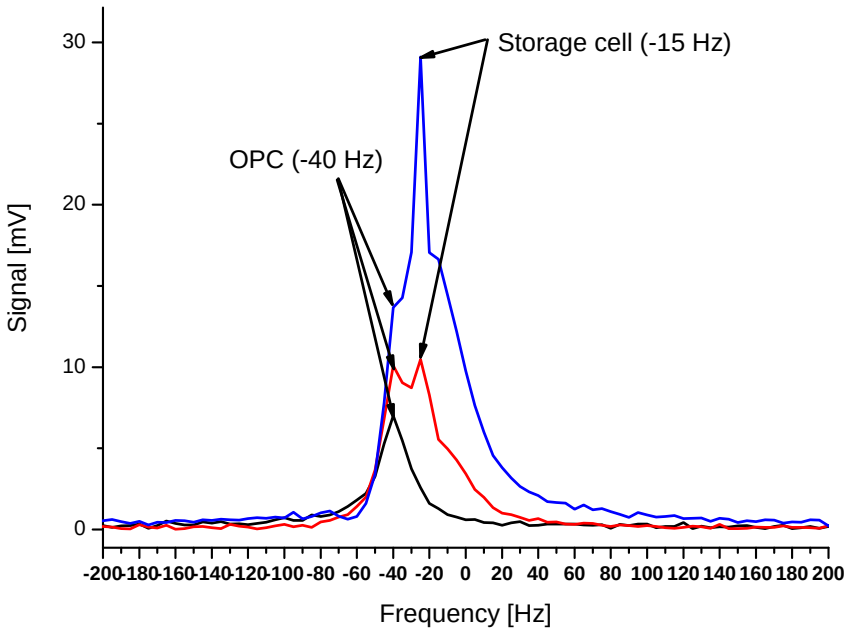


Figure 4.16: Due to its location near the receiver coil, the storage cell is visible as an extra peak on the NMR spectrum at +15 Hz from the OPC one. The traces show NMR spectra at different pressures in the storage cell.

**Upgraded compression system** When imaging a subject, the time to fill a bag of $^3$He up to 350 mBar was long, almost 10 minutes, and with the existing storage cell it was impossible to make more than two bags at once. There was a need for a faster system for producing bags since the goal was to use at least three bags of gas for the children study and to keep the children inside the magnet as less as possible. A second GE 180 storage cell was installed and the compression system was rearranged.

- The gas is collected using the peristaltic pump only. The pump works very well at the low pressure inside the optical pumping cell (10 mBar). It is possible to collect the gas for many hours without reaching the steady-state since relaxation time in the storage cell is much longer in GE 180 (See Fig. 4.17).

- The gas is pumped into bag with the cylinder pump. The pump works very well at the high pressures inside the storage cell (1 Bar)(See Fig. 4.18).

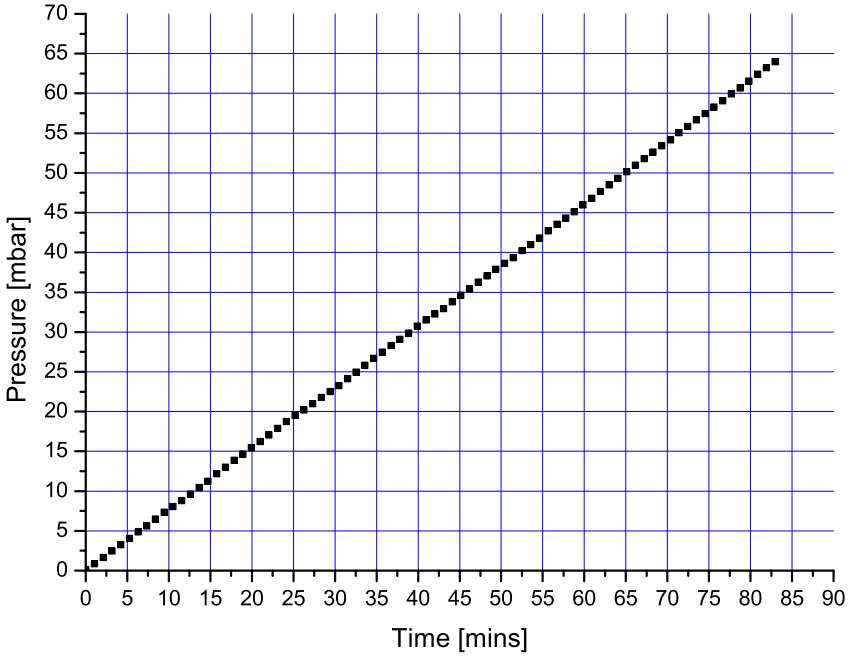


Figure 4.17: Evolution of pressure inside the storage cell with 15 mBar driving pressure (P1) and the pump on 300 rpm.

The resulting system is shown in Figure 4.8. With the new system it is possible to produce six bags of hyperpolarised $^3$He and $^4$He mixture (350 mBar each) in one batch. Each bag needs, on average, less then two minutes to be filled. As seen on Figure 4.15, first bags are filled extremely fast but once the pressure drops below 50 mBar the pump too slow and usually evacuation stops at this pressure.

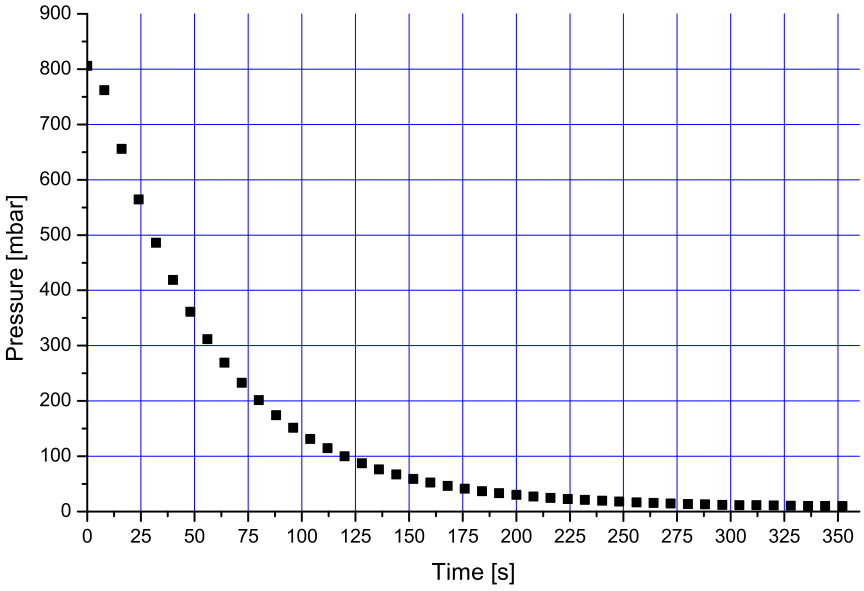


Figure 4.18: A diagram of the gas evacuation using the cylinder compressor.

## 4.3 Magnetic field orientation and strength dependence

The aim of these experiments was to investigate the longitudinal spin relaxation of $^3$He in glass cells in order to develop improved methods for producing and storing the hyperpolarised $^3$He used in lung MRI. A significant dependence of $^3$He relaxation time, $T_1$, in glass cells due to the physical orientation of the cell relative to the applied magnetic field has already been noticed [112], [113].

$T_1$ relaxation time was measured in three types of uncoated glass cell (1720 Corning, 7740 Pyrex and 180 GE) for a range of magnetic field with two different magnetic field orientations (See Fig. 4.19). The effect of demagnetization and heat treatment on $T_1$ was also investigated. A second part of the experiment was focused on the study of NMR lineshape at different orientations, gas pressures, temperature and $^3$He magnetization.

The chemical composition of these glasses is given in Table 4.1.

### 4.3.1 7740 Pyrex

The values for $T_1$ in the optical pumping cell are given in Table 4.2.

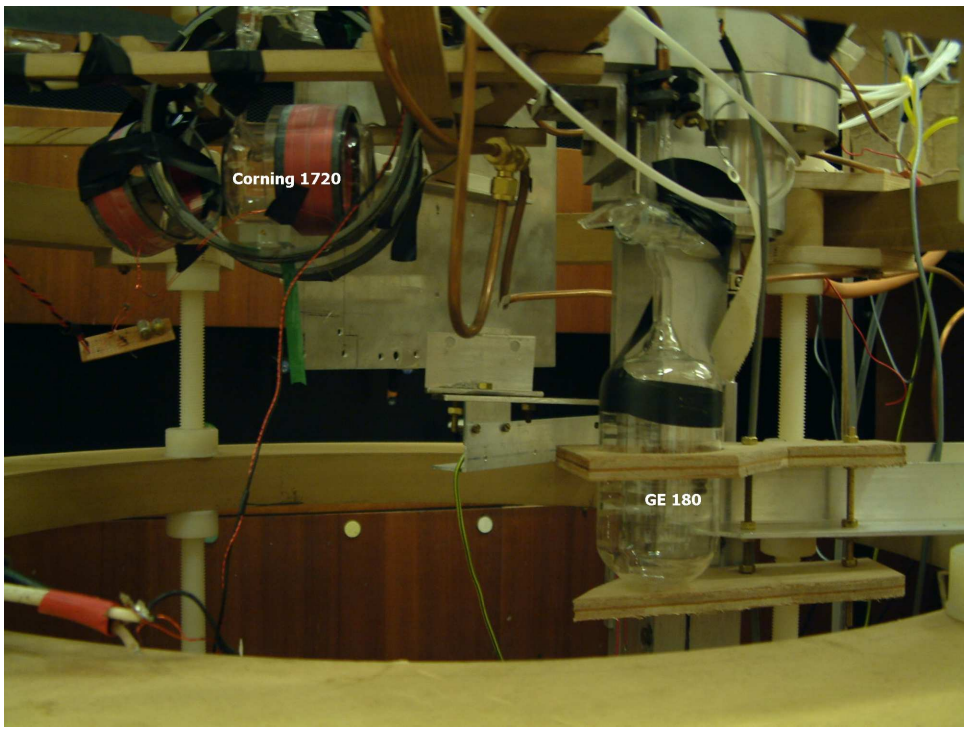


Figure 4.19: A photograph showing the Corning 1720 and GE 180 glass cells used to investigate the field orientation dependence of $T_1$. Note the 1720 has flat ends and the 180 is oval.

### 4.3.2 1720 Storage Cell

The glass cell was fixed in place and the $B_0$ orientation was set by reversing the current through the Helmholtz coils. The orientations were denoted as follows:

- + $B_0$ along Earth's magnetic field;
- - $B_0$ opposing Earth's magnetic field.

For measuring the $T_1$ relaxation time, $^3$He was polarised using metastable optical pumping at 1 mBar followed by compression with a peristaltic pump to around 20 mBar in the glass cell. The gas was then allowed to decay and every 40 minutes a NMR tipping pulse was applied and a value of the NMR free induction signal was recorded. A minimum of ten values were collected and then the FFT peak heights were plotted and fitted with an exponential decay. The NMR tipping pulse had 0.03 ms length and the loss to NMR signal due to each tipping pulse was about 2.5%which was corrected for. The magnetic field strength is given by the current through the Helmholtz coils (0.7 mT $\cdot A^{-1}$). $T_1$

Table 4.1: Chemical composition of the glass types used in the glass vessels of the polarisation system.

| Glass | Composition |
|---|---|
| 1720 Corning | 62% Si$O_2$, 17% $Al_2O_3$, 5% $B_2O_2$, 1% $Na_2O$, 7% MgO, 8% CaO |
| 7740 Pyrex | 81% Si$O_2$, 2% $Al_2O_3$, 13% $B_2O_3$, 4% $Na_2O$ |
| 180 GE | 60% Si$O_2$, 14% $Al_2O_3$, 7% CaO, $< 1\%$ SrO, 18% BaO, $< 1\%$ $TiO_2$ |

Table 4.2: $T_1$ relaxation time in the optical pumping cell.

| Orientation | $T_1$ (minutes) |
|---|---|
| + | $224 \pm 10$ |
| - | $213 \pm 10$ |

relaxation time was measured at different field strengths (0.40 mT, 1 mT, 2.4 mT and 3.4 mT) in both orientation using a field cycling technique (See Fig. 4.20). No matter what the polarisation field, $T_1$ is measured at 2.4 mT matching the Larmor frequency of 66.5 kHz. The gas was polarised at a given magnetic field strength and the field was cycled to the measurement value (2.4 mT) each time a FID was recorded. The relaxation time $T_1$ is much longer than the field-cycling time.

The NMR lineshape is obtained applying a FFT to the FID signal. NMR lineshapes were recorded at different pressures in the storage cell (therefor each preassure value).

In order to investigate the NMR lineshape changes with temperature and magnetism, the storage cell was heated up to 300° C using a hot air gun and magnetized with a strong magnet. The cell can be degaussed using a TV degaussing device. The degaussing tool is placed far from the cell and then slowly moved towards the glass surface. Then portions of the glass are scanned and the degaussing device is slowly moved away. The degaussing field is around 5 mT and degaussing was performed in the Earth's field.

**Cell Orientation dependence** Table 4.3 shows the values of $T_1$ for the 1720 Corning storage cell.

As shown in Figure 4.21 there is a significant difference between the $T_1$ relaxation time with + and - orientation, $T_1$ being longer with the $B_0$ field oriented in the direction

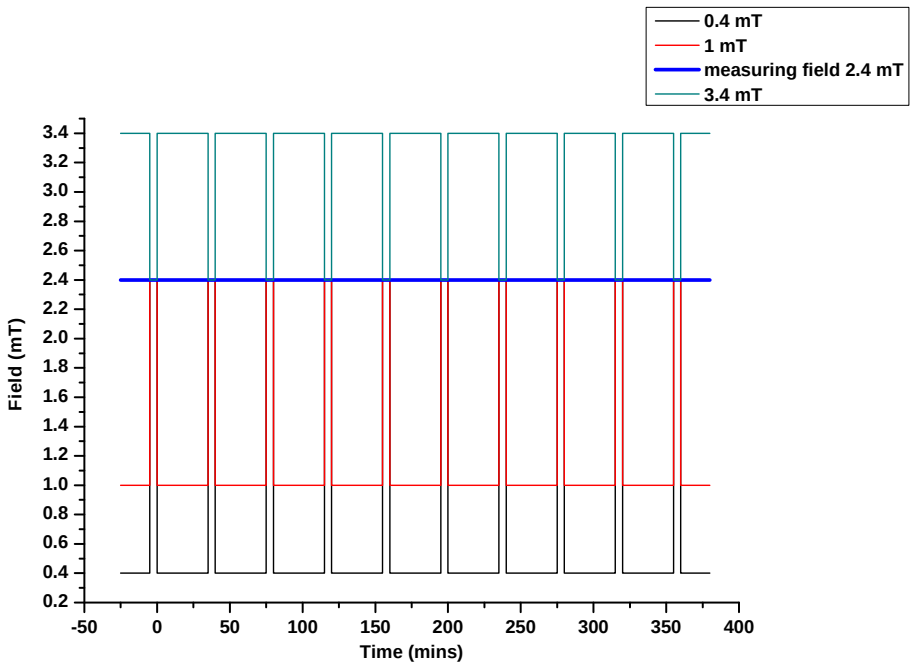


Figure 4.20: Diagram of the field cycling technique. The gas was polarised at a given magnetic field strength and the field was cycled to the measurement value (2.4 mT) each time a FID was recorded. The relaxation time $T_1$ is much longer than the field-cycling time.

of the Earth's field. We noticed a drop of $T_1$ value with + orientation when we turned off the $B_0$ field for 3 days. This did not affect the $T_1$ values with - orientation. After demagnetizing the storage cell the $T_1$ recovered.

**Magnetic field strength dependence** Looking at Table 4.3 there is a weak dependence of $T_1$ with magnetic field strength (in low magnetic field) but still $T_1$ is longer at 2.4 mT (the measuring field).

**NMR lineshape gas pressure dependence** A set of NMR spectra were collected starting at 0.2 mBar up to 250 mBar in order to observe the NMR lineshape at different pressures. The experiment was repeated for both orientations. The NMR lineshapes with + and - orientation are shown in Figure 4.22 and Figure 4.23 respectively.

With + orientation one can see that the NMR lineshape is wider than with - orientation and is more asymmetric.

The NMR lineshape shows a second peak on the right hand-side that appears at 2

Table 4.3: $T_1$ relaxation time (in minutes) in the fixed storage cell. a - before exposing the storage cell to Earth's magnetic field, b - immediately after switching on the measurement field, c - a week after switching on the measurement field, d - after heating and/or degaussing the storage cell

| Orientation | $T_1$ @0.4 mT | $T_1$ @1 mT | $T_1$ @2.4 mT | $T_1$ @3.4 mT |
|---|---|---|---|---|
| + | $82^c$ | $432^a$ | $430^a$ | $165^b$ |
| + | | $142^b$ | $202^b$ | $165^c$ |
| + | | $153^c$ | $297^c$ | |
| + | | | $315^d$ | |
| - | $45^b$ | $189^a$ | $139^a$ | $138^a$ |
| - | | $153^c$ | $148^b$ | $121^a$ |
| - | | | $161^c$ | $156^b$ |
| - | | | $188^d$ | $108^c$ |

mBar and transforms into a shoulder after 10 mBar. With - orientation this second peak disappears at 10 mBar. The NMR lineshape becomes wider with increasing pressure. For pressures exceeding 160 mBar the peak of the NMR lineshape is much more rounded. Motional narrowing occurs at low pressures and is responsible for the change in linewidth as the fast diffusion of the gas at low pressure leads to averaging of the inhomogeneous magnetic field in the cell (see Fig. 4.24).

**NMR lineshape temperature and magnetization dependance** The NMR lineshape is not affected by the thermal treatment applied to the glass cell, it is $T_1$ that is improved after heating the glass (see Fig. 4.25).

After magnetizing the cell, the NMR lineshape remains unchanged; obviously $T_1$ relaxation time drops dramatically (see Fig. 4.26). The $T_1$ returns to its previous values or is even longer after degaussing the glass cell.

### 4.3.3 180 GE Storage Cell

For this cell it was possible to rotate it and measure $T_1$ with two different orientations, denoted *up* and *down*. Accidentally, before starting the measurements, the cell was exposed to a high magnetic field ($B_0$ = 0.15 T) then stayed for 2 weeks in the Earth's magnetic

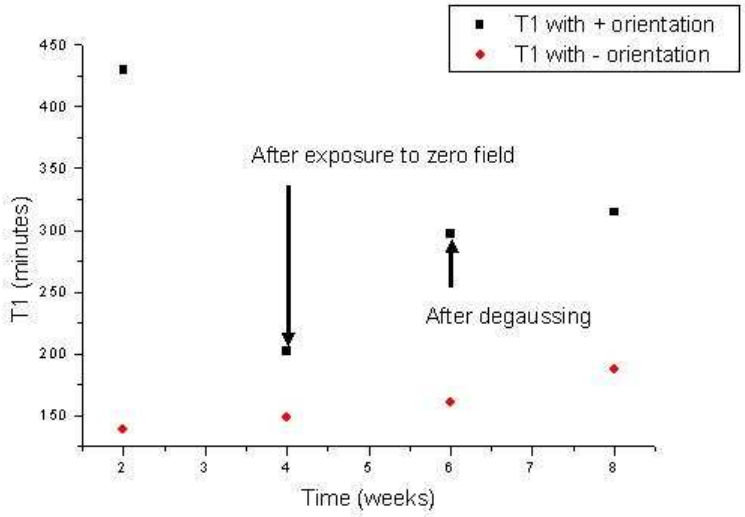


Figure 4.21: $T_1$ relaxation time variation during the experiments.

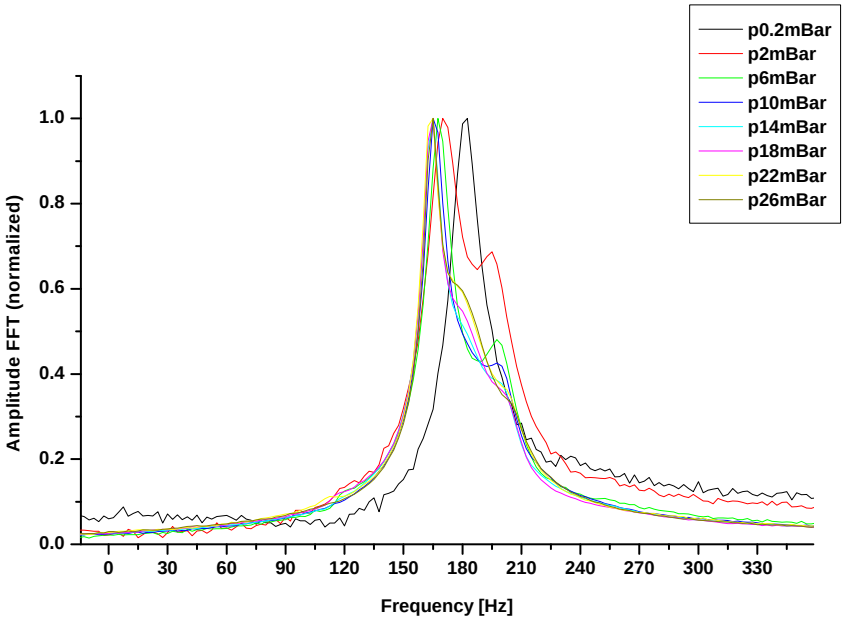


Figure 4.22: NMR lineshapes for different pressures with + orientation.

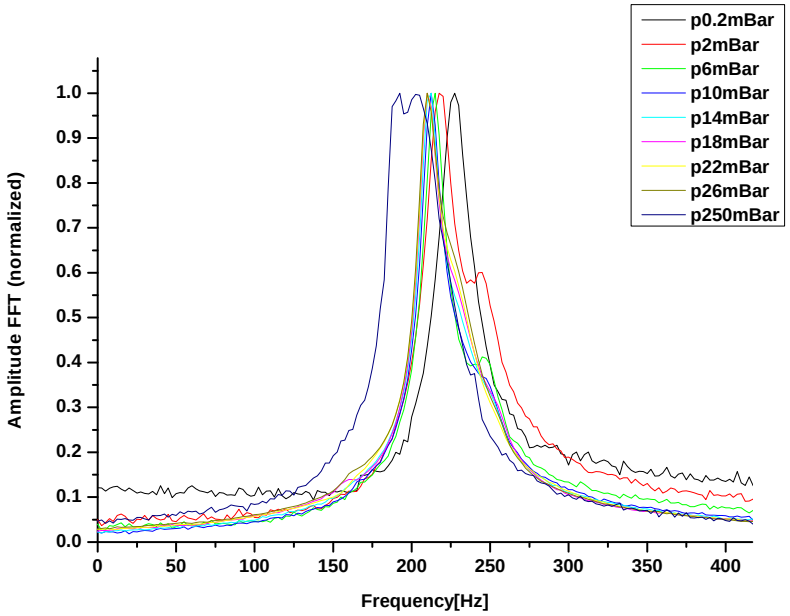


Figure 4.23: NMR lineshapes for different pressures with - orientation.

field. The measurement field ($B_0$ = 2.4 mT) was turned on for 3 days before the first measurement. The gas was polarised up to 30% and collected in the storage cell up to 40 mBar. The gas was then allowed to decay. $T_1$ measurements were done before and after degaussing the cell.

**Cell Orientation dependence** The $T_1$ values obtained for this cell are shown in Table 4.4.

Table 4.4: $T_1$ relaxation time in the GE storage cell.

| Orientation | $T_1$ (mins) before degaussing | $T_1$ (mins) after degaussing |
|---|---|---|
| up | 330 | 608 |
| down | 146 | 311 |

**Magnetic field strength dependance** The 180 GE storage cell was placed inside the MRI scanner ($B_0$=0.15 T) and $T_1$ was measured. $T_1$ values obtained were relatively short, around 30 minutes.

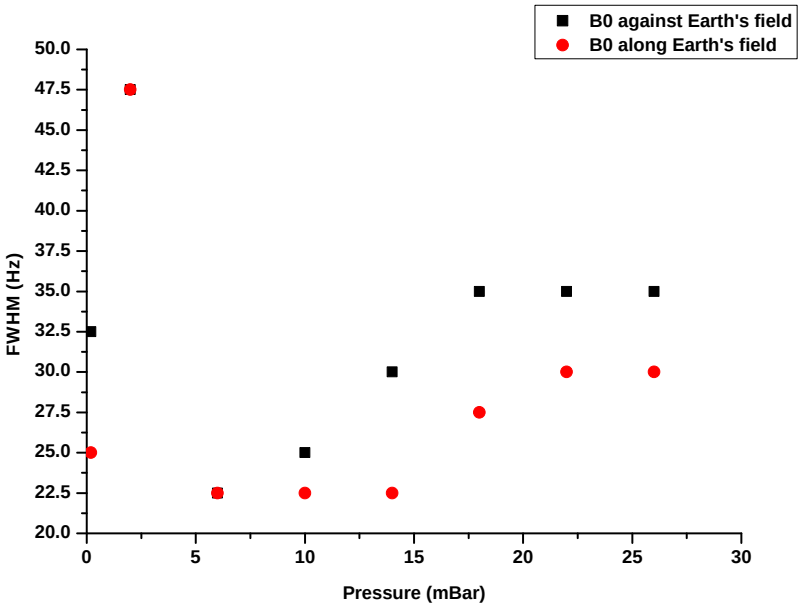


Figure 4.24: Plot of the spectral linewidth with increasing pressure in both $B_0$ orientations. Motional narrowing occurs at low pressures and is responsible for the change in linewidth as the fast diffusion of the gas at low pressure leads to averaging of the inhomogeneous magnetic field in the cell.

### 4.3.4 Conclusions

The GE 180 and Corning 1720 appear to contain magnetic materials in the wall that can be magnetized and demagnetized to some extent. It is not known whether this is due to Co or Fe in the glass or contamination with iron during fabrication. We can rule out rubidium impurities as we use MEOP and uncoated glass cells. The glass magnetization at room temperature is time and history dependent. The lineshape confirms the magnetization of the glass cell and shows unexpected structure. Classic motional narrowing is observed when the pressure is reduced and diffusion increases such that gas samples an average $B_0$ over the cell. There seems to be an optimal $B_0 \sim 2$ mT for long $T_1$ in these cells. $T_1$ is longest when the gas is stored with $B_0$ in the same direction as Earth's field and after degaussing and/or heating the cell [114].

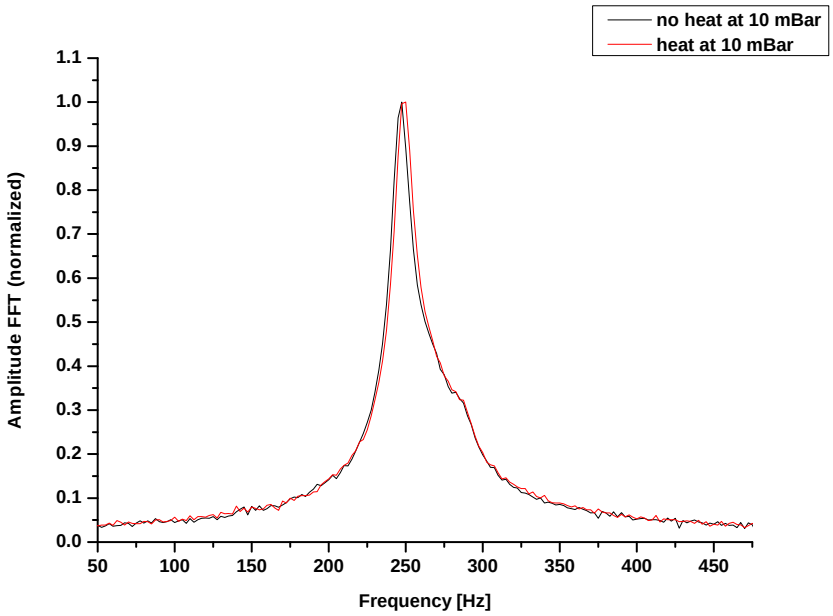


Figure 4.25: NMR lineshapes at room and high temperature.

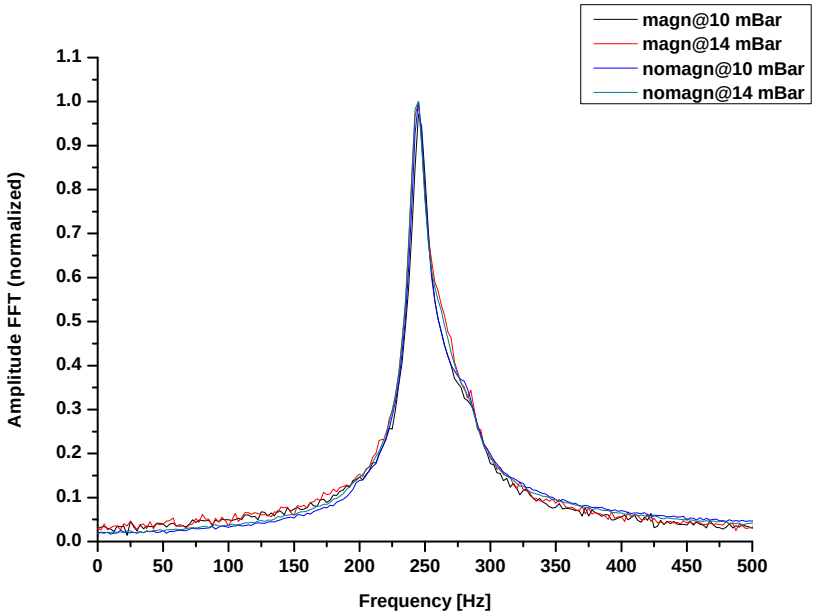


Figure 4.26: NMR lineshapes before and after magnetizing the storage cell.

## 4.4 Comparison of Two Ventilation Imaging Sequences at Low Field (0.15 T)

Much of the published work on hyperpolarised $^3$He *in vivo* was done at high field (1.5 T). In general, the sequences used are gradient echo sequences (FLASH or PR) and very rarely single-shot sequences like RARE [115], [116] or EPI [6] .

The purpose of this work was to demonstrate the possibility of using a low field magnet for lung studies as a step towards the clinical use.

All the results presented here were obtained on a IMIG® 0.15 T scanner with a SMIS console. This was previously used in a clinical environment and was installed in the laboratory back in the late 90s. The following sections presents the two types of sequences we used on this work: RARE and FLASH.

### 4.4.1 Rapid spin echo sequence (RARE)

The RARE sequence is a single-shot sequence and the read out of the Fourier space is done by spin echoes. 180° pulses (non-selective) are systematically applied to correct for the gradients and RF imperfections (Figure 4.27 and Figure 4.28).

#### Technological aspects

The RARE sequence that was used had the following characteristics:

- initial tipping pulse: 90 °
- field of view: 460 mm
- matrix 64×64
- *k*-space read out: centre-out (0, -1, +1, -2, +2, ...)
- pixel size: 7.2 mm
- $T_{CP}$: 14 ms
- read out time: $T_{obs}$ = 2.1 ms

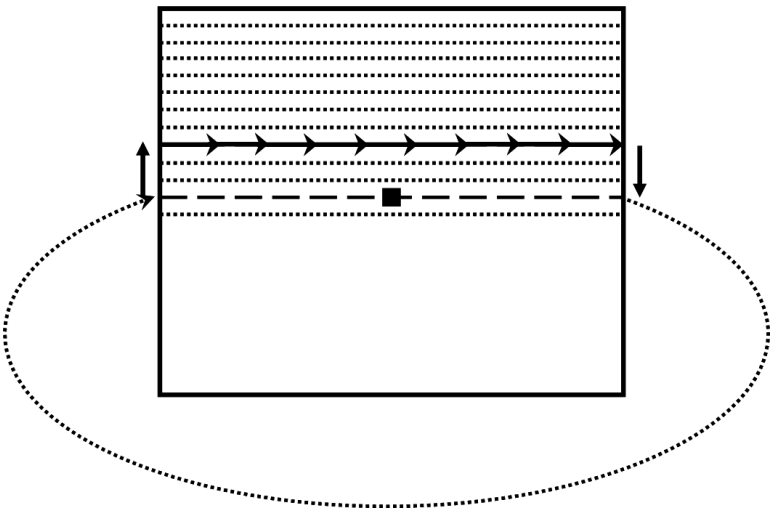

Figure 4.27: Fourier space read out on a RARE sequence: after acquiring a line, a rephasing gradient (opposite to the phase encoding gradient) restores the magnetisation on the central line of the *k*-space; a 180° pulse inverses the dephase due to the read out; another phase encoding step is applied and another line can be acquired; the fact that the lines are acquired in the same direction and the 180° pulse is applied always on the central line makes the sequence robust to artefacts.

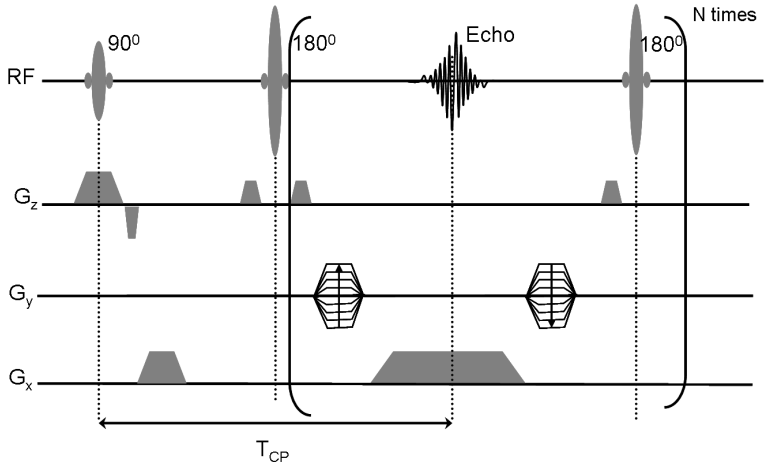


Figure 4.28: Timing of the RARE sequence. The 90° pulse is selective, the 180° pulses are non selective.

- read gradient amplitude: 3.5 $mT \cdot m^{-1}$
- total acquisition time: $T_{ACQ}$= 896 ms
- selective acquisition (50 mm slices) or non selective

- crusher gradient amplitude and duration: 5.6 mT $\cdot$ m$^{-1}$ and 10 ms
- 180° pulse duration: 900 $\mu$s

### Transverse relaxation constraints

***K*-space filtering** In general, the interval between the initial RF pulse and the signal acquisition has to be short enough compared to the transverse relaxation of the signal. If not, the signal is significantly reduced and, if the signal acquisition is long compared to the relaxation time, there will be a loss of resolution as well as distortions due to the *k*-space filtering in the phase direction. This is not a problem for the multi-shot sequences but becomes an issue when running single-shot ones.

**Attenuation induced by the gradients** The rapid gas diffusion in the magnetic field gradients create a significant signal attenuation. A more detailed study of the relaxation due to diffusion will be presented in Chapter 5.

### Imaging results

***In vitro* imaging** Figure 4.29 shows a slice selective RARE image of a 60 ml syringe (∅ 25 mm) filled with 50 mBar hyperpolarised $^3$He STP mixed with $^4$He up to 600 mBar.

The syringe edges are blurred in the phase encoding direction (vertical on Fig. 4.29). This effect can be explained by the fast decay of the signal on each line due to rapid diffusion with gradients. Considering the diffusion coefficient of $^3$He to be D = 1.8 $\cdot$ 10$^{-4}$ m$^2\cdot$ s$^{-1}$ and 64 lines we end up with a $10^6$ signal attenuation. The Fourier space is then highly filtered in the phase encoding direction.

Theoretically this can be corrected by an exponential filter:

$$S'(k_x, k_y) = S(k_x, k_y) \times \exp^{-bD(k_y)} \tag{4.30}$$

which needs to be apodised in order to prevent the imminent noise amplification.

The correction implies that the diffusion coefficient is homogeneous within the object. The restricted diffusion impedes the use of this correction *in-vivo*.

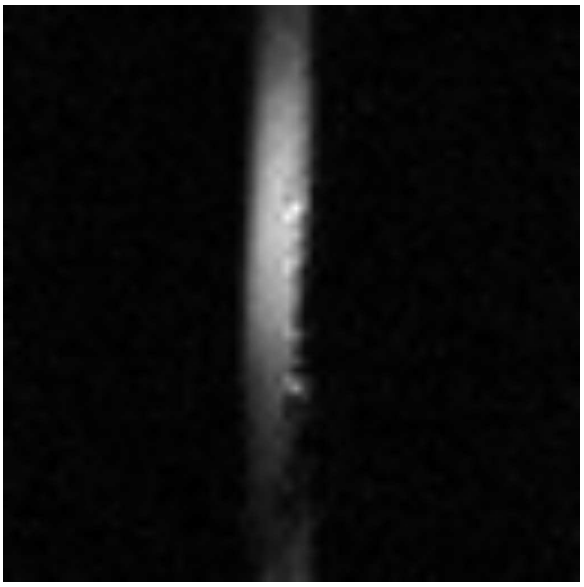

Figure 4.29: Coronal profile of a syringe using a slice selective RARE sequence. Image was obtained with 60 ml mixture of $^3$He - $^4$He (50 mBar hyperpolarised $^3$He STP and 550 mBar $^4$He); FOV = 260 mm, 64×64 matrix, acquisition time = 896 ms.

### *In vivo* imaging

**Projection images** Figure 4.30 shows breath-hold RARE *in vivo* projection images, after the inhalation of 30 mBar $^3$He STP diluted with $^4$He up to 300 mBar. SNR is high (220).

These images have slightly better quality compared to a usual ventilation scintigraphy image, with an acquisition time very much improved (896 ms compared to a few minutes for a ventilation scintigraphy image) because D is smaller in the lungs.

**Slice selective images** Applying a slice gradient it is possible to acquire images of any plane. In Figure 4.31 are shown images of axial slices.

The images have a high SNR (285) and give much more anatomical information than the scintigraphy and it takes just above 10.5 s to acquire the whole set, compared to more than 20 minutes for scintigraphy.

It was possible to acquire transverse profiles of the lungs using a 128×128 matrix, TE = 18 ms and slice thickness = 50 mm in just over 2 s. The resulting image is presented

Figure 4.30: Coronal profile of the human lungs using a non-selective RARE sequence. Image was obtained in a healthy volunteer, FOV = 350 mm, 64×64 matrix, acquisition time = 896 ms, after the inhalation of 30 mBar $^3$He STP; the image shows the heart silhouette and some big airways; left lung is not completely shown most likely because it is not fully covered by the coil.

in Figure 4.32 a). SNR was still high (167). Trying a 256×256 matrix the image was blurred showing the *k*-space filtering artifact [117](see Fig. 4.32 b) ).

**Summary**

The RARE sequence allows us to acquire *in vivo* images up to 4 mm resolution in just over 2 s. The sequence shows great performance in terms of signal-to-noise ratio. It is very easy to use it at low field since the 180° pulses can be repeated at very short intervals. The resolution is limited at 4 mm and the images present some artifacts, probably due to some phase loss of the 180° pulses and *k*-space filtering.

### 4.4.2 Gradient echo sequence (FLASH)

The FLASH sequence is a gradient echo multi-shot sequence. It is identical to the spin-warp sequence with regards to reading the *k*-space. however, it employs small tipping pulses and short repetition times, $TR$ (Fig. 4.33).

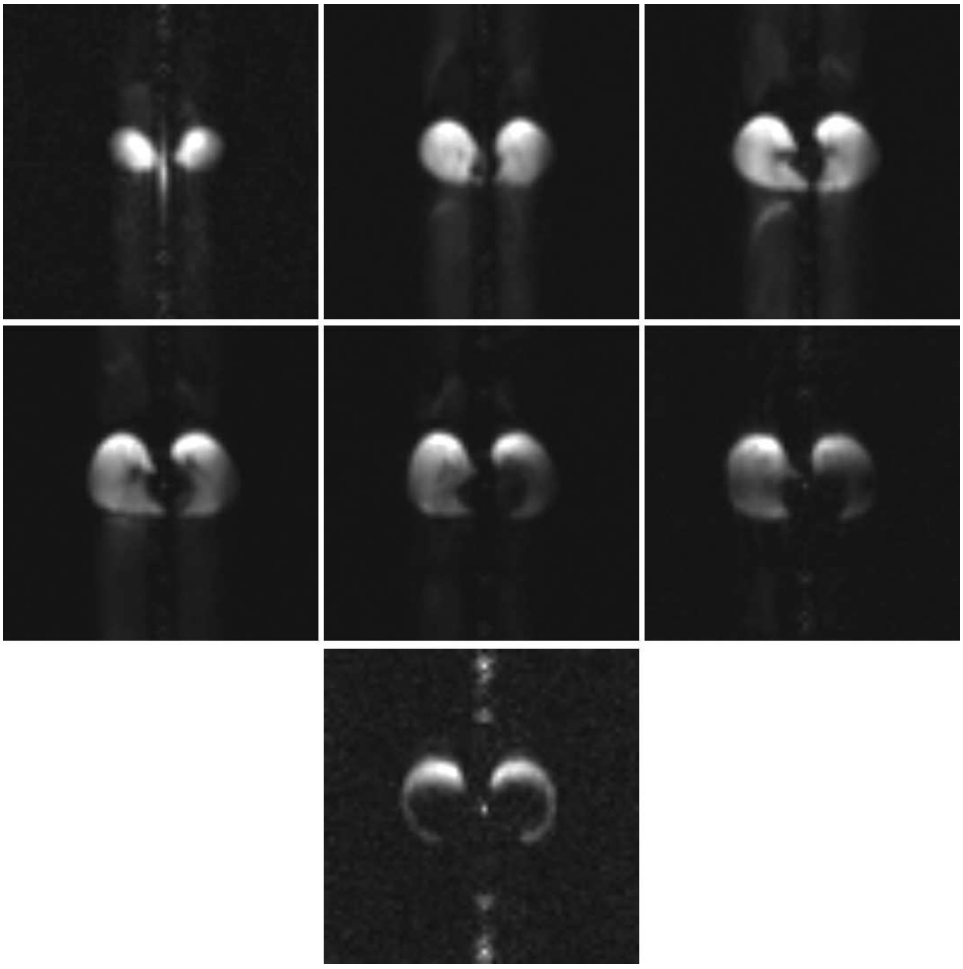

Figure 4.31: Transverse profiles of the human lungs using a multislice RARE sequence with the following parameters: 64 $\times$ 64 matrix, TE = 24 ms, FOV = 400 mm, slice thickness = 24 mm, slice separation = 28 mm, RF pulse = Gaussian 900 $\mu$s. Images show a complete coverage of the lungs, from apex to diaphragm; big airways are also visible.

**Technological aspects**

In the hyperpolarised regime, the longitudinal magnetisation decays progressively in an exponential fashion by applying a fix value tipping angle.

The sequence used in this work was a classical 2D gradient echo sequence with the following characteristics:

- matrix 64$\times$64 (128$\times$128)
- flip angle: 14°(12°)

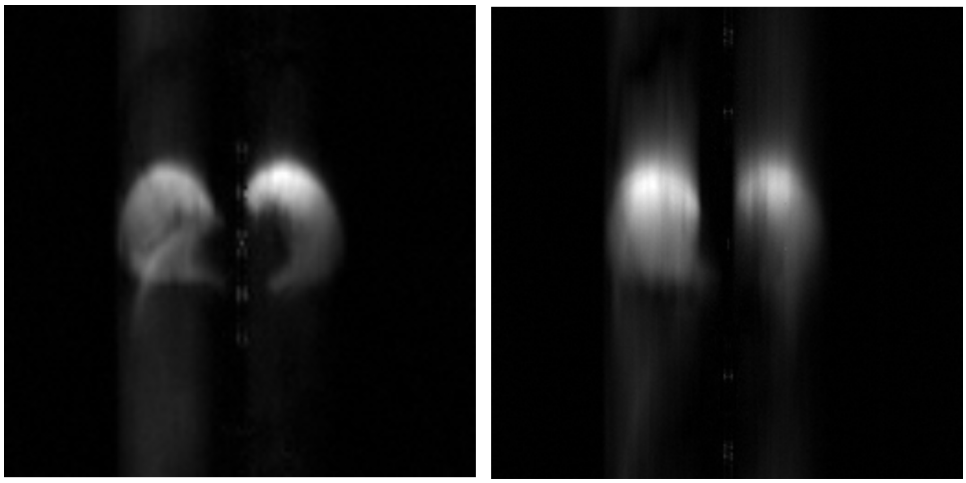

a) b)

Figure 4.32: Transverse profile of the human lungs using a multislice RARE sequence with the following parameters: a) 128×128 matrix, TE = 18 ms, FOV = 526 mm, slice thickness = 50 mm, RF pulse = Gaussian 900 $\mu$s. Image is clearly showing the anatomy with little artifacts due to *k*-space filtering; b) 256×256 matrix, TE = 24 ms, FOV = 526 mm, slice thickness = 50 mm, RF pulse = Gaussian 900 $\mu$s. Image is still showing anatomy but is distorted by the *k*-space filtering

- field of view: 460 mm
- *k*-space read out: sequential (..., -2, -1, 0, +1, +2, ...)
- pixel size: 7.2 mm (3.6 mm)
- TE: 5 ms
- read out time: $T_{obs}$ = 2.1 ms (4.2 ms)
- read gradient amplitude: 2.8 mT $\cdot$ m$^{-1}$
- total acquisition time: $T_{ACQ}$= 3.8 s
- selective acquisition (50 mm slices) or non selective
- spoiler gradient amplitude and duration: 5.6 mT $\cdot$ m$^{-1}$ and 1000 $\mu$s

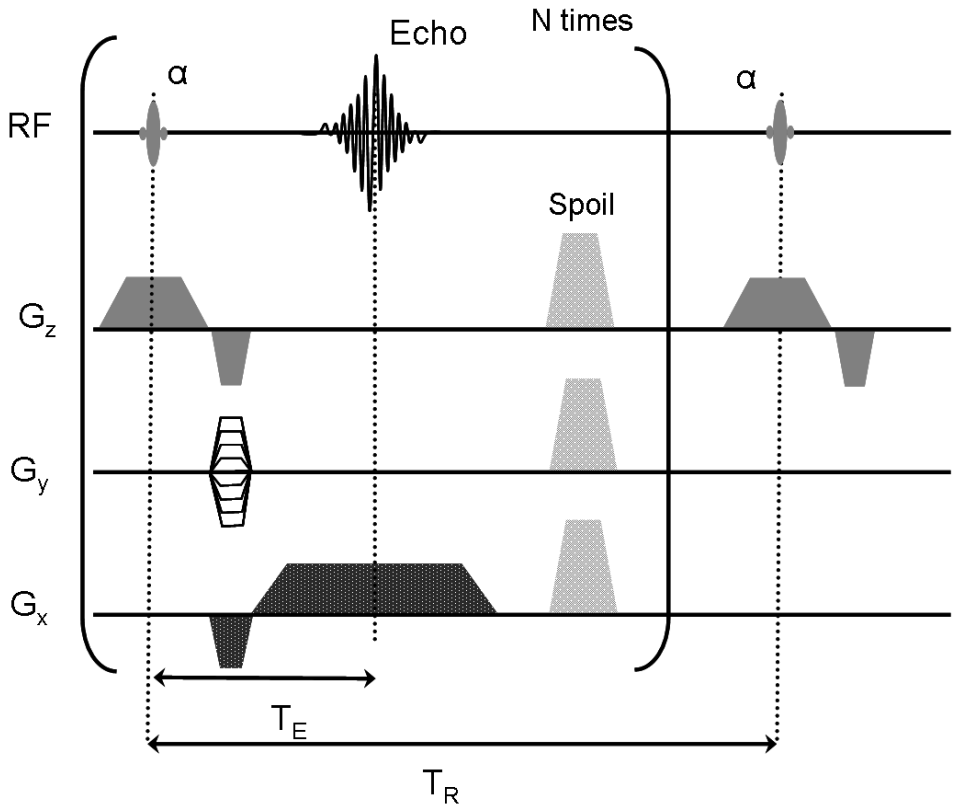


Figure 4.33: A short $TR$ and a low tipping pulse are employed. In order to suppress any remanent transverse magnetisation present from a previous excitation that could interfere with the next line of the *k*-space, large spoiling gradients can be used to completely dephase the transverse magnetisation. Notice that the phase gradients and the readout dephase lobe commence whilst the refocussing lobe of the slice gradient is still present. This reduces the acquisition time.

***In vitro* imaging** Figure 4.34 shows the image of a syringe obtained using a FLASH sequence. As expected, the artifacts related to the Fourier space filtering from Figure 4.29 disappeared.

***In vivo* imaging**

**Projection images** Figure 4.35 show *in vivo* projection image in a healthy volunteer using 30 mBar of hyperpolarised $^3$He STP. The image has less artifacts than the RARE equivalent but SNR is reduced ( 59 compared to 220 in RARE), even if the quantity of gas is identical.

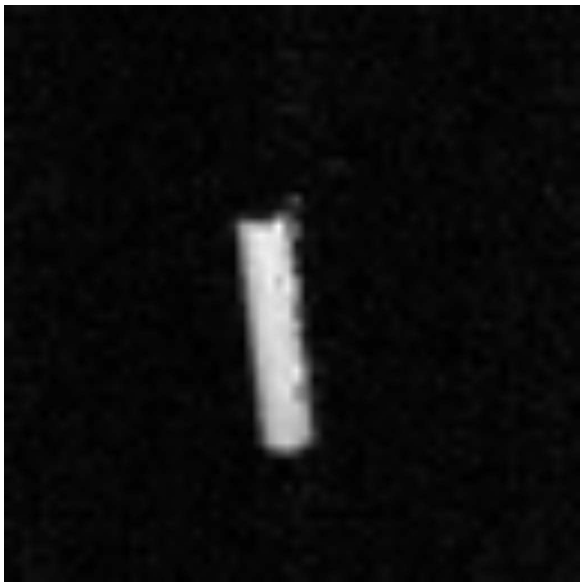

Figure 4.34: Coronal profile of a syringe using a slice selective FLASH sequence. Image was obtained with 60 ml mixture of $^3$He - $^4$He (50 mBar hyperpolarised $^3$He STP and 550 mBar $^4$He); FOV = 260 mm, 64×64 matrix, acquisition time = 1.6 s.

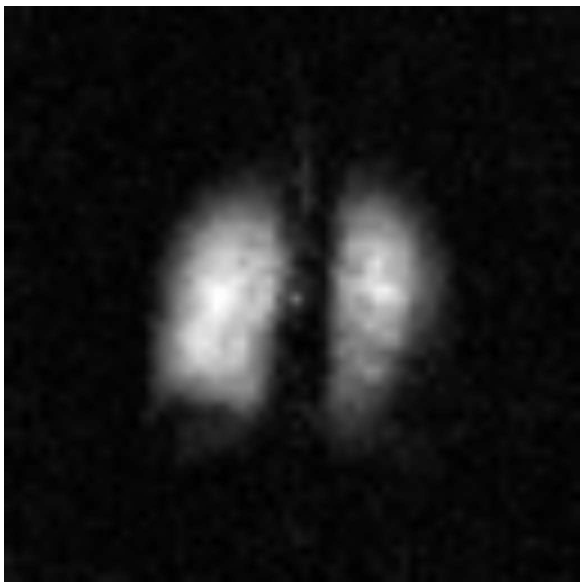

Figure 4.35: Coronal profile of the human lungs using a non-selective FLASH sequence.

**Slice selective images** As with RARE, it is possible to acquire all three planes using a slice gradient. In Figure 4.36 it is shown a set of images depicting three 50 mm slices on each plane. SNR is 78.

FLASH also allows for higher resolution 128×128 and less artifacts, although SNR

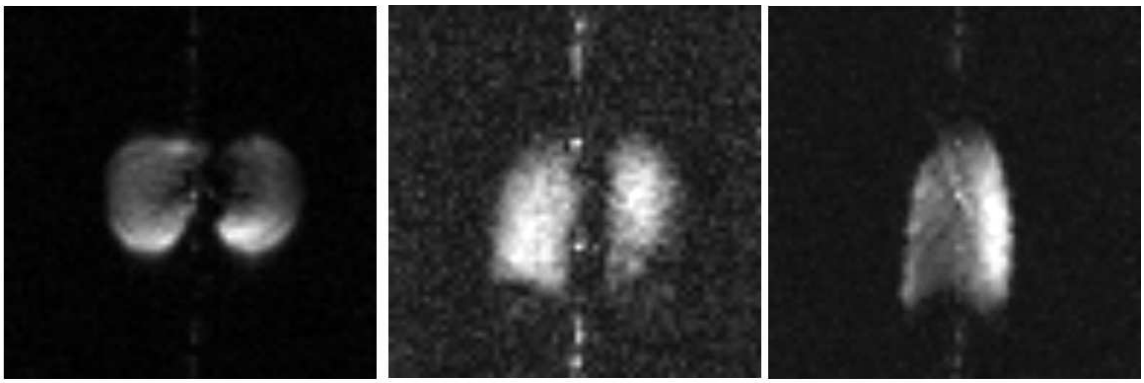


Figure 4.36: Multi-orientation profiles of the human lungs using a multislice FLASH sequence: a) Transverse plane, b) Coronal plane, c) Sagittal plane. The parameters are as follows: 64 $\times$ 64 matrix, TE = 5 ms, TR = 60 ms, FOV = 460 mm, slice thickness = 50 mm, tipping pulse = 14,$^\circ$ RF pulse = 3 lobes sinc.

is low (see Fig. 4.37).

**Summary**

According to theory, FLASH sequence allows imaging to go below the 5 mm resolution barrier. It produces less artifacts than RARE when choosing the right tipping angle. The sequence is slower than RARE and the resulting images have a lower SNR. This might be improved with centric acquisition of the k-space.

**On the use of low field for hyperpolarised $^3$He imaging** The results presented here show the possibility of obtaining hyperpolarised $^3$He images *in vivo* at low field (0.15 T). Unlike thermal polarisation, working at low field with hyperpolarisation is not affecting SNR. The polarisation is only determined by the optical pumping and hence SNR is independent of the magnetic field strength [86].

There are even some advantages when using a low magnetic field:

- it allows a rapid repetition of 180$^\circ$ pulses with no concern exceeding the SAR value, thus making the RARE sequence very easy to use

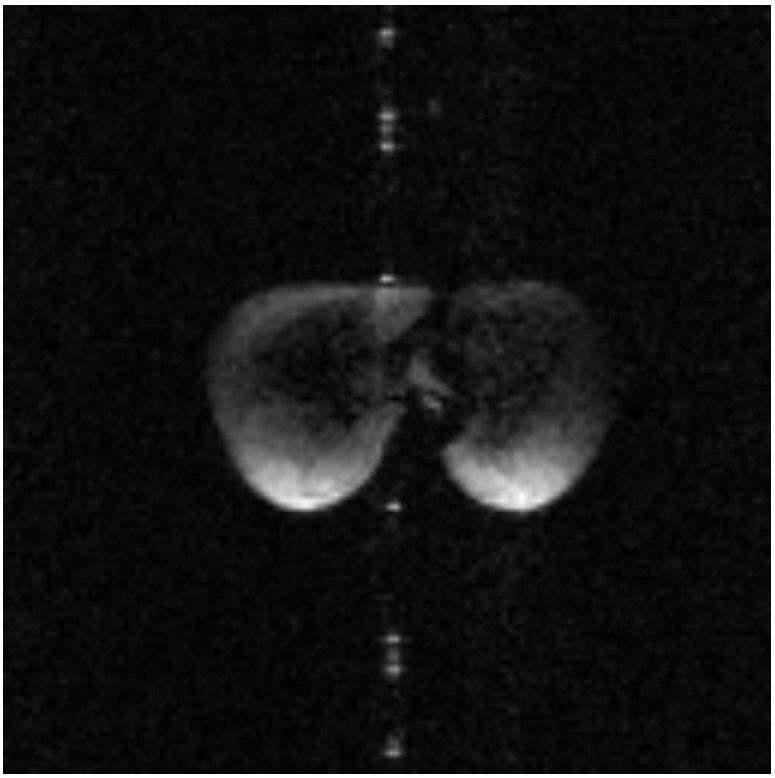

Figure 4.37: Axial profile of the human lungs using a slice selective FLASH sequence; the parameters are as follows: 128 $\times$ 128 matrix, TE = 5 ms, TR = 60 ms, FOV = 460 mm, slice thickness = 50 mm, tipping pulse = 12,$^\circ$ RF pulse = 3 lobes sinc.

- the susceptibility artefacts are smaller at low field; signal decay due to $T_2^*$ is less in gradient echo sequences at low field
- the running costs are smaller

On the other hand, low field limits the use of echo planar imaging due to the Maxwell terms artifacts which is dominant at low field [118], [119].

**On the choice of imaging sequences** The RARE sequence allows us to obtain a lung image in less than a second (projection or slice selective). The resolution is limited by the gas diffusing in the imaging gradients. Due to the imperfections of the 180$^\circ$ pulse, the acquisition is limited to only a slice at a time.

In theory, the FLASH sequence can give resolution smaller than 5 mm. It generates less artifacts than the single-shot sequences if the flip angle is correctly chosen. The

acquisition is slower than with RARE and gives a smaller SNR, unless using a variable angle.

To conclude:

- obtaining a spatial resolution smaller than 3 mm would be hard with any of the RARE or FLASH, a multi-shot sequence should prevent the *k*-space filtering artifact but as shown here, FLASH's SNR would be just to small so other sequences should be employed
- to get a high SNR with small quantities of gas, a RARE sequence is preferable, which is easy to use at low field

# Chapter 5

# Diffusion Study

## 5.1 Introduction

Normal lung physiology is extremely complex, and this complexity is further enhanced in sick lungs. The relationship between our current understanding of how lungs function, and what actually happens is perhaps similar to the relationship between counting on one's fingers and advanced matrix algebra.

The core of the respiratory function of our lungs are the alveoli. Basically it's here that oxygen passes out of the lungs and into the blood. Oxygen is needed in the process of generating energy for cells. It is therefore very interesting to be able to monitor how the alveoli develop and how they change over the human lifetime. Since respiratory diseases like COPD (Chronic Obstructive Pulmonary Disease) and emphysema are becoming more common there is the need for a tool to monitor alveoli size changes.

The distal airways are a complex porous structure where the respiratory gases transfer is realised by diffusion. The $^3$He diffusion is even faster due to its small mass.

In MRI, the diffusion of nuclei in a heterogeneous magnetic field creates a random magnetisation dephasing that is source of signal decay. As with all phenomena that destroy the signal, diffusion can be considered either as a phenomenon that limits the image acquisition or as a source of image contrast. The diffusion study inside the lungs has two goals: optimisation of the imaging sequences and to access parameters that are related to the lung microstructure.

The diffusion study in MRI is not new. It is used in clinical MRI, particulary in neurology [87], but also in non medical applications to probe structural parameters of porous media. The possibility to acquire $^3$He lung images opened the possibilities of studying helium diffusion in the airways and characterising the lung microstructure below the limits of the spatial resolution.

With the existing imaging techniques it is impossible to probe the microscopic size of human alveoli (cca. 4.2E-3 mm$^3$). What we can do instead is to measure how the alveolar walls impede the diffusion of a gas like $^3$He.

In this chapter there will be a description of the theory behind the restricted diffusion, then the heterogeneity sources inside the lung and three methods of measuring diffusion used in this work together with the results obtained.

## 5.2 Theoretical Aspects of the Signal Decay Due to Diffusion in a Heterogeneous Field

### 5.2.1 Restricted diffusion

#### Restricted diffusion in an enclosed cavity

In a restricted environment, diffusion won't follow the Einstein's law for an indefinite time due to the walls that will limit the displacement of the particle. This is the restricted diffusion (Fig. 5.1, Fig. 5.2). We can define an apparent diffusion coefficient denoted ADC or D(t) [120]:

$$D(t) = \frac{\langle d^2 \rangle}{6t} \tag{5.1}$$

$\langle d^2 \rangle$ being the square mean value of the particle displacement in time $t$.

In the case of the free diffusion, the apparent diffusion coefficient is equal to the diffusion coefficient ($D(t) = D_0$); in the case of restricted diffusion, the apparent diffusion coefficient gets smaller with time, and approaches zero in an enclosed cavity.

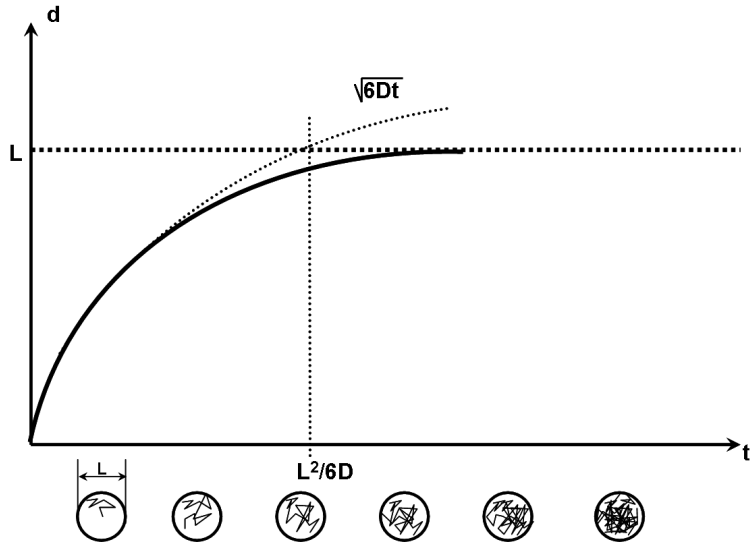


Figure 5.1: The distance traveled as a function of restricted diffusion time in an enclosed space.

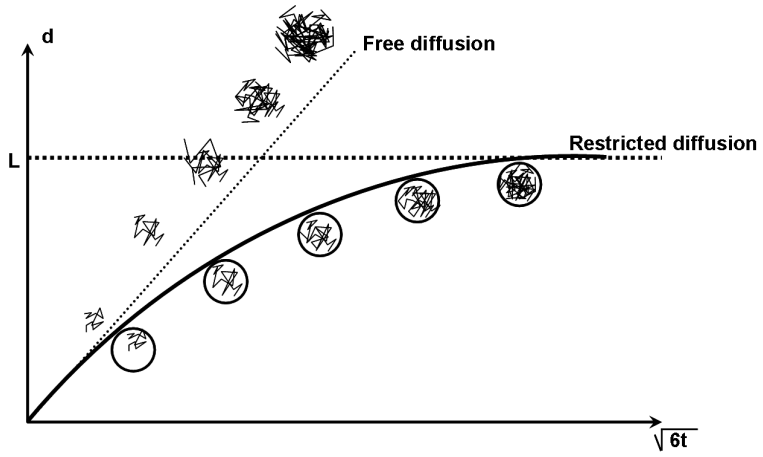


Figure 5.2: The distance travelled by the restricted diffusion in an enclosed space.

### Restricted diffusion in an open environment

In an open environment like the lungs[1], the situation is more complex. Basically, the restriction is influenced by the geometry of the environment. One model used to study restricted diffusion is liquid diffusing in a porous rock.

[1]The notion of open environment depends on the set scale: even the Universe is a closed structure. On the scales used in NMR, the lung can be considered open.

**Structural parameters: porosity and tortuosity** In a porous medium, the porosity is defined as the volume fraction accessible to the tracer. In the case of the lung it is defined as:

$$\Phi = \frac{V_{airways}}{V_{lung}} \tag{5.2}$$

In a non conductive porous medium, wetted by a liquid, we define the factor of electronic formation as the ratio of the pure liquid conductivity $\sigma_0$ and the wetted medium $\sigma$ [121]:

$$F = \frac{\sigma_0}{\sigma} \tag{5.3}$$

This ratio, always greater than 1, reflects the reduction of the effective conductive cross-section and the pores topography. To distinguish the two effects, we define tortuosity as:

$$T = F\Phi \tag{5.4}$$

which describes the elongation of the covered path due to pores topography. The tortuosity is always equal or greater to 1. Typical values of the tortuosity and porosity are given in Table 5.1.

Table 5.1: Example values of porosity and tortuosity; in the case of the isolated liquid, tortuosity equal to 1 shows the possibility of moving in a straight line.

| | porosity $\Phi$ | tortuosity $T$ |
|---|---|---|
| isolated liquid (without the rock) | 1 | 1 |
| pile of monodispersed spheres | 0.45 | 1.5 |
| sedimentary rocks | 0.2 | $\leq 3$ |

The conductivity is written as:

$$\sigma = \sigma_0 \frac{\Phi}{T} \tag{5.5}$$

This formula distinguishes the two causes of electrical conductivity reduction: the porosity $\Phi$ (effective conductive cross-section reduction) and the tortuosity $T$ (elongation of the path covered by the charge carriers).

**Modeling of the apparent diffusion coefficient in the pores** In an open environment with restricted diffusion, the ADC behaves as in Figure 5.3; ADC decays proportionally with the square root of time, the proportionality coefficient depends of the interface surface (S)-to-total volume (V) ratio. Basically, for very short times, the number of particles encountering an obstacle is proportional to this ratio (S/V Fig. 5.4). For short times, the ADC evolution is given by Mitra [120]:

$$\frac{D(t)}{D_0} \simeq 1 - \frac{4}{9\sqrt{\pi}} \left(\frac{S}{V}\right) \sqrt{D_0 t} \tag{5.6}$$

($t \ll \frac{L^2}{D}$, L being the size of the pores)

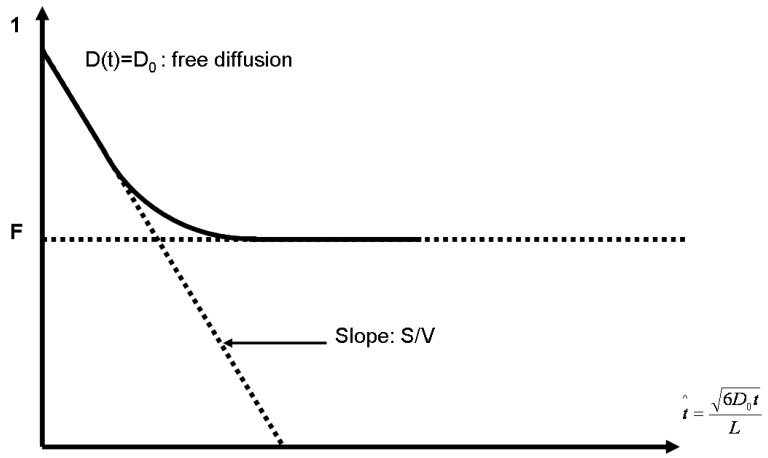


Figure 5.3: The evolution of ADC with time.

For long times, the limit of ADC ($D$) is the formation factor $F$.

In order to describe ADC in general, the following interpolation was proposed by Latour [122]:

$$\frac{D(t)}{D_0} = 1 - (1-F) \times \frac{\frac{4}{9}\sqrt{\frac{D_0 t}{\pi}}\left(\frac{S}{V}\right) + (1-F)\frac{D_0 t}{L_0^2}}{(1-F) + \frac{4}{9}\sqrt{\frac{D_0 t}{\pi}}\left(\frac{S}{V}\right) + (1-F)\frac{D_0 t}{L_0^2}} \tag{5.7}$$

$L_0$ (denoted $\sqrt{D\theta}$ by the authors of the article) being a length parameter of the environment. In the absence of an obstacle for diffusion (F = 1), we get $D(t) = D_0$.

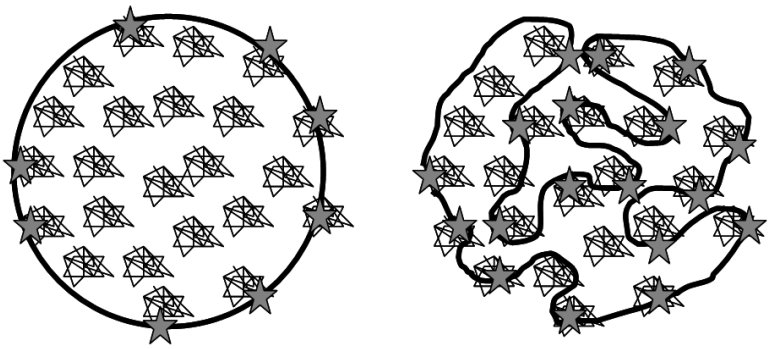

Figure 5.4: The effect of surface-to-volume ratio on the ADC decay.

In practice, for liquids in porous rocks, the $D(t)$ behaviour for very short times (the S/V ratio) is accessible by NMR, even if the measurements are different from those with other methods (measurement of the isotherm absorption ). The asymptotic behaviour (porosity and tortuosity) remains difficult to explore by NMR since the relaxation limits the length of diffusion [123], [124].

**Application of restricted diffusion models to helium in the lung** The models of restricted diffusion presented here were elaborated for the diffusion of liquids. To use these models in gases raises some questions. In particular, the restricted diffusion model used implies the lack of interaction between the gas and the alveolar wall that could slow down the diffusion or lead to a surface diffusion [125]. If for liquids, the high density impedes absorption, this is not necessarily the case for gases. We also neglect the small surface relaxation compared to relaxation induced by oxygen. The diffusion coefficient for gases is $10^5$ times higher than for liquids.

For the case of $^3$He diffusing in the lung, considering the diffusion coefficient in $^4$He at $37°C$ (Table 3.5), a typical gas volume of 2L and a exchange surface of $70m^2$ [17], applying 5.6 we get negative values for $D(t)$ at $t \geq 150\mu s$. From this we can not hope to get information on the initial section of the curve (obtain a surface-to-volume ratio) by means of NMR *in vivo*. We could though, measure tortuosity for long times, with NMR.

### 5.2.2 Sources of magnetic field heterogeneity

The magnetic field variation sensed by a magnetisation can be a temporal variation (the magnetic field varies locally in time) or spatial variation (the particle carrying nuclear spin is moving in an heterogeneous field).

The temporal variation can be created by an RF pulse application or generated by the RF noise. The latter won't be described here.

The spatial variation can occur at three levels:

#### Molecular (microscopic) scale

On the atomic scale (microscopic), the dipole-dipole interaction corresponds to both a spatial and temporal variation of the magnetic field; the mobile spins sense and induce a magnetic field. This interaction has to be treated by a phenomenological model and corresponds to $T_2$ transverse relaxation time [60].

#### Macroscopic scale

At the macroscopic level, the spatial variation is produced by: magnetic field defects due to magnet and shimming system imperfections (residual gradients); gradients induced by the gradient coils.

The gradients are supposed to be perfectly uniform and they are in reality, at least at first order.

The residual gradients are not necessarily uniform on the scale of the field of view, but can be considered uniform for the diffusion scale used in practice.

#### Mesoscopic scale: internal gradients

The mesoscopic scale is an intermediary scale between the macroscopic scale of the object and the microscopic molecular scale. On this scale, the spatial variation of the magnetic field is due to susceptibility variations in a heterogeneous environment.

The diffusion of the particles carrying spins in this heterogeneous field leads to relaxation. These field variations are normally hard to model, due to the lack of information

about the precise geometry of the environment and lack of analytical solutions for complex geometry. This is the case of the lung. A simple approximation was proposed by Gasel [126] to estimate the internal gradients in an environment having the spatial dimension $L$ and the susceptibility difference between two components $\Delta\chi$:

$$G_i \simeq \frac{\Delta\chi \cdot B_0}{L} \tag{5.8}$$

This approximation is arguable since the gradient is probably overestimated in the centre of the homogeneous region and probably underestimated in the proximity of the interfaces. For the lung (susceptibility difference air-water $\Delta\chi$ = 12 ppm over 300 $\mu m$), 5.8 gives a value of 6 mTm$^{-1}$ at 0.15 T.

### 5.2.3 Signal decay due to restricted diffusion in heterogeneous field

In the case of the restricted diffusion, there are two possible approaches.

The simplest one consists of keeping the equation from the free diffusion and replacing the diffusion coefficient $D$ with an apparent coefficient $D(t)$. For a continuous gradient, for example, we have:

$$\frac{S(T_{CP})}{S_0} = \exp\left(-\frac{\gamma^2 G^2 T_{CP}^3}{12} \cdot D(T_{CP})\right) \tag{5.9}$$

$D(t)$ is defined by:

$$D(t) = \frac{-12 \cdot \ln(S(t)/S_0)}{\gamma^2 G^2 T_{CP}^3} \tag{5.10}$$

The other approach, more complex, consists of analytically solving the equations of signal attenuation for certain cases of restricted diffusion. This has been done in practice only for diffusion in a closed geometry and for a uniform and continuous gradient, or a pair of Dirac pulses [127]. More recently, Callaghan proposed a matrix formalism for solving the restricted diffusion in uniform, time varying gradients, for the case of an environment sandwiched between two parallel planes [97]. The cases of open geometry (including the lungs) and more complex gradients weren't studied in the literature;

probably due to the complexity of the situation, it is unlikely one can get an analytical solution.

### Parameters characterizing the diffusion

During the spin echo experiment in the lungs, there are three phenomena taking place: helium diffuses in the alveolar structures, magnetisation is dephasing and 180° pulses are applied and partially rephase the magnetisation.

To describe these phenomena, it is possible to estimate diffusion considering: the size of the alveoli, the distance traveled whilst the magnetisation is dephasing and the distance travelled between two 180° pulses.

The ratio of these dimensions is very important when choosing the right model for the signal decay.

**Size of the environment** For the case of the lung, the characteristic dimension of the medium is the alveolar diameter, $L = 300\ \mu m$ [16].

**Size of the dephasing** The size of the dephasing, denoted $l_G$, is given by:

$$l_G = \sqrt[3]{\frac{D}{\gamma G}} \tag{5.11}$$

Table 5.2: Values of the dephasing size of helium inside the lungs for the applied external gradients.

| $l_G$ | $G = 0.1\ mT \cdot m^{-1}$ | $G = 1\ mT \cdot m^{-1}$ | $G = 10\ mT \cdot m^{-1}$ |
|---|---|---|---|
| $^3$He diffusion in $^4$He $D = 2\ cm^2 \cdot s^{-1}$ | 2.14 mm | 0.99 mm | 0.46 mm |

For values of the applied gradients within accessible limits, the size of dephasing is bigger than the alveolar size: $l_G > L$ (Table 5.2); the dephasing is negligible unless a helium atom travels outside the initial alveolus.

**Size of the diffusion length** The size of the diffusion length, denoted $l_D$, is the distance diffused during the inter-echo time $T_{CP}/2$ in a spin echo sequence:

$$l_D = \sqrt{D\frac{T_{CP}}{2}} \tag{5.12}$$

Table 5.3: Values of the diffusion size of helium inside the lungs.

| $l_D$ | $T_{CP} = 5\ ms$ | $T_{CP} = 10\ ms$ | $T_{CP} = 100\ ms$ |
|---|---|---|---|
| $^3$He diffusion in $^4$He $D = 2\ cm^2 \cdot s^{-1}$ | 0.71 mm | 1.00 mm | 3.16 mm |

For the accessible inter-echo times, the size of the diffusion length is bigger than the size of the alveoli (Table 5.3).

**Diffusion in a uniform magnetic field gradient**

First we consider the macroscopic level of the heterogeneity. The case of the mesoscopic gradients, will be presented in the next section.

**Free diffusion regime** Even in a porous structure, diffusion can be considered "sufficiently free" if the signal attenuation by diffusion between two consecutive echoes is very small, or [128]:

$$\left(\frac{l_D}{l_G}\right)^6 < 4 \tag{5.13}$$

or

$$l_G > 0.8 l_D \tag{5.14}$$

This is the case of the lung when the smallest gradient is applied (Table 5.2, Table 5.3).

**Motional averaging regime** In the case of free diffusion in an uniform gradient, the particles will move away from their initial position over an average distance $\sqrt{2Dt}$. The

induced dephasing can not be totally compensated by the spin echo. Diffusion is hence a source of signal decay (Fig. 5.5 a).

**Qualitative description** In the case of restricted diffusion in a closed medium, the particle can not move from its initial position, further than the size of the enclosure. The range of magnetic field gradients that the particle is sensing is limited. If the diffusion is fast enough the particle will travel through a successively strong fields and less strong fields before dephasing will take place. This will slow the signal attenuation and equalize the dephasing of the magnetisation. This is the motional averaging (Fig. 5.5b). This averaging is also present in the case of diffusion in an heterogeneous gradient (Fig. 5.5c).

In order for the motional averaging to take place, it is necessary that the time needed to move across the medium to be small compared to the time needed to substantially dephase the magnetisation.

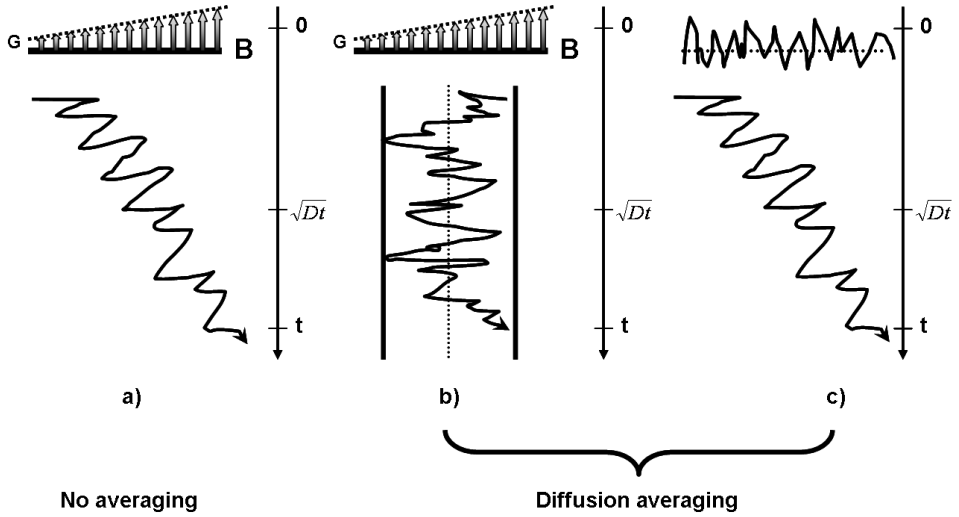


Figure 5.5: a) Free diffusion in an uniform gradient: no averaging; b) Restricted diffusion in uniform gradient: there could be an averaging process (because of the motion) if the diffusion is faster than the dephasing; the average position is shown by the dotted line; c) Free diffusion in heterogeneous gradient: there could be also a motional averaging if the magnetic field varies around a mean value.

**First condition for motional averaging** In order for the motional averaging to take place, the diffusion must be fast enough to overcome the magnetisation dephasing.

Take the case of an uniform gradient $G$ in a closed enclosure of size $L$, the condition for motional averaging is:

$$(\gamma G L) \cdot \frac{L^2}{D} \ll 1 \tag{5.15}$$

or:

$$l_G \gg L \tag{5.16}$$

meaning that the particle has to travel the size of the enclosure a number of times big enough to allow for averaging before the magnetisation dephasing gets too large [128].

There is another equation for the condition in 5.16 given by Hyslop [129]:

$$d \doteq \frac{4\pi D}{\gamma G L^3} = \sqrt[3]{\pi \frac{l_G}{L}} \tag{5.17}$$

the condition for motional averaging being now $d > 0.1$. This condition together with 5.16 leads to:

$$l_G > \frac{1}{1000\pi} L \tag{5.18}$$

More recently, Pütz proposed a third equation for the motional averaging condition [130]:

$$q \doteq \sqrt[3]{\frac{8\pi D}{\gamma G L^3}} = (2\sqrt[3]{\pi}) \frac{l_G}{L} \tag{5.19}$$

the condition transforms into $q \gg 1$.

Table 5.2 shows that for the case of helium diffusion inside the lung, the condition is fulfilled when the applied gradient is much smaller than 10 mT$\cdot$ m$^{-1}$.

**The second condition for motional averaging** In a spin echo experiment, there is a second condition for motional averaging. Basically, if the time between two $\pi$ pulses is very short compared to the time needed for dephasing, the compensation for the field heterogeneity is achieved by these pulses, not the averaging due to diffusion [128].

The condition for the $\pi$ pulses to be faster than the dephasing is:

$$l_D \ll l_G \tag{5.20}$$

In order for the motional averaging to occur, the $\pi$ pulses have to induce a fast rephasing and the second condition is:

$$l_D \geq l_G \tag{5.21}$$

Table 5.2 and Table 5.3 indicate that this condition is true for the helium NMR experiments inside the lung.

**Signal decay in the case of motional averaging** This case was theoretically described by Robertson [131] for the space between two infinite parallel planes and then by Neuman [132] for other geometries (cylinders or spheres). Simulation experiments were realized by Hyslop and Lauterbur [129] for simple and closed geometries in 1D, 2D and 3D.

For the simple case of two planes separated by a distance $L$ [131], the signal decay follows the equation:

$$\frac{S(T_{CP})}{S_0} = \exp\left(-\frac{\gamma^2 G^2 L^4 \left(T_{CP} - \frac{17}{56}\frac{L^2}{D}\right)}{120D}\right) \tag{5.22}$$

which can be rewritten considering 5.21 as:

$$\frac{S(T_{CP})}{S_0} = \exp\left(-\frac{\gamma^2 G^2 L^4 T_{CP}}{120D}\right) = \exp\left[-\frac{1}{60}\left(\frac{l_D}{l_G}\right)^2\left(\frac{L}{l_G}\right)^4\right] \tag{5.23}$$

The echo decay is, as for the free diffusion, exponential, but with a different decay time:

$$T_2^{\dagger} = \frac{120D}{\gamma^2 G^2 L^4} \tag{5.24}$$

In this case, the relaxation speed is independent of the inter-echo time. Diffusion is slowing down the signal attenuation. For a very fast diffusion, $T_2^{\dagger}$ is infinite and the observed $T_2$ is thus "raw" $T_2$ . This regime causes resolution loss in MR microscopy

since a particle in an enclosure and diffusing fast will appear as located in the center of the enclosure (Fig. 5.6c).

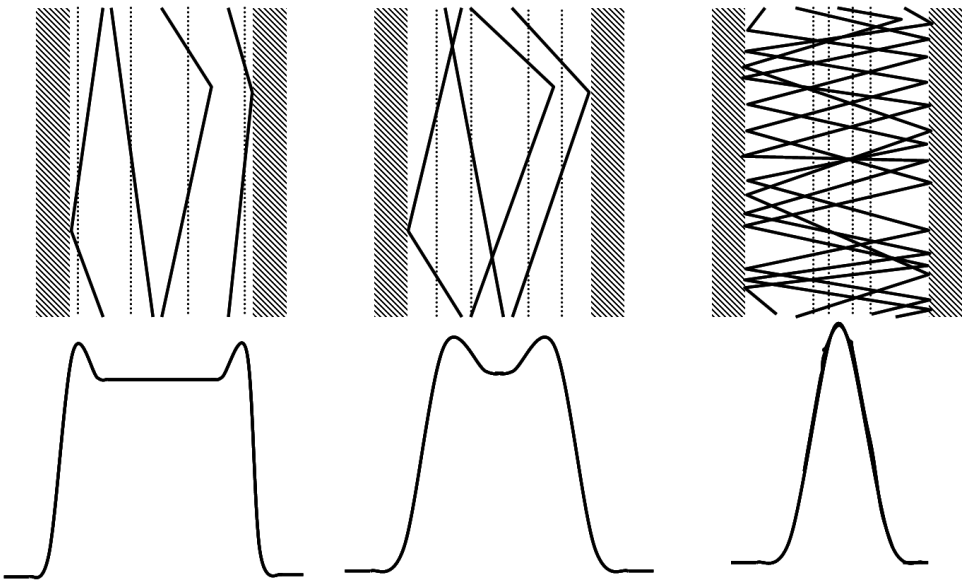

Figure 5.6: Motional averaging in a 1D closed enclosure; the lower curve represents the spins localisation by MRI; diffusion speed increases from a) to c); the averaged trajectories are moving to the centre (dotted line); when diffusion is slow a), there is a edge enhancement; when diffusion is very fast c) there is only a central peak (motional averaging): there is a loss of spatial resolution.

**Localised regime** There is a third regime that was described more recently: the localised regime or static dephasing regime (heterogeneous broadening) . The theory was described in the 90s [133], [134], [135] and it was experimentally proven in 1995 by Hürlimann [128].

**Conditions for occurence of the localised regime** The localised regime occurs for restricted diffusion outside motional averaging, when:

$$l_D \gg L \gg l_G \tag{5.25}$$

**Signal decay in the localised regime** In this regime, the particles move slow enough that the transverse relaxation is determined by the spatial distribution of the magnetic

field. The decay does not follow a simple exponential decay with time but it depends strongly on geometry; as a result, $T_2^\dagger$ is independent of $T_{CP}$:

$$\frac{S(T_{CP})}{S_0} = c\frac{\sqrt[3]{\frac{D}{\gamma \cdot G}}}{L} \exp\left(-\frac{a \cdot d^{1/3} \cdot \gamma^{2/3} \cdot G^{2/3} \cdot T_{CP}}{2}\right) \propto \frac{l_G}{L} \exp\left[-a\left(\frac{l_D}{l_G}\right)^2\right] \quad (5.26)$$

$a$ and $c$ being geometry constants [83], [128], [133], [134], [135].

**Edge enhancement in the localised regime** In the localised regime, accentuated NMR signal near the walls was described and shown by numerical simulation [130] and experiments [136], [137]. The experimental evidence is not always possible due to the spatial resolution demands. This paragraph will discuss the causes of phenomenon.

According to Pütz [130], the phenomenon occurs due to a spectral peak of diffusion (diffusive-spectral edge enhancement) when $l_G \approx L$ (Fig. 5.6 a) and b)).

After Callaghan [136], the dominant cause of this effect is strictly the restriction near the edges (diffusive-relaxation edge enhancement). In the case of very fast dephasing, a variation of D(t) due to proximity of the wall diminishes the decay thus the edge enhancement.

Finally, the last hypothesis for the cause of this phenomenon could be: formation of an enhanced spin echo, rephasing effect can be seen for $l_D = T_{CP}/2$ (Fig. 5.7).

**Review of restricted diffusion regimes in uniform gradient** Hürlimann has summarized the different diffusion regimes in a monodimensional closed enclosure in the presence of a uniform gradient [128]. These regimes are shown in Figure 5.8. The figure clearly illustrates the complexity of the problem, even for the simple case of a monodimensional closed enclosure.

For the case of the lung, since it is an open structure with various length scales , it is obvious that the problem is more complex and difficult to model in an analytical fashion. Figure 5.9 uses the Hürlimann diagram to predict the diffusion of helium inside the lung. This diagram shows that, considering the applied gradients, the regime that occurs is motional averaging.

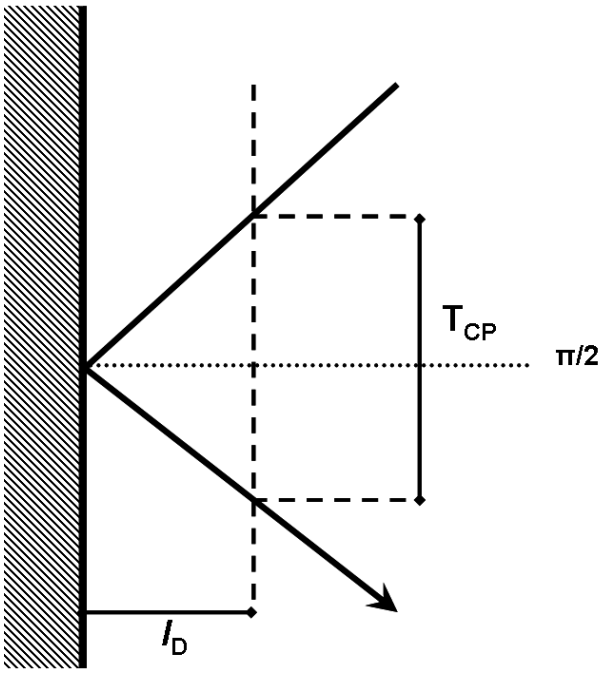


Figure 5.7: A particle traveling through similar magnetic field regions before and after the $\pi$ pulse, and colliding with a wall, could explain the edge enhancement.

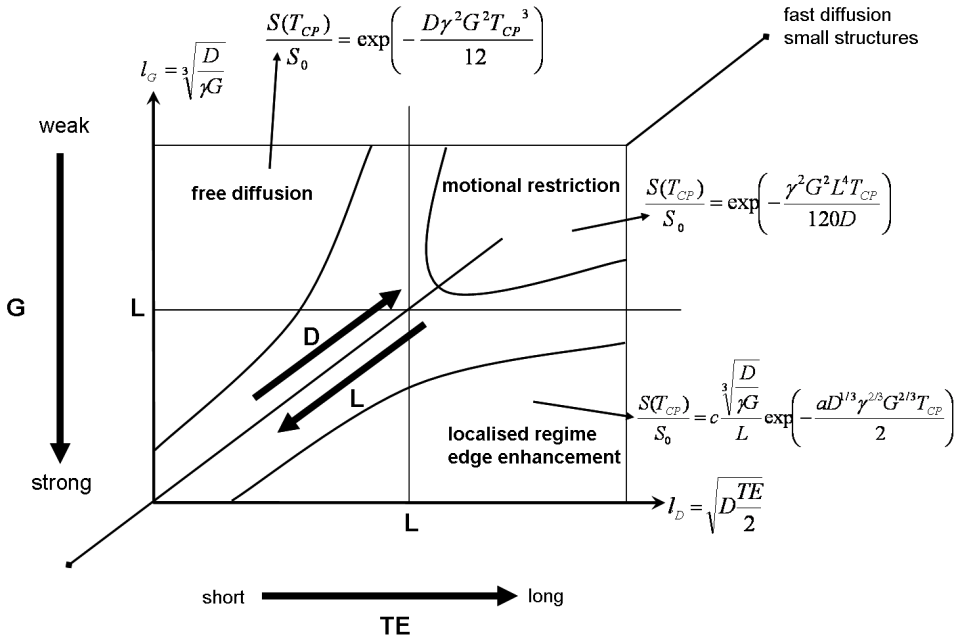


Figure 5.8: Different diffusion regimes in a 1D enclosed space in an uniform gradient G [128]: the regions where the three described regimes exist are depicted as a function of the parameters $l_D$, $l_G$ and L.

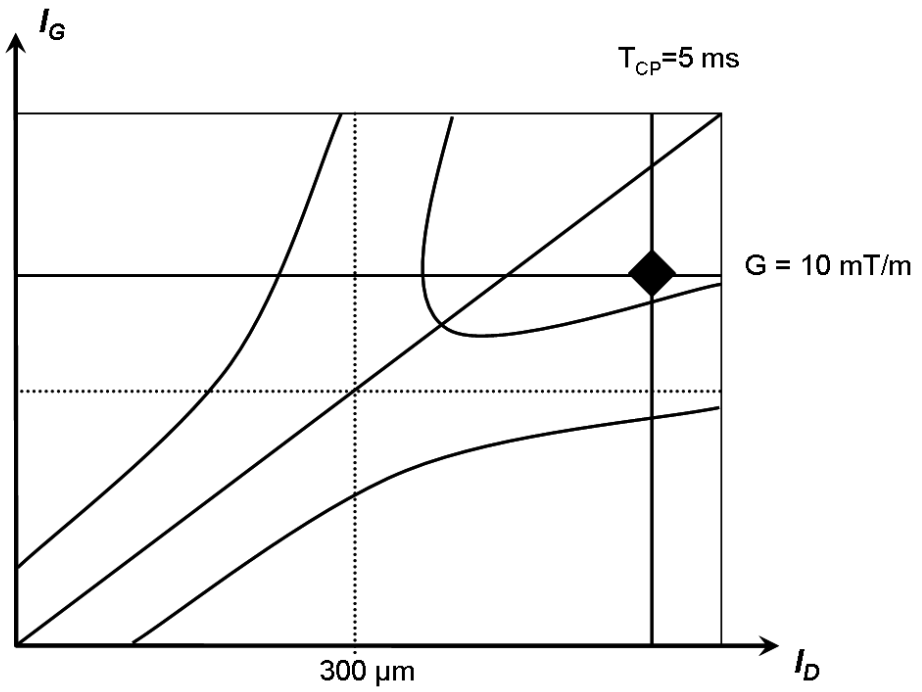


Figure 5.9: Diagram of $^3$He diffusion in $^4$He inside the lung, derived from [128] (5.8): for the inter-echo time and gradients used in this work, the diagram predicts a motional averaging regime.

**Restricted diffusion in a non uniform gradient**

Up to this point we only considered the case of a uniform gradient. The situation is more complex for the case of internal gradients due to the magnetic susceptibility.

Some have tried to analytically model the diffusion [138]; however, the models are very simple (in this case, a monodimensional sinusoidal variation of the field is considered) and can be far from reality.

Other authors used Monte-Carlo numerical methods to model [139]; this type of model, focused on one application, provides information only on the specific study without giving details of the general problem.

Finally Packer et.al. used a qualitative comparison between the diffusion in uniform and heterogeneous gradients [140] and found a great resemblance to reality. If the dephasing is small during the diffusion over the size of the heterogeneity, Packer suggests that there exists a motional averaging similar to the one previously described, occuring under the same conditions and with the same equation for relaxation. We can apply this

model for the internal gradients in the lung (estimated at 6 mT$\cdot$ m$^{-1}$ at 0.15 T) by considering the alveolar size $L$ as the parameter characterizing the field heterogeneity. The dephasing length for the estimated internal gradients is 0.63 mm.

Applying the Hürlimann model for the internal gradients of the lung, we obtain the diagram in Figure 5.10. At 0.15 T the conditions are fulfilled for the motional averaging to occur. This model might not be a very robust one but it gives the foundation to study the phenomena that control the signal decay in the lungs.

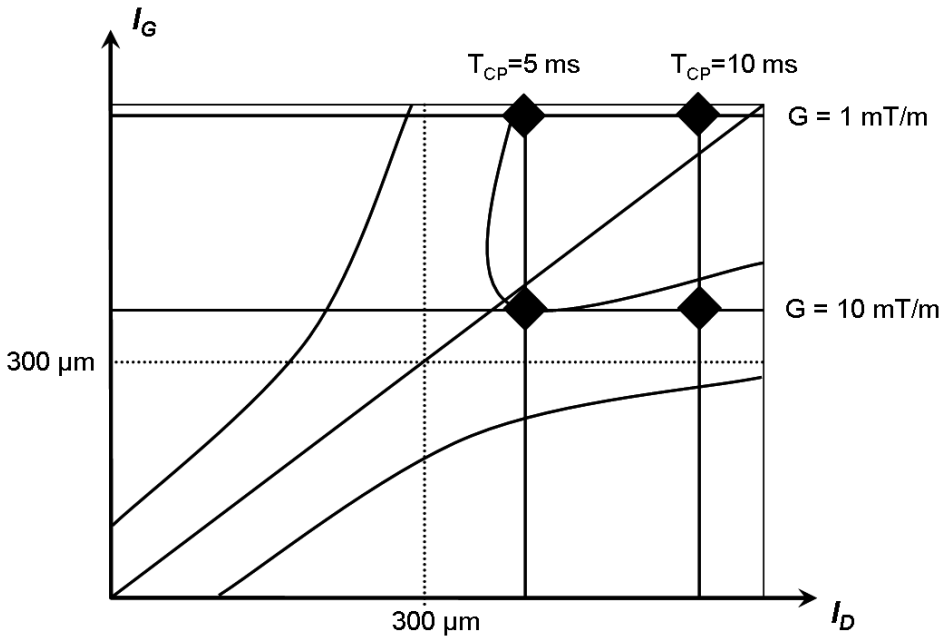


Figure 5.10: Application of Figure 5.8 to the case of $^3$He diffusion in the lung.

### 5.2.4 Summary

The combined effect of diffusion and gradients in a porous structure such as the lung is complex. There are two approaches for analyzing this effect.

The first approach implies applying the established formulas for signal attenuation and replacing the diffusion coefficient D with an apparent diffusion coefficient (ADC or D(t)). The ratio D/ADC varies depending on the time scale and the structural parameters of the lung: porosity, tortuosity and the surface-to-volume ratio. It is theoretically possible to measure these structural parameters by studying the ADC evolution depending on the

time scale of the measurement. However, due to limitations of the MRI, the surface-to-volume ratio can not be investigated in the lung.

The second approach is more analytical and was only applied to simple models (monodimensional closed cavity). It considers three regimes: free diffusion, motional averaging and the localised regime. The ratio of the three characteristic dimensions, $L$, $l_D$ and $l_G$ determines which regime occurs. For the case of the lung, considering the typical used gradients, the theory predicts the dominance of motional averaging. For the internal gradients, taking into account that the models are not very robust, at 0.15 T, it's also the motional averaging that dominates.

## 5.3 Methods for studying diffusion

$^3$He diffusion weighted MRI is a promising new technique for evaluating lung microstructure and has been demonstrated to detect alterations in lung microstructure in lung diseases such as emphysema/COPD, and bronchopulmonary dysplasia. Unfortunately, the world wide supply of $^3$He is limited and as typically performed, diffusion weighted MR imaging requires a relatively large dose (250 -500 cc) of hyperpolarised $^3$He gas, that might limit its widespread clinical utility. Alternatively, a global (non-localized) diffusion weighted spectroscopy technique which requires a very low volume of $^3$He might be a good alternative to diffusion weighted hyperpolarised $^3$He MR imaging, especially if global measurements can provide clinically useful information about the lung microstructure.

In MR imaging, the standard method for measuring D is the pulse field gradient (PFG) technique of Stejskal and Tanner. PFG techniques are very sensitive to the environment, and in the presence of restriction, yield an "apparent" diffusion coefficient or ADC, that is smaller than the free diffusion coefficient. The ADC thus provides a quantitative measure that reflects the relative difficulty with which a group of particles may move within a given environment. In healthy human lungs, the measured $^3$He ADC (0.2 cm$^2\cdot$ s$^{-1}$, observation time of 1-2 ms) is nearly a factor of 10 smaller than the free diffusion coefficient of $^3$He (1.8 cm$^2\cdot$ s$^{-1}$).

During this work there were three methods used for studying diffusion. This section will present technical aspects of these sequences and how they were implemented in practice. There will be also details on data analysis.

### 5.3.1 Spin echo diffusion weighted sequence

This method was well established during the work of Waters [107] so, was the first to be used in this work.

The RARE sequence is well suited to measuring global ADCs and ADC profiles. It consists of a 90° RF pulse followed by a train of 180° pulses. Between the RF pulses an incremented phase encode lobe and a read out gradient lobe are applied to acquire data from the whole of *k*-space in a single acquisition. If the phase gradient and slice select gradients are turned off then the positive read out gradient lobe before and after the 180° pulse act as a monopolar diffusion weighting gradient along the read direction. This reduces the signal from spins which move or diffuse but leaves the signal from stationary spins unchanged. Each read out gradient lobe increases the diffusion weighting so that the final exponentially decaying echo train represents identical profiles with incremented levels of diffusion weighting. Therefore a normal RARE sequence can be used for measuring diffusion by switching off the slice select and phase encode gradients giving a sequence similar to Figure 5.11. ADC in this case is measured from the decay of the transverse magnetisation. The experiment is sensitive to displacements during the gradient waveform that is typically several milliseconds (14 ms) in duration, corresponding to displacements of a few hundred microns. This time is limited by the short $T_2^*$ of $^3$He in lung (20 ms at 1.5 T). This diffusion coefficient is therefore denoted $ADC_{msec}$.

For data analysis, the raw data from the scanner were transferred to a dedicated computer for post processing. An updated version of a MATLAB script developed by Waters [107] was used to analyze the results. The program automatically calculates the ADC value for each selected data set, with the operator only adjusting the range of data fitting. The data set consists of a series of 64 echoes with heights that fall off exponentially due to diffusion of the helium. To measure the rate of diffusion the peak value of each echo was selected to give an exponential decay. Natural logarithms were then taken of the data

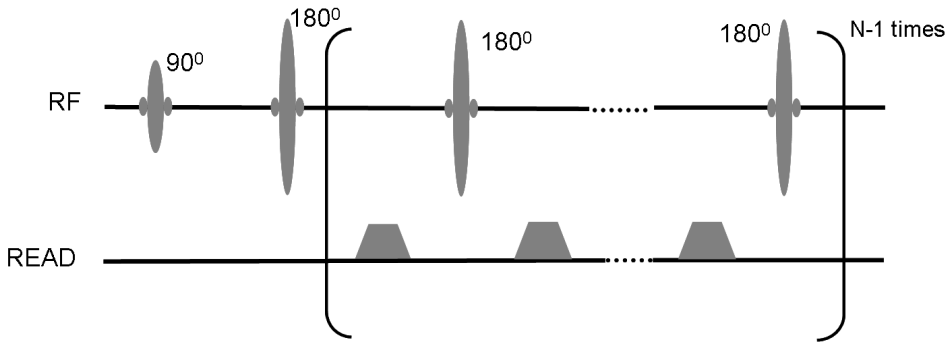


Figure 5.11: Diffusion weighted RARE sequence diagram.

to give a straight line with a gradient proportional to the apparent diffusion coefficient. This gradient was obtained by carrying out a least squares linear fit to the data. A typical output of the analyzing software is presented in Figure 5.12

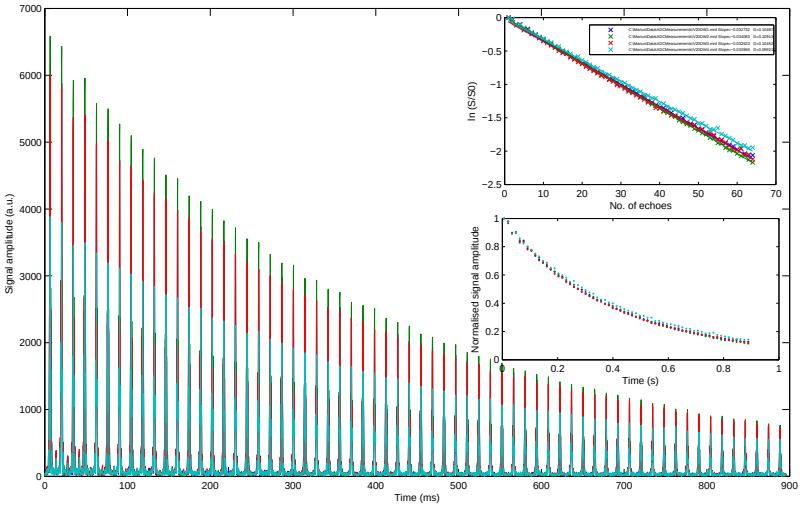


Figure 5.12: Output of the diffusion measurement software.

Some data sets did not display monoexponential decay indicating an inhomogeneous distribution of ADC. As the DW Rare data set is acquired with the Read gradient switched on each echo can be Fourier transformed to give a profile across the lungs. By selecting the same pixel from each of the 64 diffusion weighted profiles and applying the same analysis as detailed above for global ADC measurements, an ADC can be calculated for each point in the profile (5.13.

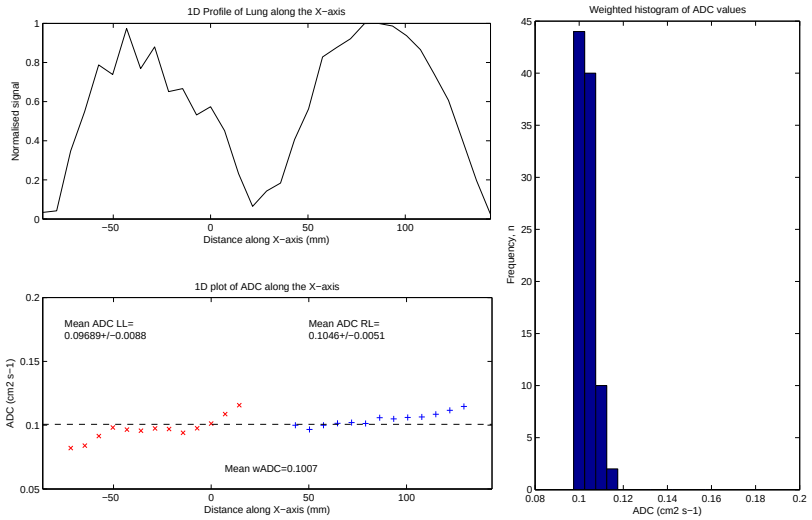


Figure 5.13: Output of the 1D profile analysis software.

### 5.3.2 SPAMM tagging method

Measuring the diffusion coefficient was demonstrated using a SPAMM tagging method [141]. This technique produces a spatial modulation of magnetisation (SPAMM) prior to imaging, by using a sequence of two nonselective RF pulses separated by a magnetic field gradient pulse (Figure 5.14).

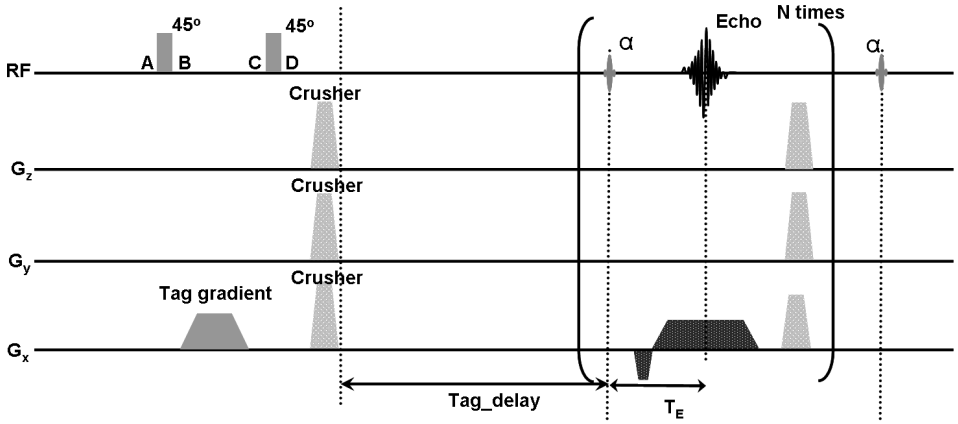


Figure 5.14: Diagram of the tagging diffusion weighted sequence. Letters mark times that are described in Figure 5.15.

Starting with a uniform longitudinal magnetisation (Figure 5.15 A), the first RF pulse turns some of the magnetisation into transverse magnetisation without changing the phase

(Figure 5.15 B). With the gradient pulse, the phase of the transverse magnetisation is spatially modulated (”wrapped”) along the direction of the applied gradient (Figure 5.15 C). The second RF pulse will mix the modulated transverse magnetisation with the longitudinal one and eventually restore the longitudinal component to its initial value since it has the same flip angle (Figure 5.15 D). The second gradient is used to spoil the remaining transverse magnetisation. The amplitude of the modulation will decrease by the time imaging starts, due to longitudinal relaxation and diffusion of the gas (Figure 5.15 E). The result is the production of bands of modulated magnetisation.

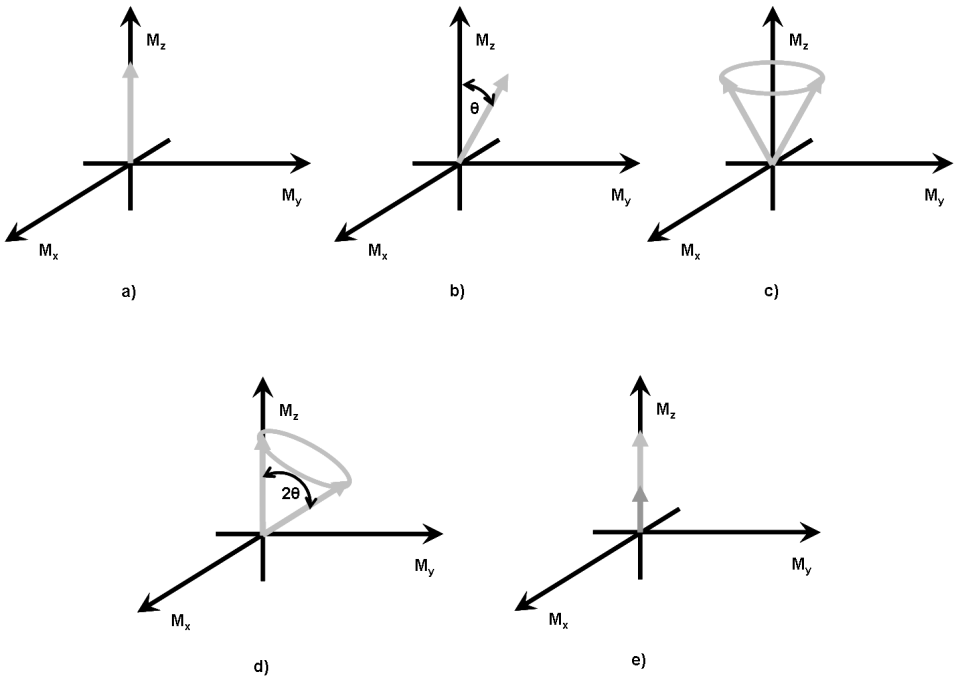


Figure 5.15: Magnetisation evolution at different times in the pulse sequence. a) Magnetisation before the modulation sequence initiation. b) Magnetisation after the first 45° RF pulse. c) Magnetisation after the modulation gradient pulse. d) Magnetisation after the second 45° RF pulse having the same value as first. e) Magnetisation before imaging (significant relaxation has occurred). [142]

The amplitude of the initial magnetisation modulation is given by the choice of tipping angle (eg. a 45° pulse produces bands of saturation at the troughs, while a 90° pulse produces bands of inversion.)

### Attenuation of the tags due to diffusion

Due to the large diffusion coefficient of $^3$He in free space (1.8 cm$^2$s$^{-1}$), the lifetime of the tags is limited. Spins with one polarity will mix with spins of different polarity which causes the macroscopic cancelation of magnetisation. The rate of this cancelation for the sinusoidally tagged magnetisation is determined by the wavelength of the modulation.

Consider the Bloch-Torrey diffusion equation in 1D:

$$\frac{d}{dt}M(\underline{x},t) = D \bigtriangledown^2 M(\underline{x},t) - \frac{M(\underline{x},t)}{T_1} \tag{5.27}$$

where D is the diffusion coefficient and $M(\underline{x},t)$ is the longitudinal magnetisation at position $x$ and time $t$. For unbounded spins, the analytical solution is found to be a Fourier series:

$$M(x,t) = \int_{-\infty}^{\infty} M_k(0)\exp(-k^2Dt)\exp(-t/T_1)\exp i(kx+\phi)dk \tag{5.28}$$

where $k = \frac{2\pi}{\lambda}$ is the spatial frequency, $M_k(0)$ is the initial amplitude of the magnetisation corresponding to the harmonic, $k$, and $\lambda$ is the wavelength.

In the case where the modulated magnetisation is a sinusoid, the effective amplitude of magnetisation will decay exponentially in time:

$$M_k(t) = M_k(0)\exp(-k^2Dt)\exp(-t/T_1) \tag{5.29}$$

In the case of hyperpolarised $^3$He in the lungs we can correct for or ignore $T_1$ since it is in the order of tens of seconds, and hence, the decay of tags is exponential in time with a rate $-k^2D$.

### Implementation and data analysis

The tagging of longitudinal magnetization is limited by the longest relaxation time in the spin system, $T_1$ which allows diffusion over much greater times and distances to be probed. Therefore, this diffusion coefficient is denoted $ADC_{sec}$.

Measuring diffusion using this method implies using a sequence that has a tagging part followed, after a certain delay, by any imaging sequence. First we used a RARE sequence

to image the tags. Since the sequence uses a 90° pulse to tip all magnetisation in the XY plane it is not possible to image the tags more than once. A fresh bag of hyperpolarised $^3$He is needed for each delay time. This method proved to be inefficient for clinical studies due to the large quantities of $^3$He needed. Even if the ADC is calculated by fitting the tag decay with only two points, our standards of time and gas quantity were not met.

The only viable solution to overcome the above mentioned constraints was the use of a 1D FLASH sequence to image the tags as they decay. The idea is to disable the phase encoding so every line in the *k*-space represents the modulated magnetisation of the entire lung at different times. Considering there were $N$ lines acquired, the tags are allowed to decay for a period of time equal to $N \cdot TR$, where $TR$ is the repetition time. Generally, 32 lines were acquired with a TR of 400 ms giving a total time of 12.8 s. A relatively large tipping pulse (18°) had to be used to image in order to get a high SNR needed for high accuracy ADC calculation. This reduces the SNR after the 15th line. It is why the fit was done using only the first 15 points from the decay.

In order to maximize the diffusion effect introduced by the tags the wavelength has to be small; 1.6 cm is a typical value for the experiments described in this work. The size of wavelength is inversely proportional to the size of the wrap gradient. For a gradient pulse of amplitude $G$ and effective duration $t$, $\lambda$ is given by $\gamma G \lambda t = 2\pi$. Given the maximum available gradient strength for our system, the minimum wavelength that can be obtained is 0.3 cm. Especially for small wavelengths the number of samples needs to be large (128 or 256) in order to have well defined stripes. The data is padded with zeros up to 2048 sample points for extra accuracy in tags analysis.

Data analysis consists in isolating the stripes and finding the peaks and troughs, and the average magnetisation for each wavelength. The ratio of the distance between the peak and trough and the average value of the magnetisation is plotted against time. These are fitted to a monoexponential decay to determine the decay rate and then the diffusion coefficient. The procedure automatically excludes pixels that are outside the lung and/or of inadequate SNR. A diagram of the data analysis is shown in Figure 5.16

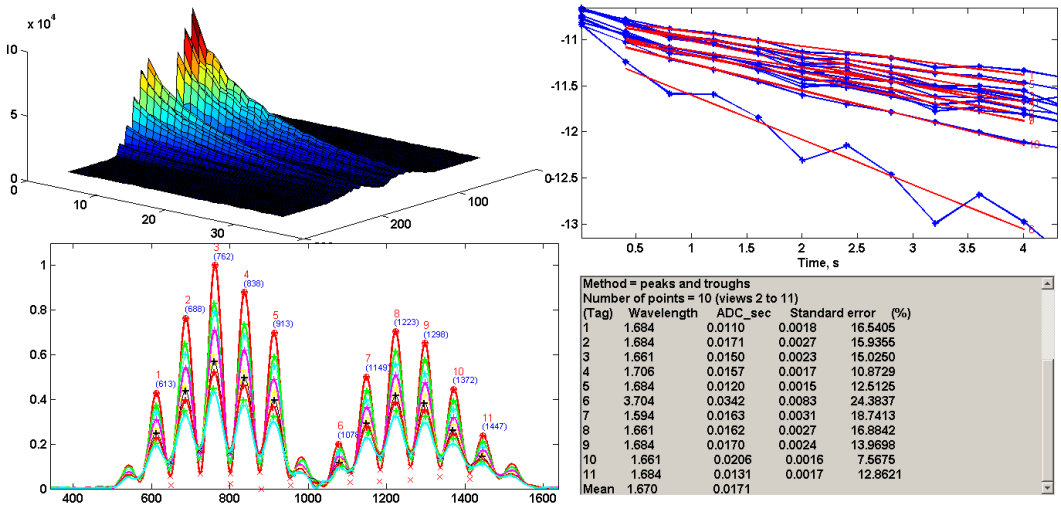


Figure 5.16: Output of the tags analyzing software.

**Results**

The aim of this method was to get a better measure of ADC by directly measuring the gas molecule displacement within the voxel. The method was hard to implement for routine use in the clinical study because it needs a great amount of magnetisation that was not always achieved. The results available from the study group are shown in Section 5.4.2.

Here are presented the results of an experiment ran on the same healthy volunteer in order to check how is ADC varying with wavelength ($\lambda$). Since $\lambda$ is related to diffusion time this is also an indication of how ADC changes with time. The idea behind the experiment was to probe if a SPAMM technique with a really short diffusion time (i.e. short $\lambda$) could get ADC values closer to the ADC$_{msec}$ obtained using the spin echo diffusion weighted sequence.

A set of 33 values of the ADC$_{sec}$ for wavelength ranging from 0.4 cm to 10 cm was recorded on a healthy volunteer. The results are presented in Figure 5.17.

### 5.3.3 MR diffusion spectroscopy sequence

Global diffusion studies by Owers-Bradley et. al have looked at multi b-value diffusion in human lungs, albeit at lower b-values (0.3 s/cm$^2$) by utilizing the mono-exponential model [107]. However, in a heterogeneous structure, such as the lung, this assumption

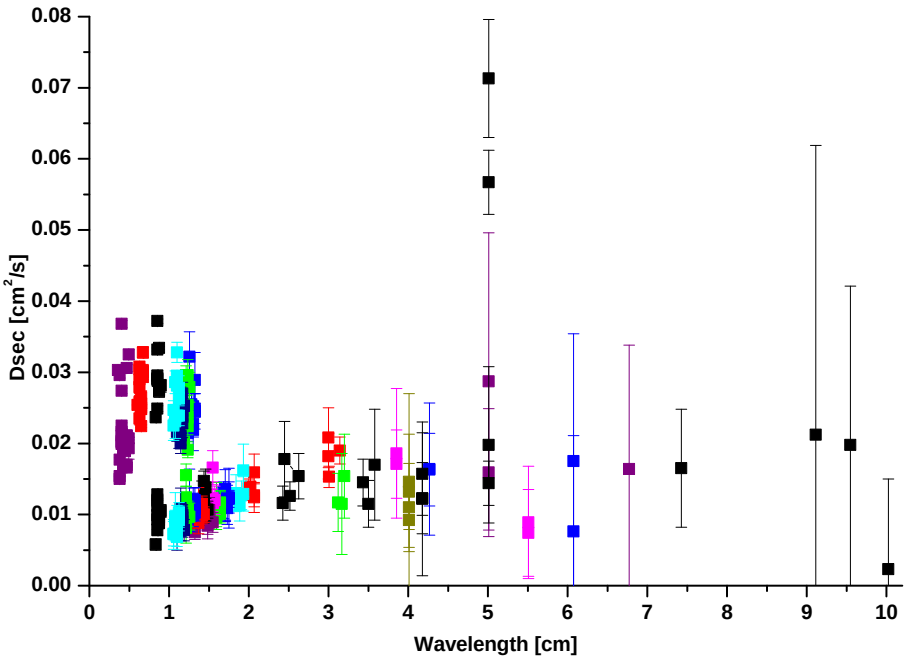


Figure 5.17: ADC $_{sec}$ variation with wavelength. At very short $\lambda$ the diffusion coefficient tends to be higher.

is no longer valid [82]. Yablonskiy et. al demonstrated this non-monoexponential nature by increasing the number of sampled points along the diffusion curve from two to six, increasing the sampled portion of the diffusion curve, and analyzing the data assuming a regular geometrical structure of the lung [143]. The result was a dataset that was distinctly non-monoexponential for healthy adults. Fichele et. al [144] also showed show that the apparent diffusion coefficient (ADC) is a function of diffusion time and gradient strength, and suggests diffusion is locally anisotropic.

The strategy described in this section is also a global diffusion measurement gADC of hyperpolarised $^3$He where the diffusion curves are densely sampled and nearly the entire dynamic range of the curve acquired.

### Sequence Design

The gADC data were collected using the pulse field gradient technique. A non-selective 900 $\mu s$ Gaussian RF pulse was used for spin excitation. Diffusion weighting was accomplished by applying trapezoidal bipolar diffusion gradients along the x axis (right-left).

The timing parameters for the diffusion sensitizing gradient are presented in Figure 5.18.

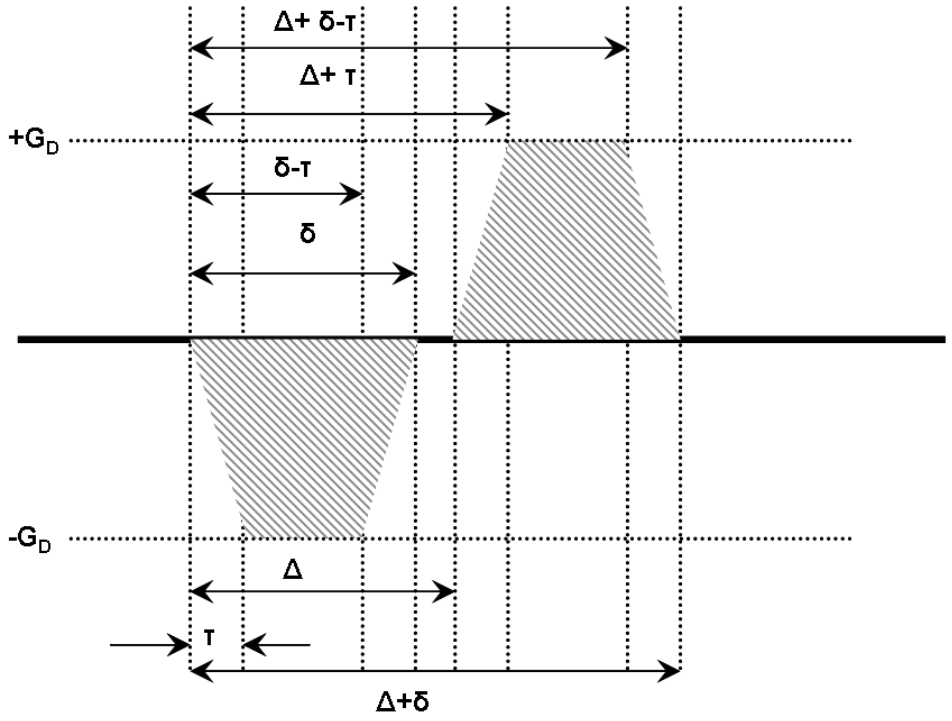


Figure 5.18: Timing parameters for the diffusion sensitizing gradient.

The sequence is divided into blocks. Each block consists of four discrete diffusion weighted signal acquisitions along the x-axis, and one block of single non-diffusion-weighted signal (b-value = 0 s/cm$^2$). The b-value was varied by changing the strength of the diffusion sensitizing gradients $G_D$, where the b-value for trapezoidal gradient waveform given by (see Table 3.7):

$$b_{trapezoid} = \gamma^2 G_D^2 \left[ \delta^2 \left( \Delta - \frac{\delta}{3} \right) + \frac{\tau^3}{30} - \frac{\delta \tau^2}{6} \right] \tag{5.30}$$

where, $\gamma$ is the gyromagnetic ratio of the observed nuclei, $\tau$ is the ramp time of gradient, $\delta$ is the duration of one lobe of the bipolar gradient and $\Delta$ is the diffusion time. Every block is repeated 10 times (Fig. 5.19), to yield a total of 50 FIDs. The diffusion gradient amplitude was logarithmically sampled for 40 of the FIDs and for the remaining 10 was set to zero. As described below, these latter acquisitions were used to correct for the effects of $T_1$ relaxation and RF depletion The diffusion gradient parameters, were: $\tau$ = 0.15 ms, $\delta$ = 4.7 ms and $\Delta$ = 5.2 ms. Since the hyperpolarized magnetization de-

creases throughout the scan, the b values were ordered from highest to lowest to maximize the signal-to-noise ratio for the most strongly diffusion-weighted signals. The diffusion weighted signals were acquired with gradient amplitudes ranging from 16.5 mT/m to 0 mT/m, with the corresponding b-values from ranging from 50 s/cm$^2$ to 0.006 s/cm$^2$. The data acquisition was started after a 500 $\mu$s ringdown time, at the end of the bipolar diffusion gradient. Repetition time was fixed at 200 ms with spectral bandwidth of 12.5 kHz and 2048 sample points. At the end of the acquisition, a set of bipolar crushers (5 ms duration , 11 mT/m amplitude) were applied on all axes to depolarise any residual transverse magnetization after signal acquisition.

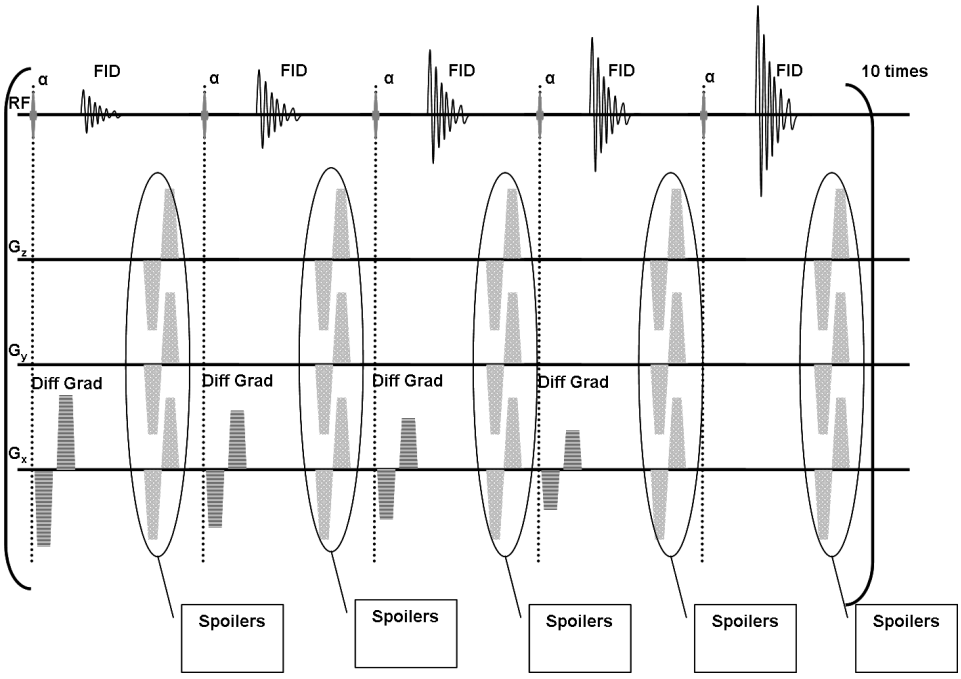


Figure 5.19: Diagram of the diffusion spectroscopy sequence.

**$T_1$ and tipping angle attenuation correction** The resulting FIDs have non-recoverable longitudinal decay due to $T_1$ relaxation time and RF time. It is necessary for diffusion measurements to be corrected for these effects, otherwise the gADC measurements will be underestimated. The detected signal from a series of n RF pulses of constant flip angle ($\tau$), constant TE, and constant TR for a $^3$He diffusion experiment is given by [105]:

$$S_{xy}(n) = S_{DW}(n)\left[\cos\tau \exp\left(-\frac{TR}{T_1}\right)\right]^{n-1} \tag{5.31}$$

where,

$$S_{DW}(n) = f_n(D)S_z(0)\sin\tau \exp\left(-\frac{TE}{T_2^*}\right) \tag{5.32}$$

where $S_{DW}(n)$ are the diffusion weighted signals, $f_n(D)$ is the DW after $n^{th}$ RF pulse, $T_2^*$ is the apparent transverse relaxation time, and $S_z(0)$ is the signal intensity that would have been measured at time t=0 if a 90° RF pulse had been applied. Since $\cos\tau \exp\left[-\frac{TR}{T_1}\right]$ is constant for the given experimental conditions, equation 5.31 can be rewritten as:

$$S_{xy}(n) = S_{DW}(n)K^{n-1} \tag{5.33}$$

where, $K = \cos\tau \exp\left(-\frac{TR}{T_1}\right)$. The attenuation parameter K is obtained by fitting the non-diffusion-weighted signals to equation 5.33.

**Data analysis** The corrected diffusion weighted data were fit to three different models, mono-exponential, multi-exponential, and geometric using Matlab functions.

**Mono-exponential model** The mono-exponential model is the most commonly used model in hyperpolarised $^3$He diffusion imaging, even though it is known to be incorrect for diffusion in a restricted environment. The model is: $S = S_0 \exp^{-bADC}$.

**Multi-exponential model**

$$S = \sum_{n=1}^{m} S_n \exp^{-bADC_n}, m \geq 2 \tag{5.34}$$

where $S_n$ are the signal fractions obtained for the respective apparent diffusion coefficients $ADC_n$.

The data were analyzed for *m*=2 and 3.

**Geometrical model** In this model, suggested by Yablonskiy et. al. [143], the respiratory airways are modeled geometrically as cylindrical tubes embedded in alveolar sleeve (Fig. 5.20).

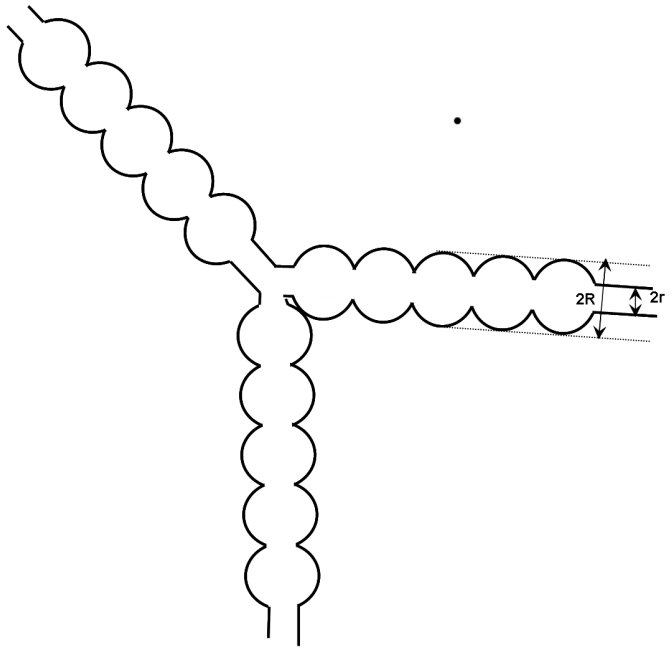


Figure 5.20: Schematic diagram of two levels of respiratory airways. Open spheres represent alveoli forming an alveolar sleeve around each airway. Each respiratory airway can be considered geometrically as a cylindrical object consisting of a tube embedded in the alveolar sleeve. The diagram defines inner (r) and outer (R) radii [21].

The signal decay is characterized in terms of $D_L$ and $D_T$, the ADC along and perpendicular to the long axis of the cylinder. The signal expression is given by,

$$S = S_0 \exp(-b\overline{D}) \left(\frac{\pi}{4bD_AN}\right)^{1/2} \exp\left(\frac{bD_AN}{3}\right) \Phi[(bD_AN)^{1/2}] \tag{5.35}$$

where $\Phi(x)$ is the error function, and the quantities $\overline{D}$ and $D_AN$

$$\overline{D} = \frac{1}{3}D_L + \frac{2}{3}D_T, D_AN = D_L - D_T \tag{5.36}$$

represent the mean ADC and the anisotropy of ADC, respectively.

A diagram of the analyzing software is depicted in Figure 5.21.

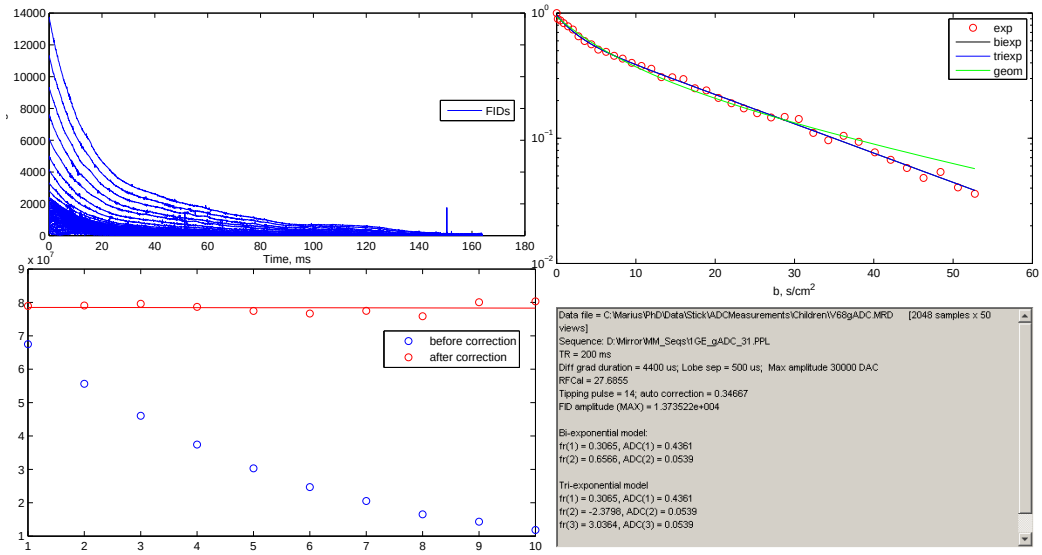


Figure 5.21: Output of the gADC analyzing software.

## 5.4 Lung development in children

The methods described in the previous sections were developed as part of a lung development study on children. This study was aimed at identifying changes in specific lung parameters in different groups of young children. A description and size of the groups is given in Table 5.4.

This section will describe in detail the methodology and the results of the tests performed in this laboratory in correlation with the lung function measurements performed in Leicester University Hospital. These methods were described in Appendix A.

### 5.4.1 Method

Subjects from the control group were recruited amongst children born at term, with no recorded illnesses, from a group in the Leicester area (called the Leicester cohort) monitored since birth. The preterm subjects are born between 24-36 weeks of gestation, some of them being very premature born. The actual treatment in this situation consists of oxygen therapy for the baby after the birth and steroids for the mother plus surfactants for baby, before birth. All these methods are potentially harmful to the lung and could cause changes in structure.

Table 5.4: Population distribution within the groups.

| Group | Description | Boys | Girls | Total |
|---|---|---|---|---|
| control | completely healthy individuals (11-12 years old) | 13 | 10 | 23 |
| preterm | 11-12 years old extreme preterms with chronic lung disease - oxygen dependent to 36 weeks | 5 | 3 | 8 |
| preterm2 | 11-12 years old extreme preterms who were oxygen dependent to 4 weeks postnatal | 4 | 3 | 7 |
| preterm3 | 11-12 years extreme preterms who were not oxygen dependent to 4 weeks postnatal | 1 | | 1 |
| preterm4 | 11-12 years old moderate preterm | 2 | 5 | 7 |
| 12-14 healthy | 12-14 years old control group | 8 | 9 | 17 |
| 12-14 test | 12-14 years old with risk factors(low birth weight, maternal smoke and viral wheeze in the past) | 3 | 4 | 7 |
| | TOTAL | 36 | 34 | 70 |

In general all PFTs are performed before starting the MR experiments, in the Leicester laboratory. At least an FEV1 measurement is necessary in order to comply with the safety regulations for this kind of study.

The MR procedure for volunteers is as follows. First, there are two or more trials with a bag of air to allow the child to practice the technique of breathing in the sample. After a magnetic safety check, the subject is positioned inside the magnet with the $^3$He coil around their thorax. A second test is run to identify if the person is claustrophobic or not and to measure the noise induced by the presence of the body. This will be eventually subtracted before calculating ADC. The tests are run by two persons; one is producing and transporting the hyperpolarised $^3$He gas and initiates the acquisition; the other is delivering the gas and instructing the subject. The operator loads the sequence, collects the gas, transports the $^3$He to the scanner room, passes the gas to the other person who then helps the subject handle the Tedlar bag. Once the subject inhaled all the gas (cca. 350 ml), the operator presses the gating button next to the magnet. The procedure is repeated up to four times depending on subject cooperation. It takes approximately 5 minutes between two scans so usually the subject is kept outside the magnet and is positioned inside just before scan. This is to prevent any claustrophobic manifestations from the subject. The magnet has a large bore and is well illuminated to minimize this complication. Only one subject was claustrophobic and was impossible to continue scanning after the second run.

A set of diffusion measurements using the RARE method was acquired for each individual. The tagging and MR spectroscopy method was also used for some of the volunteers. At the time of writing, there were only five subjects that had a complete set of measurements (i.e. RARE, tagging, MR spectroscopy) as these techniques were under development.

### 5.4.2 Results

#### Spin echo diffusion weighted method

A histogram of the ADC distribution within the subjects is depicted in Figure 5.22.

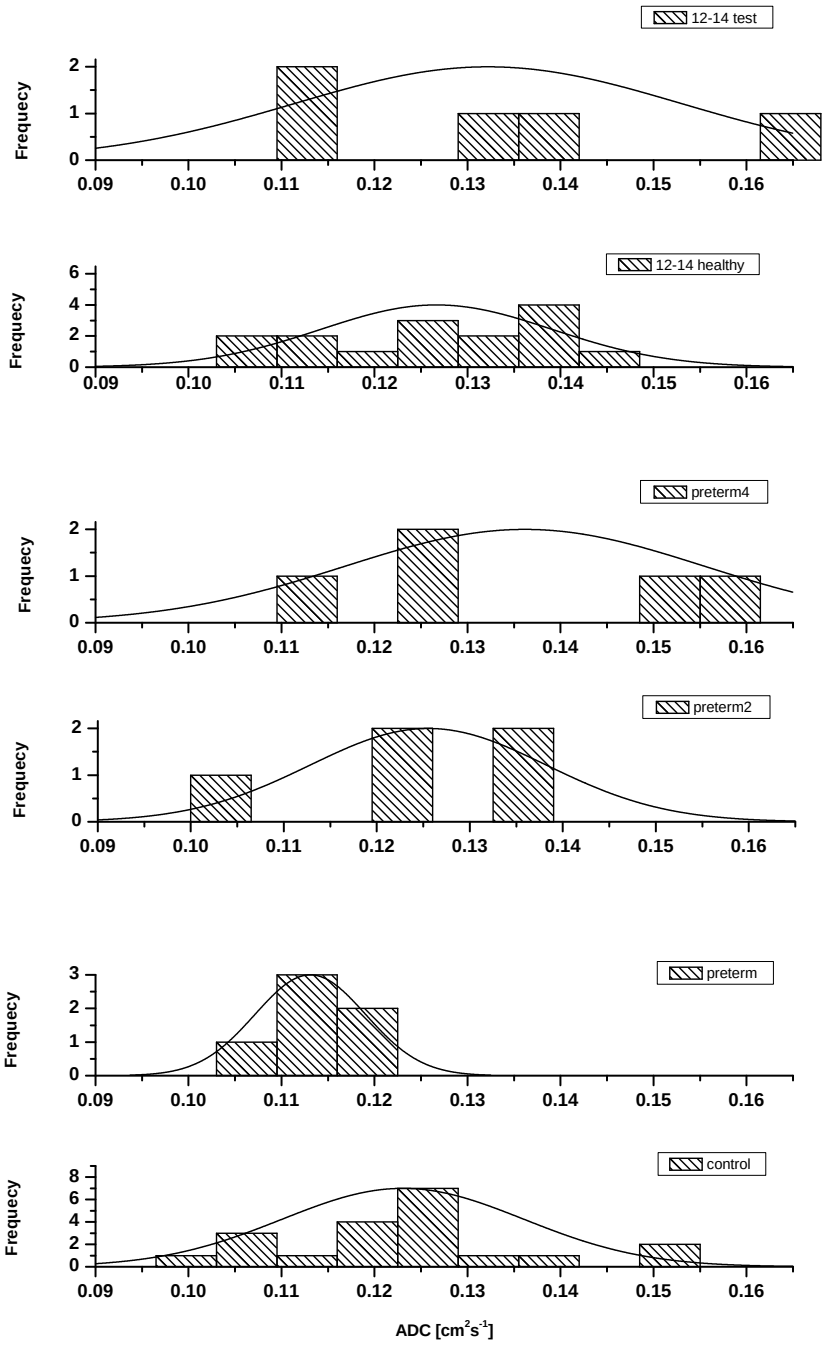


Figure 5.22: Distribution of the ADC values within the groups.

There is a wide range of ADC values in these subjects, ranging from 0.1007 $cm^2.s^{-1}$ to 0.1630 $cm^2.s^{-1}$ with the mean 0.1252 $cm^2.s^{-1}$. One of the subjects from Waters's study was used as reference and his ADC was periodically measured to check the robustness of the results.

There is a series of graphs that shows the ADC values against some important lung function parameters such as FRC, FEV1, FVC, TLC, FEV1/FVC, and the values from the multi breaths Nitrogen wash-outs ($S_{cond}$ and $S_{acin}$). In Figure 5.23 there is a plot of ADC against a) TLC, b) FRC, c) FEV1 and d) FEV1/FVC. The FEV1/FVC ratio is smaller for the majority of the preterms. There is no correlation of the ADC value with the BMI (Body Mass Index) or FVC indicating that ADC is not related to the size of the lung (Figure 5.24).

Figure 5.25 shows no relevant correlation of ADC with $S_{cond}$ or $S_{acin}$.

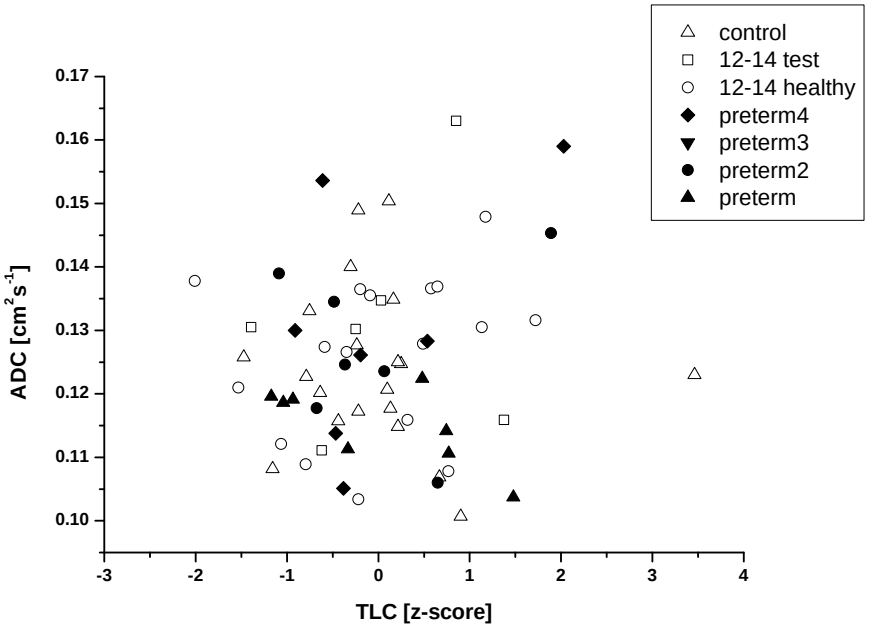
control
12-14 test
12-14 healthy
preterm4
preterm3
preterm2
preterm
ADC [cm$^2$s$^{-1}$]
TLC [z-score]
0.17
0.16
0.15
0.14
0.13
0.12
0.11
0.10
-3
-2
-1
0
1
2
3
4

(a) TLC

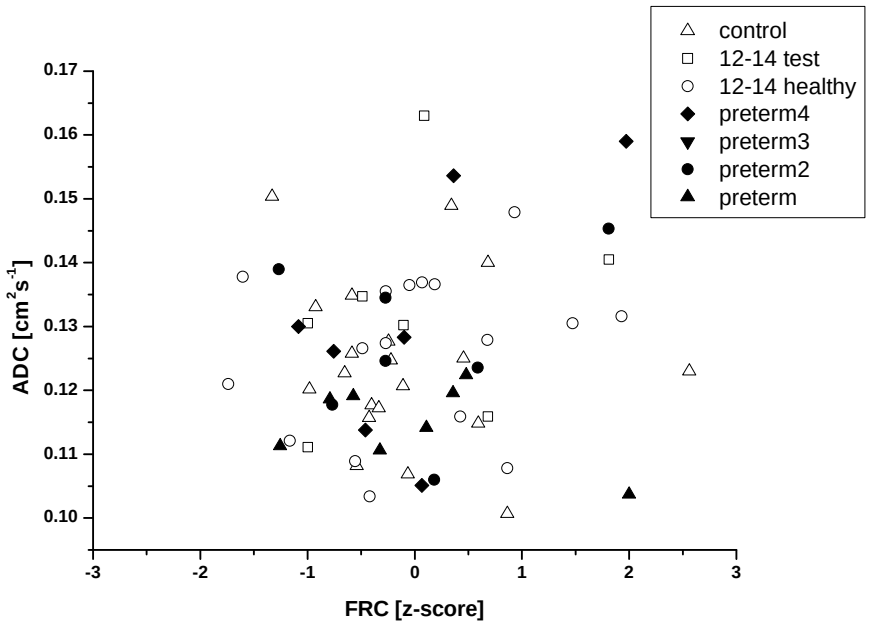
control
12-14 test
12-14 healthy
preterm4
preterm3
preterm2
preterm
ADC [cm$^2$s$^{-1}$]
FRC [z-score]
0.17
0.16
0.15
0.14
0.13
0.12
0.11
0.10
-3
-2
-1
0
1
2
3

(b) FRC

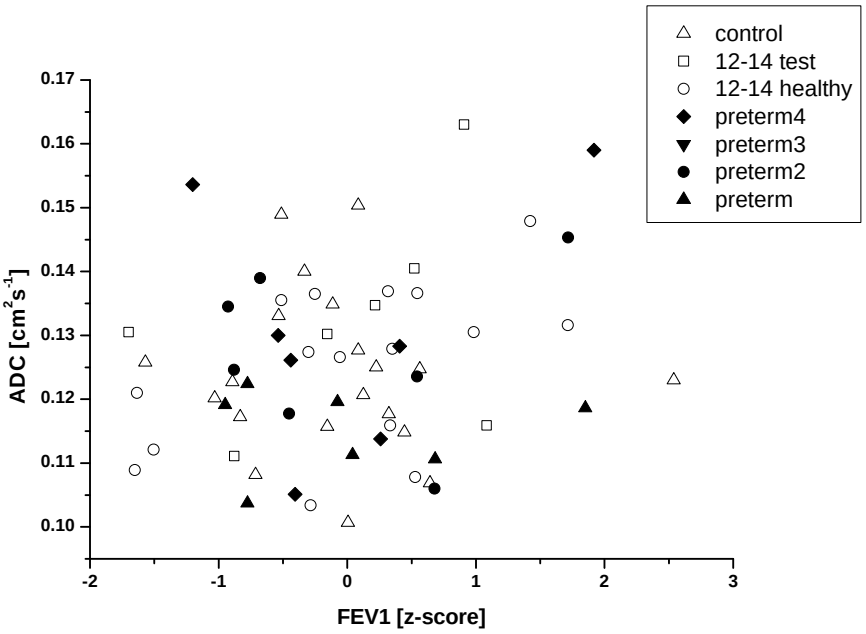


(c) FEV1

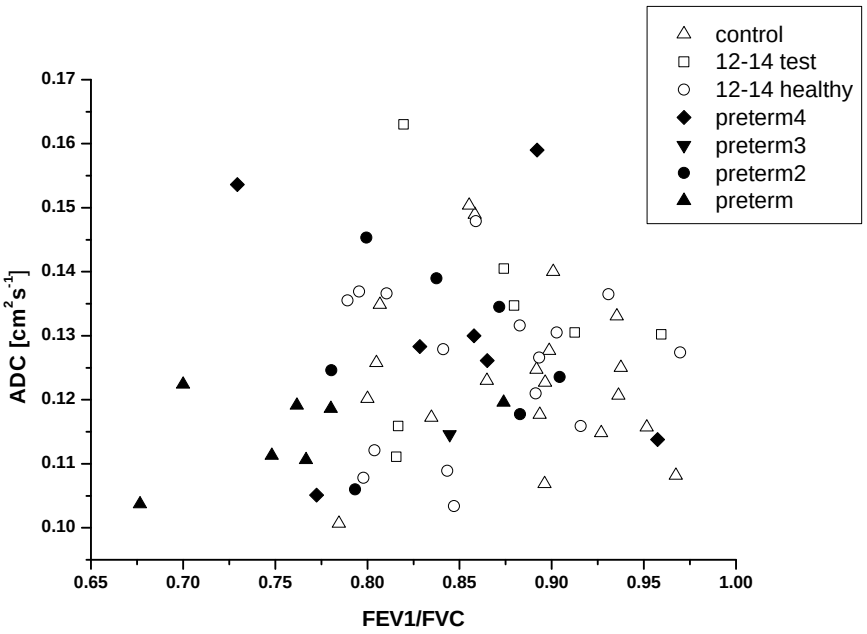


(d) FEV1/FVC

Figure 5.23: ADC against Pulmonary Functional Tests.

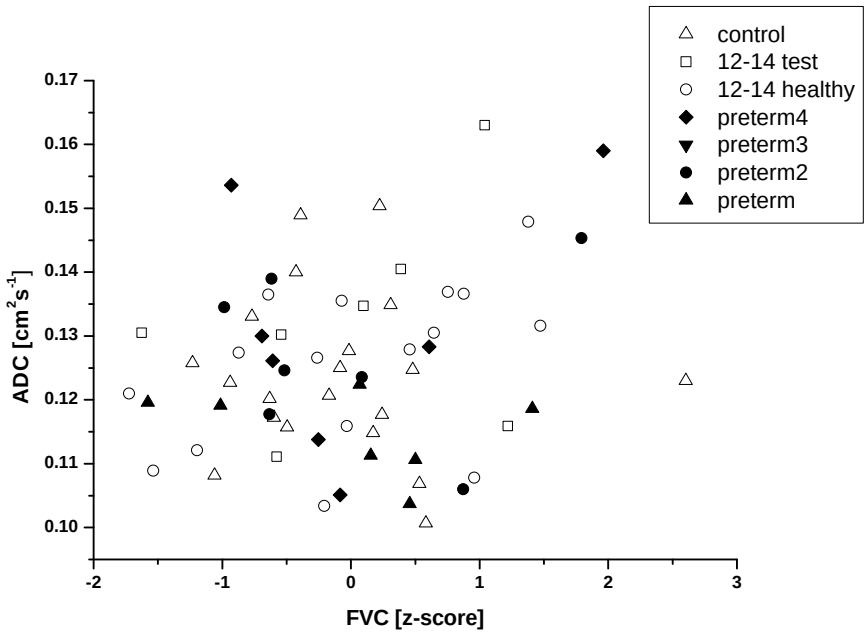


(a) FVC

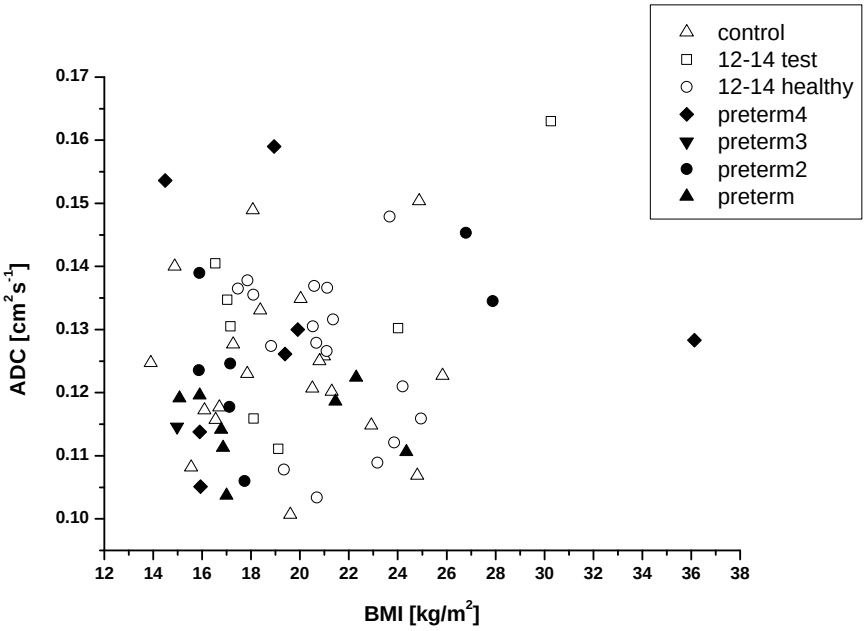


(b) BMI

Figure 5.24: ADC against BMI and FVC.

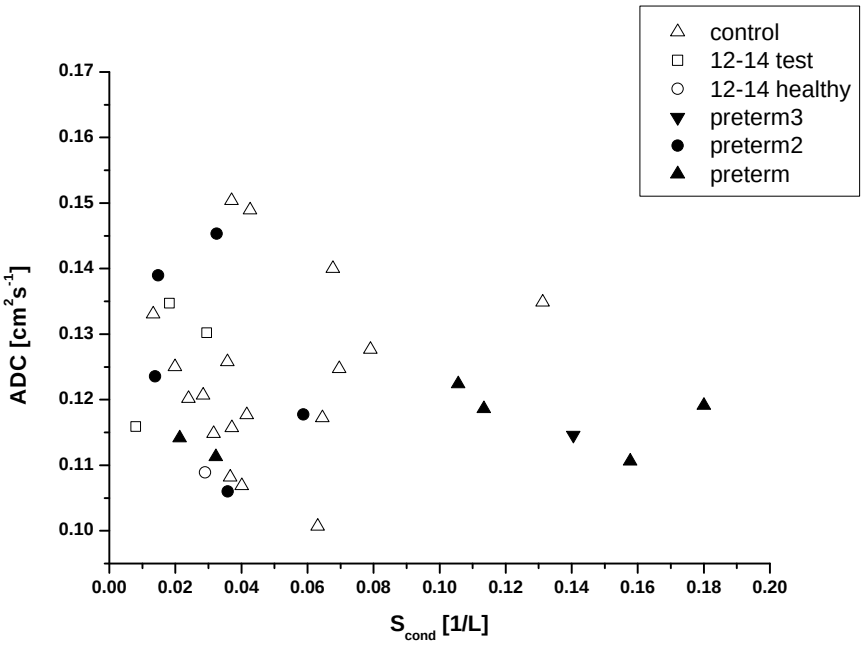


(a) $S_{cond}$

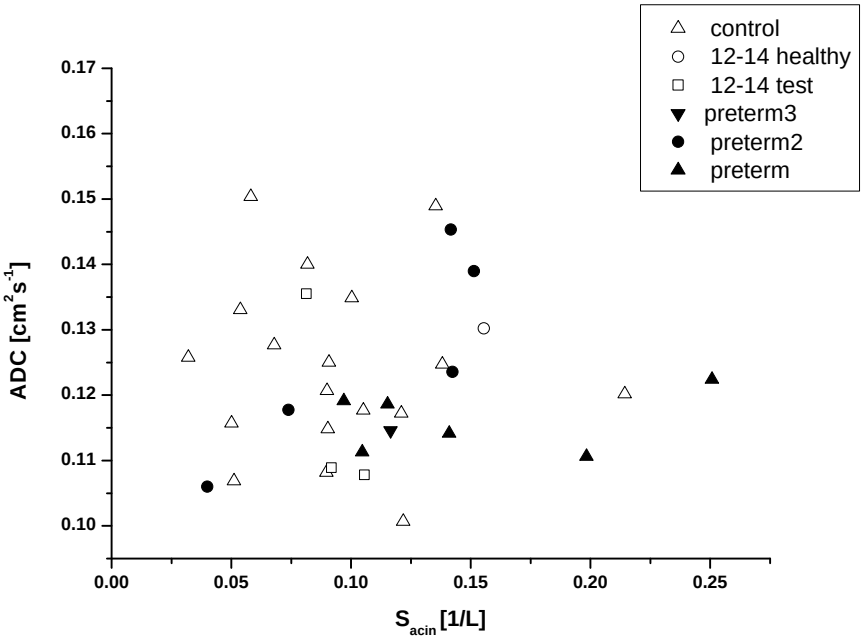


(b) $S_{acin}$

Figure 5.25: Plot of ADC vs. $S_{cond}$ and $S_{acin}$.

### SPAMM tagging method

The SPAMM tagging technique reflects more directly the gas displacement. The value is related to actual diffusion of the gas over long distances and is probably sensitive to collateral pathways. As stated previously, the method employs a great amount of magnetisation and it was difficult to use for our study. 10 of the volunteers were sampled using this method and the results are shown in Table 5.5.

Table 5.5: Value of the $ADC_{sec}$ measured on 10 volunteers. The results are mean values. Lambda was set to 1.7 cm.

| Volunteer ID | Group | $ADC_{sec}$ LL [$cm^2s^{-1}$] | $ADC_{sec}$ RL [$cm^2s^{-1}$] |
|---|---|---|---|
| V44 | 12-14 healthy | 0.00754 | 0.00786 |
| V46 | 12-14 healthy | 0.00699 | 0.00769 |
| V47 | 12-14 healthy | 0.00617 | 0.00571 |
| V49 | 12-14 test | 0.01513 | - |
| V51 | 12-14 healthy | 0.01213 | 0.01107 |
| V52 | 12-14 healthy | 0.0049 | 0.00523 |
| V53 | 12-14 healthy | 0.00625 | 0.00865 |
| V54 | 12-14 healthy | 0.00413 | 0.00283 |
| V55 | 12-14 healthy | 0.00683 | - |
| V69 | preterm3 | 0.00682 | - |

### MR diffusion spectroscopy sequence

Table 5.6: Value of the gADC according to Yablonskiy's geometrical model measured for the study group. $T_1$ inside the lung is also shown for most of the volunteers.

| Volunteer ID | Group | D [$cm^2s^{-1}$] | D(AN) [$cm^2s^{-1}$] | D(L) [$cm^2s^{-1}$] | T | SO | $T_1$ [s] |
|---|---|---|---|---|---|---|---|
| V48 | 12-14 test | 0.0660 | 0.1430 | 0.1613 | 0.0184 | 0.9565 | |
| V49 | 12-14 test | 0.1264 | 0.3120 | 0.3345 | 0.0224 | 1 | 26.9 |
| V51 | 12-14 healthy | 0.1029 | 0.2657 | 0.2800 | 0.0143 | 0.8370 | 50.6 |
| V52 | 12-14 healthy | 0.0919 | 0.2076 | 0.2304 | 0.0227 | 0.9568 | |
| V53 | 12-14 healthy | 0.0976 | 0.2127 | 0.2394 | 0.0267 | 1.0204 | 36 |
| V58 | 12-14 healthy | 0.0810 | 0.2603 | 0.2546 | -0.0058 | 0.9831 | |
| V59 | preterm4 | 0.1071 | 0.2761 | 0.2912 | 0.0150 | 0.8758 | 29.6 |
| V60 | preterm4 | 0.0394 | 0.0568 | 0.0773 | 0.0205 | 0.6464 | 33.3 |
| V63 | 12-14 test | 0.0955 | 0.2075 | 0.2338 | 0.0263 | 0.9804 | 17.8 |
| V64 | 12-14 test | 0.0645 | 0.1962 | 0.1954 | -0.0009 | 0.9265 | |
| V65 | preterm4 | 0.1029 | 0.2489 | 0.2689 | 0.0200 | 0.9647 | 37.3 |
| V66 | preterm4 | 0.0797 | 0.2419 | 0.2409 | -0.0009 | 0.9507 | |
| V67 | preterm4 | 0.1351 | 0.3310 | 0.3558 | 0.0247 | 0.9754 | 19 |
| V68 | preterm2 | 0.1224 | 0.2929 | 0.3177 | 0.0248 | 0.9341 | 24.7 |
| V69 | preterm3 | 0.0841 | 0.2151 | 0.3110 | 0.0124 | 0.9736 | |
| V70 | 12-14 healthy | 0.1171 | 0.2909 | 0.3110 | 0.0201 | 1.0026 | 36 |

This method put no stress on the volunteers and on the magnetisation size so it was available for more volunteers. The results are presented in Table 5.6. The output of this technique is a set of numerous parameters described in Section 5.3.3.

### 5.4.3 Discussion

This study was based on the following hypothesis:

- Children are supposed to have a smaller ADC value compared to adults.
- ADC in preterms is higher than in children born at term because they have less number of enlarged alveoli.

The results presented in the previous sections were not envisaged when starting this study.

The ADC values for these children are higher than expected. The wide range of values may be correlated with the fact that they are in different stages of puberty when the thorax is growing faster than the lungs and the alveoli are enlarged due to the traction exercised by the rib cage [145].

We found volunteers with inhomogeneous ADC distribution across the lungs. Running a 1D analysis on the data is possible to measure the inter- and intra-lung ADC distribution. A comparison between a typical and inhomogeneous ADC distribution is shown in Figure 5.26.

This distribution pattern is more evident in girls (see Fig. 5.27).

We are using the same protocol and method for measuring the ADC as Waters et al. [146] and a subject from his study is used as reference. It is hard to believe the methodology is wrong since this method was successfully used in the above mentioned study on people aged 18 to 74 years. As for the similar ADC values in pre terms and control subjects this is clearly an independent fact since all subjects undergo the same procedure.

- ADC for normal and preterms show no difference; in fact preterms are less scattered.

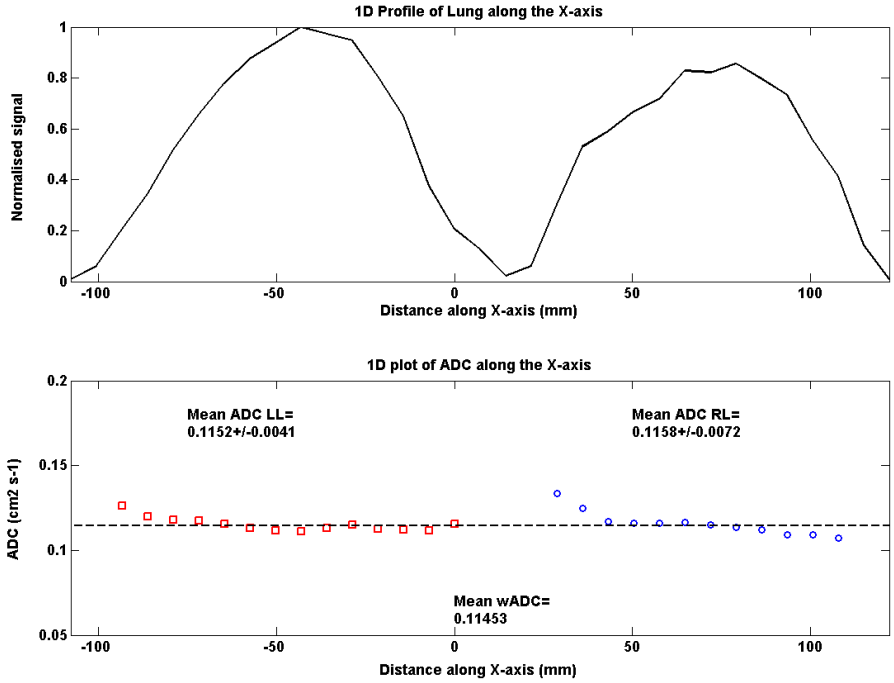


(a) Typical ADC distribution across the x-axis of the lung

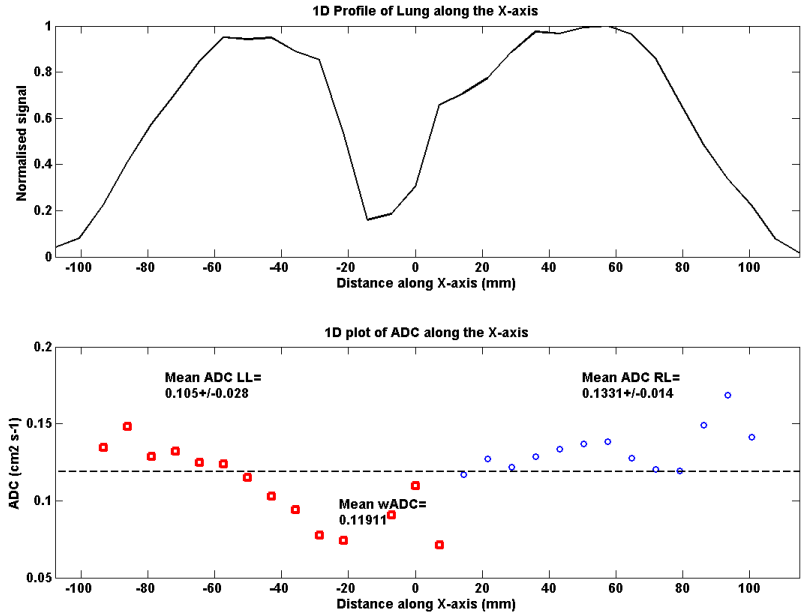


(b) Heterogeneous ADC distribution across the x-axis of the lung

Figure 5.26: Comparison of typical (a) and heterogeneous (b) ADC distribution across the lung.

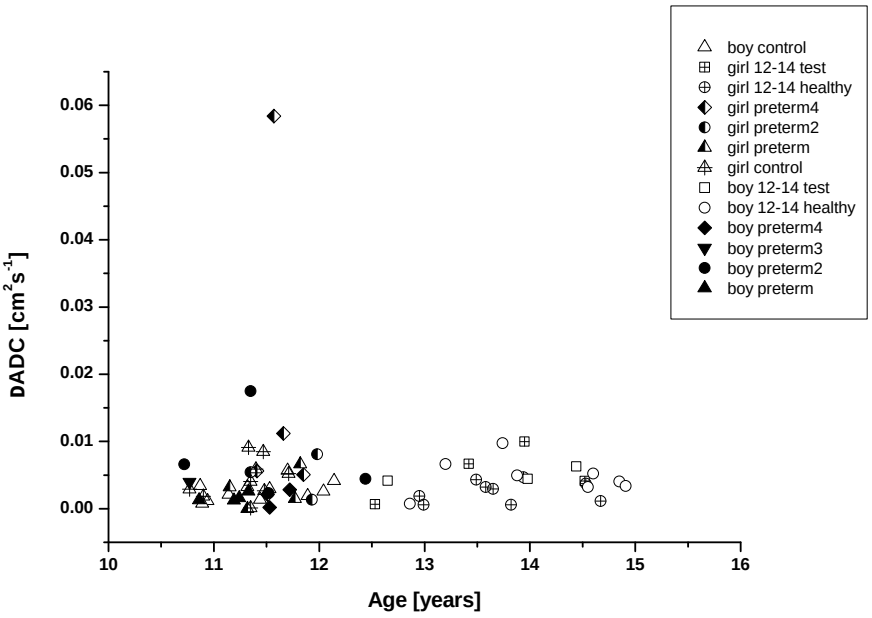


Figure 5.27: ADC variability across the lung with age and gender within the groups

- ADC vs age for children for all subjects shows very little variation.

So what does ADC measure?

We know ADC increases as volume of gas in lungs increases [107],[146]. So does simple expansion of lungs give a greater ADC increase than seen? Plotting ADC vs FRC (5.23(b)) can not distinguish between the groups.

- Preterms catch up - at least the microstructure - they may still have airways problems as suggested by the MBNW data

The suggestion is that there is alveolar number growth after age 8, up to adulthood probably. Research of Schittny et al. on rats [147] and Hyde et al. on Rhesus monkey [145] show that alveolarisation continues after birth till early adulthood. Extrapolating the rat and Rhesus monkey data to humans would mean that alveolar septa are formed until growth stops and that half of the alveolar septa are formed roughly between the age of 3 to 18 yr. This opinion was already present 30 to 40 yrs ago ([148], [149], [16]), but, for theoretical reasons, it was changed later to the present view that alveolarisation stops after microvascular maturation took place (2 to 3 yrs of age [150], [151]).

Clinically, this insight has large significance, especially for humans 3 to 18 yrs of age. Steroids are widely used during the treatment of lung diseases like asthma and wheezing illnesses or other diseases like inflammatory bowel diseases [152], [153]. Furthermore, retinoids are used for the treatment of psoriasis and severe acne [154]. In rats, both drugs are known to alter the lung structure when given neonatally or during the phase of classical alveolarisation [155],[156]. So far, there was little concern regarding possible side effects of these drugs in children and adolescents due to the view that alveolarisation is most likely already completed at this time point. Further studies are necessary to understand the influence of these drugs on the structure of the lungs during the second phase of developmental alveolarisation.

Also, there are studies available which suggest the possibility of the lung to stimulate a vigorous compensatory growth of alveolar tissue in excess of maturational lung growth, resulting in complete normalization of aerobic capacity and gas-exchange function [157].

- Tagging does not seem to correlate with $\text{ADC}_{msec}$

Probably $\text{ADC}_{sec}$ is due to lateral pathways e.g. holes of Kohn and other pores.

This study limits our understanding of what is happening with ADC before the age of 10 and after 14, till 18.

# Chapter 6

# Conclusion

Apart from being a report on the research work carried on during the last three years, this thesis intends to provide a comprehensive guide on the lung structure, physiology, pathology and means of analyzing its parameters. The work described here was divided in two main directions: first part aimed to improve the $^3$He polarisation facility and second to asses the lung micro structure by measuring diffusion.

Although there exists a strong background and know-how on building a $^3$He polarisation facility there is always room for improvement especially with the increased demand for higher polarisation and faster production. In this case the system was performing well but it was never put to real test before this research was started. Measuring the longitudinal relaxation time in three different glasses (7740 Pyrex, 1720 Corning and GE 180) and observing how the orientation of the holding magnetic field is influencing its values it was possible to get an idea about what can be changed in order to improve the production. Having in mind a system capable of providing enough $^3$He for up to six measurements in one run with minimum delays between each measurement and each run, it was obvious that the system had to be fast and to deliver high amounts of hyperpolarised $^3$He. The initial layout had a big dead volume due to the long gas path. By shortening this path the dead volume was halved. In the first configuration the peristaltic pump was also used to dispense the bags of hyperpolarised $^3$He which was introducing long delays. The use of a piston pump to fill the bags reduced the time between measurements by almost five times. This is very important when the volunteers are young children. The storage cells were

replaced by GE 180 glass cells having larger volume and the peristaltic pump was set to its maximum speed. A more powerful laser (20 W) was also used which has doubled the production rate but there were limitations induced by the compressor and optical pumping cell. These should be further improved if larger quantities of gas are required.

The study on the two categories of children: born at term and premature was the main result of this research. This was just a part of a larger study (200 children) aimed to asses the functionality of hyperpolarised $^3$He as a tool for pulmonary studies. The RARE based global measurement of diffusion that was first used showed no variation between the two categories of volunteers. Also, the values were very high for the age and very scattered. A second method using SPAMM taging was implemented and tested on children. This had the disadvantage of requiring higher magnetisation in order to reduce the error on the measurements. Even so, the analysis of the data was hard to perform on most of the volunteers. Later, a new diffusion measurement modality was tested. The MR diffusion spectroscopy sequence was relatively easy to implement and use because it did not require high amounts of signal. It was not possible to compare the groups using all three methods due to the lack of complete set of results for every volunteer. The conclusions were drawn only using the well establish RARE based method. The $\mathrm{ADC}_{msec}$ values for these children were much higher than expected. The wide range of values may be correlated with the fact that they were in different stages of puberty when the thorax is growing faster than the lungs and the alveoli are enlarged due to the traction exercised by the rib cage. There were volunteers with inhomogeneous ADC distribution across the lungs, more evident in girls. Extending this study to a longitudinal one is very important if we want to understand the high values of the ADC. If puberty is to blame then the ADC of these children should return to normal values in the next few years. The preterms had values similar to the control group, less scattered suggesting that they can catch-up - at least the microstructure. They may still have airways problems as suggested by the MBNW data. This can only be explained if alveolarisation continues after the age of 8, contrary to the current view.

To summarize, this study supports the new view on lung growth and should be continued and refined in order to be used as evidence of the continuous alveolarisation. If this is

confirmed, then it has large clinical significance. So far, there was little concern regarding possible side effects of steroids, used to treat asthma, in children and adolescents due to the view that alveolarisation is most likely already completed at this time point. Further studies are necessary to understand the influence of these drugs on the structure of the lungs during the second phase of developmental alveolarisation.

# Appendix A

# Pulmonary Functional Tests

## A.1 Lung Volumes

Figure A.1 is a graphical representation of the lung volumes. A definition of each volume is given below:

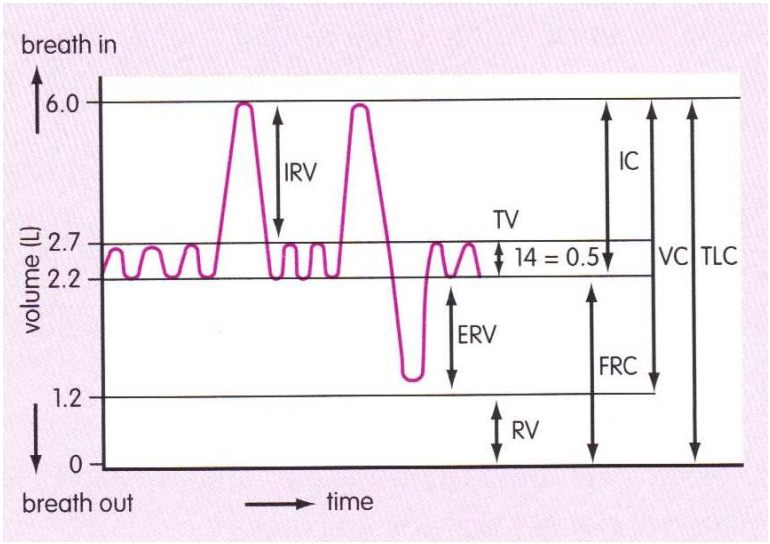


Figure A.1: Typical spirometer trace. Note that functional residual capacity (FRC) and residual volume (RV) can not be measured using a spirometer; thus, neither can total lung capacity (TLC). ERV = expiratory reserve volume; IRV = inspiratory reserve volume; TV = tidal volume; IC = inspiratory capacity; VC = vital capacity.

**FEV1** (Forced Expiratory Volume in 1 Second) = The amount of air that you can

forcibly blow out in one second, measured in litres. Along with FVC it is considered one of the primary indicators of lung function.

**FVC** (Forced Vital Capacity) = The total amount of air that you can forcibly blow out after full inspiration, measured in liters.

**PEF** (Peak Expiratory Flow) = The speed of the air moving out of your lungs at the beginning of the expiration, measured in liters per second.

**MEF 75,50,25%** (Maximal Mid-Expiratory Flow) = The average flow (or speed) of air coming out of the lung during the middle portion of the expiration.

**FRC** (Functional residual capacity) = The amount of air left in the lungs after a tidal breath out. The amount of air that stays in the lungs during normal breathing.

**RV** (Residual volume) = The amount of air left in the lungs after a maximal exhalation. The amount of air that is always in the lungs and can never be expired (i.e.: the amount of air that stays in the lungs after maximum expiration).

**TLC** (Total lung capacity) = The volume of gas contained in the lung at the end of maximal inspiration. The total volume of the lung (i.e. the volume of air in the lungs after maximum inspiration).

**VC** (Vital capacity) = The amount of air that can be forced out of the lungs after a maximal inspiration. Emphasis on completeness of expiration. The maximum volume of air that can be voluntarily moved in and out of the respiratory system.

## A.2 Measuring Lung Volumes

Spirometry is the most commonly used lung function screening study. It requires a voluntary maneuver in which a seated patient inhales maximally from tidal respiration to total lung capacity (TLC) and then rapidly exhales to the fullest extent until no further volume is exhaled at residual volume (RV)(Fig. A.1). The maneuver may be performed in a forceful manner to generate a forced vital capacity (FVC) or in a more relaxed manner to generate a slow vital capacity (SVC) (Figure A.2). In normal individuals, the inspiratory vital capacity, the expiratory SVC, and expiratory FVC are essentially equal. However, in patients with obstructive airways disease, the expiratory SVC is generally higher than the FVC.

A spirogram is a graphic representation of bulk air movement depicted as a volume-time tracing or as a flow-volume tracing. Values generated from a simple spirogram provide important graphic and numeric data regarding the mechanical properties of the lungs, including airflow (FEV1, along with other timed volumes) and exhaled lung volume (FVC or SVC). The measurement is typically expressed in liters for volumes or in liters per second for flows and is corrected for body temperature and pressure of gas that is saturated with water vapor. Data from a spirogram provides important clues to help distinguish obstructive pulmonary disorders that typically reduce airflow, such as asthma and emphysema, from restrictive disorders that typically reduce total lung volumes, including pulmonary fibrosis and neuromuscular disease.

Because spirometry is an expiratory maneuver, it measures exhaled volume or vital capacity but does not measure residual volume, functional residual capacity (or the resting lung volume), or TLC. Vital capacity is a simple measure of lung volume that is usually reduced in restrictive disorders; however, vital capacity is only an indirect measure of other lung volumes. Because residual volume is not exhaled through the mouth, it is not measured by a spirometer.

Other pulmonary function methodology is required to formally measure TLC, which is derived from the addition of FRC to inspiratory capacity obtained from spirometry. FRC is usually measured by a gas dilution technique or body plethysmography. Gas dilution techniques are based on a simple principle, are widely used, and provide a good

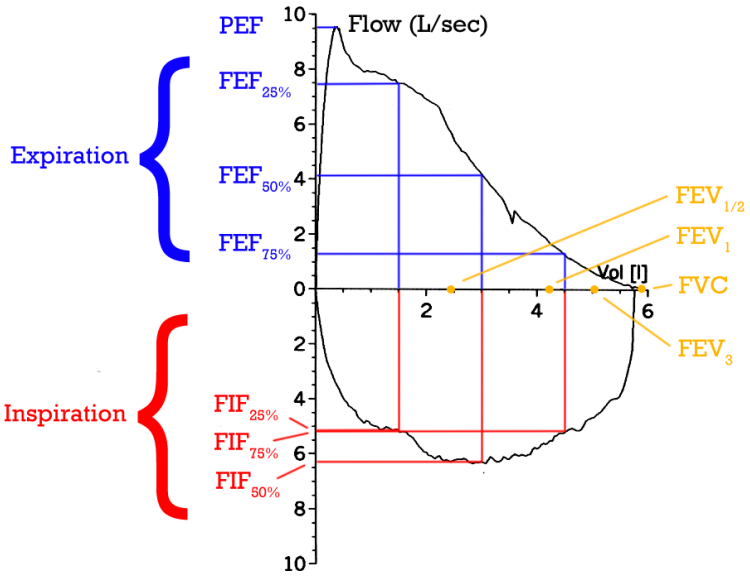


Figure A.2: Flow-Volume loop showing successful FVC maneuver. Positive values represent expiration, negative values represent inspiration. The trace moves clockwise for expiration followed by inspiration. (Note the FEV1, FEV1/2 and FEV3 values are arbitrary in this graph and just shown for illustrative purposes, they must be recorded as part of the experiment).

measurement of all air in the lungs that communicates with the airways. A limitation of this technique is that it does not measure air in ”noncommunicating” bullae and, therefore, may underestimate TLC, especially in patients with severe emphysema.

Gas dilution techniques use either closed-circuit helium dilution or open-circuit nitrogen washout. They are based on the inhalation of a known concentration and volume of an inert tracer gas, such as helium, followed by equilibration of 7 to 10 minutes in the closed-circuit helium dilution technique. The final exhaled helium concentration is diluted in proportion to the unknown volume of air in the patient’s chest (RV). Usually the patient is connected at the end-tidal position of the spirometer; therefore, the lung volume measured is FRC. In the nitrogen-washout technique, the patient breathes 100% oxygen and all the nitrogen in the lung is ”washed out.” The exhaled volume and the nitrogen concentration in that volume are measured. The difference in nitrogen volume at the initial concentration and at the final exhaled concentration allows a calculation of intrathoracic volume, usually FRC.

Body plethysmography is an alterative method of measuring lung volume that takes

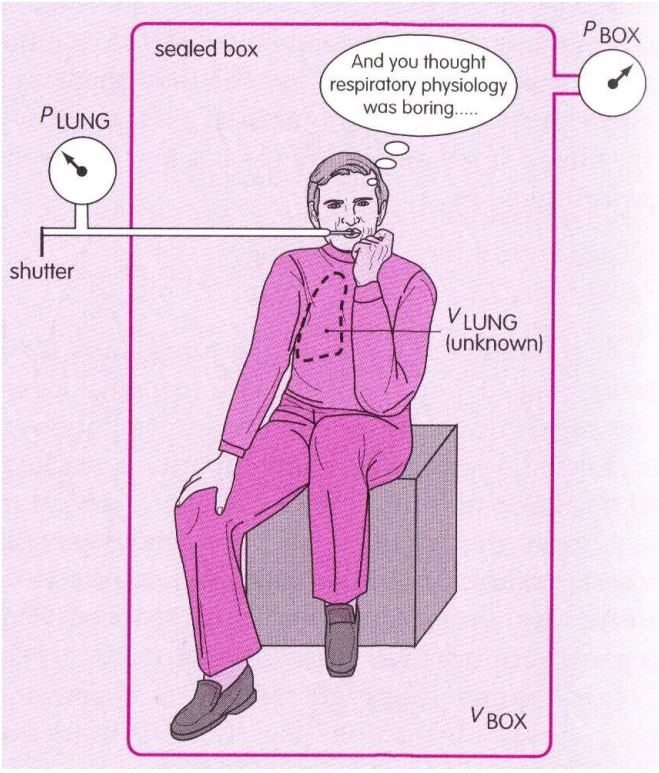


Figure A.3: Schematic of a ”body box” or plethysmograph.

advantage of the principle of Boyle's law, which states that the volume of gas at a constant temperature varies inversely with the pressure applied to it. The primary advantage of body plethysmography is that it can measure the total volume of air in the chest, including gas trapped in bullae. Another advantage is that this test can be performed quickly. Drawbacks include the complexity of the equipment as well as the need for a patient to sit in a small enclosed space. A patient is placed in a sitting position in a closed ”body box” with a known volume (Figure A.3). From the FRC, the patient pants against a closed shutter to produce changes in the box pressure proportionate to the volume of air in the chest. The volume measured by this technique is referred to as thoracic gas volume (TGV) and represents the lung volume at which the shutter was closed, typically FRC.

## A.3 Multiple Breath Nitrogen Washout

Conventional lung function tests such as the flow-volume loop and derived parameters such as FEF25-75% and FEV1 are limited in their capacity to differentiate subtle abnor-

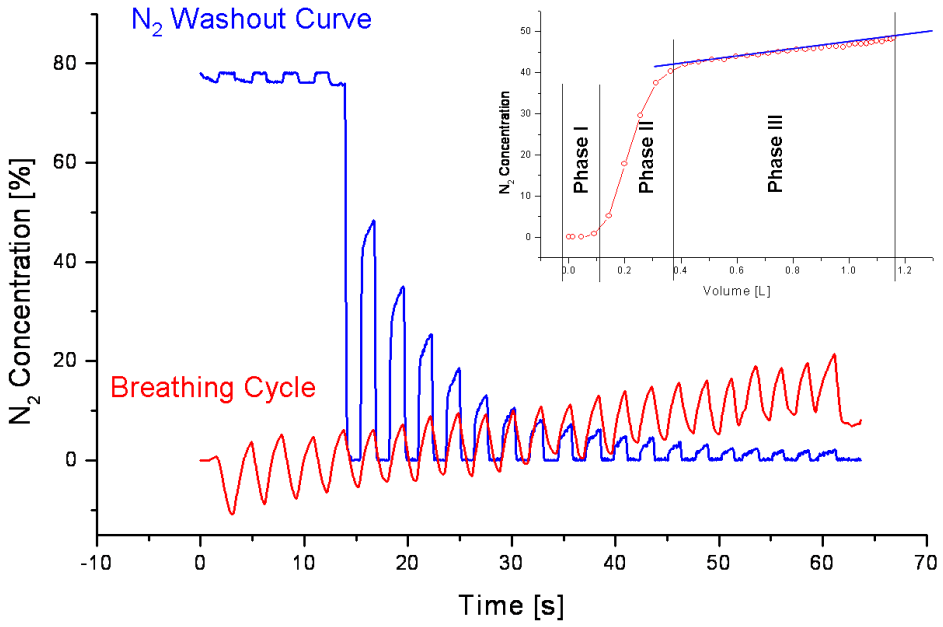


Figure A.4: Typical $N_2$ washout curve and breathing analysis showing the Phase III slope (inset).

malities in airway function arising independently in these two lung regions. There are two main reasons for this. Firstly, this test requires full inspiration followed by a maximal expiratory effort, which imposes unphysiologically large compressive pressures on the airways that can mask subtle changes in airway function. Secondly, the interpretation of the flow-volume loop remains uncertain as it is not yet clear what the exact contributions are from airway calibre, lung compliance and the mechanical linkage between airways and parenchyma. A far more specific and sensitive measure of peripheral versus proximal airway function has recently been described and is based on the multiple breath nitrogen washout (MBNW) test. This test is performed during tidal breathing and has been shown to provide a specific measure of structural asymmetries in the peripheral (acinar) and proximal (conducting) airways. Therefore, the MBNW test is ideal for our study as it provides indices of airway function that are representative of lung structure and sensitive to changes due to lung disease. Non-uniform ventilation within the normal lung is due to: (a) convection-dependent inhomogeneity and interaction between diffusion, and (b) convection in the presence of branching asymmetry or inequality in airway

cross-section. The latter occurs in the lung periphery, the former among the larger lung zones subtended more proximally. The MBNW test measures nitrogen concentration and volume during expiration following a breath of 100% oxygen. The slope of the expired nitrogen concentration versus volume is referred to as the slope of phase III (see Fig. A.4) and provides information about non-uniform ventilation within the acinar space. If all the alveoli emptied synchronously during expiration, the nitrogen gradient measured at the lips would be zero. However, in normal lungs and in particular lungs with abnormal airways, alveoli fill and empty at different rates according to the relative resistance of the airways serving them. This means that during a single tidal inspiration of oxygen most of the oxygen will be delivered to alveoli served by airways with least flow resistance. This creates a nitrogen gradient across alveoli. In the MBNW test the effect of airway asymmetry on the nitrogen gradient is deliberately amplified by measuring the change in slope of phase III in consecutive tidal breaths of oxygen.

# Appendix B

# Calculation of the Signal Attenuation Due to Diffusion for a Pair of Trapezoid Gradients

## B.1 The Half Trapezoid Case

Given trapezoid pulses with plateau time $\delta$ and ramp time $m$, the integral consists of three parts:

$$I = 2(I_1 + I_2 + I_3) \tag{B.1}$$

$$I_1 = \int_0^{\delta/2} \left( \int_0^t G(\tau) d\tau \right)^2 dt \tag{B.2}$$

$$I_2 = \int_{\delta/2}^{\delta/2+m} \left( \int_0^t G(\tau) d\tau \right)^2 dt \tag{B.3}$$

$$I_3 = \int_{\delta/2+m}^{\Delta/2} \left( \int_0^t G(\tau) d\tau \right)^2 dt \tag{B.4}$$

$$G(\tau) = \begin{cases} G & \text{if } \tau \in [0, \delta/2] < 0 \\ \mathbf{G}\big(1 + \frac{\delta}{2m} - \frac{1}{m} \cdot \tau\big) & \text{if } \tau \in [\delta/2, \delta/2 + m] \\ 0 & \text{if } \tau \in [\delta/2 + m, \Delta/2] \end{cases} \tag{B.5}$$

The $I_1$ and $I_3$ calculation is simple:

$$I_1 = \frac{G^2\delta^3}{24} \tag{B.6}$$

$$I_3 = \int_{\delta/2+m}^{\Delta/2} \left[ G\left(\frac{m+\delta}{2}\right)\right]^2 dt \tag{B.7}$$

$$I_3 = G^2\left[\frac{1}{8}\Delta\delta^2 + \frac{1}{4}\Delta\delta m + \frac{1}{8}\Delta m^2 - \frac{1}{8}\delta^3 - \frac{1}{2}\delta^2 m - \frac{5}{8}\delta m^2 - \frac{1}{4}m^3\right] \tag{B.8}$$

$I_2$ is more difficult to calculate; using $a \doteq \frac{\delta}{2}$ $I_2$ is:

$$\begin{aligned} I_2 = & G^2 \int_a^{a+m} \Bigg[ \underbrace{\left(\frac{a^4}{4m}\right)}_{I_{2-1}} + \underbrace{\left(-\frac{a^2}{m} - \frac{a^3}{m^2}\right) t}_{I_{2-\infty}} + \underbrace{\left(1 + \frac{2a}{m} + \frac{3a^2}{2m}\right) t^2}_{I_{2-3}} + \\ & \underbrace{\left(-\frac{1}{m} - \frac{a}{m^2}\right) t^3}_{I_{2-4}} + \underbrace{\left(\frac{1}{4m^2}\right) t^4}_{I_{2-5}} \Bigg] dt \end{aligned} \tag{B.9}$$

where

$$\frac{I_{2-1}}{G^2} = \frac{1}{4m}a^4 \tag{B.10}$$

$$\frac{I_{2-2}}{G^2} = -\frac{1}{2}ma^2 - \frac{3}{2}a^3 - \frac{a^4}{m} \tag{B.11}$$

$$\frac{I_{2-3}}{G^2} = \frac{1}{3}m^3 + \frac{5}{3}m^2 a + \frac{7}{2}ma^2 + \frac{7}{2}a^3 + \frac{3a^4}{2m} \tag{B.12}$$

$$\frac{I_{2-4}}{G^2} = \frac{1}{4}m^3 - \frac{5}{4}m^2a - \frac{5}{2}ma^2 - \frac{5}{2}a^3 - \frac{5a^3}{2} - \frac{a^4}{m} \tag{B.13}$$

$$\frac{I_{2-5}}{G^2} = \frac{1}{20}m^3 + \frac{1}{4}m^2a + \frac{1}{2}ma^2 + \frac{1}{2}a^3 + \frac{a^4}{4m} \tag{B.14}$$

finally:

$$\frac{I_2}{G^2} = \frac{2}{15}m^3 + \frac{2}{3}m^2a + ma^2 \tag{B.15}$$

$$\frac{I_2}{G^2} = \frac{2}{15}m^3 + \frac{1}{3}m^2\delta + \frac{1}{4}m\delta^2 \tag{B.16}$$

and,

$$\frac{I}{G^2} = \frac{-7}{30}m^3 + \frac{1}{4}\Delta m^2 + \frac{1}{2}\Delta\delta m - \frac{7}{12}\delta m^2 + \frac{1}{4}\Delta\delta^2 - \frac{1}{2}\delta^2 m - \frac{1}{6}\delta^3 \tag{B.17}$$

$$I = \frac{G^2\delta^2\Delta}{12}\left[3 - 2\left(\frac{\delta}{\Delta}\right) + 6x\left(1 - \frac{\delta}{\Delta}\right) + 3x^2\left(1 - \frac{7\delta}{3\Delta}\right) - \frac{14}{5}x^3\left(\frac{\delta}{\Delta}\right)\right] \tag{B.18}$$

where $x \doteq \frac{m}{\delta}$.

## B.2 The Full Trapezoid Case

Given trapezoid pulses with plateau time $\delta$ and ramp time $m$, the integral consists of four parts:

$$I = 2(I_1 + I_2 + I_3 + I_4) \tag{B.19}$$

$$I_1 = \int_0^{m/2}\left(\int_0^t G(\tau)d\tau\right)^2 dt \tag{B.20}$$

$$I_2 = \int_{m/2}^{m/2+\delta}\left(\int_0^t G(\tau)d\tau\right)^2 dt \tag{B.21}$$

$$I_3 = \int_{m+\delta}^{2m+\delta} \left( \int_0^t G(\tau) d\tau \right)^2 dt \tag{B.22}$$

$$I_4 = \int_{2m+\delta}^{\Delta/2-m-\delta/2} \left( \int_0^t G(\tau) d\tau \right)^2 dt \tag{B.23}$$

$$G(\tau) = G \times \begin{vmatrix} \tau/m & \text{if } \tau \in [0, m] \\ 1 & \text{if } \tau \in [m, m+\delta] \\ 2+\delta/m - \tau/m & \text{if } \tau \in [m+\delta, 2m+\delta] \\ 0 & \text{if } \tau \in [m+2\delta, \Delta/2 - m - \delta/2] \end{vmatrix} \tag{B.24}$$

$$I_1 = \frac{G^2 m^3}{20} \tag{B.25}$$

$$I_2 = G^2 \int_m^{m+\delta} \left[ \left( t - \frac{m}{2} \right) \right]^2 dt \tag{B.26}$$

$$I_2 = G^2 \left( \frac{1}{3}\delta^3 + \frac{1}{2}\delta^2 m + \frac{1}{4}\delta m^2 \right) \tag{B.27}$$

$$I_2 = G^2 \int_0^m \left( t' - \frac{t'^2}{2m} + \frac{m}{2} + \delta \right)^2 dt' \tag{B.28}$$

$$I_3 = G^2 \left( \delta^2 m + \frac{5}{3}\delta m^2 + \frac{43}{60} m^3 \right) \tag{B.29}$$

$$I_4 = G^2 \int_{m+\delta}^{\Delta} /2 - m - \delta/2 (m+\delta)^2 dt \tag{B.30}$$

$$I_4 = G^2 \left( \frac{1}{2}\Delta\delta^2 + \Delta\delta m^2 + \frac{1}{2}\Delta m^2 - \frac{1}{2}\delta^3 - 2\delta^2 m - \frac{5}{2}\delta m^2 - m^3 \right) \tag{B.31}$$

$$I = G^2 \left( \Delta\delta^2 + 2\Delta\delta m + \Delta m^2 - \frac{1}{3}\delta^3 - \delta^2 m - 76\delta m^2 - \frac{7}{15} m^3 \right) \tag{B.32}$$

$$I = G^2 \Delta\delta^2 \left[ \left( 1 - \frac{1}{3}\frac{\delta}{\Delta} \right) + \left( 2 - \frac{\delta}{\Delta} \right) x + \left( 1 - \frac{7}{6}\frac{\delta}{\Delta} \right) x^2 - \frac{7}{15}\frac{\delta}{\Delta} x^3 \right] \tag{B.33}$$

# Appendix C

# Swagelok Pneumatic Valves

## C.1 Ultra-high-Purity Fluoropolymer Diaphragm Valve

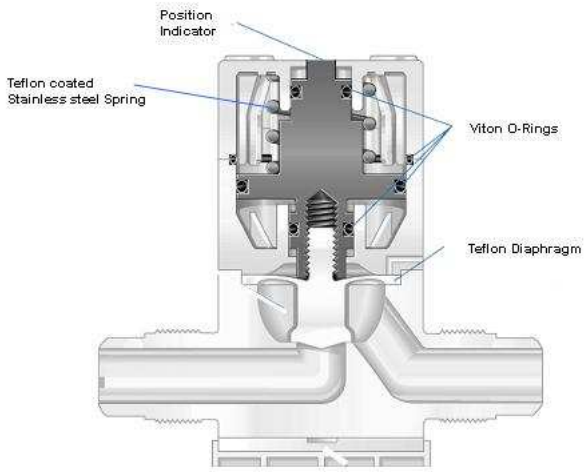


Figure C.1: Diagram of the pneumatic valve.

Table C.1: Pressure and temperature ratings and flow data.

| Media Temperature ($^{\circ}C$) | Pressure Rating (forward and reverse) (Bar) | Flow Coefficient ($C_V$) |
|---|---|---|
| 23-65 | 5.5 | 0.5 |

### C.1.1 Pressure and temperature ratings and flow data

### C.1.2 Materials of construction

Table C.2: Materials of construction for the valves components.

| Component | Material |
|---|---|
| 1 Hole plugs | Polypropylene |
| 2 Cap screws | Teflon-coated stainless steel |
| 3 Washers | Teflon-coated stainless steel |
| 4 Actuator housing | 20 % glass-filled polypropylene |
| 5 Diaphragm | DuPont Teflon (modified PTFE |
| 6 Body | DuPont Teflon (modified PTFE) |
| 7 Nuts | PFA |
| 8 Sleeve | PFA |
| 9 Gauge ring | ETFE |
| 10 Mounting bracket | 20 % glass-filled polypropylene |

# Appendix D

# Standard Operating Procedure $^3$He ADC. $^3$He Production and Administration for Clinical Trials

## D.1 Scope and Application

This method is used to measure the Apparent Diffusion Coefficient of $^3$He inside the human lung. It is used to investigate the lung microstructure of volunteers from different study groups (e.g. preterm, asthma, smoking, pollutants)

## D.2 Method Summary

A 30 ml hyperpolarised $^3$He sample mixed with high purity 250 ml $^4$He is administrated from a Tedlar® bag via a mouth piece connected through a one-way valve. No other substances are involved during gas production. During a breath hold of maximum 15 s a set of measurements is collected from the volunteer placed supine inside a permanent magnet at 0.15 T. ADC is measured by means of magnetic resonance.

## D.3 Definitions

- Apparent Diffusion Coefficient - is a measure of restricted movement of a substance across a unit area through a unit concentration gradient in unit time. This is related to the microstructure of the lung
- $^3$He - is an inert gas that is used, after optical pumping hyperpolarisation, as a contrast agent for NMR (Nuclear Magnetic Resonance) measurements
- Optical pumping - is a method to enhance the polarization of $^3$He in order to be NMR visible. It involves a laser shinning on a glass cell containing the $^3$He

## D.4 Health and Safety Warnings

- Optical polarization involves a high power laser in the polariser laboratory. Standard laser safety precautions for class IIIb should be followed. Note this apparatus is in a separate room from the scanner with keypad access and no access for volunteers
- The measurements are obtained in a high magnetic field environment. Standard high magnetic field safety precautions should be followed
- All mouthpieces shall be disposed after each measurement
- Laboratory equipment and benches shall be disinfected weekly
- Safety warning labels detailing the hazards of media are available in the polariser laboratory

## D.5 Equipment

- Polarising System - comprises of an electromagnet that produces a 20 gauss magnetic field, a 20 W NIR fiber laser, a system of tubes and glass cells for gas circulation and storage, a set of pumps for gas compression, a high vacuum pumping

system to prevent air contamination, $^3$He and $^4$He gas supply, a spectrometer to monitor the gas polarisation. (No access for volunteers)

- MR Scanner - permanent magnet 0.15 T, magnetic resonance spectrometer console
- Tedlar® bag
- Mouthpieces and one way valve

## D.6 Quality Control

- Run at least weekly an analysis on a reference volunteer (i.e. JOB or RG) to ensure the results are consistent
- Check monthly the tubing of the peristaltic pump
- Check monthly the integrity of the Tedlar® bag to ensure it doesn't leak
- Check monthly the tuning of the receiver coil to enable maximum signal
- Check daily the one way valve is functional

## D.7 Procedures

### D.7.1 General Procedures

- Disinfect work area before and after analysis
- Prepare the mouthpiece and one way valve
- Prepare the MR scanner - shim, tune the frequency, acquire a scout image, measure noise, attach the $^3$He coil, verify gating

### D.7.2 Sample Preparation

Ensure the vacuum pressure falls below $4{\cdot}10^{-2}$ mBar. Start flushing approximate 200 ml $^4$He to clean the gas manifold and glass cells. Start plasma discharge to clean the optical pumping cell (OPC). When the pressure in the OPC drops to 0 start the laser and release $^3$He into the system. Monitor the signal with the spectrometer and start collecting the gas in the storage cell as soon as the signal has reached the set value. Keep collecting for as long as needed. When ready, add $^4$He up to the set pressure, plug the Tedlar® bag and transfer the gas. Unplug when finished and attach the one way valve and mouthpiece.

### D.7.3 Volunteer preparation

Remove all magnetic objects, shoes and other unnecessary items before entering the magnet area and deposit them in the box provided. Place the volunteer supine on the bed with the coil on his/her chest. Position the volunteer in the centre of the magnet. Do two trial runs with a bag full of air to ensure the volunteer is familiar with the procedure and can hold breath for the duration of the acquisition.

### D.7.4 Sample Administration

Bring the sample into the scanner area. Put the mouthpiece into volunteer's mouth Once empty, remove the bag, wait a second for the volunteer to settle and trigger the acquisition. Keep the volunteer inside till all the measurements are finished or allow him/her to rest outside between measurements if necessary.

### D.7.5 Analysis

– ADC$_{msec}$ - Run the RARE based sequence with 64 views and 64 samples and get the echo decay. Plot the heights on a log scale, do a fit and find the slope. Calculate ADC from that slope

- ADC$_{sec}$ - Run the tagging sequence with 32 views and 128 samples. Set the repetition time to 400 ms and the wavelength to 1.7 cm. Plot the profiles versus time. Follow each stripe and fit their decay. Calculate ADC from the fit
- gADC - Run the global ADC measurement sequence with 50 views and 2048 samples, 12.5 KHz bandwidth. Plot the FIDs versus $b$ value. Using the multi-exponential and geometric model fit the data and derive ADC

## D.8 Data Storage

The results are saved in a spreadsheet for future reference and comparison. All the raw data are archived daily on at least two computers and regularly on optical support.

## D.9 Waste Management

All mouthpieces are disposable. The Tedlar® bag is reused.

# Bibliography


[1] H. U. Kauczor and B. Eberle, "Elucidation of structure-function relationships in the lung: contributions from hyperpolarized 3-helium MRI," *Radiology*, vol. 201, pp. 564–568, 1996.

[2] X. J. Chen, M. S. Chawla, L. W. Hedlung, H. E. Möller, J. R. MacFall, and G. A. Johnson, "MR microscopy of lung airways with hyperpolarised $^3$He," *Magnetic Resonance in Medicine*, vol. 39, pp. 79–84, 1998.

[3] D. Dupuich, Y. Berthezène, P. L. Clouet, V. Stupar, E. Canet, and Y. Crmillieux, "Dynamic 3He imaging for quantification of regional lung ventilation parameters," *Magnetic Resonance in Medicine*, vol. 50, pp. 777–783, 2003.

[4] K. K. Gast, M. U. Puderbach, I. Rodriguez, B. Eberle, K. Markstaller, A. T. Hanke, J. Schmiedeskamp, N. Weiler, J. Lill, W. G. Schreiber, M. Thelen, and H. U. Kauczor, "Dynamic ventilation helium-3 magnetic resonance imaging with lung motion correction gas flow distribution analysis," *Investigative Radiology*, vol. 37, no. 3, pp. 126–134, 2002.

[5] D. S. Gierada, B. Saam, D. Yablonskiy, J. D. Cooper, S. S. Lefrak, and M. S. Conradi, "Dynamic echo planar MR imaging of lung ventilation with hyperpolarized 3He in normal subjects and patients with severe emphysema," *NMR in Biomedicine*, vol. 13, no. 4, pp. 176–181, 2000.

[6] B. Saam, D. A. Yablonskiy, D. S. Gierada, and M. S. Conradi, "Rapid imaging of hyperpolarized gas using EPI," *Magnetic Resonance in Medicine*, vol. 42, no. 3, pp. 507–514, 1999.

[7] M. Salerno, T. A. Altes, and J. R. Brookeman, "Dynamic spiral MRI of pulmonary gas flow using hyperpolarized he-3: Preliminary studies in healthy and diseased lungs," *Magnetic Resonance in Medicine*, vol. 46, pp. 667–677, Oct 2001.

[8] M. Viallon, G. P. Cofer, S. A. Suddarth, H. E. Möller, X. J. Chen, M. S. Chawla, L. W. Hedlund, Y. Crémillieux, and G. A. Johnson, "Functional MR microscopy of the lung using hyperpolarized 3He," *Magnetic Resonance in Medicine*, vol. 41, pp. 787–792, 1999.

[9] M. Viallon, Y. Berthez'ene, V. Callot, M. Bourgeois, H. Humblot, A. Briguet, and Y. Crémillieux, "Dynamic imaging of hyperpolarized 3He distribution in rat lungs using interleaved-spiral scans," *NMR in Biomdeicine*, vol. 13, no. 4, pp. 207–213, 2000.

[10] J. M. Wild, M. P. Paley, L. Kasuboski, A. Swift, S. Fichele, N. Woodhouse, P. D. Griffiths, and E. J. R. van Beek, "Dynamic radial projection MRI of inhaled hyperpolarised helium-3 gas," *Magnetic Resonance in Medicine*, vol. 49, pp. 991–997, June 2003.

[11] A. J. Deninger, B. Eberle, M. Ebert, T. Grossmann, W. Heil, H. U. Kauczor, L. Lauer, K. Markstaller, E. Otten, J. Schmiedeskamp, W. Schreiber, R. Surkau, M. Thelen, and N. Weiler, "Quantification of regional intrapulmonary oxygen partial pressure evolution during apnea by helium-3 MRI," *Journal of Magnetic Resonance*, vol. 141, pp. 207–216, 1999.

[12] A. J. Deninger, B. Eberle, M. Ebert, T. Grossmann, G. Hanisch, W. Heil, H. U. Kauczor, K. Markstaller, E. Otten, W. Schreiber, R. Surkau, and N. Weiler, "3He-MRI-based measurements of intrapulmonary pO2 and its time course during apnea in healthy volunteers: first results, reproducibility, and technical limitations," *NMR in Biomedicine*, vol. 13, no. 4, pp. 194–201, 2000.

[13] A. J. Deninger, B. Eberle, J. Bermuth, B. Escat, K. Markstaller, J. Schmiedeskamp, W. Schreiber, R. Surkau, E. Otten, and H. U. Kauczor,

"Assessment of a single-acquisition imaging sequence for oxygen-sensitive helium-3-MRI," *Magnetic Resonance in Medicine*, vol. 47, pp. 105–114, 2002.

[14] B. Eberle, N. Weiler, K. Markstaller, H. U. Kauczor, A. Deninger, M. Ebert, T. Grossmann, W. Heil, L. O. Lauer, T. P. L. Roberts, W. G. Schreiber, R. Surkau, W. F. Dick, E. W. Otten, and M. Thelen, "Analysis of intrapulmonary O2 concentration by MR imaging of inhaled hyperpolarized helium-3," *Journal of Applied Physiology*, vol. 87, pp. 2043–2052, December 1999.

[15] B. Saam, W. Happer, and H. Middleton, "Nuclear relaxation of helium-3 in the presence of $O_2$," *Physical Review A*, vol. 52, no. 1, pp. 862–865, 1995.

[16] E. R. Weibel, *Morphometry of the Human Lung*. Berlin: Springer Verlag, 1963.

[17] B. Lebeau, "Pneumologie," *Paris: Ellipses*, 1989.

[18] J. Comroe, "Physiology of respiration.," *Chicago: Year book medical publishers*, 1965.

[19] J. West, "Physiologie respiratoire.," *Montral: HRW*, 1975.

[20] E. Weibel and R. Cristal, "Design of the airways and blood vessel considered as branching trees.," *The Lung: Specific Foundations. New York: Raven Press*, p. 717, 1991.

[21] E. Weibel and B. Haefeli-Bleuer, "Morphometry of the human pulmonary acinus.," *Anat Rec*, vol. 220, p. 413, 1988.

[22] M. Grippi, "Pulmonary pathophysiology," *Lippincott Williams&Wilkins*, 1995.

[23] B. Siegel and E. Potchen, "Radionuclides studies of pulmonary function.," *Prog Nucl Med*, vol. 3, pp. 49–66, 1973.

[24] H. Susskind, H. Atkins, J. Klopper, A. Ansari, P. Richards, and R. Fairchild, "Xenon-127 ventilation studies.," *Prog Nucl Med*, vol. 5, pp. 144–70, 1978.

[25] J. B. West, *Respiratory Physiology - the essentials*. Baltimore: Williams and Wilkins, 5th ed., 1995.

[26] C. Bergin, G. Rios, M. King, E. Belezzuoli, J. Luna, and W. Auger, "Accuracy of high-resolution CT in identifying chronic pulmonary thromboembolic disease," *Am. J. Roentgenol.*, vol. 166, no. 6, pp. 1371–1377, 1996.

[27] R. Coulden, "State-of-the-Art Imaging Techniques in Chronic Thromboembolic Pulmonary Hypertension," *Proc Am Thorac Soc*, vol. 3, no. 7, pp. 577–583, 2006.

[28] J. B. West, *Pulmonary Pathophysiology - the essentials*. Baltimore: Lippincott Williams and Wilkins, 6th ed., 2000.

[29] I. Murray and P. Ell, "Nuclear medicine in clinical diagnosis and treatment.," *Edinburgh: Churchill-Livingstone*, 1994.

[30] G. N. Hounsfield, "Computerized transverse axial scanning (tomography): Part 1. Description of system," *Br J Radiol*, vol. 46, no. 552, pp. 1016–1022, 1973.

[31] G. Prenier, "Imagerie thoracique de l'adulte.," *Paris: Flammarion*, 1996.

[32] H. Arakawa, W. Webb, M. McCowin, G. Katsou, K. Lee, and R. Seitz, "Inhomogeneous lung attenuation at thin-section CT: diagnostic value of expiratory scans.," *Radiology*, vol. 206(1), pp. 89–94, 1998.

[33] D. Alsop, H. Hatabu, M. Bonnet, J. Listerud, and W. Gefter, "Multi-slice, breathhold imaging of the lung with submillisecond echo times.," *Magn Reson Med*, vol. 33(5), pp. 678–82, 1995.

[34] M. Schmidt, G. Yang, P. Gatehouse, and D. Firmin, "FID-based lung MRI at 0.5 T: theoretical considerations and practical implications.," *Magn Reson Med*, vol. 39(4), pp. 666–72, 1998.

[35] J. Mayo, A. MacKay, and N. Muller, "MR imaging of the lungs: value of short TE spin-echo pulse sequences.," *Am J Roentgenol*, vol. 159(5), pp. 951–6, 1992.

[36] C. Bergin, D. Noll, J. Pauly, G. Glover, and A. Macovski, "MR imaging of lung parenchyma: a solution to susceptibility.," *Radiology*, vol. 183(3), pp. 673–6, 1992.

[37] R. M. Heidemann, M. A. Griswold, A. Haase, and P. M. Jakob, "VD-AUTO-SMASH imaging," *Magnetic Resonance in Medicine*, vol. 45, p. 10661074, 2001.

[38] R. M. Heidemann, M. A. Griswold, B. Kiefer, M. Nittka, V. Jellus, and P. M. Jakob, "Resolution enhancement in lung $^{1}$H imaging using parallel imaging methods," *Magnetic Resonance in Medicine*, vol. 45, p. 10661074, 2001.

[39] I. Young, D. Bailes, M. Burl, A. Collins, D. Smith, M. McDonnell, J. Orr, L. Banks, G. Bydder, R. Greenspan, and R. Steiner, "Initial clinical evaluation of a whole body nuclear magnetic resonance (NMR) tomograph.," *J Comput Assist Tomogr*, vol. 6(1), pp. 1–18, 1982.

[40] R. Edelman, H. Hatabu, E. Tadamura, W. Li, and P. Prasad, "Noninvasive assessment of regional ventilation in the human lung using oxygen-enhanced magnetic resonance imaging.," *Nature medicine*, vol. 2(11), pp. 1236–9, 1996.

[41] G. Caputo, C. Kondo, T. Masui, S. Geraci, E. Foster, M. O'Sullivan, and C. Higgins, "Right and left lung perfusion: in vitro and in vivo validation with oblique-angle, velocity-encoded cine mr imaging.," *Radiology*, vol. 180(3), pp. 693–8, 1991.

[42] Y. Berthezene, V. Vexler, D. Price, J. Wisner-Dupon, M. Moseley, K. Aicher, and R. Brasch, "Magnetic resonance imaging detection of an experimental pulmonary perfusion deficit using a macromolecular contrast agent. polylysine-gadolinium-DTPA40.," *Invest Radiol*, vol. 27(5), pp. 346–51, 1992.

[43] Y. Berthezene, V. Vexler, O. Clement, A. Muhler, M. Moseley, and R. Brasch, "Contrast-enhanced mr imaging of the lung: assessments of ventilation and perfusion.," *Radiology*, vol. 183(3), pp. 667–72, 1992.

[44] H. Hatabu, J. Gaa, D. Kim, W. Li, P. Prasad, and R. Edelman, "Pulmonary perfusion: qualitative assessment with dynamic contrast-enhanced MRI us-

ing ultra-short TE and inversion recovery turbo FLASH.," *Magn Reson Med*, vol. 36(4), pp. 503–8, 1996.

[45] H. Hatabu, J. Gaa, D. Kim, W. Li, P. Prasad, and R. Edelman, "Pulmonary perfusion and angiography: evaluation with breath-hold enhanced three-dimensional fast imaging steady- state precession MR imaging with short TR and TE.," *Am J Roentgenol*, vol. 167(3), pp. 653–5, 1996.

[46] H. Kauczor, "Contrast-enhanced magnetic resonance angiography of the pulmonary vasculature.," *Invest Radiol*, vol. 33(9), pp. 606–17, 1998.

[47] T. Amundsen, J. Kvaerness, R. Jones, A. Waage, L. Bjermer, G. Nilsen, and O. Haraldseth, "Pulmonary embolism: detection with MR perfusion imaging of lung–a feasibility study.," *Radiology*, vol. 203(1), pp. 181–5, 1997.

[48] M. Chawla, X. Chen, H. Moller, G. Cofer, C. Wheeler, L. Hedlund, and G. Johnson, "In vivo magnetic resonance vascular imaging using laser-polarized 3He microbubbles.," *Proc Natl Acad Sci U S A*, vol. 95(18), pp. 10832–5, 1998.

[49] J. Friedli, C. Paschal, J. Loyd, and S. Halliburton, "Quantitative 3D VUSE pulmonary MRA.," *Magn Reson Imaging*, vol. 17(3), pp. 363–70, 1999.

[50] H. Hatabu, D. C. Alsop, J. Listerud, M. Bonnet, and W. B. Gefter, "T2* and proton density measurement of normal human lung parenchyma using submillisecond echo time gradient echo magnetic resonance imaging," *European Journal of Radiology*, vol. 29, pp. 245–252, 1999.

[51] V. Mai and S. Berr, "MR perfusion imaging of pulmonary parenchyma using pulsed arterial spin labeling techniques: FAIRER and FAIR.," *J Magn Reson Imaging*, vol. 9(3), pp. 483–7, 1999.

[52] V. Mai, K. Hagspiel, J. Christopher, H. Do, T. Altes, J. Knight-Scott, A. Stith, T. Maier, and S. Berr, "Perfusion imaging of the human lung using flow-sensitive alternating inversion recovery with an extra radiofrequency pulse (FAIRER).," *Magn Reson Imaging*, vol. 17(3), pp. 355–61, 1999.

[53] A. Abragam, *Principles of Nuclear Magnetism.* London: Oxford University Press, 1996.

[54] C. Slichter, *Principles of Magnetic Resonance.* Springer-Verlag, third edition ed., 1990.

[55] B. Cowan, *Nuclear Magnetic Resonance and Relaxation.* Cambridge University Press, 1997.

[56] E. Fukushima and S. B. W. Roeder, *Experimental Pulse NMR. A Nuts and Bolts Approach*. Reading MA: Addison Wesley Publishing Co., 1981.

[57] E. Purcell, H. Torrey, and R. Pound, "Resonance absorption by nuclear magnetic moments in a solid," *Phys Rev*, vol. 69, p. 37, 1946.

[58] W. H. F. Bloch and M. Packard, "Nuclear induction.," *Phys Rev*, vol. 69, p. 127, 1946.

[59] P. Lauterbur, "Image formation by induced local interactions: Examples employing nuclear magnetic resonance," *Nature*, vol. 242, p. 190, 1973.

[60] P. Mansfield and P. Grannell, "NMR 'diffraction' in solids?," *J Phys C*, vol. 6, p. L442, 1973.

[61] M. G. R. Damadian and L. Minko, "NMR in cancer: XVI. fonar images of the live human body," *Physiol Chem Phys*, vol. 9, p. 97, 1977.

[62] D. Twieg, "The k-trajectory formulation of the NMR imaging process with applications in analysis and synthesis of imaging methods.," *Med Phys*, vol. 10, no. 5, pp. 610–21, 1983.

[63] S. Ljunggren, "A simple graphical representation of Fourier-based imaging methods.," *J Magn Reson*, vol. 54, pp. 338–43, 1983.

[64] J. Tropp, "An extended reciprocity principle for NMR reception.," in *12th annual SMRM*, 1993.

[65] D. I. Hoult and R. E. Richards, "The Signal to Noise Ratio of the Nuclear Magnetic Resonance experiment," *Journal of Magnetic Resonance*, vol. 24, pp. 71–85, 1976.

[66] P. L. DI Hoult, "The sensitivity of the zeugmatographic experiment involving human samples.," *J Magn Reson*, vol. 34, pp. 425–33, 1979.

[67] J. Ginefri, *Antenne de surface supraconductrice miniature pour l'imagerie RMN ´ 1.5 tesla.* PhD thesis, Orsay: Universit de Paris Sud, 1999.

[68] D. Lide, *CRC Handbook of Chemistry and Physics.* St. Louis: Boca Raton: CRC Press, 1991.

[69] A. Overhauser, "Polarisation of nuclei in metals.," *Phys Rev*, vol. 92, no. 9, pp. 411–5, 1953.

[70] T. Guiberteau and D. Grucker, "Dynamic nuclear polarisation at very low magnetic fields.," *Phys Med Biol*, vol. 43, pp. 1887–92, 1998.

[71] M. S. Albert, G. D. Cates, B. Driehuys, W. Happer, B. Saam, C. S. Springer, and A. Wishnia, "Biological magnetic resonance imaging using laser-polarised 129Xe," *Nature*, vol. 370, pp. 199–201, 1994.

[72] M. Slaman and R. Aziz, "Accurate transport properties and second virial coefficients for helium based on a state-of-the art interatomic potential.," *International Journal of Thermophysics*, vol. 12, no. 5, pp. 837–54, 1991.

[73] L. Wittenberg, J. Santarius, and G. Kulcinski, "Lunar source of $^3$He for comercial fusion power.," *Fusion technology*, vol. 10, pp. 167–79, 1986.

[74] C. Faisy, J. Diehl, E. Guerot, N. Rezgui, and J. Labrousse, "Utilisation du mélange hélium-oxygène en pratique pneumologique.," *Rev Mal Respir*, vol. 16, no. 6, pp. 1063–73, 1999.

[75] E. Gluck, D. Onorato, and R. Castriotta, "Helium-oxygen mixtures in intubated patients with status asthmaticus and respiratory acidosis.," *Chest*, vol. 98, no. 3, pp. 693–8, 1990.

[76] F. D. Colegrove, L. D. Schearer, and G. K. Walters, "Polarisation of helium-3 gas by optical pumping," *Physical Review*, vol. 132, pp. 2561–2572, 1963.

[77] J. Brossel, "Optical pumping in weak discharges.," *Fundamental Appl LASER Phys*, pp. 769–90, 1971.

[78] T. R. Gentile, G. L. Jones, A. K. Thompson, R. R. Rizi, D. A. Roberts, I. E. Dimitrov, R. Reddy, D. A. Lipson, W. Gefter, M. D. Schnall, and J. S. Leigh, "Spin-polarising 3He nuclei with an arc lamp pumped neodymium-doped lanthanum magnesium hexaluminate laser," *Physical Review A*, vol. 47, no. 1, pp. 456–467, 1993.

[79] E. Stoltz, M. Meyerhoff, N. Bigelow, M. Leduc, P. Nacher, and G. Tastevin, "High nuclear polarization in 3He and 3He-4He gas mixtures by optical pumping with a laser diode.," *Appl Phys B*, vol. B63, pp. 629–33, 1996.

[80] E. Stoltz, B. Villard, M. Meyerhoff, and P. Nacher, "Polarisation analysis of the light emitted by an optically pumped $^3$He gas.," *Appl Phys B*, vol. 63, pp. 635–40, 1996.

[81] F. Kober, *L'imagerie des gaz rares par résonance magnétique nucléaire*. PhD thesis, Grenoble: Joseph Fourier, 1998.

[82] F. Kober, P. Wolf, J. Leviel, G. Vermeulen, G. Duhamel, A. Delon, J. Derouard, M. Decorps, and A. Ziegler, "Low-temperature polarised helium-3 for MRI applications.," *Magn Reson Med*, vol. 41, pp. 1084–7, 1999.

[83] W. Happer, E. Miron, D. Schreiber, and W. A. van Wijngaarden X. Zeng, "Polarization of the nuclear spins of noble-gas atoms by spin exchange with optically pumped alkali-metal atoms," *Physical Review A*, vol. 29, no. 5, pp. 3092–3110, 1984.

[84] T. Walker and W. Happer, "Spin-exchange optical pumping of noble-gas nuclei.," *Rev Mod Phys*, vol. 69, no. 2, pp. 629–42, 1997.

[85] A. Nikiel, T. Palasz, M. Suchanek, M. Abboud, A. Sinatra, Z. Olejniczak, T. Dohnalik, G. Tastevin, and P.-J. Nacher, "Metastability exchange optical pumping of 3He at high pressure and high magnetic field for medical applications," *The European Physical Journal - Special Topics*, vol. 144, no. 1, pp. 255–263, 2007.

[86] J. Parra-Robles, A. R. Cross, and G. E. Santyr, "Theoretical signal-to-noise ratio and spatial resolution dependence on the magnetic field strength for hy-

perpolarized noble gas magnetic resonance imaging of human lungs," *Medical Physics*, vol. 32, no. 1, pp. 221–229, 2005.

[87] D. L. Bihan, R. Turner, P. Douek, and N. Patronas, "Diffusion MR imaging: clinical applications.," *Am J Roentgenol*, vol. 159, pp. 591–9, 1992.

[88] M. Brandl and A. Haase, "Molecular diffusion in NMR microscopy.," *J Magn Reson B*, vol. 103, pp. 162–7, 1994.

[89] F. Reif, *Cours de physique de Berkeley.* Paris: Armand Colin, 1967.

[90] J. Liner and S. Weissman, "Determination of the temperature dependance of gaseous diffusion coefficients using gas chromatographic apparatus.," *J Chem Phys*, vol. 56, no. 5, p. 2288, 1972.

[91] J. Brookeman, J. Mugler, J. Knight-Scott, E. D. Lange, and P. Bogorad, "Studies of $^3$He diffusion coefficient in the human lung: age-related distribution patterns.," *Eur Radiol*, vol. 9, no. 5, p. B21, 1999.

[92] B. Saam, D. A. Yablonskiy, V. Kodibagkar, J. C. Leawoods, D. S. Gierada, J. D. Cooper, S. S. Lefrak, and M. S. Conradi, "MR imaging of diffusion of $^3$He gas in healthy and diseased lungs," *Mag. Reson. Med.*, vol. 44, pp. 174–179, 2000.

[93] T.-S. Maier, J. Mai, J. M. III, and J. Brookeman, "Restricted diffusion of hyperpolarized 3He in the human lung.," in *6th congress of the International Society for Magnetic Resonance in Medicine*, p. 1913, 1998.

[94] T. Farrar and E. Becker, *Pulse and Fourier transform NMR.* Orlando: Harcourt Brace Jovanovich, 1971.

[95] H. Torrey, "Bloch equations with diffusion terms.," *Phys Rev*, vol. 104, no. 3, p. 563, 1956.

[96] E. P. H. Carr, "Effects of diffusion on free precession in nuclear magnetic resonance experiments.," *Phys Rev*, vol. 94, no. 3, pp. 630–8, 1954.

[97] P. Callaghan, "A simple matrix formalism for spin echo analysis of restricted diffusion under generalised waveforms.," *J Magn Reson*, vol. 129, pp. 74–84, 1997.

[98] E. O. Stejskal and J. E. Tanner, "Spin diffusion measurements: Spin echoes in the presence of a time-dependent field gradient," *Journal of Chemical Physics*, vol. 42, no. 1, pp. 288–292, 1965.

[99] W. Heil, H. Humblot, E. Otten, M. Schafer, R. Sarkau, and M. Leduc, "Very long nuclear relaxation times of spin polarized helium-3 in metal coated cells," *Physics Letters A*, vol. 201, pp. 337–343, 1995.

[100] E. E. D. Lange, J. P. Mugler, J. R. Brookeman, J. Knight-Scott, J. D. Truwit, and C. D. Teates, "Lung air spaces: MR imaging evaluation with hyperpolarized He-3 gas," *Radiology*, vol. 210, pp. 851–857, Mar 1999.

[101] N. R. Newbury, A. S. Barton, G. D. Cates, W. Happer, and H. Middleton, "Gaseous 3He-3He magnetic dipolar spin relaxation," *Physical Review A*, vol. 48, pp. 4411–4420, December 1993.

[102] E. Haacke, "The effects of finite sampling in spin-echo or field-echo magnetic resonance imaging.," *Magn Reson Med*, vol. 4, no. 5, pp. 407–21, 1997.

[103] P. Mansfield, "Multi-planar image formation using NMR spin echoes.," *J Phys C*, vol. 10, pp. L55–L8, 1977.

[104] J. Hennig, A. Nauerth, and H. Friedburg, "RARE imaging: a fast imaging method for clinical MR," *Magnetic Resonance in Medicine*, vol. 3, pp. 823–833, December 1986.

[105] L. Zhao, "Gradient-echo imaging considerations for hyperpolarised 129Xe MR.," *J Magn Reson B*, vol. 113, pp. 179–83, 1996.

[106] S. Fichele, *Hyperpolarised 3He Gas Production for Magnetic Resonance Imaging of the Human Airways*. PhD thesis, The University of Nottingham, School of Physics and Astronomy, 2002.

[107] B. Waters. PhD thesis, University of Nottingham, Nottingham, 2006.

[108] M. Leduc, P. J. Nacher, G. Tastevin, and E. Courtade, "Kinetics of helium-3 laser optical pumping," *Hyperfine Interactions*, vol. 127, pp. 443–449, 2000.

[109] T. R. Gentile, G. L. Jones, A. K. Thompson, R. R. Rizi, D. A. Roberts, I. E. Dimitrov, R. Reddy, D. A. Lipson, W. Gefter, M. D. Schnall, and J. S. Leigh,

"Demonstration of a compact compressor for application of metastability-exchange optical pumping of 3He to human lung imaging," *Magnetic Resonance in Medicine*, vol. 43, pp. 290–294, 2000.

[110] J. Becker, W. Heil, B. Krug, M. Leduc, M. Meyerhoff, P. Nacher, E. Otten, T. Prokscha, L. Schearer, and R. Surkau, "Study of mechanical compression of spin-polarised 3He gas," *Nuclear Instruments and Methods in Physics Research A*, vol. 346, pp. 45–51, 1994.

[111] D. Hussey, D. Rich, A. Belov, X. Tong, H. Yang, C. Bailey, C. Keith, J. Hartfield, G. R. Hall, T. Black, W. Snow, T. Gentiel, W. Chen, G. Jones, and E. Wildman, "Polarized 3He gas compression system using metastability-exchange optical pumping," *Review of Scientific Instruments*, vol. 76, pp. 053503–1–12, 2005.

[112] R. E. Jacob, S. Morgan, B. Saam, and J. C. Leawoods, "Wall relaxation of 3He in spin-exchange cells," *Physical Review Letters*, vol. 87, p. 143004, October 2001.

[113] R. Jacob, J. Teter, B. Saam, W. Chen, and T. Gentile, "Low-field orientation dependence of 3He relaxation in spin-exchange cells," *Physical Review A*, vol. 69, pp. 021401–1–4, 2004.

[114] J. Schmiedeskamp, W. Heil, E. Otten, R. Kremer, A. Simon, and J. Zimmer, "Paramagnetic relaxation of spin polarized 3He at bare glass surfaces," *The European Physical Journal D*, 2006.

[115] E. Durand, D. Vattolo, L. Darrasse, G. Guillot, P. J. .Nacher, and G. Tastevin, "Comparison of different sequences for imaging human lungs with hyperpolarised $^3$He at 0.1 T," in *Proceedings of 7th ISMRM Meeting*, p. 131, International Society for Magnetic Resonance in Medicine, 1999.

[116] E. Durand, G. Guillot, L. Darrasse, G. Tastevin, P.-J. Nacher, A. Vignaud, D. Vattolo, and J. Bittoun, "CPMG measurements and ultrafast imaging in human lungs with hyperpolarised helium-3 at low field (0.1 T)," *Magnetic Resonance in Medicine*, vol. 47, pp. 75–81, 2002.

[117] J. M. Wild, M. N. J. Paley, M. Viallon, W. G. Schreiber, E. J. R. van Beek, and P. D. Griffiths, "k-space filtering in 2D gradient-echo breath-hold hyperpolarized $^3$He MRI: spatial resolution and signal-to-noise ratio considerations," *Magnetic Resonance in Medicine*, vol. 47, p. 687695, 2002.

[118] D. A. Yablonskiy, A. L. Sukstanskii, and J. J. Ackerman, "Image artifacts in very low magnetic field MRI: The role of concomitant gradients," *Journal of Magnetic Resonance*, vol. 174, no. 2, pp. 279 – 286, 2005.

[119] D. A. Yablonskiy, A. L. Sukstanskii, and J. J. Ackerman, "Correction of concomitant magnetic field-induced image artifacts in nonaxial echo-planar imaging," *Magnetic Resonance in Medicine*, vol. 48, no. 3, pp. 509–515, 2002.

[120] P. Mitra, P. Sen, and L. Schwartz, "Short-time behaviour of the diffusion coefficient as a geometrical probe of porous media.," *Phys Rev B*, vol. 47, no. 14, pp. 8565–74, 1993.

[121] Dullien, *Porous media - fluid transport and pore structure.* San Diego: Academic Press, 1979.

[122] L. Latour, P. Mitra, R. Kleinberg, and C. Sotak, "Time-dependent diffusion coefficient of fluids in porous media as a probe of surface-to-volume ratio.," *J Magn Reson A*, vol. 101, no. 14, pp. 342–6, 1993.

[123] R. W. Mair, G. P. Wong, D. Hoffmann, M. D. Hürlimann, S. Patz, L. M. Schwartz, and R. L. Walsworth, "Probing porous media with gas diffusion NMR," *Physical Review Letters*, vol. 83, no. 16, pp. 3324–3327, 1999.

[124] L. Latour, R. Kleinberg, P. Mitra, and C. Sotak, "Pore-size distributions and tortuosity in heterogeneous porous media.," *J Magn Reson A*, vol. 112, no. 16, pp. 83–91, 1995.

[125] K. Brownstein and C. Tarr, "Importance of classical diffusion in NMR studies of water in biological cells.," *Phys Rev A*, vol. 19, no. 6, pp. 246–53, 1978.

[126] Glasel, "On the interpretation of water nuclear magnetic resonance relaxation times in heterogeneous systems.," *J Am Chem Soc*, vol. 96, no. 4, pp. 970–8, 1974.

[127] P. Mitra and P. Sen, "Effects of microgeometry and surface relaxation on NMR pulsed-fieldgradient experiments: simple pore geometries.," *Phys Rev B*, vol. 45, no. 1, pp. 143–56, 1992.

[128] M. Huerlimann, K. Helmer, T. D. Swiet, P. Sen, and C. Sotak, "Spin echoes in a constant gradient and in the presence of simple restriction.," *J Magn Reson A*, vol. 113, pp. 260–4, 1995.

[129] W. Hyslop and P. Lauterbur, "Effects of restricted diffusion on microscopic NMR imaging," *J Magn Reson*, vol. 94, pp. 501–10, 1991.

[130] B. Puetz, D. Barsky, and K. Schulten, "Edge enhancement by diffusion in microscopic magnetic resonance imaging.," *J Magn Reson*, vol. 97, no. 1, pp. 27–53, 1992.

[131] B. Robertson, "Spin-echo decay of spins diffusion in a bounded region.," *Phys Rev*, vol. 151, no. 1, p. 273, 1966.

[132] C. Neuman, "Spin echo of spins diffusing in a bounded medium.," *J Chem Phys*, vol. 60, no. 11, pp. 4508–11, 1973.

[133] P. L. Doussal and P. Sen, "Decay of nuclear magnetisation by diffusion in a parabolic magnetic field: an exactly solvable model.," *Phys Rev B*, vol. 46, no. 6, pp. 3465–85, 1992.

[134] S. Stoller, W. Happer, and F. Dyson, "Transverse spin relaxation in homogeneous magnetic fields.," *Phys Rev A*, vol. 44, no. 11, p. 7459, 1991.

[135] D. Swiet and P. Sen, "Decay of nuclear magnetisation by bounded diffusion in a constant field gradient.," *J Chem Phys*, vol. 100, pp. 5597–604, 1994.

[136] P. Callaghan, A. Coy, L. Forde, and C. Rofe, "Diffusive relaxation and edge enhancement in NMR microscopy.," *J Magn Reson A*, vol. 101, pp. 347–50, 1993.

[137] Y. Song, B. Goodson, B. Sheridan, T. D. Swiet, and A. Pines, "Effects of gas diffusion on magnetic resonance imaging of laser-polarised xenon gas.," *J Chem Phys*, vol. 108, no. 15, pp. 6233–9, 1998.

[138] P. Joseph, "An analytical model for diffusion of spins in a homogeneous field gradient.," *J Magn Reson B*, vol. 105, no. 15, pp. 95–7, 1994.

[139] J. Boxerman, L. Hamberg, B. Rosen, and M. Weisskoff, "MR contrast due to intravascular magnetic susceptibility perturbations.," *Magn Reson Med*, vol. 35, pp. 555–66, 1995.

[140] K. Packer, "The effects of diffusion through locally inhomogeneous magnetic fields on transverse fields nuclear spin relaxation in heterogeneous systems. proton transverse relaxation in striated muscle tissue.," *J Magn Reson*, vol. 9, pp. 438–44, 1973.

[141] J. R. Owers-Bradley, S. Fichele, A. Bennattayalah, C. J. S. McGloin, R. W. Bowtell, P. S. Morgan, and A. R. Moody, "MR tagging of human lungs using hyperpolarised He3 gas," *Journal of Magnetic Resonance Imaging*, vol. 17, pp. 142–146, 2003.

[142] L. Axel and L. Dougherty, "Mr imaging of motion with spatial modulation of magnetization," *Radiology*, vol. 171, pp. 841–845, 1989.

[143] D. A. Yablonskiy, A. L. Sukstanskii, J. C. Leawoods, D. S. Gierada, G. L. Bretthorst, S. S. Lefrak, J. D. Cooper, and M. S. Conradi, "Quantitative in vivo assessment of lung microstructure at the alveolar level with hyperpolarized He3 diffusion MRI," *Proceedings of the National Academy of Sciences*, vol. 99, pp. 3111–3116, March 2002. Also www.pnas.org/cgi/doi/10.1073/pnas.052594699 March 5, 2002 vol 99 no 5 3111-3116.

[144] S. Fichele, M. N. J. Paley, N. Woodhouse, P. D. Griffiths, E. J. R. van Beek, and J. M. Wild, "Investigating 3He diffusion NMR in the lungs using finite difference simulations and in vivo PGSE experiments," *Journal of Magnetic Resonance*, vol. 167, no. 1, pp. 1 – 11, 2004.

[145] D. M. Hyde, S. A. Blozis, M. V. Avdalovic, L. F. Putney, R. Dettorre, N. J. Quesenberry, P. Singh, and N. K. Tyler, "Alveoli increase in number but not size from birth to adulthood in rhesus monkeys.," *Am J Physiol Lung Cell Mol Physiol*, vol. 293, no. 3, pp. L570–579, 2007.

[146] B. Waters, J. Owers-Bradley, and M. Silverman, "Acinar structure in symptom-free adults by helium-3 magnetic resonance," *Am J Respir Crit Care Med*, vol. 173, pp. 847–851, 2006.

[147] J. C. Schittny, S. I. Mund, and M. Stampanoni, "Evidence and structural mechanism for late lung alveolarization," *Am J Physiol Lung Cell Mol Physiol*, vol. 294, no. 2, pp. L246–254, 2008.

[148] G. Davies and L. Reid, "Growth of the alveoli and pulmonary arteries in childhood.," *Thorax*, vol. 25, pp. 669–681, 1970.

[149] W. Thurlbeck, "Postnatal growth and development of the lung.," *Am Rev Respir Dis*, vol. 111, pp. 803–844, 1975.

[150] P. Burri, "The postnatal growth of the rat lung. III. morphology.," *Anat Rec*, vol. 180, pp. 77–98, 1974.

[151] J. Caduff, L. Fischer, and P. Burri, "Scanning electron microscopic study of the developing microvasculature in the postnatal rat lung.," *Anat Rec*, vol. 216, pp. 154–164, 1986.

[152] R. M. Beattie, N. M. Croft, J. M. Fell, N. A. Afzal, and R. B. Heuschkel, "Inflammatory bowel disease," *Arch Dis Child*, vol. 91, no. 5, pp. 426–432, 2006.

[153] R. S. Irwin and N. D. Richardson, "Side Effects With Inhaled Corticosteroids," *Chest*, vol. 130, no. 1 suppl, pp. 41S–53S, 2006.

[154] A. Brecher and S. Orlow, "Oral retinoid therapy for dermatologic conditions in children and adolescents.," *J Am Acad Dermatol*, vol. 49, p. 171182, 2003.

[155] G. D. Massaro and D. Massaro, "Retinoic acid treatment partially rescues failed septation in rats and in mice," *Am J Physiol Lung Cell Mol Physiol*, vol. 278, no. 5, pp. L955–960, 2000.

[156] S. Tschanz, B. Damke, and P. Burri, "Influence of postnatally administered glucocorticoids on rat lung growth.," *Biol Neonate*, vol. 68, p. 229245, 1995.

[157] S.-I. Takeda, C. C. Hsia, E. Wagner, M. Ramanathan, A. S. Estrera, and E. R. Weibel, "Compensatory alveolar growth normalizes gas-exchange function in immature dogs after pneumonectomy," *J Appl Physiol*, vol. 86, no. 4, pp. 1301–1310, 1999.

# Index